Superauflösende Fluoreszenzmikroskopie von biohybriden Polymersystemen an der fest-flüssig Grenzfläche

Von der Fakultät für Mathematik, Informatik und Naturwissenschaften der RWTH Aachen University zur Erlangung des akademischen Grades einer Doktorin der Naturwissenschaften genehmigte Dissertation

vorgelegt von

Laura Rebecca Hoppe Alvarez (M.Sc.)

aus

Darmstadt

Berichter*:* Universitätsprofessor Dr. rer. nat. Dominik Wöll

Universitätsprofessor Dr. rer. nat. Ulrich Simon

Tag der mündlichen Prüfung*:* 03.11.2020

Diese Dissertation ist auf den Internetseiten der Universitätsbibliothek verfügbar.

Eidesstattliche Erklärung

I, Laura Rebecca Hoppe Alvarez erklärt hiermit, dass diese Dissertation und die darin dargelegten Inhalte die eigenen sind und selbstständig, als Ergebnis der eigenen originären Forschung, generiert wurden.

Hiermit erkläre ich an Eides statt

1. Diese Arbeit wurde vollständig oder größtenteils in der Phase als Doktorand dieser Fakultät und Universität angefertigt;

2. Sofern irgendein Bestandteil dieser Dissertation zuvor für einen akademischen Abschluss oder eine andere Qualifikation an dieser oder einer anderen Institution verwendet wurde, wurde dies klar angezeigt;

3. Wenn immer andere eigene- oder Veröffentlichungen Dritter herangezogen wurden, wurden diese klar benannt;

4. Wenn aus anderen eigenen- oder Veröffentlichungen Dritter zitiert wurde, wurde stets die Quelle hierfür angegeben. Diese Dissertation ist vollständig meine eigene Arbeit, mit der Ausnahme solcher Zitate;

5. Alle wesentlichen Quellen von Unterstützung wurden benannt;

6. Wenn immer ein Teil dieser Dissertation auf der Zusammenarbeit mit anderen basiert, wurde von mir klar gekennzeichnet, was von anderen und was von mir selbst erarbeitet wurde;

7. Ein Teil oder Teile dieser Arbeit wurden zuvor veröffentlicht und zwar in

Kapitel 3:

1. L. Hoppe Alvarez, S. Eisold, R. A. Gumerov, M. Strauch, A. Rudov, P. Lenssen, D. Merhof, I. Potemkin, U. Simon, D. Wöll, **2019**, Deformation of µGs at Solid–Liquid Interfaces Visualized in Three-Dimension, *Nano Letters*, *19*(12), 8862-8867.
2. L. Hoppe Alvarez, S. Schog, E. Siemes, P. Lenssen, M. Strauch, D. Merhof, D. Wöll, **2019**, µBerry, https://publications.rwth-aachen.de/record/770675.

Kapitel 5:

1. Patentanmeldung: “Verfahren zum Strecken eines Nukleinsäuremoleküls”, Registrierungsnummer: DE 10 2019 119 782.1.

Düsseldorf, 03.11.2020

_____

Danksagung

Ich möchte mich in erster Linie bei Herrn Prof. Wöll für die Möglichkeit der Promotion in seiner Arbeitsgruppe bedanken. Herr Prof. Wöll hat mich als mein Mentor und Unterstützer seit meiner Bachelorarbeit bis hin zur Dissertation geprägt, gefördert und stets gefordert. Das Vertrauen und den mir stets gewährten Freiraum, weiss ich sehr zu schätzen.

Weiterhin möchte ich mich bei Herrn Prof. Simon für die Übernahme der Rolle des Zweitgutachters und die hervorragende Zusammenarbeit im Projekt A6 bedanken. Herr Prof. Simon hat sich immer viel Zeit für die wissenschaftliche Diskussion genommen und ist stets bemüht, uns Nachwuchswissenschaftlern viel mit auf den Weg zu geben. Danke!

Auch möchte ich mich bei Herrn Prof. Richtering und Frau Dr. Schneider für die Zusammenarbeit im SFB 985 bedanken. Ich habe als Doktorandenvertreterin viel gelernt und bin dankbar für das Vertrauen, welches mir geschenkt wurde. Durch die aktive Arbeit im Graduiertenkolleg war es mir möglich mein Netzwerk zu erweitern und Kooperationen ins Leben zu rufen die vielleicht sonst nicht entstanden wären.

Besonders möchte ich mich bei meinen Kollegen des AK Wölls, insbesondere Eric Siemes, Ashvini Purohit, Thomas Schmidt, Lukas Schubert und Silvia Centeno, sowie den Alumni Alex Oppermann, Oleksii Nevskyi und Mattis Hoffmann, für die konstruktiven wissenschaftlichen Diskussionen, aber auch für die tolle Arbeitsatmosphäre bedanken. Mein Dank gilt auch meinen wunderbaren Studenten Pia Lenßen, Kenneth Koziol, Lars Pritzlaff, Simon Schog und Lars Lohmann. Ich bin stolz auf euch und hoffe, dass Ihr euren wissenschaftlichen Weg auch weiterhin mit Spaß und Neugierde geht.

Auf Doktorandenebene möchte ich mich bei meinen Kolleginnen Sabine Eisold, Sabine Schneider und Rebecca Hengsbach für die spannende und erfolgreiche Zusammenarbeit im „Frauenpower“ Projekt A6 des SFB 985 bedanken. Ich bin stolz meine Arbeit an meine Studentin und Freundin Pia Lenßen übergeben zu können. Pia wird das A6 Team mit ihrer Motivation und wissenschaftlichen Gründlichkeit unterstützen und ich wünsche ihr hierbei Durchhaltevermögen und ganz viel Spaß. Meinen Kollegen Rustam Gumerov und Andrey Rudov möchte ich für die Zusammenarbeit an der Thematik „Mikrogele an der fest-flüssig Grenzfläche“ bedanken. Den Laboranten Birgit Hahn und Niklas Lothmann des AK Simon möchte ich für Unterstützung bei der Vorbereitung der Substrate und der Durchführung der Elektronenstrahlithographie danken.

Der DFG danke ich für die finanzielle Unterstützung im Rahmen des Sonderforschungsbereichs 985 „Funktionelle Mikrogele und Mikrogelsysteme“.

Meinen Freunden, meiner Familie und besonders meinem Mann gilt mein Dank für ihre bedingungslose Unterstützung.

“*Wenn die Menschen nur über das sprächen, was sie begreifen, dann würde es sehr still auf der Welt sein“*

- Albert Einstein

“*On ne fait jamais attention à ce qui a été fait; on ne voit que ce qui reste à faire*.“

- Marie Curie

Publikationsliste

Veröffentlichungen

2. L. Hoppe Alvarez, S. Eisold, R. A. Gumerov, M. Strauch, A. Rudov, P. Lenssen, D. Merhof, I. Potemkin, U. Simon, D. Wöll, **2019**, Deformation of µGs at Solid–Liquid Interfaces Visualized in Three-Dimension, *Nano Letters*, *19*(12), 8862-8867.

3. D. Wöll, A. Oppermann, O. Nevskyi, A. Purohit, S. Centeno Beningo, A. Purohit, E. Siemes, L. Hoppe Alvarez, **2018**, Superresolved fluorescence microscopy of soft matter: from the development of novel photoswitches to the visualization of compartmentalized µGs, *Bulletin of the American Physical Society*, *63.*

Software Veröffentlichungen

L. Hoppe Alvarez, S. Schog, E. Siemes, P. Lenssen, M. Strauch, D. Merhof, D. Wöll, **2019**, µBerry, https://publications.rwth-aachen.de/record/770675.

Patentanmeldungen

Registrierungsnummer: DE 10 2019 119 782.1.

Anmeldedatum der Prioritätsanmeldung: 22.07.2019

Titel: “Verfahren zum Strecken eines Nukleinsäuremoleküls”

Status (am Tag der Einreichung dieser Dissertation): Patentanmeldung beim Deutschen Patent- und Markenamt. Patentanmeldung ist noch nicht offengelegt.

Abstract

Die vorgestellte Dissertation fand unter der Anleitung von Prof. Dr. Dominik Wöll an Institut für Physikalische Chemie der RWTH Aachen University im Rahmen des Sonderforschungsbereiches 985 „Funktionelle Mikrogele und Mikrogelsysteme“ statt.

Bei den hier vorgestellten Ergebnissen steht die Erforschung von Mikrogelen an der fest-flüssig-Grenzfläche, sowie die Analyse mittels fluoreszenzspektroskopischer Verfahren im Vordergrund. Im Laufe der Dissertation ist auch die automatisierte Datenanalyse durch die Entwicklung entsprechender Software und Algorithmen hinzugekommen.

Eines der in dieser Arbeit vorgestellten SFB-Projekte beschäftigt sich mit dem Deformationsverhalten von Mikrogelen an der Oberfläche. Dabei wurde die Mikrogelkonformation auf Oberflächen unterschiedlicher Hydrophilie mittels moderner 3D Fluoreszenzmikroskopiemethoden untersucht. Es konnte gezeigt werden, dass eine hydrophile Oberfläche das Lösungsmittel imitiert und das Mikrogel dadurch seine native, sphärische Struktur behält. Auf hydrophoben Oberflächen dagegen konnte die sogenannte „Spiegelei“-Konformation abgebildet werden.

Die Deformation von Mikrogelen wurde weiterhin in Abhängigkeit der Depositionsmethode auf der Oberfläche untersucht. Die gängigen Labortechniken „drop-casting“, „spin-coating“, sowie Adsorption aus der Lösung wurden dafür verglichen. Es konnte gezeigt werden, dass der Einfluss des Lösungsmittelverdampfens eine wichtige Rolle neben der Oberflächenhydrophilie einnimmt. Die Ergebnisse wurden ferner im Rahmen einer SFB-Kooperation mittels Computersimulationen verifiziert, und die Kompatibilität der existierenden theoretischen Modelle zur Mikrogeldeformation mit den empirischen Ergebnissen der hier vorgestellten Arbeit gezeigt.

Weiterhin wurde in einem zweiten Projekt in einer Kooperation innerhalb des Sonderforschungsbereichs eine neue Methode zur Immobilisierung von Mikrogelen an ein definiertes Oberflächenmuster entwickelt. Hierfür wurden die bekannten Techniken der chemischen Elektronenstrahllithographie und der Photolithographie kombiniert. Die Forschungsergebnisse konnten zeigen, dass es möglich ist, DNA-funktionalisierte Mikrogele gezielt über DNA-Hybridisierung an ein Oberflächenmuster anzubringen.

Durch die gewonnene Expertise im Bereich vernetzter Polymere an Oberflächen wurde im Rahmen dieser Arbeit eine Kooperation mit dem Institut für Organische Chemie der RWTH Aachen University ins Leben gerufen. Es wurde eine neue Methode zum Strecken von DNA-Molekülen in thermoresponsiven Hydrogelen entwickelt. Dies erlaubt die Analyse von DNA-Proben in Hinblick auf (epi-)genetische Veränderungen durch fluoreszenzbasierte optische Kartierung (optical Mapping). Das zugrundeliegende Konzept zum Linearisieren von DNA-Molekülen wurde in Form eines Verfahrenspatents angemeldet, welches zum Zeitpunkt der Abgabe dieser Dissertation geprüft wird.

Abbreviations

Abbreviation	Full Term
(d)STORM	(Direct) Stochastic Optical Reconstruction Microscopy
µG	Microgel
2D	Two Dimensional
3D	Three Dimensional
A	Adenine
AdoMet	S-Adenosyl-L-Methionine
AFM	Atomic Force Microscopy
Ai-NP	Gold-Nanoparticles
bp	Base-Pair
C	Cytosine
CCD	Charge-Coupled Device
c-EBL	Chemical-Electron Beam Lithography
CRC	Collaborative Research Center
DH	Double-Helix
DNA	Deoxyribonucleic acid
DPD	Dissipative Particle Dynamics
DSC	Differential Scanning C35alorimetry
EBL	Electron-Beam Lithography
FIB	Focused Ion Beam
FENE	Finitely Extensible Nonlinear Elastic
FOCTS	Trichloro(1H,1H,2H,2H-perfluorooctyl)silane
FSHD	Facioscapulohumeral Muscular Dystrophy
G	Guanine
GSD	Ground State Depletion
IC	Internal Conversion
ISC	Intersystem Crossing
ITO	Indium-Tin-Oxide
MD	Molecular Dynamics
NP	Nano Particles
NPPOC	2-(2-nitrobenzyl) ethyl
ODS	n-OctaDecyltrimethoxySilane
PALM	Photoactivated Localization Microscopy
PBS	Phosphate-Buffered Silane
PEG	O-(2-aminoethyl)PolyEthylene Glycol

pNIPAM	Poly (N-isopropylacrylamide)
pNIPMAM	Poly (N-isopropylmethacrylamide)
PPG	Photolabile or Photocleavable Protecting Group
PSF	Point Spread Function
REases	Restriction Endonucleases
RESOLFT	Reversible Saturated Optical Fluorescence Transitions
RNA	Ribonucleic Acid
SAM	Self-Assembled Monolayer
sDNA	Single DNA Strands
SEM	Scanning Electron Microscopy
SFM	Scanning Force Microscopy
SIM/SSIM	(Saturated) Structured Illumination Microscopy
SMCC	Succinimidyl 4-(N-Maleimidomethyl)Cyclohexane-1-Carboxylate
SMPB	Succinimidyl 4-(p-Maleimidophenyl)Butyrate
SOFI	Super-Resolution Optical Fluctuations Imaging
SRFM	Super-Resolution Fluorescence Microscopy
STED	Stimulated Emission Depletion
T	Thymine
TIRF	Total Internal Reflection Fluorescence
ULC	Ultra-Low Crosslinked
UV	Ultraviolet
ViSP	Visual Serving Platform
VPT	Volume Phase Transition
VPTT	Volume Phase Transition Temperature
VR	Vibrational Relaxation

Content

1. Introduction

Recent developments in the fluorescence microscopy community have fundamentally changed the scope of fluorescence microscopy techniques.(Möckl, Lamb et al. 2014) Nowadays, super-resolution fluorescence microscopy methods allow us to resolve structures below the diffraction limit of light which has especially impacted and revolutionized biological and biomedical research. The number of research groups performing super-resolution techniques has increased significantly in the last years due to the flexibility of the different methods. The variety of techniques that can be added in order to gain 3D information has furthermore been a gamechanger in the structural analysis. The adoption of these techniques by the materials science community has taken place at a slower pace, as imaging of materials has been typically performed with electron microscopy or scanning probe microscopy.(Wöll and Flors 2017) Even though these techniques allow for an extremely high resolution, novel 3D super-resolution measurements also offer spatial resolution of tens of nanometers and thereby close the gap between the existing techniques. Furthermore, super-resolution techniques have the advantage of being non-invasive and offer the possibility of measuring dynamics in situ or probing below the outer surface of a material.(Wöll and Flors 2017)

An increasing number of articles has been published in recent years, showing that super-resolution fluorescence techniques are used for structural analysis in polymer sciences.(Boott, Laine et al. 2015, Nevskyi, Sysoiev et al. 2016) Subsequently, these techniques have penetrated to more specialized areas, amongst others the investigation on polymeric crosslinked structures like microgel (µG) systems.(Conley, Nöjd et al. 2016, Siemes, Nevskyi et al. 2018) µGs can be defined as crosslinked polymer networks in the micro or nanometer range. They exhibit the ability to swell or collapse upon external stimuli due to their characteristic volume phase transition temperature (VPTT). This makes them promising candidates as actuators or micro-reactor systems. The synthesis of a variety of different µG systems has shown that there are diverse fields of applications. One promising example for application uses biodegradable µGs for drug uptake and release.(Pich and Richtering 2010) The increasing demand for complex applications of µG systems makes it extremely important to understand their fundamental structure in different situations.

On the one hand, the degree of crosslinking dramatically impacts the µG characteristics, including its VPTT. On the other hand, the µG behavior at different interfaces has to be studied in order to develop reliable applications.

For example, when µGs shall be applied in technical devices, they typically need to be immobilized on solid supports. Therefore, controlling and analyzing their shape at the solid-liquid interface is of great importance.(Schmidt, Hellweg et al. 2008, Wellert, Kesal et al. 2015) It is known that one of the properties that clearly differentiates µGs from particles is their ability to spread at the interface. This spreading behavior into the so-called fried egg conformation has to be suppressed for most applications, as the µG needs to function in its native, spherical conformation.

This dissertation is embedded in the framework of the Collaborative Research Center (CRC, Sonderforschungsbereich) 985, funded by the German Research Association (Deutsche Forchungs Gemeinschaft, DFG). This CRC focuses on functional µGs and µG systems. Different disciplines being Chemistry, Biology, Physics, Engineering and Medicine collaborate within this framework in order to investigate the complex synthesis, characteristics and applications of µGs. The collaborative research center is built in a way that a variety of sub-projects focus on specialized scientific questions. The research presented in this dissertation focuses on µGs at the solid-liquid interface from the fundamental surface-µG interactions up to new methods for immobilization at the interface illustrated in Fig. 1-1. It is therefore important to point out that every project presented in this dissertation stems from a successful cooperation between different scientific disciplines.

Chapter 3 outlines how modern fluorescence microscopy techniques can be employed in order to investigate the deformation of µGs at the solid-liquid interface. The spreading behavior was investigated on highly crosslinked µGs, instead of low crosslinked µGs which have been subject to investigations in the past.(Schulte, Scotti et al. 2019) Furthermore, this chapter outlines the differentiation of the spreading behavior of poly (N-isopropylmethacrylamide) µGs at surfaces of different hydrophilicities. The different laboratory techniques used for µG deposition at the solid substrate was also investigated regarding the spreading of µGs. Due to a combined analysis of computer simulation data and 3D super-resolution data, chapter 3 additionally provides a guideline on how to choose the ideal laboratory techniques in order to retain the native, spherical µG shape. Finally, an approach to parametrize the µG shape enabling the quantitative comparison of 3D data independent from its acquisition method, is presented.

Chapter 4 builds on the parameters investigated in the first chapter regarding the ideal surface conditions to maintain the native µG shape. These findings are of great importance for the joint lithographic approach that is presented in this second chapter.

Chemical-electron beam lithography (c-EBL) is combined with photolithography in order to circumvent the diffraction limit of light which is the limiting factor for photolithography. The combined lithographic approach is used to immobilize deoxyribonucleic-acid (DNA)-functionalized µGs to DNA strands at a surface pattern. The resulting biohybrid system represents a promising candidate for future biomedical applications.

The accumulated expertise in the field of surface bound, biohybrid polymer systems leads to the investigations presented in chapter 5. In this final chapter, a method to stretch DNA molecules in hydrogels at the surface will be presented. This new approach challenges the cost-intensive state-of-the-art DNA stretching methods that are used for methods like optical mapping. DNA stretching is of paramount importance when it comes to epigenetic analysis or to the identification of structural variations causing diseases.

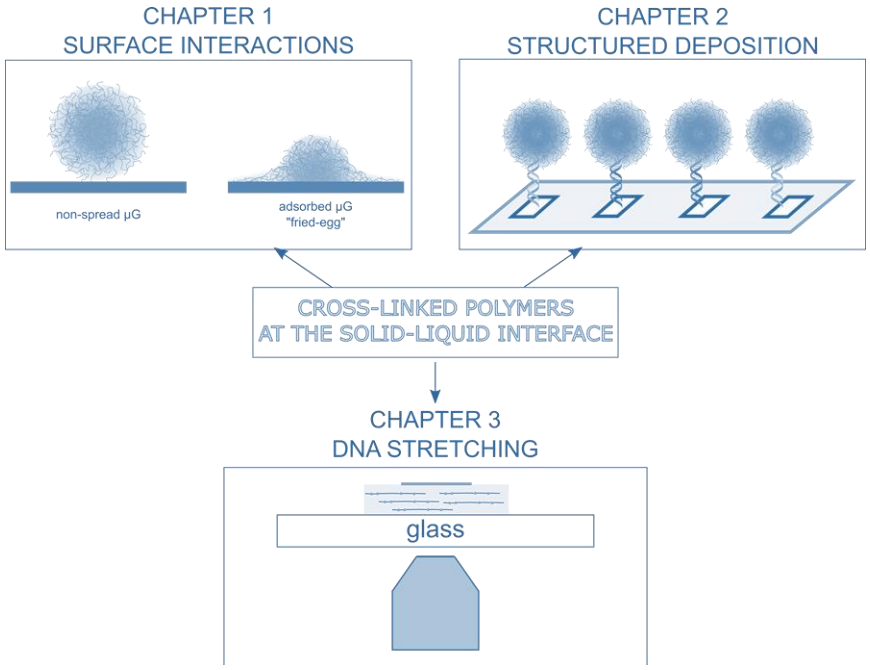

Fig. 1-1: Schematic overview of the different projects represented in this work.

Furthermore, every chapter in this dissertation not only covers the experimental optimization but also the automated analysis of the acquired data. The importance of the incorporation of modern analysis techniques and image analysis algorithms will be demonstrated throughout the different chapters. To summarize, this dissertation outlines the topic of crosslinked polymer systems at the solid support. Thereby fundamental findings will be combined with new methods and applications.

2. Scientific background

This chapter serves as a scientific basis for the interpretation of the results discussed in chapters 3, 4 and 5. The analysis method that is employed throughout all the different chapters is fluorescence microscopy. Therefore, the different techniques and fundamentals are presented in section 2.1. It should be noted that the focus lies on super resolution fluorescence microscopy (SRFM) techniques presented in section 2.1.4. The two lithographic methods that are the basis of the combined lithographic approach presented in Chapter 3, are presented in section 2.2. As this dissertation is embedded in the CRC for functional µGs and µG systems, and introduction to µG systems – with a focus on µGs at the interface – is given in section 2.3. Even though this dissertation does not focus on bio-chemistry, the theoretical introduction of DNA and its properties is of great importance for chapters 4 and 5. One of the main findings in chapter 4 involves the hybridization of DNA-functionalized µGs to DNA strands at the surface. It is therefore crucial to understand the basic concepts of hybridization and melting for this chapter. However, a biomedical application to stretch DNA molecules in hydrogels is presented in chapter 5. Therefore, the concept of optical DNA mapping is presented. This chapter informs the reader about the alternative methods, which play an important role for the motivation of the patent application that was filed with the presented idea.

2.1. Fluorescence microscopy

Fluorescence microscopy is an essential tool in several fields ranging from biological applications (Pepperkok and Ellenberg 2006) to material sciences (Wöll and Flors 2017). It is an optical microscopy technique, used to image the collected emission-light from a fluorescing sample. Fluorescence microscopy is a technique that offers a high contrast in combination with high specificity.

The specificity is given through the various options of labeling specific functional groups or regions within a specimen. Fluorescence microscopy additionally allows for quantitative analysis that can be extracted from the intensity information. It furthermore can be used for live imaging as it is a non-invasive technique.

The limitations of optical microscopy methods directly depend on the diffraction limit of light which has been described by Ernst Abbe.(Abbe 1873) Abbe reported that the smallest resolvable distance between two points using a conventional microscope may never be smaller than half the wavelength of the imaging light. The Abbe formula (1) describes the diffraction limit as proportional to the wavelength and inversely proportional to the angular distribution of the light observed.

$$d = \frac{\lambda}{2 \cdot n \cdot \sin(\alpha)} \tag{1}$$

Therefore, a lens-based microscope cannot resolve objects that are closer in distance than approximately half the wavelength of the light in the imaging plane For visible light, this limit is approximately 200 nm of spatial resolution.(Nevskyi, Wöll et al. 2018)

The image of a point-shaped emitter is not a point but a smeared spot with a characteristic intensity profile. This profile is referred to as the point spread function (PSF) of the imaging lens (see Fig. 2-1). The objective lens collects only a limited fraction of the diffraction pattern and projects it into its back focal plane. Therefore, the spatially extended, complete Fourier transformation in the back focal plane is restricted to the set of frequencies below the limiting frequency. It contains only those frequencies that can be transmitted by the lens.(Kubitscheck and Peters 2013)

Mathematically, the PSF for a perfect optical system is referred to as the “Airy Pattern” derived from the Fraunhofer diffraction theory (von Fraunhofer 1823) given by the squared modulus of the Fourier transform of the circular aperture:

$$I(u) = \frac{1}{(1-\varepsilon^2)}\left[\frac{2J_1(u)}{u} - \varepsilon^2 \frac{2J_1(\varepsilon u)}{\varepsilon u}\right]^2 = \left[\frac{2J_1(u)}{u}\right]^2 \tag{2}$$

J_1 is the Bessel function of the first kind and ε is the fraction radius of the central obscuration of the primary aperture. $I(u)$ describes the surface brightness in the focal plane, normalized to its maximum at $u = 0$. The dimensionless distance from the optical axis in the focal plane is given by u, and is related to the angular radius θ (measured from the primary aperture).

u is also related to D, the diameter of the primary aperture, resulting in the following equation with the wavelength λ:

$$u = \frac{\pi}{\lambda} D\theta \tag{3}$$

The Airy pattern consists of a series of sharp dark rings alternating with broader bright rings. The pattern drops to 50% power at a radius of 0.514 λ / D . Its full width half maximum (FWHM) can be calculated to $(FWHM) = 1.028\lambda / D$.The core of the Airy Pattern, inside the first minimum is often called the “Airy Disk” after Sir George Biddell Airy, an English astronomer.(Hecht 2001) It contains 86% of the total light in the image, it is depicted in Fig. 2-1.

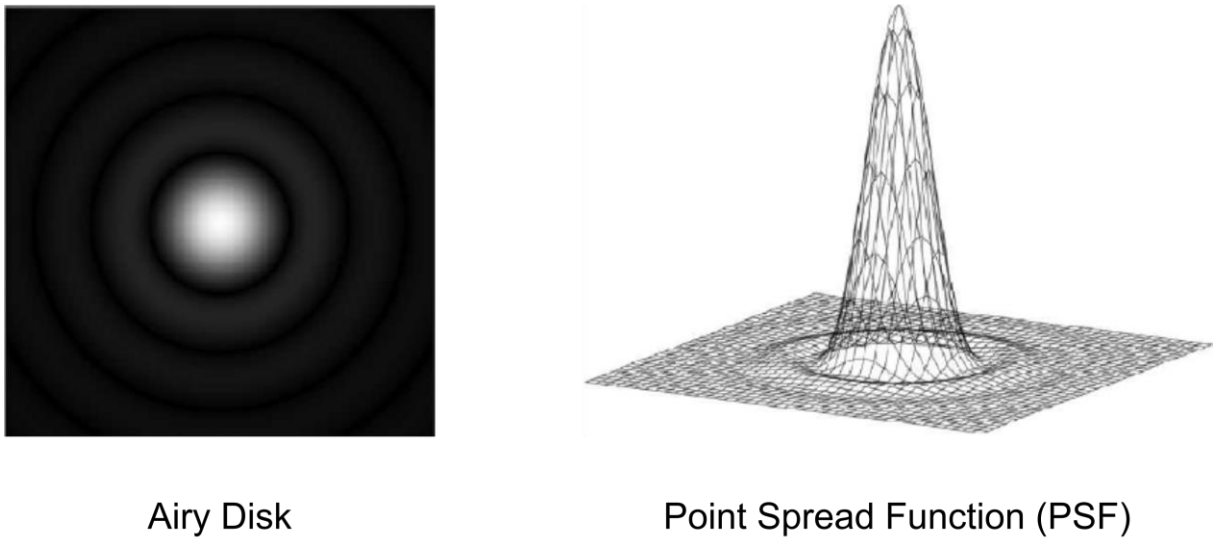

Fig. 2-1: The PSF describes the intesity profile of a point-shaped emitter. The Airy Disk describes the intensity distribution of the signal depending on the radius. The figure has been adapted from Schmolte et al.(Schmolze, Standley et al. 2011)

Based on these fundamentals, different microscopy techniques will be presented in the following paragraphs. First the diffraction limited techniques wide-field microscopy (see 2.1.1), confocal microscopy (see 2.1.2) and total internal reflection fluorescence (TIRF) microscopy (see 2.1.3) will be introduced. Afterwards, the principle of SRFM will be explained in section 2.1.4 focusing on localization-based methods (see 2.1.5) and 3D techniques (see 2.1.6).

2.1.1. Wide-field microscopy

Conventional microscopy, also referred to as wide-field microscopy is the most commonly used technique in fluorescence microscopy. The basic idea consists of guiding excitation light to the sample through the objective lens. This excites the fluorophores in the sample, which leads to emission of light. Fluorescence light is then re-emitted through the sample, passes the objective as well as a tube lens and is finally focused onto a detector, e.g. a charge-coupled device (CCD) camera. One of the factors that have to be taken into account when choosing wide-field microscopy is that it might give rise to blurry, out-of-focus light and eventually lead to an image that has some in-focus regions and many out-of-focus regions. There are two optical modes that can be differentiated in a wide-field microscopy setup.

Especially when it comes to transmission light experiments, *Köhler illumination* is one of the most appropriate techniques (see Fig. 2-2). For this method, the sample is usually illuminated with a white light source, for example, a halogen lamp or a light-emitting diode (LED). The light from the light source first passes a collector lens and then a field lens. The objective focuses the non-diffracted, parallel beams onto its back focal plane where the image is formed. The back focal plane of the objective lens and the front focal plane of the condenser lens are conjugate to each other. In the *critical illumination* mode, the light source is directly imaged by the so-called condenser lens, onto the object plane (see Fig. 2-2). This means that an image of the light source is projected onto the sample itself. The draw-back here is that in case of an uneven light source (e.g. because of filaments), an uneven illumination is passed onto the sample. In this case, techniques like the already described Köhler-illumination will lead to a uniform light intensity.

The two commonly used illumination modes in wide-field microscopy are *bright-field illumination* and *epi-illumination*. In *bright-field* mode, the sample is placed between the light source and the objective. The light, that is diffracted by the sample, is then collected in the objective. This method offers high contrast but – in comparison to fluorescence-based methods – offers no specificity. *Epi-illumination* is performed as a fluorescence – based method in an inverted microscope setup. The sample is illuminated through the objective lens, passing a dichroic mirror, which allows to separate the emission and excitation light. Epi-illumination mode works both with critical and Köhler illumination.(Kubitscheck and Peters 2013, Nevskyi, Wöll et al. 2018)

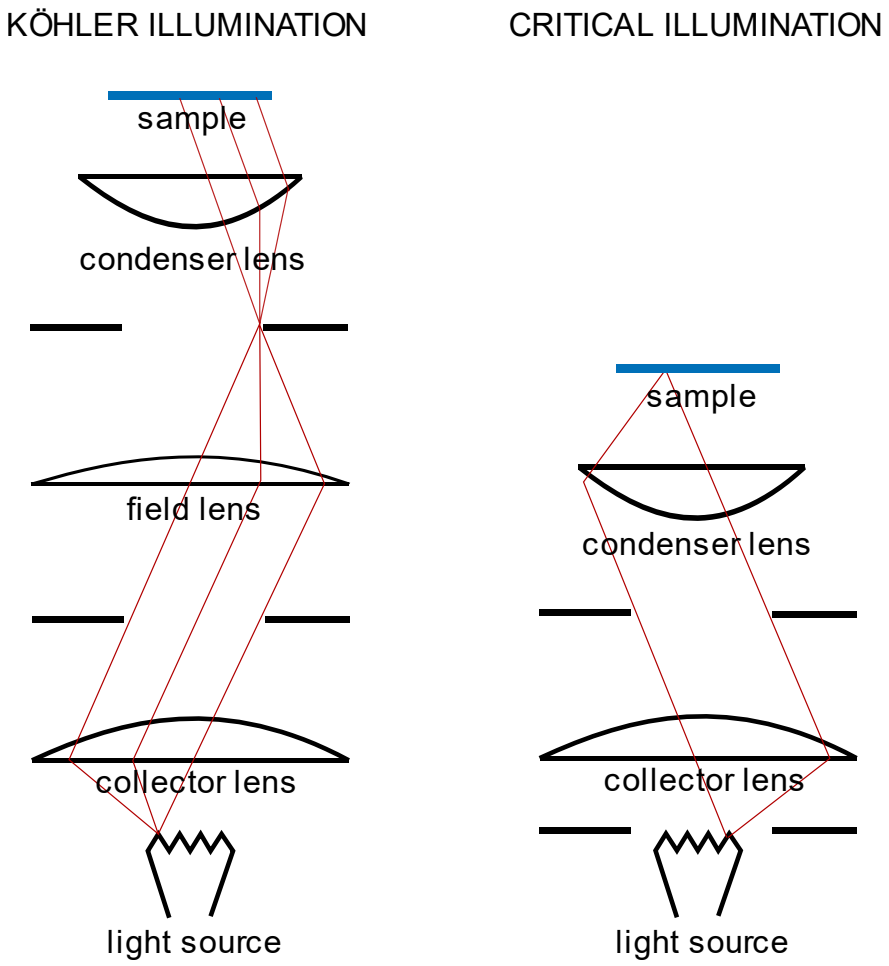

Fig. 2-2: Schematic illumination path in Köhler mode and critical mode.

2.1.2. Confocal microscopy

Confocal microscopy is a technique that was developed in order to overcome the challenges in wide-flied microscopy regarding the limited in-focus regions in an image. The trick in confocal microscopy consists of introducing a pinhole to the emission path, which blocks out-of-focus light, see Fig. 2-3. The term confocal derives from the fact that the pinhole is in the same focal plane as the sample – in other words – it is confocal with the sample. One draw-back in confocal microscopy is that this method only allows to image a single spot of the sample at once. In order to overcome this challenge, different methods like raster-scanning techniques have been developed.

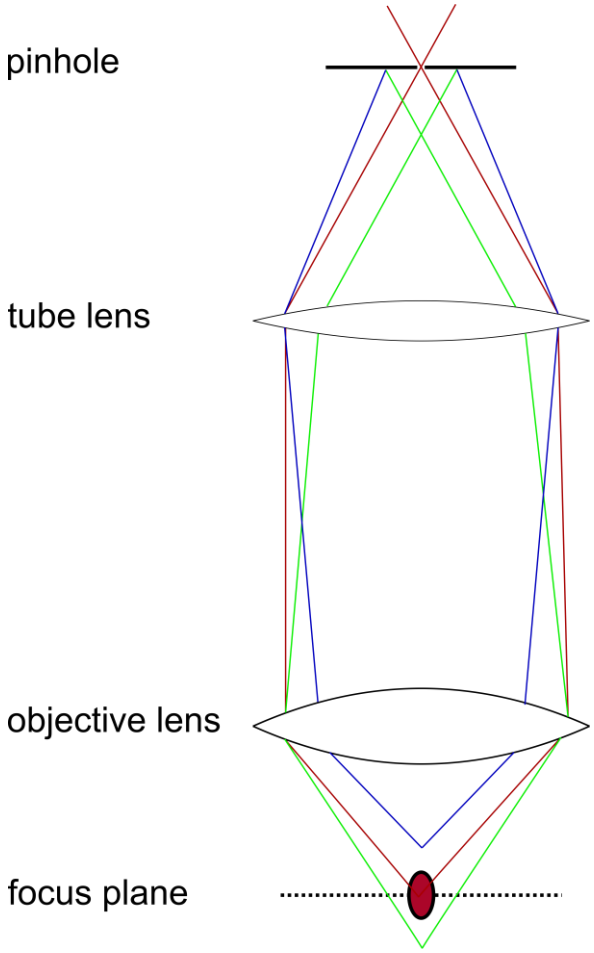

Fig. 2-3: The purpose of the pinhole is depicted in the optimal beam path (red). The detection volume is at the correct distance from the lens, the light is focused in the pinhole and the emission can pass. The blue beam path describes a case in which the detection volume is too close to the pinhole, whereas the distance in the green beam path is too large.

Another possibility to overcome the draw-back of confocal microscopy is the introduction of multiple pinholes in one setup. This type of technique is referred to as Spinning-Disk-Confocal microscopy. Here, the single pinhole is replaced with a disk containing multiple pinholes. The pinholes in the disk are arranged in a spiral, such that by spinning the disk around its axis, the pinholes sweep over the sample only once. Thereby, the sample area is not scanned multiple times. In order to image the sample, a second disk containing multiple micro-lenses is placed on top of the first disk. These micro-lenses can focus laser beams through the pinholes. The emission light then goes back through the pinholes and is collected in the camera.

The spinning velocity of a conventional spinning disk lies at around 5000 rpm, allowing for illumination of the entire sample once every 33 ms.(Sisan, Arevalo et al. 2006)

This technique allows to include the main advantages of wide-field microscopy and confocal microscopy, as it is possible to image many spots at once and in focus.

2.1.3. Total internal reflection fluorescence microscopy

TIRF microscopy, also known as evanescent wave/field microscopy, is a technique that uses a special mode of sample illumination to exclusively excite fluorophores that are within approximately 100 nm of the cover glass/sample interface.(Poulter, Pitkeathly et al. 2015) In TIRF microscopy, an evanescent field is produced when light rays are totally internally reflected at the cover glass/substrate interface. The evanescent field does not propagate deeper into the sample; therefore, images are not contaminated with fluorescence from out-of-focus planes. As a result, TIRF microscopy provides a possibility to image fluorophores near the cover glass/substrate interface with a high signal-to-noise ratio, thus making it the current gold standard for investigations of events at the solid/liquid or solid/air interface.(Poulter, Pitkeathly et al. 2015) Total internal reflection can only be achieved when the propagating light encounters a boundary to a medium of lower refractive index.(Snape 2017) This refractive behavior is described by Snell's law (4).

$$n_1 \cdot \sin\theta_1 = n_2 \cdot \sin\theta_2 \tag{4}$$

The refractive index n of an optical medium conveys information about the propagation of visible light through it, relative to its propagation through vacuum. The refractive index is defined as $n = c / c_m$ with c being the velocity of light in vacuum and c_m the velocity of light in the investigated optical medium.(Hentschel 2001, Poulter, Pitkeathly et al. 2015) In microscopy, the refractive indices n_1 and n_2 commonly refer to the glass substrate and the air or water medium above the substrate. If both refractive indices and the angle of incidence θ_1 are known, the angle at which light is reflected or transmitted can be derived by Snell's law, as illustrated in Fig. 2-4.

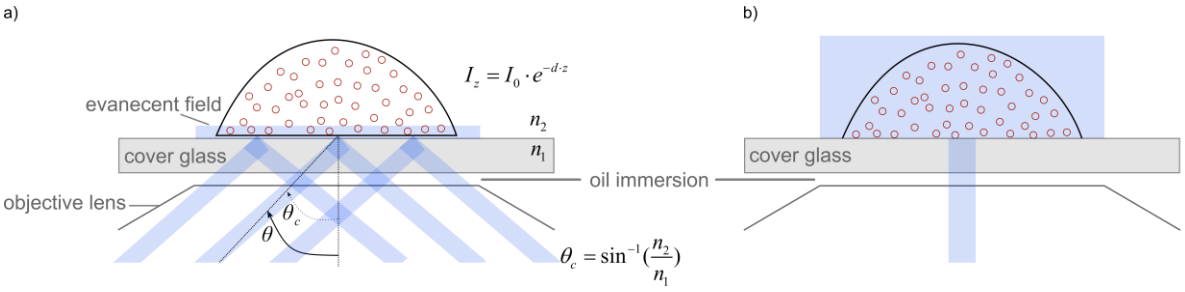

Fig. 2-4: Illumination schematic for TIRF (a) and epi-fluorescence (b). In TIRF mode, an evanescent field is produced which excites only fluorophores in close proximity to the surface.

For TIRF microscopy, the refractive index of the first medium must be larger than that of the second. Furthermore, the angle of incidence must be larger than the critical angle θ_c. In the case of $\theta_c = \theta_1$, θ_2 is exactly 90°. This leads to the following relation for the critical angle:

$$\begin{aligned} n_1 \cdot \sin\theta_c &= n_2 \cdot \sin 90° \\ n_1 \cdot \sin\theta_c &= n_2 \\ \theta_c &= \sin^{-1}(\frac{n_2}{n_1}) \end{aligned} \tag{5}$$

The total reflection of light into the first medium, which is the fundamental key of TIRF microscopy, is achieved for angles of incidence greater than θ_c.

The evanescent field, which is used for imaging in TIRF, is a direct consequence of the total reflection. Fresnel's equations can be solved for total internal reflection.(King, Graham-Smith et al. 2000, Born and Wolf 2013) It reveals that even though the propagation of the light rays is totally reflected, an electric component of light crossing the boundary, remains. This electric field in the second medium is called the evanescent field and its intensity decays exponentially with perpendicular distance from the boundary, as follows from equation (6).(Poulter, Pitkeathly et al. 2015)

$$I_z = I_0 \cdot e^{-d \cdot z} \tag{6}$$

Here I_z is the field intensity at the distance z from the interface, d is the decay constant of the field, and I_0 is the intensity of the field at the interface with $z = 0$.

In order to design a TIRF experiment, the estimation of the penetration depth of the evanescent field can be helpful. Equation (7) describes which parameters determine the penetration depth of an evanescent field.

$$d = \frac{\lambda_0}{4 \cdot \pi \cdot \sqrt{n_1^2 \cdot \sin\theta_1 - n_2^2}} \quad (7)$$

The penetration depth depends on the wavelength of the excitation light λ_0 as well as on the angle of incidence of this excitation beam and the refractive indices.

Besides the penetration depth, one other important consideration for the design of a TIRF experiment is the choice of the objective lens used, and therefore, especially the choice of the numerical aperture (NA). The scientific community agrees on a minimal NA of 1.40 for TIRF microscopy.(Poulter, Pitkeathly et al. 2015)

A large part of the research in this work concerns the modification and functionalization of glass substrates. TIRF microscopy is therefore used as an essential tool for the analysis and validation of surface reactions, as it allows the observation of surface events and strongly reduces background fluorescence.(Möckl, Lamb et al. 2014)

2.1.4. Super-resolution microscopy

Even though techniques like confocal and TIRF microscopy have assisted in making a step forward towards better imaging quality and higher resolutions, the physical limitations described by Abbe, see eq. (1), remain.

Recent developments in the scientific community gave rise to new solutions on how to circumvent the physical diffraction limit of light. As pioneers in this field, Eric Betzig, Stefan Hell, and William E. Moerner were awarded with the Nobel-prize in chemistry in 2014 “for the development of super-resolved fluorescence microscopy”.(Möckl, Lamb et al. 2014)

Nowadays there is a variety of super-resolution methods such as stimulated emission depletion (STED)(Hell 2007), ground state depletion (GSD)(Fölling, Bossi et al. 2008), reversible saturated optical fluorescence transitions (RESOLFT)(Hell, Jakobs et al. 2003), photoactivated localization microscopy (PALM)(Betzig, Patterson et al. 2006), (direct) stochastic optical reconstruction microscopy ((d)STORM)(Heilemann, Van De Linde et al. 2008, Huang, Wang et al. 2008), super-resolution optical fluctuations imaging (SOFI), (saturated) structured illumination microscopy (SIM or SSIM)(Gustafsson 2005, Chasles, Dubertret et al. 2007).

For this work, dSTORM was chosen as super-resolution technique. It belongs to the so-called localization-based methods, a principle which will be described in more detail in this chapter.

The basic idea of localization microscopy is to circumvent the Abbe limit through the introduction of stochastically blinking fluorophores. The sample is labeled with fluorophores that have the ability to switch between a bright on-state and a dark off-state as illustrated in Fig. 2-5. This switching behavior enables the temporal separation of the emission of fluorophores that are in a diffraction-limited distance to each other. The temporal separation furthermore allows to acquire multiple frames over the total acquisition time, that can finally be reconstructed to a super-resolved image. In a case in which conventional microscopy could not resolve two emitters, a localization-based method would allow to acquire different frames in which one of the two emitters is stochastically on and the other is off. The sum of the signals in these frames then gives the reconstructed image (see Fig. 2-5).

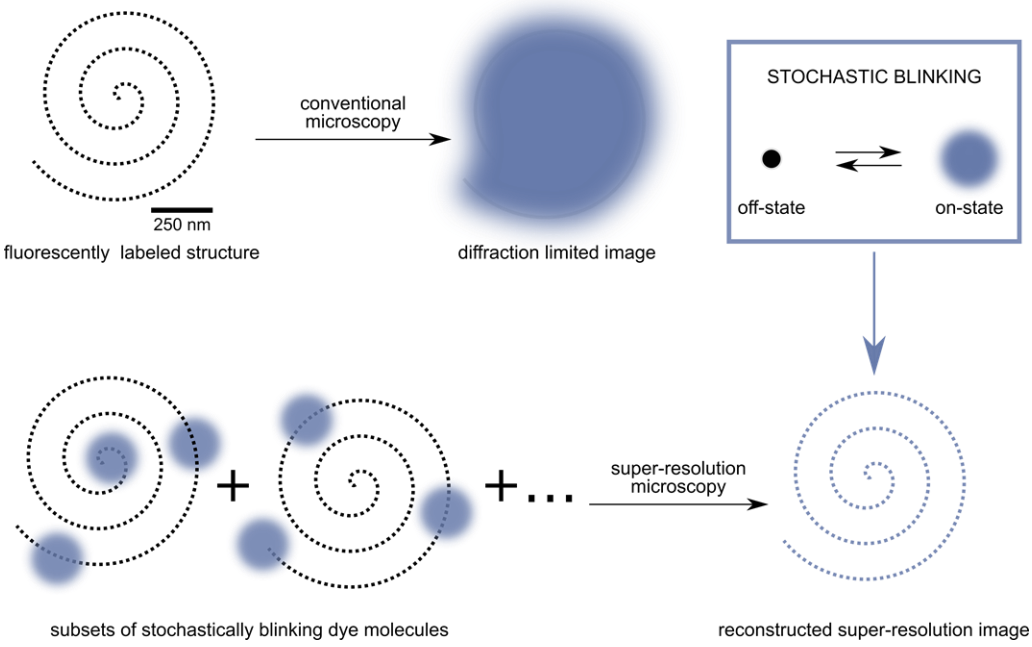

Fig. 2-5: Schematic representation of localization microscopy in comparison to conventional microscopy. The stochastic blinking of the fluorophores allows to reconstruct a super-resolved image of the specimen (represented by the spiral).

Even though the intensity profile of a single fluorescent emitter is subject to diffraction, its center can be localized with much higher precision as the maximum value of its Gaussian brightness distribution. Although the size of an emitter molecule is about 1 nm, the fluorescent spot produced by diffraction within the microscope has a size of about 200 nm.(Möckl, Lamb et al. 2014)

The intensity profile of such a point-shaped emitter has already been introduced. The corresponding PSF can be approximated by a two-dimensional Gaussian function (8). (Endesfelder and Heilemann 2015)

$$I(x_c, y_c, A, B) = \frac{A}{2 \cdot \pi \cdot \sigma_x \cdot \sigma_y} \cdot e^{-\left(\frac{(x - x_c)^2}{2 \cdot \sigma_x^2} - \frac{(y - y_c)^2}{2 \cdot \sigma_y^2}\right) + B} \tag{8}$$

with σ_x and σ_y as standard deviations, (x_c, y_c) the coordinates of the center, and the amplitude A and the background signal B.

The accuracy of the peak position of the PSF and therefore the localization of the emitter improves with the number of detected photons per emitter. For various localization-based methods, Mortensen et al. (Mortensen, Churchman et al. 2010) presented a description of the localization precision σ_x, see eq. (9).

$$\sigma_x = \frac{\sigma^2 + \frac{a}{12}}{N} \left(\frac{16}{9} + \frac{8 \cdot \pi \cdot \sigma^2 \cdot b^2}{N \cdot a^2}\right) \tag{9}$$

Here, σ is described by the standard deviation of the PSF, *a* refers to the pixel size of the imaging detector, *b* refers to the background signal in photons/pixel and *N* describes the number of emitted collected photons. The final image resolution σ^2, see eq. (11), can be calculated from eq. (9) and the Nyquist resolution $\sigma_{Nyquist}$, see eq. (10), with the labeling density N_{label} and the density *d*.

$$\sigma_{Nyquist} = 2 \cdot N_{label}^{\frac{-1}{d}} \tag{10}$$

$$\sigma^2 = \sigma_x^{\,2} + \sigma^2_{Nyquist} \tag{11}$$

2.1.5. Direct stochastic optical reconstruction (dSTORM) microscopy

The dSTORM method belongs to the localization-based super-resolution techniques. It can be performed with conventional fluorophores as photoswitches and provides an optical resolution of ~20 nm.(Endesfelder and Heilemann 2015)

The main classes of common organic fluorophores that can be photoswitched are carbocyanines,(Heilemann, Van De Linde et al. 2008) rhodamines, and oxazines.(Heilemann, van de Linde et al. 2009) In this work the carbocyanine dye Alexa Fluor 647 (see Fig. 2-6) is used for all dSTORM experiments.

The Jablonski diagram depicted in Fig. 2-6 are used to describe the redox-induced switching behavior of a fluorophore during dSTORM measurement. The excitation of a fluorophore from an electronic ground state S_0 into a higher electronic state S_N (with $N \geq 1$) is initiated with the appropriate wavelength $\lambda_{excitation}$. After internal conversion (IC) and vibrational relaxation (VR) to the lowest excited state S_1, fluorescence with $\lambda_{emission}$ brings the molecule back into the ground state S_0. Alternative processes can either be a non-radiative transition into S_0 or an intersystem crossing (ISC) into the triplet state T_1.

The long-lived triplet state can further react with molecular oxygen to recover the singlet ground state or react with reducing agents (such as thiols) to form a radical anion $F^{\bullet -}$. In this work, a cysteamine blinking buffer is used as reducing agent. The singlet ground state can be recovered by oxidization with oxygen or excitation of the radical with near-ultraviolet (UV) light. Some fluorophores (e.g. Atto 655) can be fully reduced to the leuco-form FH, which can also recover into the ground state by reaction with oxygen.(Endesfelder and Heilemann 2015)

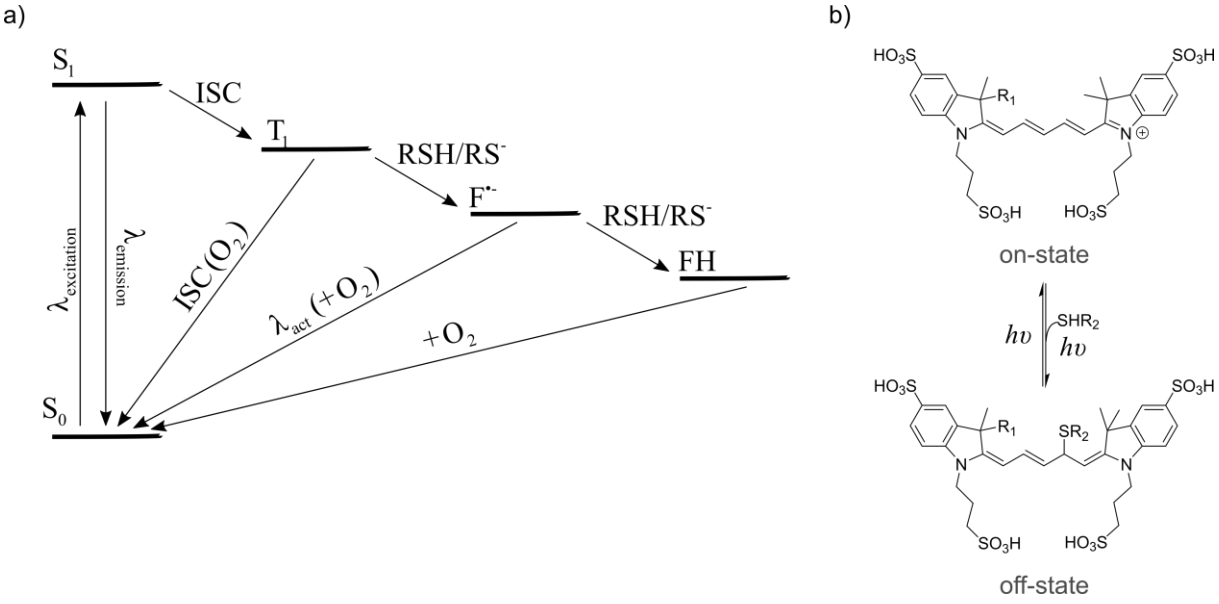

Fig. 2-6: Redox induced photoswitching depicted in a Jablonski diagram (a),(Endesfelder and Heilemann 2015); reversible chemical reaction between the fluorescent on-state and the dark off-state of the Alexa Fluor 647(Karlsson, Laude et al. 2019), figure adapted from Dempsey at al. (b).(Dempsey, Bates et al. 2009)

dSTORM experiments are preferably conducted using an inverted microscope, equipped with an oil-immersion objective suitable for TIRF microscopy. Excitation and emission light should be separated by a dichroic mirror. For biological samples typically, a stack of 4,000-20,000 images with a frame rate between 10 Hz and 2 kHz is recorded.(Endesfelder and Heilemann 2015) Literature shows that higher stacks of around 60,000 images with a frame rate of 10 Hz are more suitable for the investigation of soft matter objects like µGs.(Gelissen, Oppermann et al. 2016)

2.1.6. 3D Super-resolution fluorescence microscopy

Although SRFM has proven to be an important tool to further investigate a variety of scientific questions, novel three-dimensional (3D) imaging methods provide additional means for the deeper understanding of µGs at different interfaces. Gelissen et al.(Gelissen, Oppermann et al. 2016) have shown that it is possible to reconstruct 3D information from two-dimensional (2D) projections for non-uniform soft matter objects. Through the combination of the appropriate optical setup and processing algorithms, it is possible to extract 3D information using existing microscopy methods. Several methods were introduced in recent years that allow for the lateral localization of a single emitter as well as the localization along the optical axis, resulting in a 3D SRFM image. Among the most popular approaches are astigmatic imaging (Huang, Wang et al. 2008), bi-plane imaging (Juette, Gould et al. 2008), helica (Pavani, Thompson et al. 2009) and wavefront shaping (Shtengel, Galbraith et al. 2009). The method that is used for the investigations presented in this work is the helical shaping with a so-called double-helix (DH) phase mask. The DH-PSF was invented by Rafael Piestun with the goal to measure depth. He developed a special PSF or – more precisely – a special optical field that is formed of a superposition of the base functions, the Gauss-Laguerre modes of light. In contrast to conventional microscopy, where an object is focused to a single point and subsequently diverged after focusing, the optical field of the DH-PSF has two foci that rotate around each other for different positions along the z-axis, see Fig. 2-7.

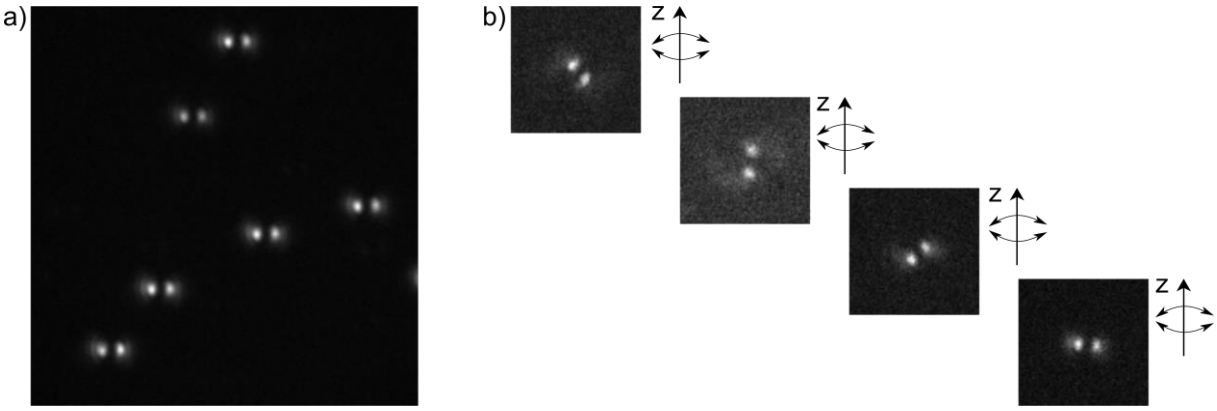

Fig. 2-7: Example of a calibration measurement of TetraSpeck beads in TIRF mode with the addition of an DH-PSF phase mask through which each bead is represented by two spots (a). The angle of revolution of those two spots around one another encodes the z-position of that molecule (b).

This means that the image of a single molecule is represented by two spots through the DH-PSF and the angle of revolution of those two spots around one another encodes the z-position of that molecule. The molecule can therefore not only be localized along x and y, but also in z by fitting the shape of the two spots and their angle of revolution with respect to one another. In combination with SRFM methods like dSTORM or PALM, the addition of the DH-PSF finally allows to reconstruct the super-resolved 3D image of a structure.

2.2. Lithography

The term lithography describes a planographic printing technique that has evolved over time. Historically this technique involved a hydrophilic trass that was pre-treated in a way that the areas to be printed were converted to a lipophilic surface. This enabled the use of an aliphatic printing ink that would only stick to these lipophilic areas.(Zeidler 1994) The treated trass was then used to print a certain pattern onto a paper. Modern lithography techniques like photolithography and electron-beam lithography (EBL) are derived from the basic idea of this method.

In this section the different lithographic techniques that are combined in chapter 4 will be introduced. First, the principle of c-EBL will be discussed in section 2.2.1. Here, the focus lies in summarizing the relevant findings that Patrick Schaal reported in his dissertation.(Schaal and Simon 2013)

Afterwards, the principle of photolithography and the use of protecting groups will be introduced in section 2.2.2. Chapter 4 builds on these two methods as a joint lithographic process is developed in order to immobilize µGs on specific spots at the solid support.

2.2.1. Chemical electron beam lithography

EBL is a powerful lithographic method that allows for the fabrication of patterns in the sub-nm range.(Lercel, Craighead et al. 1996) This advantage in comparison to techniques like photolithography is due to the fact that the de-Broglie wavelength of an electron is much smaller than that of a photon. Furthermore, this technique can be performed without the usage of masks, as the electrons can easily be directed using electromagnetic coils. EBL is mainly used to locally change the properties of a resist and is amongst others employed for the study of processor prototypes.(Müller 1989, Küller, Eck et al. 2003) c-EBL is a variation of classical EBL.(Schaal and Simon 2013) Here, the electron beam does not only induce a change in the chemical sustainability of the photoresist, but also selectively reduces functional groups in the resist.(Zharnikov, Geyer et al. 1999, Harnett, Satyalakshmi et al. 2000, Zharnikov, Grunze et al. 2002) Schaal et al. have developed a method to deposit gold-nanoparticles (Au-NP) to the substrate surface by using top-down and bottom-up methods. Starting from organic monoliths on oxidic surfaces, they generated thiol-patterns by electron beam lithography. These patterns were then targeted to selectively deposit the Au-NP. The first step in this approach consists of the silanization of the indium-tin-oxide (ITO)-surface, of the glass substrate. The generation of sulfonyl groups on the surface is performed in the silanization process. The ITO surface is necessary in order to provide the conductivity needed for the C-EBL procedure, see Fig. 2-8.

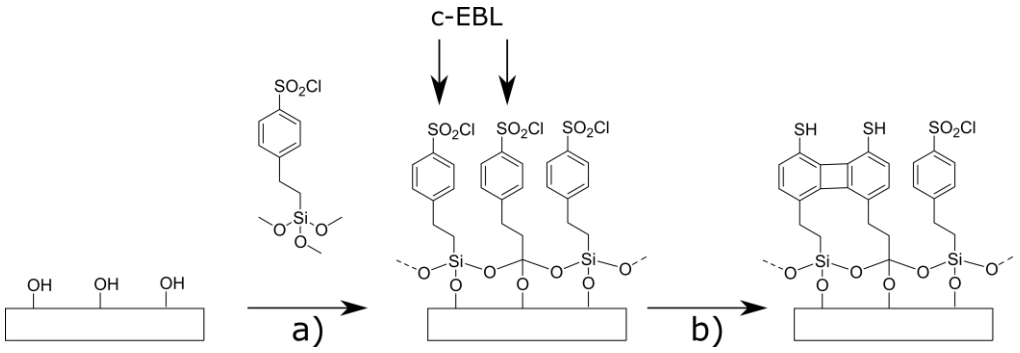

Fig. 2-8: Schematic overview of the c-EBL process, the glass substrate is modified with an ITO layer providing the needed conductivity. The silanized surface is obtained after addition of 2-(4-chlorosulfonylbenzene)trimethoxysilane (a). The surface containing sulfonic acid end-groups is locally reduced to thiols by c-EBL (b).

2.2.2. Photolithography with photolabile protecting groups

Photolithography is a well-established method that is mostly used in the production of semiconductor and micro-system technology to build integrated circuits. The manufacturing of small features in the (sub-)µm range is a requirement to fabricate (e.g. mobile) devices. This is only possible because of the advances in lithographic technologies. In the conventional photolithographic process, the image of a photomask is transferred to a photo-sensitive photoresist by exposure to light. A distinction is made between positive and negative lithography depending on whether the exposed or unexposed areas are transferred to the surface in the desired pattern.(Waser, Keller et al. 2004, Menz and Paul 2012) Apart from the conventional photolithographic approaches used in industry, the use of photolabile or photocleavable protecting groups (PPGs) to create responsive surfaces or even surface patterning has been studied in recent years.(Cui, Miguel et al. 2013) Therefore, first an introduction to the nature of these protecting groups will be given and finally relevant state-of-the-art applications will be presented. Protecting groups are compounds which protect certain functions within a molecule and thus prevent unwanted reactions with specific reagents. They can be cleaved under characteristic conditions for example in the presence of acidic or basic reagents.(Wuts and Greene 2006) PPGs represent an alternative to the chemically cleavable protecting groups. They are cleaved by irradiation with light of suitable wavelength. The quality of a protecting compound depends on several factor: A promising candidate should fit the orthogonality criterion which defines the following requirement: When two different protecting compounds are used to protect two different functional groups of a molecule, each protecting compound has to be cleavable independently from the other one.(Merrifield, Barany et al. 1977) This is easily feasible when the two protecting compounds can be cleaved at e.g. different pH-values. PPGs that are orthogonal to other photolabile protecting groups are classified as chromatically orthogonal. In this case each protecting compound is cleaved at a different wavelength than the remaining protecting groups.(Bochet 2004) An important advantage, that photolabile protecting compounds have in comparison to chemically cleavable protecting compounds, is that the sample is irradiated homogeneously with light. Chemical reagents on the other hand are distributed in the sample through diffusion, which can lead to an inhomogeneous distribution of the protecting groups. Thanks to modern laser techniques and high laser powers it is possible to excite a majority of PPGs in the sample homogeneously at once. PPGs have been applied in a variety of different fields. An important application for this work is the fabrication of DNA-chips or DNA micro-arrays.(Wöll 2006)

Both terms are very broad and describe systems in which oligonucleotide strands are immobilized to a surface.(Brown and Botstein 1999) The advantage of using PPGs in DNA chip synthesis is that it allows to attach the DNA strands to a specific location on the surface, so-called spots. As soon as the protecting group is bound to the entire surface, specific areas can be selectively irradiated with light. DNA strands can then be attached to these deprotected spots. The combination of c-EBL with such a DNA-chip technique will be introduced and discussed in section 4.

2.2.3. Photochemistry of the o-nitrobenzyl protecting group

The selection of a PPG for an experiment is highly dependent on the desired molecular functionalities and the available wavelengths for irradiation. For this work, the focus lies on the 2-nitrobenzyl PPGs (Fig. 2-9) which have initially been developed to protect the carboxyl function in amino acids and peptides.(Barltrop, Plant et al. 1966) However, it is now commonly used in nucleic acid chemistry, where it is employed as a phosphate protecting group in the synthesis of mono-nucleotide building blocks.(Ohtsuka, Tanaka et al. 1974) The o-nitrobenzyl group is very similar to the previously introduced 2-nitrobenzyl group (Fig. 2-9). The o-nitrobenzyl PPGs are especially important to this work, as Wöll et al. employed them in the DNA-Chip synthesis.(Wöll 2006) The fundamental process concerning the photo sensitivity of this PPG was already discovered in 1901 by Chiamician and Silber.(Ciamician and Silber 1901) They first described the conversion of o-nitrobenzaldehyde to o-nitrobenzoic-acid (Fig. 2-9).

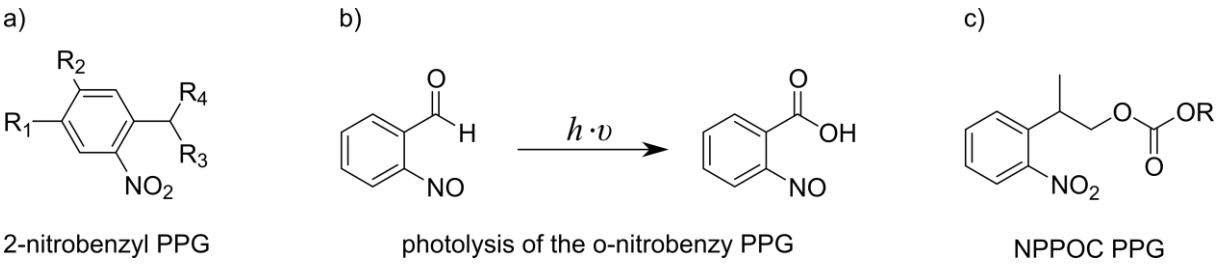

Fig. 2-9: The most common PPGs belong to the 2-nitrobenzyl group and its derivatives (a). The photolysis of o-nitrobenzaldehyde to o-nitrobenzoic-acid is depicted in (b). The PPG used in this work is a 2-(2-nitrobenzyl) ethyl (NPPOC) derivative (c).

Only three years later, Sachs an Hilpert postulated that every aromatic compound that has a nitro-group in ortho position to a CH-group is photosensitive.(Sachs and Hilpert 1904)

The respective reaction mechanism consists of an intramolecular Red-Ox reaction where an oxygen atom of the nitro group is inserted into the CH bond of the aldehyde, thereby reducing the nitro group to the nitroso group and simultaneously oxidizing the benzylic carbon atom.

The relevant findings for the elucidation of this reaction mechanism can be found in the dissertation of Walbert.(Walbert 2003) A new class of photolabile protecting groups was investigated and synthesized by the research group of Pfleiderer in order to develop cleavable protecting groups with an phenylethyl structural element for the synthesis of oligonucleotides. This promising photolabile class has a 2-(2-nitrobenzyl) ethyl (NPPOC) structure (Fig. 2-9).(Giegrich, Eisele-Bühler et al. 1998) An NPPOC derivative will be employed in chapter 4 to immobilize µGs to a DNA chip.

2.3. Microgel systems

As already outlined in the introduction of this dissertation, this work is embedded in the CRC 985 for functional µGs and µG systems. Within this strong scientific environment, interdisciplinary research ranging from the fundamental level to relevant biomedical or engineering applications, is conducted. The scientific complexity of the CRC illustrates the relevance of µGs and their applications. In this paragraph, a general introduction to µGs will be given, which will be followed by a more detailed focus on µGs at the solid-liquid interface and DNA-functionalized µG systems. The understanding of µGs at the interface as well as the immobilization of DNA-functionalized µGs to a solid support will be a crucial part of this dissertation.

2.3.1. Stimuli-responsive microgels

µGs can be defined as crosslinked polymer networks that are specified by their size ranging from 50 nm to 5 µm.(Pich and Richtering 2010) Even though the term *microgel* was only introduced in 1949 by Baker,(Baker 1949) his colleagues Staudinger and Husemann were the first ones to synthesize and characterize these systems already in 1935.(Staudinger and Husemann 1935) µGs are macro molecular networks swollen by the solvent in which they are dissolved. It is important to distinguish µGs from other known physical objects like colloids, flexible macromolecules, or surfactants (see Fig. 2-10).

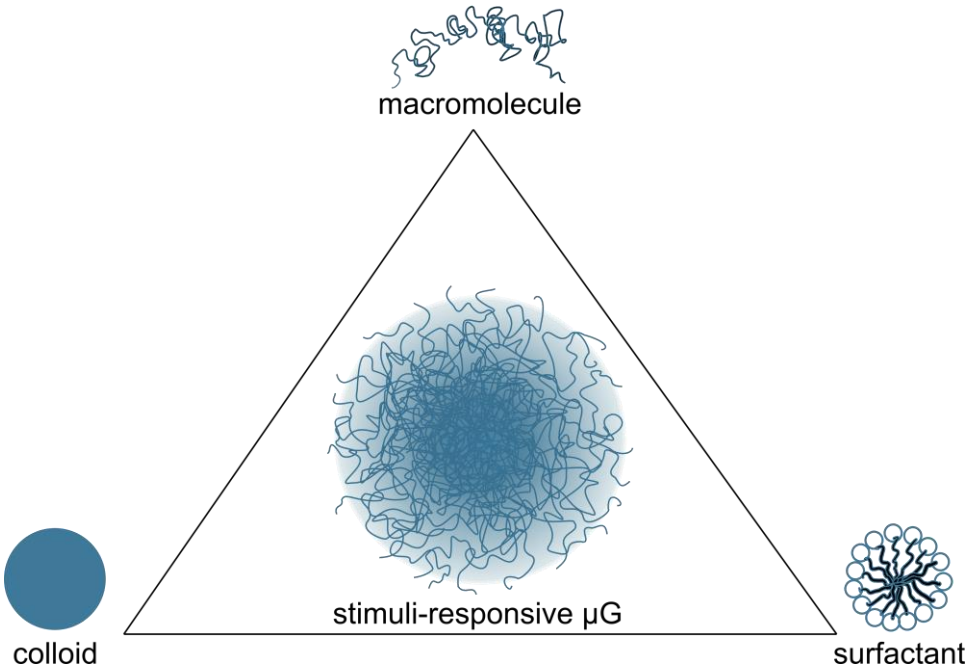

Fig. 2-10: Depending on the surrounding, a µG (center) can fit different physical definitions like a macromolecule, a surfactant or a colloid, adapted from Plamper et al.(Plamper and Richtering 2017)

Depending on the swelling-degree and their surroundings, µGs can fit different physical definitions. In the collapsed state they resemble hard colloids, whereas in the swollen state they are soft and have a fuzzy surface. The colloidal or macro molecular properties of a specific µG can be controlled by the crosslinker content. The presence of crosslinks also allows for a distinction between µGs and branched polymers, as it provides structural integrity.(Plamper and Richtering 2017) µGs form stable dispersions in aqueous environments and have the capability to adjust their properties, depending on the interplay between polymer/polymer and polymer/solvent interactions.

The swelling/contraction degree of a µG can be influenced by internal factors, such as the crosslinking density, or by external factors, such as pH, temperature, ionic strength or electro-chemical potential, depending on the monomer composition.(Pich and Richtering 2010) The crosslinker density of a µG decreases from the center outwards, resulting in so-called dangling ends in the periphery of the gel. As the µG surface is not clearly defined, it is referred to as being “fuzzy”. This can also be seen in the smeared density distribution. Because of their unique ability to swell and collapse upon different external stimuli, µGs are promising candidates in a variety of scientific fields.

In the biomedical field e.g., the application of µGs for uptake and release experiments represents preliminary experiments for interesting applications. Other possible applications involve the advantages of the actuating properties for micro or even nano devices like peristaltic pumps.

2.3.2.Thermo-responsive microgels

Thermo-responsive µGs undergo their transition from the swollen to the collapsed state upon a system-specific temperature, the VPTT. The volume phase transition (VPT) is defined as the point at which either the polymer-water or the polymer-polymer interactions win over the other one resulting in swelling/collapse. Poly(N-isopropylmethacrylamide) (pNIPAM) forms hydrogen bonds to water through the amide side chains. At the same time, the isopropyl group induces hydrophobic structuring of the water and this leads to entropy-controlled polymer–polymer interactions. If the solvent–polymer interactions are stronger than the polymer–polymer interactions, the pNIPAM chains exhibit a random-coil structure. If the hydrogen bonds with the water molecules break due to temperature increase, the release of structured water takes place and polymer–polymer interactions become dominant, leading to coil–globule transition. pNIPAM -based microgels swell at temperatures below VPTT and collapse (hence shrink) if the temperature increases above VPTT. This allows for the preparation of stimuli-sensitive microgels for which the solvation of polymer chains can be reversibly triggered by influencing the balance between solvent–solvent, solvent–polymer, and polymer–polymer interactions due to the change of temperature, pH, ionic strength, solvent composition, etc.(Pich and Richtering 2010) The VPT is not only dependent on the molecular structure of the µG, but also on the crosslinking density of the system. At higher crosslinking densities, the volume phase transition temperature broadens over a larger temperature interval. Differential scanning calorimetry (DSC) studies have shown that pNIPAM µGs undergo a conformational transition at ~34 °C as compared to the homopolymer which has an LCST of ~32 °C (Pelton 2000). It is therefore expected that the amount of crosslinker concentration within µG would determine how closely the microgel's properties compare to those of either spherical particles or linear/branched polymers. Woodward and Chowdhry were amongst the first to investigate the effect of the crosslinker concentration on the VPT of pNIPAM µGs. They could experimentally confirm their hypothesis and described the increase of the VPTT with increasing crosslinker concentration due to a decreased diffusion rate of water within the particles with increasing crosslinker concentration.

Complementary fluorescence studies showed an increased hydrophobicity as the crosslinker density increased.(Woodward, Chowdhry et al. 2003) The temperature-responsive µGs used in this work are based on poly(N-isopropylacrylamide) (pNIPAM) or poly(N-isopropylmethacrylamide) (pNIPMAM). These polymers belong to the class of lower critical solution temperature (LCST) polymers. pNIPAM has a VPTT of 32 °C (Heskins and Guillet 1968) whereas the structural change in pNIPMAM leads to a higher VPTT of 42 °C.(Wedel, Hertle et al. 2016) The synthesis of a pNIPMAM µG with a VPTT of 42 °C is depicted in Scheme 2-1.(Eisold 2018)

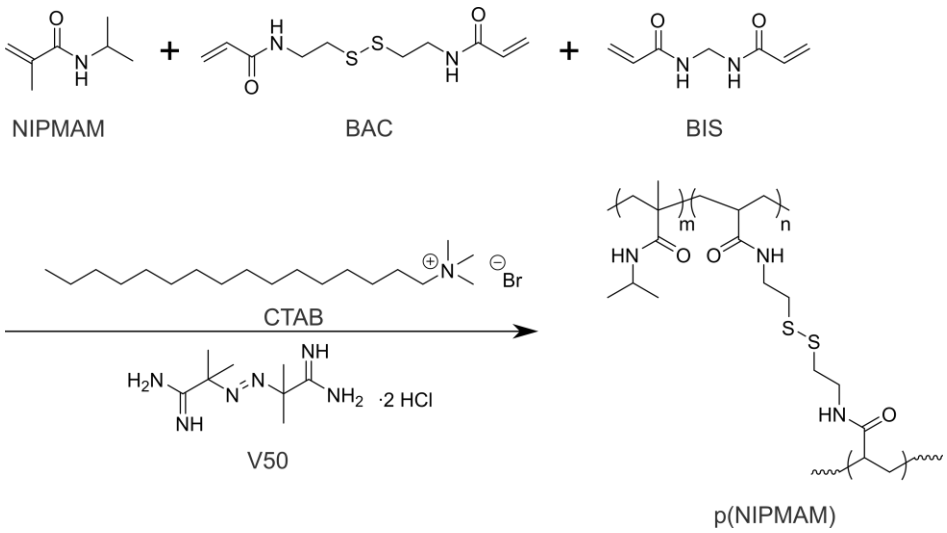

Scheme 2-1 Synthesis of a pNIPMAM µG with NIPMAM as monomer, N,N'-Bis(acryloyl)cystamine (BAC) as co-monomer and N,N'-methylenebisacrylamide (BIS) as crosslinker. The radical initiatior 2,2'-azobis(2-methylpropionamidine) dihydrochloride (V50) is added as well as the cationic surfactant Cetyltri-methylammonium bromide (CTAB).(Eisold 2018)

To characterize a µG, information about the synthesis including the crosslinker amount, the polymerization method and the resulting VPTT is needed. In order to estimate the size of the µG, the hydrodynamic radius R_h can be estimated using the following formula:

$$D = \frac{k_B \cdot T}{6 \cdot \pi \cdot \eta_s \cdot R_h} \tag{12}$$

Here, D is the diffusion coefficient, k_B represents the Boltzmann constant, T is the temperature and η_S is the viscosity of the solvent. Additionally, a distance distribution curve can be derived after applying an inverse Fourier transform to the scattering function.

This distance distribution curve can then be deconvoluted for particles with centro symmetry, resulting in the radial scattering length profile. This profile provides real space information about the structure of the particle and can be used to characterize the monodispersity of a µG.

2.3.3.Microgels at the solid-liquid interface

Beside the scientific interest in the temperature-responsiveness of µGs, growing attention arises from potential applications of these materials. Prominent examples amongst others are their use as surface coatings for smart cultivation of vertebrate cells and as etalons.(Schmidt, Zeiser et al. 2010, Sorrell and Serpe 2012, Islam and Serpe 2013, Smiley-Wiens and Serpe 2013, Uhlig, Wegener et al. 2016) One of the properties that clearly differentiate µGs from particles is their ability to spread at the interface. Hendrickson et al. reported µGs passing filter pores of a size ten times smaller than the hydrodynamic radius of these µGs.(Hendrickson and Lyon 2010) This example depicts the ability that µGs have to adapt to their environment through deformation. When a µG adsorbs it spreads parallel along the solid surface while an orthogonal compression takes place.(Cors, Wrede et al. 2017) The extend of adsorption and subsequent spreading of the gel results from the counterplay between adhesion energy, favoring a large contact area on the one hand, and elastic energy, avoiding deformation on the other hand.(Carrillo, Raphael et al. 2010) The non-spherical conformation of the gel at the interface is described as the so-called fried-egg conformation (see Fig. 2-11).(Mourran, Wu et al. 2016) As the µG corona is less dense/more fuzzy than the center regions, the corona tends to deform stronger, leading to the fried-egg conformation. Furthermore, it is possible to rehydrate µGs while being adsorbed at the surface. Hereby, a lateral size reduction and a vertical size increase take place.(Burmistrova, Richter et al. 2011)

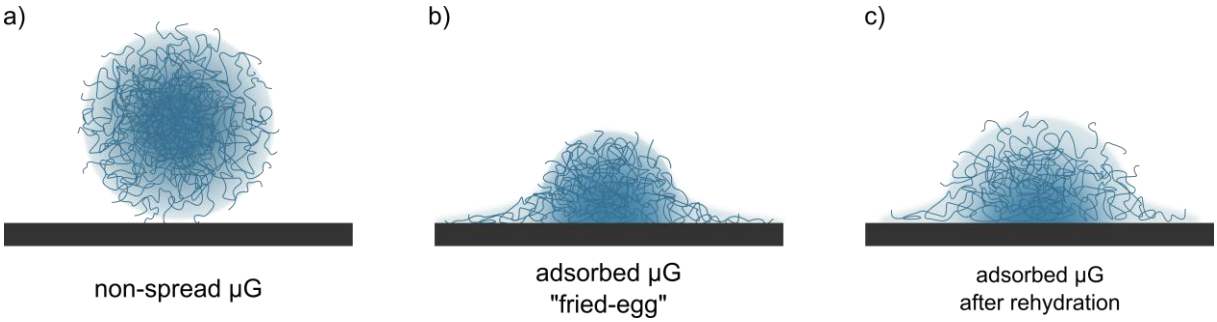

Fig. 2-11: Immobilized µG at the surface without spreading (a), after strong adsorption resulting in the "fried-egg" conformation (b) and after rehydration of the adsorbed µG (c). The "fried-egg" structure can be explained due to the density distribution within the gel. As the outer regions are "fuzzier" and less crosslinked than the inner regions, the gel deforms stronger in its periphery.

It is well known that the spreading behavior of µGs highly dependens on the crosslinking density.(Rey, Hou et al. 2017) Low crosslinking will result in a soft and easily deformable µG tending to strongly spreading at the solid support.

The local density of surface-adsorbed pNIPAM-µGs was investigated with scanning force microscopy (SFM) by Schulte et al.(Schulte, Scotti et al. 2018) This method allows to probe the internal structure of µGs that are physically adsorbed at the solid-water interface. Schulte et al. also compared the deformation behavior of ultra-low crosslinked µGs and conventional µGs with a 5% crosslinker content. They furthermore investigated different types of adsorption, i.e. in situ adsorption from solution, spin-coating and Langmuir-Blodget. The results demonstrate that the morphology and the temperature-induced collapse of µGs adsorbed onto a solid substrate are very different for ultra-low crosslinked (ULC) µGs as compared to regularly crosslinked µGs, despite the fact that their general behavior in solution is very similar. Scotti et al. reported that after deposition of ULC µGs onto a solid substrate a concentration-dependent topography is observed using atomic force microscopy (AFM). Depending on the compression, these microgels can behave as flexible polymers, covering the substrate with a uniform film, or as colloidal microgels leading to a monolayer of particles.(Scotti, Bochenek et al. 2019) Furthermore, the morphology of ULC µGs can be controlled by the type of adsorption onto the substrate. Schulte et al. report a strong deformation upon adsorption by spin-coating or by Langmuir–Blodgett deposition from an oil–water interface. After rehydration, the ULC µGs cannot collapse as entire objects, instead small globules are formed.(Schulte, Scotti et al. 2019)

2.4. Deoxyribonucleic acid

In this paragraph, an introduction to the nature and characteristics of DNA molecules is given. Even though the focus of this work does not lie on DNA-chemistry, DNA molecules serve as an important tool throughout the different topics of this dissertation. It illustrates the versatile possibilities to use DNA molecules in different fields ranging from conventional biomedical environments (optical mapping, paragraph 5) to materials sciences (DNA-functionalized µGs, paragraph 4.2.4). DNA is a biopolymer that carries the genetic information in all organisms as well as in some viruses. It consists of two antiparallely oriented, complementary single strands forming a double helix in their combined form.(Watson and Crick 1953) The two strands are held together by the collective interactions through hydrogen bonding. Each strand represents a polymer consisting of four different nucleotides that function as monomer units (Fig. 2-12).

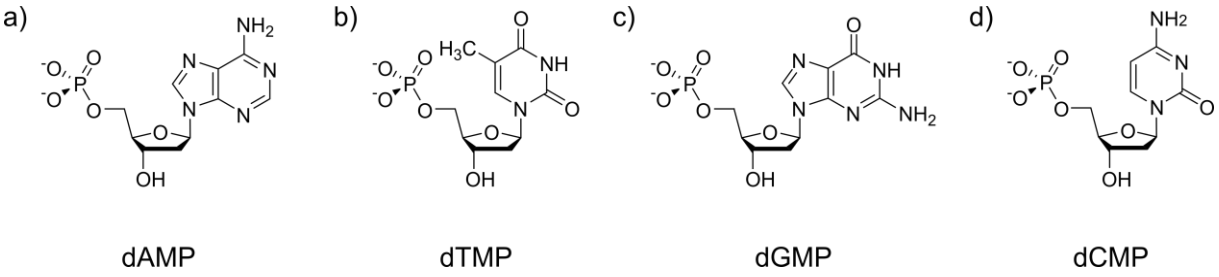

Fig. 2-12: The four nucleotides that are part of DNA: 2'-deoxyadenosine monophosphate (dAMP, (a)) (a), 2'-deoxythymine monophosphate (dTMP, (b)), 2'-deoxyguanosine monophosphate (dGMP, (c)) and 2'-deoxycytidine monophosphate (dCMP, (d)).

Every nucleotide is built up from a phosphoric acid group, a deoxyribose molecule and one of the four nucleobases adenine (A), cytosine (C), guanine (G) or thymine (T). The phosphoric acid is connected to the sugar moiety by an ester bond at its 5'-position and the nucleobase replaces the 1'-hydroxy group of the sugar moiety. For the formation of the DNA polymer the 3'-carbon of each nucleotide is connected to the phosphate rest of the following one via another ester bond. A and T as well as guanine and C form two or three hydrogen bonds, respectively, due to a complementary arrangement of hydrogen bond donors and acceptors.(Watson and Crick 1953) In contrast to most synthetic polymers, the order of the four different monomers within a DNA molecule is well defined and encodes the genetic information in all organisms.(Crick 1970)

The formation of the complementary base-pairs (bp) leads to an antiparallel arrangement of the single DNA (sDNA) strands finally forming the double helix structure.(Watson and Crick 1953) One convolution within this structure is formed by 10 basepairs resulting in a length of ~3.4 nm. The stability of a DNA double strand is strongly sequence dependent. As a rule of thumb it can be stated that the higher the amount of CG pairs in comparison to the amount of AT pairs, the more thermodynamically stable the system.(Wells, Larson et al. 1970) To denature a double helix, the binding energy has to be overcome by heating the system above its characteristic melting temperature T_m.(Yakovchuk, Protozanova et al. 2006)

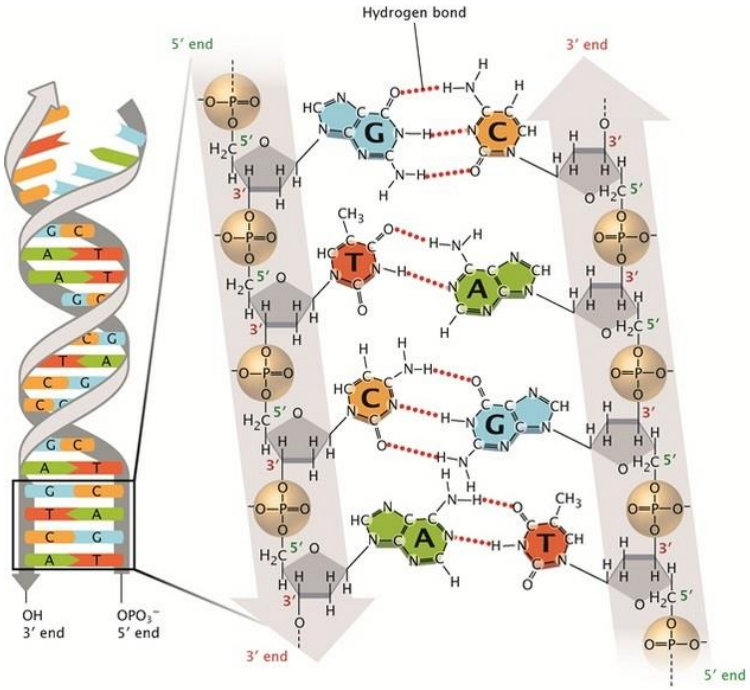

Fig. 2-13: DNA-structure in the Watson-Crick-structure with the four nucleobases adenine (A), cytosine (C), guanine (G) or thymine (T). Two hydrogen bonds connect T to A; three hydrogen bonds connect G to C. The sugar-phosphate backbones (grey) run anti-parallel to each other, so that the 3' and 5' ends of the two strands are aligned. Figure adapted from Pray et al. (Pray 2008)

2.5. Optical DNA mapping

This section will give a background on the field of optical DNA-mapping. In order to do so, the relevance of epigenetics will be outlined. Afterwards, basic principles of optical DNA-mapping will be illustrated. It will be shown that one of the important requirements for optical mapping consists of the analysis of linearly stretched DNA molecules.

Therefore, several well-known methods for DNA-stretching will be presented. This section allows to embed the pending patent for a novel DNA-stretching method – which will be discussed in section 5 – into the state of the art.

2.5.1. Genetics and epigenetic

Every information deposited in the sequence of the DNA is referred to as genetics. It encodes all information required for an organism to develop and live. The central dogma of genetics illustrates the information flow from the genome to the function. The DNA is transcribed to a ribonucleic acid (RNA) sequence which itself is translated into an amino acid sequence forming proteins.(Crick 1970) The proteins then undertake certain functions. Phenotypical features can be affiliated to the genetic information.(Johannsen 1911) However, many features, or illnesses cannot be explained by genetics. One example is the formation of several different cell types during development, even though all cells contain the same genome. Instead, the cells differ in the expression of the genes which is controlled by an information layer on top of the nucleobase sequence. This layer is referred to as epigenetics.(Sharma, Kelly et al. 2010) It includes modifications of the DNA molecule itself as well as modifications of the histones that are structure-giving proteins for the DNA.(Feinberg and Fallin 2015) Important epigenetic marks are received by the methylation of cytosine to 5-methylcytosine (5mC), see Fig. 2-14).(Levy and Huebner 1970) In procaryotic cells the methylation of adenine to N6-methyladenine (6mA) plays an important role as well, see Fig. 2-14.(Dunn and Smith 1958)

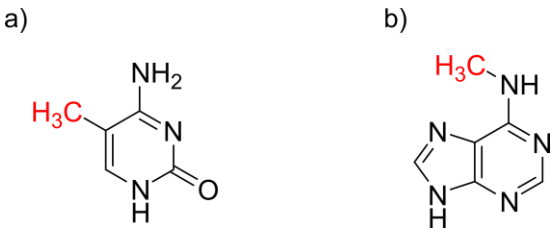

Fig. 2-14: The methylated nucleobases 5-methylcytosine (a) and N_6-methyladenine (b).

Even though the field of epigenetic diagnostics is very young, epigenetic changes, like increased methylation variation, were found across cancer types.(Hansen, Timp et al. 2011, Shin, Lee et al. 2016, Valdés-Mora and Stirzaker 2018) In another example, Donkin et al. were able to show that sperm-DNA is likely to undergo epigenetic changes. They found changes in the methylation pattern of human DNA-sperm of normal weight man in comparison to that of man with diagnosed adiposity. Additionally, they reported a drastic change in the methylation pattern of man after surgically induced weight loss.(Donkin, Versteyhe et al. 2016)

The field of epigenetics has thrived on discoveries from in vitro, in vivo, and human clinical and epidemiologic studies, leaving yet a large number of scientific questions to be answered.(Virani, Colacino et al. 2012) These epidemiologic studies have challenged the classic view of illnesses like e.g. cancer, which has traditionally been hypothesized as a disease that results from the successive accumulation of genetic alterations in oncogenes and tumor-suppressor genes, leading to uncontrolled cell growth. It is now known that epigenetic alterations contribute to carcinogenesis and a mechanistic link exists between environmental and dietary exposures and disease.(Virani, Colacino et al. 2012) It should be noted, that the most important questions regarding the underlying processes - and how to stop them - are yet to be understood.

2.5.2. DNA methyltransferases and restriction endonucleases

One approach to encode epigenetic changes consists of monitoring epigenetic marks. Methylations of the nucleobases C and A function as such epigenetic marks which are created by the enzyme class of DNA MTases. For these enzymes, the DNA acts as a substrate. It recognizes specific, short, palindromic sequences. The enzyme binds to this sequence and catalyzes the transfer of a methyl group from a cofactor to the nucleobase that is modified. The natural cofactor is S-adenosyl-L-methionine (AdoMet) which carries the transferable methyl group at a tertiary sulfonium center (see Scheme 2-2).(Ho, Wu et al. 1991)

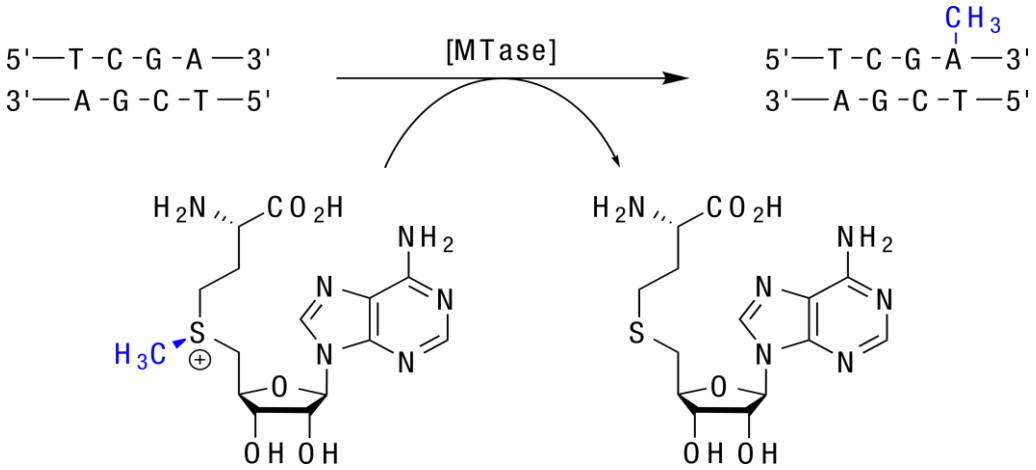

Scheme 2-2: Transfer of a methyl group form the cofactor AdoMet to double stranded DNA catalyzed by an MTase.(Klimašauskas and Weinhold 2007)

In general, there are two distinguishable types of DNA MTases in living organisms. De novo MTases, like DNMT 3 in mammels, have non-methylated DNA as a substrate and methylate the recognized sequences without an existing mark. In contrast, maintenance MTases play an important role in mitotic inheritability of methylations. If these enzymes, like DNMT 1A or 1B in mammals, bind to their recognition pattern where only one strand is methylated, they catalyze the methylation of the second strand.(Edwards, Yarychkivska et al. 2017) In bacteria, MTases form a system with restriction endonucleases (REases). They also have palindromic recognition sequences on the DNA where they can bind to.(Vasu and Nagaraja 2013) In contrast to the MTases, they do not catalyze a modification of the DNA but cleavage of both strands by hydrolysis of a phosphate ester bond for each strand. Many organisms are known, in which a pair consisting of one MTase type and one REase type have the same recognition sequence and the REase can only then cleave the DNA if the sequence is not methylated at this position.(Vasu and Nagaraja 2013) Therefore, REases are used to examine the completeness of methylation by MTases.

2.5.3. Optical DNA mapping

Next-generation sequencing technologies are considered the state of the art in DNA analysis, as they provide single-base resolution on a whole-genome scale.(Michaeli and Ebenstein 2012) Despite this progress, every sequencing platform to date relies on reading the genome in small, abstract fragments, typically of less than 1000 bases in length. (Neely, Deen et al. 2011) Repetitive genomic regions, which account for half of the human genome, cannot be directly mapped.(Treangen and Salzberg 2012) Therefore DNA sequencing is a technology that relies on ensemble measurements and is thus unable to detect rare genomic variations or small subpopulations, which are increasingly recognized as important for assessing disease states and progression. (Consortium 2010, Michaeli and Ebenstein 2012) In optical DNA mapping, intact, large, single DNA molecules are labeled, stretched out, and imaged using a fluorescence microscope.(Müller and Westerlund 2017) This means that sequence information ranging over hundreds of kilobasepairs (kbp) can be obtained in one single image. (Müller and Westerlund 2017)

2.5.4. AdoMet analogues

MTases cannot only catalyze the transfer of a methyl group from AdoMet but also the transfer of other alkyl groups from synthetic AdoMet analogues, which are derivates of the natural cofactor.(Deen, Vranken et al. 2017) The methyl group at the sulfonium center is substituted by a larger rest which can be a functional or a reporter group.(Deen, Vranken et al. 2017) Functional groups may be used to enable further introduction of desired properties. Important reporter groups are fluorophores that are connected to the AdoMet root by a linker chain. In the case of AdoYnTAMRA, the commercially available TAMRA fluorophore is connected to the sulfonium center via a triple bond at the ß-position (Fig. 2-15).

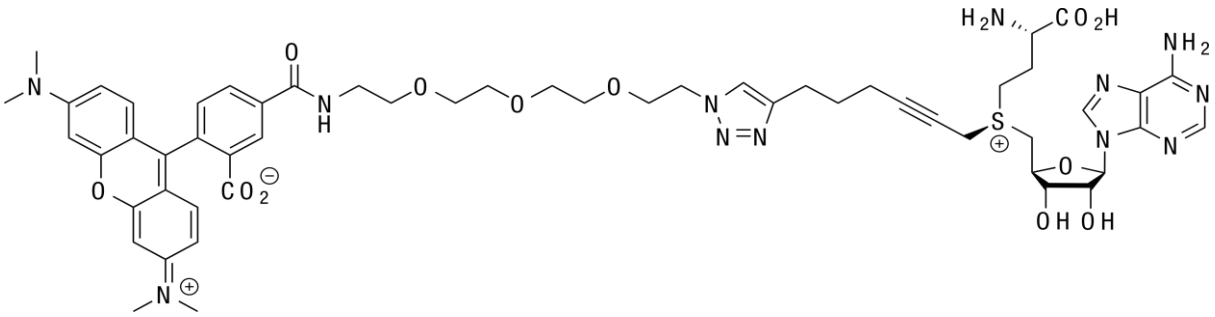

Fig. 2-15: Synthetic fluorescent AdoMet analogue Ado Yn TAMRA.

If DNA is modified by MTases with fluorescent cofactors, the fluorophores function as labels that mark the positions of the specific recognition sequence. Since these positions are individual for each gene, the labeling of DNA is suitable as a method for DNA barcoding.(Grunwald, Dahan et al. 2015, Deen, Vranken et al. 2017) After linearization of the DNA strands, the barcode can be analyzed by means of fluorescence microscopy.

2.5.5.DNA staining reagents

Fluorescent dyes are used in order to visualize entire DNA double strands. Different mechanisms for the staining of DNA can be found in literature.(Waring 1965, Le Pecq and Paoletti 1966, Latt, Stetten et al. 1975, Rye, Yue et al. 1992, Vega, García Sáez et al. 1994) One possibility consists of embedding fluorophores in the backbone of the double helix. The minor groove of the DNA is used as a binding site by the Hoechst stains.(Latt, Stetten et al. 1975, Vega, García Sáez et al. 1994) Another mechanism lies in the intercalation of an aromatic dye between two neighboring nucleobases by π-stacking. This is the case for reagents commonly used in agarose gel electrophoresis like ethidium bromide or GelRed®.(Waring 1965, Rye, Yue et al. 1992) Another molecule that stains the DNA by intercalation is YOYO-1®, which has one fluorescent aromatic group on both ends (Fig. 2-16).

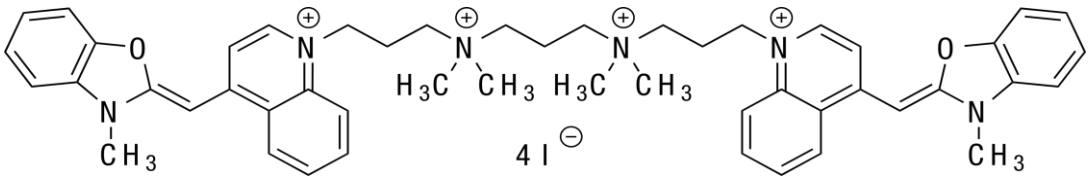

Fig. 2-16: DNA intercalating, fluorescent staining reagent YOYO-1.

When solved in water YOYO-1® has a very low fluorescence quantum yield. However, when both aromatic ends of YOYO-1® are intercalated to double stranded DNA, the fluorescence emission intensity increases by more than three orders of magnitude. Additionally, the absorption maximum wavelength of YOYO-1® is shifted from 458 to 489 nm by DNA intercalation.(Rye, Yue et al. 1992) Furthermore, it should be noted that the YOYO fluorophore even allows for super-resolution imaging of DNA.(Flors 2010)

2.5.6. DNA-stretching

Optical DNA mapping relies on the analysis of intact large single DNA molecules that are stretched out.(Müller and Westerlund 2017) Therefore, different methods were developed to immobilize DNA in a linearized conformation instead of the entropically more favorable coil conformation. In this section, two relevant methods being (a) stretching in nanochannels and (b) DNA combing, will be presented.

2.5.7. Nanochannels

The nanochannel technique consists of exposing the coiled, labeled DNA molecules to an electric field which drives the molecules through a series of progressively smaller nanoscale obstacles. This first step detangles the DNA molecules without breaking them. The nanoscale obstacles funnel the molecules into channels of 45 nm in diameter, leaving the DNA molecules no degree of freedom to go back to their coiled conformation. Once the DNA molecule is stretched and confined within the channels, the distances between the fluorescent labels can be accurately measured using a fluorescence microscope. DNA molecules with similar patterns of labels are clustered, and software is used to generate a consensus map of the sequence motifs recognized by the nicking enzyme. The company Bionano Genomics represents the most prominent vendor offering the nanochannel technique. As pioneers in the field of optical mapping they have developed the diagnostics system *Saphyr* which is capable of analyzing single molecules with an average length of approximately 250,000 base pairs long.

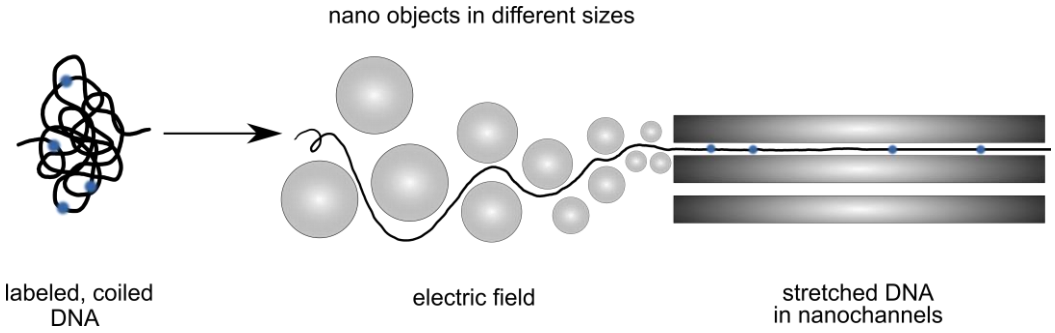

Fig. 2-17: The future perspective of DNA nano-channeling consists of detangling coiled, labeled DNA strands through nanoscopic objects. The direction of the flow through these objects is obtained by an external electric field. As the nanoscopic objects decrease in size, the DNA molecules are linearized until their degree of freedom is restricted to a point where they are guided in their stretched conformation into nanochannels. The read-out of the labels by means of fluorescence microscopy takes place within the nanochannels where a sequence-specific barcode is generated which can later be used for the analysis of e.g. structural variations or cancer diagnostics, depending of the labeled functionalities within the DNA molecules. Figure adapted from Ebensteil et al. (Levy-Sakin and Ebenstein 2013)

2.5.8. DNA combing

DNA combing is a laboratory technique that allows to stretch DNA without the purchase of a special device or instrument. It relies on a specific type of surface modification. The basic experiment consists of a drop of DNA-solution that is deposited on an unmodified glass slide. A modified (silanized) cover slip is then placed on top of the solution and pulled ("combed") sidewise on top of the underlying substrate. The capillary flow drags the solution leaving the stretched and immobilized molecules on the unmodified substrate. Deproteinized DNA molecules in solution with a random-coil conformation attach with non-sequence specificity to a silanized hydrophobic glass surface by their extremities.(Lebofsky and Bensimon 2003) The immobilization of DNA molecules can be enhanced by introducing sparse charged functionalities to the silanized surface to bind the negatively charged DNA molecules by their ends. Although the molecule extremity-surface attachment process is not well understood, it has been proposed that pH-induced denaturation of the DNA ends exposes the hydrophobic domains of the bases, allowing a strong interaction with the hydrophobic surface.(Allemand, Bensimon et al. 1997, Lebofsky and Bensimon 2003)

The glass surface is mechanically pulled out of the solution at a constant speed where the receding air–water meniscus exerts a constant perpendicular force on the attached DNA molecules.(Lebofsky and Bensimon 2003) This constant perpendicular force is central to obtaining uniformly stretched DNA of a singular orientation.(Lebofsky and Bensimon 2003)

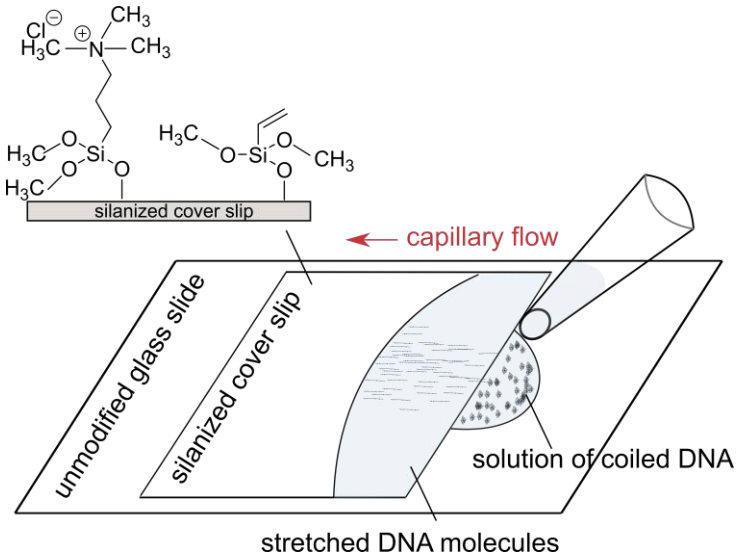

Fig. 2-18: Basic principle of DNA combing where a solution of coiled DNA is dragged over an unmodified glass substrate due to capillary forces and a surface modification (with e.g. N-Trimethyl[(3-methoxysilyl)propyl]ammonium chloride) of the cover slip on top. The positively charged functionalities of the coverslip immobilize the (sticky) ends of the DNA molecules while the rest of the molecule is stretched due to the hydrophobic parts of the cover slip. The immobilized and stretched DNA strands can be read out using fluorescence microscopy techniques in case of fluorescently labeled DNA.

3. Microgels at the solid/liquid interface

This chapter focuses on the fundamental behavior of µGs at the solid-liquid interface. Their deformation behavior was analyzed under different circumstances with the help of SRFM and computer simulations. Relevant theoretical background for this chapter has been introduced in the theoretical background section of this dissertation. This chapter mainly builds on fundamentals concerning the presented section on fluorescence microscopy (see 2.1) and section 2.3 introducing µG systems.

The short introduction in section 3.1 intends to clarify the motivation for the fundamental analysis of µG behavior at the solid-liquid interface. The results and discussion part in chapter 3.2 covers the analysis of the SRFM data as well as the results of computer simulations, the accompanying image analysis and data visualization approaches. Finally, the summarized results, as well as an outlook for future research is given in section 3.3.

3.1. Introduction

Stimuli-responsive µGs can be defined as soft, colloid-like macromolecular objects with complex inner structure. As introduced in section 2.3, they bear a high potential for applications in biotechnology (Lynn, Amiji et al. 2001, Murthy, Xu et al. 2003, Cao, Gu et al. 2004, Serpe, Yarmey et al. 2005, Ali, Su et al. 2007, Saunders, Laajam et al. 2009), drug delivery (Murthy, Thng et al. 2002, Nayak, Lee et al. 2004, Lopez, Hadgraft et al. 2005, Nolan, Reyes et al. 2005, Varma, Kaushal et al. 2005, Das, Mardyani et al. 2006, Vinogradov 2006), electronics (Gao and Hu 2002, Zhang, Xu et al. 2004) and sensor technology (Hendrickson and Lyon 2009). When it comes to the development of new applications, a fundamental understanding on how the µG shape and inner structure affects their properties is essential. In order to monitor the shape of µGs at the interface, different experimental techniques as well as theoretical and computer simulation approaches are available.

As already mentioned in section 2.1.4, SRFM methods have been adapted for materials science in recent years.(Wöll and Flors 2017) Together with well-established techniques such as scanning probe microscopy (Herruzo, Perrino et al. 2014) and modern electron microscopy, SRFM gives unprecedented views to the nanoscale. Additionally, SRFM bears the advantage of imaging non-invasively. This way, also adaptive behavior and dynamic processes can readily be elucidated.

The adaptive properties of µGs, i.e. the ability to swell and collapse depending on the solvent quality (Pich and Richtering 2010) and external stimuli (Plamper and Richtering 2017), as well as their high elasticity are focus of current research. The responsiveness to external stimuli results from the crosslinked molecular structure that allows solvent uptake and release. This leads to an environment-dependent surface constitution which limits the validity of the term "shape" for what is in fact a highly flexible and structurally variable fuzzy exterior. The presence of an interface makes the situation even more complicated, as interactions between the soft objects and the surface may induce changes in their shape and inner structure. For an attractive interaction, this causes strong adsorption of the sub-chains, resulting in spreading of the µGs. The degree of spreading on the surface depends on the elasticity of the network, mainly defined by the crosslinking density.(Mourran, Wu et al. 2016) For low crosslinking density and strong adsorption, the resulting shape of µGs resembles that of a fried-egg.(Witte, Kyrey et al. 2019) Schulte et al.(Schulte, Scotti et al. 2018) report that low crosslinking will result in a soft and easily deformable µG tending to strongly spread at the solid support after investigating the local density of surface-adsorbed pNIPAM-µGs with SFM. This method allows to probe the internal structure of µGs that are physically adsorbed at the solid-water interface. However, such a deformation is not always desired, neither for applications nor for the imaging of µGs. A possible approach to maintain the native, spherical shape of a µG at a surface lies in the modification of the surface in order to control the µG-surface interactions. Surface modifications with PEG, for example, are well known in biological applications, where they are used as anti-fouling coatings.(Ostuni, Chapman et al. 2001, Balamurugan, Ista et al. 2005, Ekblad, Bergström et al. 2008, Yu, Zhang et al. 2011) The behavior of µGs at the interfaces has been addressed in different studies, both experimentally and by the aid of computer simulations.(Burmistrova, Richter et al. 2011, Witte, Kyrey et al. 2019) The latter serve as a powerful tool to study the properties of µGs of different topology in bulk solution (Gnan, Rovigatti et al. 2017, Brugnoni, Scotti et al. 2018, Keidel, Ghavami et al. 2018, Nikolov, Fernandez-Nieves et al. 2018) and at various surfaces and interfaces.(Mourran, Wu et al. 2016, Gumerov, Rudov et al. 2017, Portnov, Möller et al. 2018, Song, Bao et al. 2018, Camerin, Fernandez-Rodriguez et al. 2019, Gumerov, Filippov et al. 2019)

In particular, in the work by Geisel et al.(Geisel, Rudov et al. 2015) the authors investigated core-shell and hollow pNIPAM µGs at liquid interfaces by means of compression isotherms and dissipative particle dynamics (DPD) simulations. They further provide information about the influence of a solid core or a central void, respectively, and the crosslink density on the deformation and internal structure of µGs for different conditions.

When µGs shall be applied in technical devices, they typically need to be immobilized on solid supports. Therefore, controlling and analyzing their shape at the solid-liquid interface is of great importance.(Schmidt, Hellweg et al. 2008, Wellert, Kesal et al. 2015) In this chapter, a combined experimental and theoretical approach to visualize, parametrize and elucidate the µG-surface interaction and its structural consequence on a mesoscopic level is presented. Selected surface functionalization with different hydrophilicity are employed to control the spreading behavior of pNIPMAM µGs on the surface. One of the goals consists of achieving the maximum hydrophilicity of the surface while keeping the µGs at a swollen state. As shown by Léonforte et al. (Léonforte and Müller 2015), the PEG brush becomes highly swollen around 32 °C, this is also the main reason for not choosing pNIPAM µGs in the described use case, as they would undergo a phase transition at this temperature. The selected pNIPMAM µGs can be classified as thermoresponsive soft objects, possessing a VPTT of ~ 42 °C.

3.2. Results and discussion

The structural change of the µG – and thereby its surface interactions on different substrates – is investigated in section 3.2.1. Building on these results, the most commonly employed sample preparation methods, and how these can affect the deformation of pNIPMAM µGs on surfaces with varying hydrophilicities, is analyzed in section 3.2.3. Throughout both sections, 3D dSTORM measurements were used to elucidate the µG shape at different surfaces. Since the surface of a µG has a fuzzy boundary, a novel method is introduced to describe this shape with a well-defined, geometrical object (see 3.2.2). The parameters obtained from this fit to the observed data allow for a quantitative comparison of µG shapes, independent from the acquisition method. Hence, an algorithmic solution allowing to parametrize the shape of a µG point cloud resulting from 3D SRFM is applied. This approach highly simplifies the quantitative comparison of deformation. The experimental data are complemented with mesoscopic computer simulations (DPD) in order to (i) rationalize the experimental results and (ii) to track the evolution of the shape with changing surface hydrophilicity.

3.2.1. 3D Super-resolution fluorescence microscopy

The spreading behavior of pNIPMAM µGs was investigated on glass substrates with three different surface modifications (see Fig. 3-2). Hydrophilic surface coatings were formed by surface modification with *O*-(2-aminoethyl)polyethylene glycol (PEG).(King, Rathore et al. 1992, Deng and Mani 2006) The modification was verified via contact angle measurements (see section 7.1.3), resulting in a contact angle of 27° in accordance with literature data. (Jo and Park 2000) To obtain hydrophobic surface properties, a glass substrate was coated with n-octadecyltrimethoxysilane (ODS), resulting in a contact angle of 102°, also in agreement with previous measurements.(Markovich and Mandler 2001) Teflon-like surface coatings are commonly referred to as non-philic / non-phobic. In order to fabricate such a surface, the glass surface was functionalized with trichloro(1H,1H,2H,2H-perfluorooctyl)silane (FOCTS), resulting in a contact angle of 103°. It should be noted that the functionalization of the glass substrates was performed in (i) liquid for ODS and PEG and (ii) from the gas phase in case of FOCTS, resulting in different surface coverages. Therefore, similar contact angles were obtained in both cases. The three different surface modifications are depicted in Fig. 3-1.

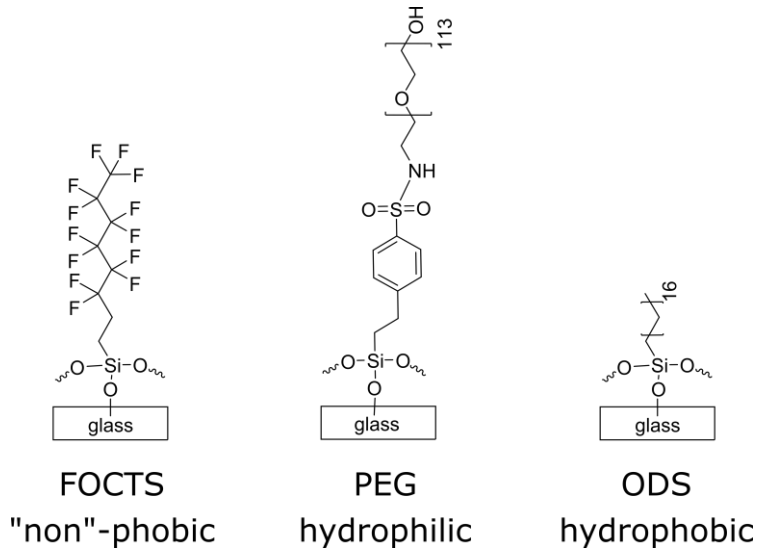

Fig. 3-1: Overview of the three investigated surfaces: FOCTS (trichloro(1H,1H,2H,2H-perfluorooctyl)silane) as non-phobic coating, ODS (n-octadecyltrimethoxysilane) as the hydrophobic modification, and PEG (O-(2-aminoethyl)polyethylene glycol) being a hydrophilic modification.

For the deposition of pNIPMAM µGs on the respective surface, spin-coating was performed in the case of the PEG and FOCTS surfaces. Due to the high hydrophobicity of the surface, a drop of µG solution was left to dry in the case of ODS (drop-casting method).

The latter procedure was necessary because no µGs were surface-immobilized with the spin-coating process due to poor surface-µG interactions. The impact of the chosen deposition method will be further discussed in section 3.2.3.

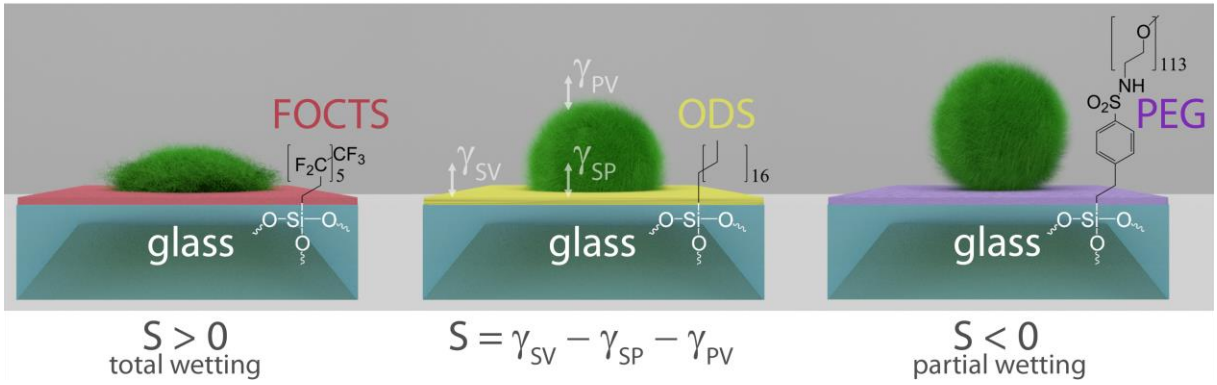

Fig. 3-2: Investigation of the spreading behavior of pNIPMAM µGs on surfaces with varying hydrophilicities achieved by modification of the interface with different silanes. S, the theoretical spreading parameter (Gnan, Rovigatti et al. 2017), is derived from the Young equation(Young 1805) and allows for the differentiation between total spreading at $S > 0$ (fried-egg) and partial wetting at $S < 0$ (weakly disturbed native, spherical conformation). γ describes the surface tension between the different phases: surface (s), polymer (p) and the surrounding liquid (v). The different colors represent the differently modified glass substrates: FOCTS and ODS represent relatively hydrophobic surfaces, whereas the PEG modification results in a strongly hydrophilic system.

The investigated pNIPMAM µGs were labeled with Alexa 647 Fluor. Appropriate blinking conditions were adjusted with 50 mM cysteamine blinking buffer. To achieve the swelling of the PEG brush and simultaneously keep the µGs in the swollen state, all experiments were conducted at 33 °C.(Léonforte and Müller 2015) The adsorbed µGs were visualized in TIRF mode employing the well-established dSTORM technique described in 2.1.5.(Heilemann, Van De Linde et al. 2008, Whelan, Holm et al. 2014) This method was selected as it is straight-forward in terms of equipment and analysis. For 3D localization, the DH-PSF method described in section 2.1.6 was implemented using a double Helix SPINDLE™ module (Double Helix LLC, Boulder). The 3D information was acquired from the z-dependent rotation angle of the two lobes, by which a single object is imaged after the emission light passes an appropriate phase mask.

The results are depicted in Fig. 3-3 showing a strongly pronounced fried-egg shape for the non-phobic FOCTS surface and a less pronounced fried-egg shape for the hydrophobic ODS surface. The PEG substrate on the other hand leads to a spherical µG conformation in the native conformation.

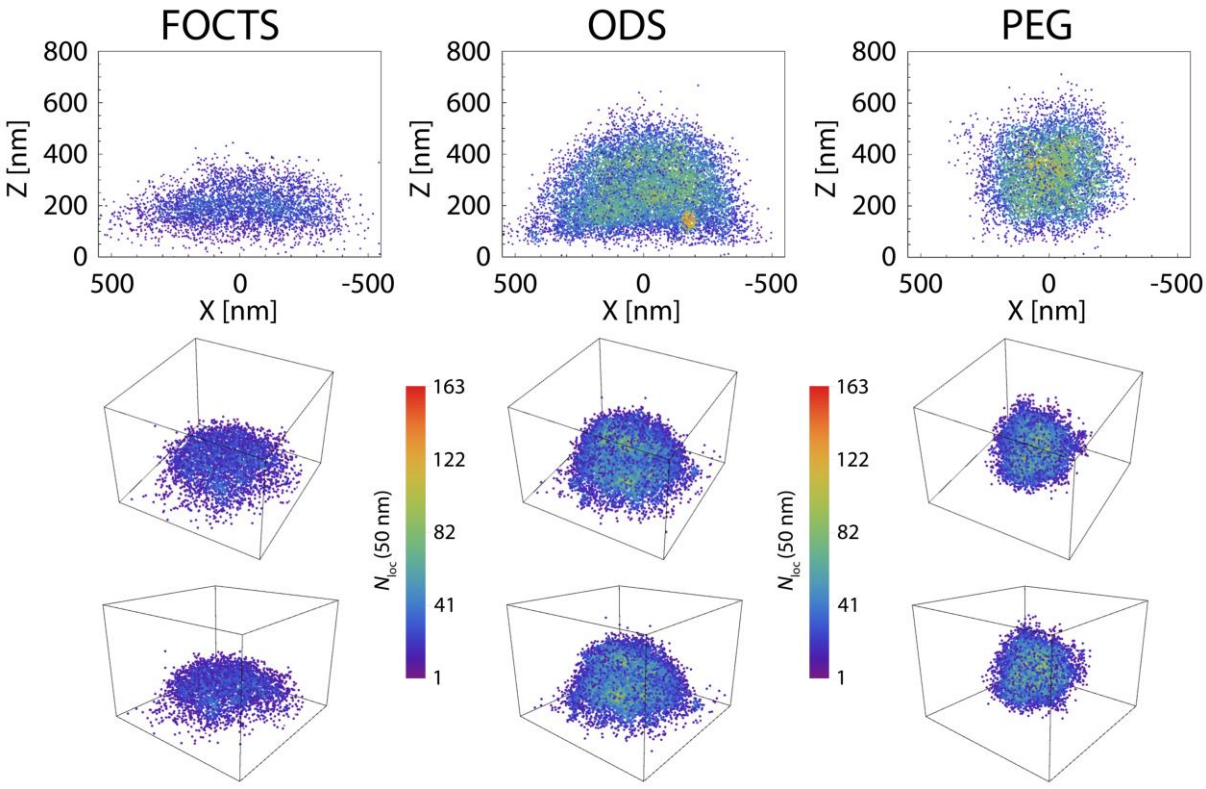

Fig. 3-3: 3D dSTORM measurements of pNIPMAM µGs on different surfaces. FOCTS is a non-phobic Teflon-like surface, ODS consists of a long hydrophobic alkyne chain and the PEG substrate represents the hydrophilic surface. The µG conformation changes from a fried-egg shape at hydrophobic surfaces (FOCTS, ODS) to a spherical shape at the hydrophilic surface.

Since the contact angles of ODS and FOCTS are similar due to the sample preparation (see above), both the experimental and simulation results reflect that a contact angle measurement is not enough to approximate the spreading behavior of strongly hydrated µGs on a solid surface. The experimental data were supported with computer simulations, specifically with DPD simulations conducted by the cooperation partner Rustam Gumerov (research group of I. Potemkin at Moscow State University). The DPD simulations were performed with single µG particles in a water environment on the solid surface functionalized with grafts of various hydrophilicity. The coarse-grained model µGs of pNIPMAM are constructed from a regular network (Mourran, Wu et al. 2016, Gumerov, Rudov et al. 2017, Keidel, Ghavami et al. 2018, Gumerov, Filippov et al. 2019) with a fraction of crosslinks similar to the real systems.

They contain over 100000 segments (beads) which were placed in orthogonal simulation boxes containing about 6 × 106 beads. For each type of surface, the simulation parameters including the interactions between the different substances were estimated to achieve the closest representation of the real systems. The resulting equilibrium conformations of simulated µGs are presented in Fig. 3-4.

In agreement with the experiments, the contact area between the µGs and the PEG-covered surface (shown in green) is minimal. In contrast, for hydrophobic surfaces, strong flattening of µGs to pronounced fried-egg conformations is observed. This flattening is especially pronounced at the FOCTS surface. These results clearly demonstrate that maintaining the native shape of a µG at the solid-liquid interface is highly dependent on the composition of the µG and its respective molecular interactions with the respective surface modification. DPD simulations have shown to give an estimate about the appropriate surface modification and thus allow for a targeted fabrication of the surface.

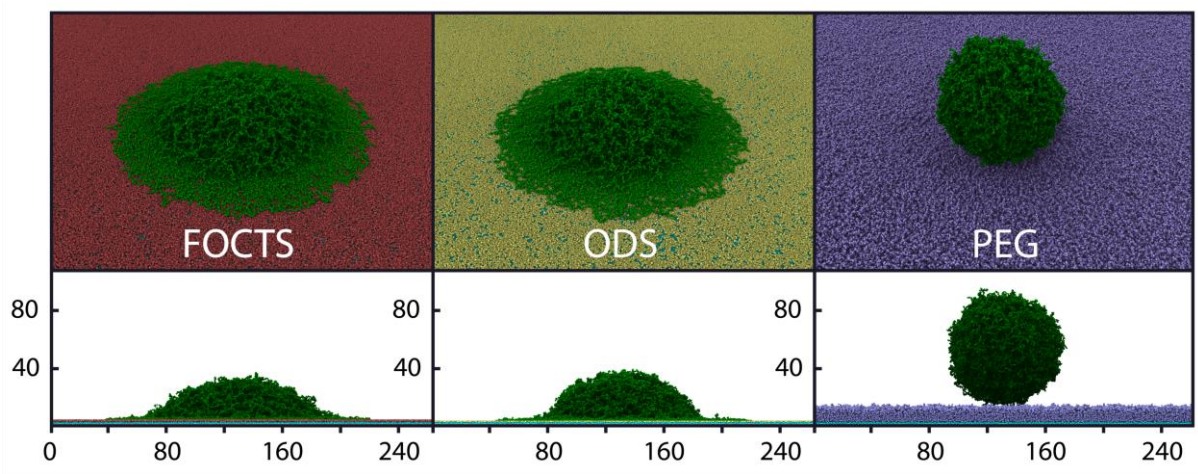

Fig. 3-4: DPD simulation of pNIPMAM µGs at surfaces of different hydrophilicity. As in the experimental case, the µG conformation changes from a fried-egg shape at hydrophobic surfaces (FOCTS, ODS) to a spherical shape at the hydrophilic surface.

The results acquired at the PEG-ylated surface reveal low surface-µG interactions, as the particles appear to be in their native, spherical shape. The results are in complete accordance with theoretical expectations as the PEG surface can be understood as a solvent-like system.(Léonforte and Müller 2015) Therefore, it is energetically more favorable for the surface to interact with the solvent than with the crosslinked polymer system. From the physical point of view, both FOCTS and ODS can be regarded as hydrophobic surfaces: the contact of the two surfaces with the polymer chains of the µG is more favorable than the one with water.

In other words, the sub-chains adsorb on the surface to minimize unfavorable surface-water contacts. Such adsorption is opposed by the elasticity of the network which is controlled by the crosslinking density. Thus, the ultimate shape of the µG adsorbed on a hydrophobic surface is determined by the competition between a gain in the adsorption energy and a penalty in the elastic free energy. This can also be rationalized by a comparison with ultra-low crosslinked µGs, yielding a pancake-like shape when absorbed.(Scotti, Bochenek et al. 2019) This is a consequence of weak elasticity of the µGs, as a high fraction of the adsorbed sub-chains facilitates the flattening of µGs. However, the µGs utilized in this chapter are higher crosslinked pNIPMAM µGs, which still reveal a fried-egg-like shape in both FOCTS and ODS cases. This structure reveals that some of the peripheral sub-chains (including dangling chains) are adsorbed, whereas inner sub-chains are not. Otherwise, it would cause high elastic stress. The 3D measurements show a stronger adsorption to the surface in case of FOCTS in comparison to that of ODS. This is rather counterintuitive, considering the fact that long alkyne chains of ODS are chemically more compatible with the polymer than the fluoride groups of the FOCTS. In case of ODS, the adsorption should therefore not only be driven by the adsorption energy but also by a significant affinity between pNIPMAM and the alkyne chain. Nevertheless, the experimental results clearly show a stronger adsorption in case of FOCTS. The reason for such a behavior lies in the microscopic structure of the functionalized surfaces and will be discussed as follows. One possible explanation for this unexpected behavior could lead back to the level of incompatibility of the fluorinated surface terminal groups with water, which can be estimated by the Flory-Huggins parameter χ. This parameter can directly be derived from the Hansen solubility parameter.(Hansen 2002) It shows that FOCTS is less compatible with water than the alkyne chains are. With this higher surface energy for the case of water-FOCTS compared to the case of water-ODS, the spreading parameter S can be rationalized. Additionally, the difference in surface coverage f between FOCTS and ODS can play an important role. It can be estimated from the surface contact angle θ using the well-known Cassie equation.(Cassie 1948)

$$\cos\theta = f_1 \cos\theta_1 + f_2 \cos\theta_2 \tag{13}$$

where $f_1 = f$ and $f_2 = 1 - f$ are fractional coverages of the first and second constituents (namely, the hydrophobic oligomers and bare glass regions) of the surface and θ_1 and θ_2 are the respective contact angles of the pure constituents.

In this work, the contact angles of the glass surfaces before the functionalization were estimated to 5° and 1° for FOCTS and ODS respectively (see 0). As a result, concerning the values of the contact angles of modified surfaces, a surface coverage of $f = 0.85$ for ODS and $f = 0.91$ for FOCTS is obtained.

Simultaneously, the respective glass surfaces can be considered as slightly hydrophobic and hydrophilic, while it is known that the acrylamide-based µGs have an affinity to such substrates.(Mourran, Wu et al. 2016) Thus, in case of FOCTS the probability of contact between the µG and the bare substrate is higher which results in a stronger flattening of the particles in comparison to the other cases. For the experimentally investigated µGs with a size of 1 µm, these nanoscopic inhomogeneities in surface coverage can be neglected whereas they play a role in the simulated systems which are approximately one order of magnitude smaller. Finally, the preparation method may play a role, since for ODS, the sample preparation consisted of drop-casting, while the particles were spin-coated in the case of FOCTS, and could therefore be subjected to additional spreading due to the inertia forces. This effect will be analyzed in section 3.2.3. Altogether, it can be stated that the surface should be modified with the aim of mimicking the solvent itself. For pNIPMAM µGs a highly hydrophilic surface (PEG) performs very well. This observation was validated by the good accordance between experimentally obtained 3D SRFM data and simulated DPD results.

3.2.2. Parametrization of microgels as 3D point cloud data

The characterization of the µG conformation as spherical or fried-egg-like, is usually based on a qualitative or visual estimation. The open question regarding the possibility of fitting a 3D shape with a defined surface to a soft object with a fuzzy and undefined surface was already stated in the introduction of this chapter. Although this question is legitimate, it is also fair to say that the visual estimation or comparison of an object's conformation does not provide a quantitative measure. As the next logical step in analysis, a parametrization approach was introduced, allowing for the quantitative shape analysis of soft matter particles like µGs. This method can be applied completely independent from the data acquisition method and can therefore be used to compare experimental results that were acquired through a variety of measurement methods, such as AFM and SRFM. Furthermore, the shape parametrization does not only allow for the distinction of different shapes, but also for the comparison of experimentally and theoretically acquired data.

For the analysis of the 3D point cloud data presented in the previous section 3.2.1, a new fitting algorithm, yielding an isosurface of constant density, is introduced. This algorithm defines the deformation of µGs at different surfaces. Thereby, a sphere cap is fitted around the 3D point cloud data, approximating the shape of the µG on the surface (see.Fig. 3-5).

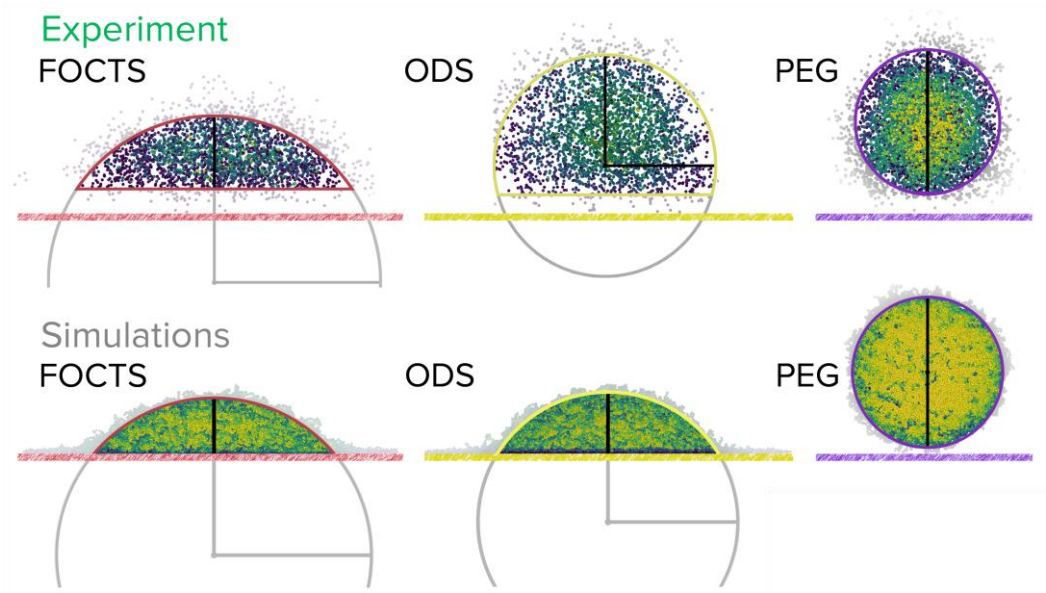

Fig. 3-5: Parametrization of µG point cloud data extracted from SRFM experiments (top) and simulations (bottom). A sphere cap is fitted around the 3D point cloud data, approximating the shape of the µG on the surface.

Subsequently, the ratio of the volume of the fitted sphere cap to the volume of the entire fitted sphere is taken, which results in a scalar between zero and one. Hereby, a µG of perfectly spherical shape would yield a ratio of one, whereas a total “fried egg” would result in a ratio of zero. For the simulated µGs, the positions of each of the monomers within the colloidal network was analyzed. The degree of spreading of the µG on the surfaces was estimated with their surface points in simulations fitted with the LSQR approximation (Paige and Saunders 1982) The resulting quantitative comparison of the experimentally and theoretically acquired data sets is depicted in Fig. 3-6. The parametrization clearly allows for the distinction of different degrees of spreading on a surface.

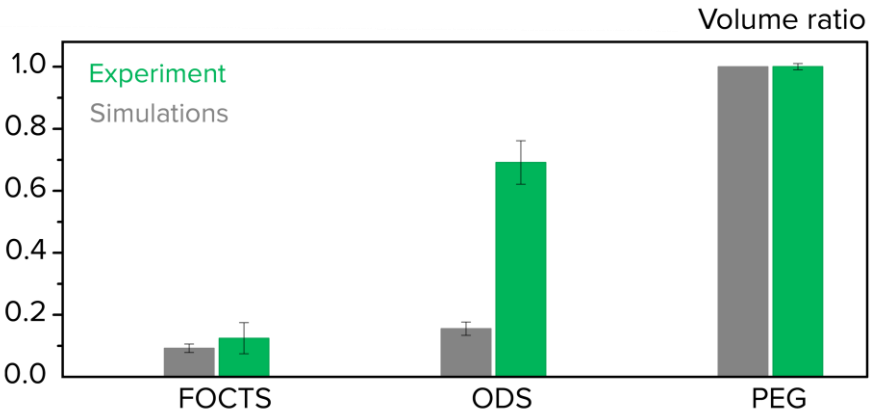

Fig. 3-6: Comparison of the volume ratio deduced from the parametrization approach. The ratio of the volume of the fitted sphere cap to the volume of the hole fitted sphere is taken, which results in a number between zero and one. Hereby, a µG of spherical shape would yield a ratio of one, whereas a total pancake would result in a ratio approaching zero. The error bar for the volume ratio extracted from simulations for the case of PEG is omitted as it is smaller than 0.001 and therefore not displayable.

As anticipated, the quantitative analysis results in a value of one for the PEG system, for both experimental and simulated data sets. As already seen in the results described in section 3.2.1, the gel maintains its native, spherical shape on the solvent-like PEG surface. Furthermore, the two hydrophobic surfaces are clearly distinguishable when analyzing the experimental (point cloud) data. Hereby, the calculated volume ratios in case of FOCTS and PEG surface demonstrate a good agreement between the experiments and simulation. However, a pronounced mismatch is found in case of the ODS surface. It can be assumed that this mismatch is related to the different methods of the preparation of the sample for ODS, which will be discussed in section 3.2.3. Another possible reason for the mismatch could lie in the smaller size of simulated µGs in comparison to the µGs studied in the experiments as smaller µGs bear higher liquid-solid surface energy which might outweigh the elastic energy of the network and, thus, the spreading on the surface will be more pronounced.(Rumyantsev, Gumerov et al. 2016)

3.2.3. Investigation on different deposition methods

It was recently shown that both temperature and the deposition method have a strong influence on the shape of ultra-low crosslinked µGs. (Schulte, Scotti et al. 2019) In brief, these µGs can be selectively trapped, either in a more particle-like or in a more polymer-like behavior. However, it was still unclear how the deposition method affects the overall shape in case of regularly crosslinked µGs. Therefore, I addressed the question of the impact of the drying process on the deposition. This question is especially important when analyzing SRFM data, as for most microscopy methods a rehydration of the adsorbed µGs is needed due to e.g. the addition of a blinking buffer in dSTORM. The goal of this investigation therefore consists of deepening these observations and analyzing the effect of solvent evaporation on a µG sample. To the best of the authors' knowledge, most laboratories use either drop-casting or spin-coating as their method of choice to deposit a µG film at the solid-liquid interface. Furthermore, µGs can be deposited through adsorption without any evaporation of the solvent. The latter case is simulated in most computational methods. It is therefore not only important to analyze the effect of solvent evaporation for the experimental case, but also for simulations. As already shown in the previous section, the deformation behavior of µGs at the solid interface strongly depends on the surface hydrophilicity. Therefore, the investigation of the different preparation methods was conducted on surfaces of different hydrophilicity: (i) glass, (ii) PEG and (iii) FOCTS. For spin-coating, the sample solutions were spin-coated onto the substrate at 4000 rpm. In the case of drop-casting, a drop was placed onto the substrate and left to dry for one hour at room temperature. Afterwards, the blinking buffer was added to the dry substrate as it was placed on the microscope. The third investigated deposition method consisted of an adsorption experiment. This means that in contrast to the other two presented methods, the sample is never left to dry and the µGs remain always surrounded by solvent. Therefore, a droplet of the µG sample was deposited onto the substrate and covered afterwards in order to prevent strong evaporation of the solvent. In this case it was crucial to immediately apply the blinking buffer for the 3D d-STORM measurements in order to guarantee no drying effects taking place at the solid-liquid interface. The dSTORM measurements were conducted in TIRF mode. The investigated pNIPMAM µGs were labeled with Alexa 647 Fluor. Appropriate blinking conditions were adjusted with 50 mM cysteamine blinking buffer. To achieve the swelling of the PEG brush and simultaneously keep the µGs in the swollen state, all experiments were conducted at 33 °C.(Léonforte and Müller 2015) The adsorbed µGs were visualized in TIRF mode applying the dSTORM technique described in 2.1.5.(Heilemann, Van De Linde et al. 2008, Whelan, Holm et al. 2014)

For 3D localization, the DH-PSF method described in section 2.1.6 was implemented using a double Helix SPINDLE™ module (Double Helix LLC, Boulder). The 3D information was acquired from the z-dependent rotation angle of the two lobes, by which a single object is imaged after the emission light passes an appropriate phase mask. A more detailed documentation of the experimental conditions can be found in section 7.1.4.

It is important to underline that even though the deposition methods, meaning the adsorption process of the µG to the surface, are achieved through different methods, SRFM imaging is always conducted in aqueous solution due to the necessary presence of the blinking buffer. Thus, the main question answered in this section is whether the initial deposition method influences the partly reswollen µG.

(i) Glass

First, the deposition of µGs to a bare glass substrate without any hydrophilic or hydrophobic surface functionalization is presented. The experimental dSTORM results after partial rehydration with the blinking buffer are depicted in Fig. 3-7 for all three deposition methods.

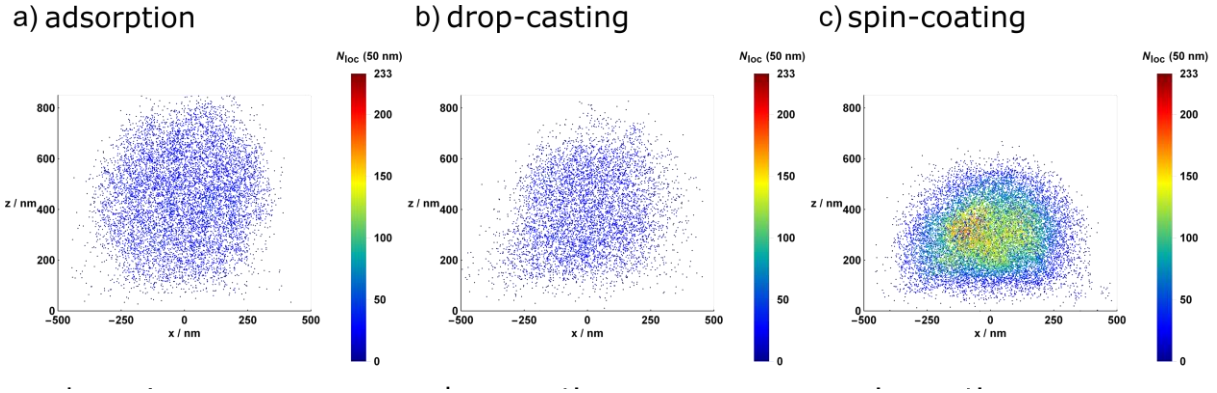

Fig. 3-7: 3D dSTORM measurements of one pNIPMAM µGs on a glass substrate. The deposition method varies from (a)-(c) as follows: (a) adsorption, (b) drop-casting, (c) spin-coating.

The native, spherical shape is achieved in the adsorbed case in image (a) of Fig. 3-7. The contact area between µG and surface is significantly higher for the two remaining deposition methods. The comparison between drop-casting and spin-coating clearly shows that the spin-coating case results in stronger adsorption. These results are in accordance with theoretical expectation, as for the case of drop-casting it is more likely that residual solvent is still left after the finished procedure. In case of spin-coating, however, most solvent is pushed out during the spin-coating process and the air flow during spinning assists water evaporation.

Therefore, in the latter case the polymer-substrate interactions are stronger than the solvent-water interactions, resulting in a higher contact area.

ii) PEG

The deposition of µGs to a hydrophilic PEG presented in Fig. 3-8. The experimental dSTORM results after partial rehydration with the blinking buffer are depicted for all three deposition methods. The expectation for the hydrophilic surface coating in the case of PEG are straight-forward as the µG is surrounded by solvent and deposited on a solvent-like substrate.

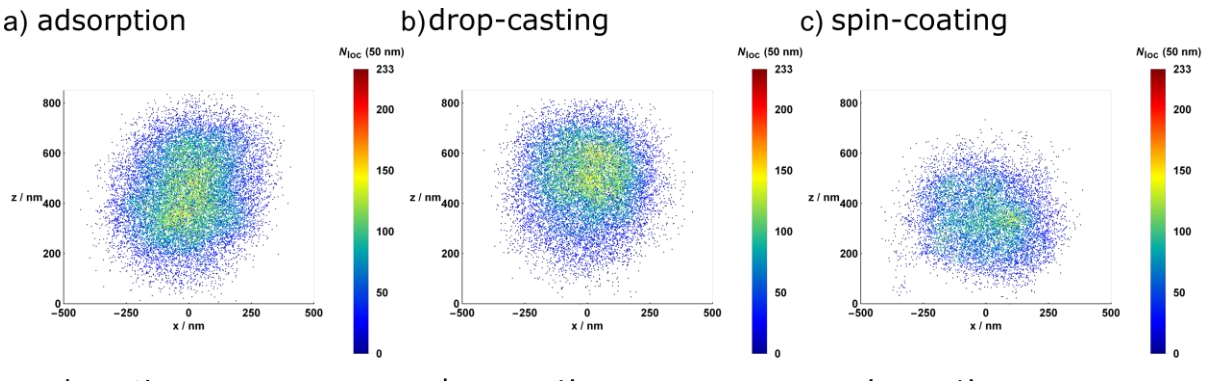

Fig. 3-8: 3D dSTORM measurements of one pNIPMAM µGs on a PEG substrate. The deposition method varies from (a)-(c) as follows: (a) adsorption, (b) drop-casting, (c) spin-coating.

A nearly native µG conformation can be observed in the adsorption case. In comparison to the measurements on bare glass, an even smaller contact area can be observed by eye for all three cases. As anticipated, this is due to the fact that the µG is surrounded by a solvent-like system in all dimensions. In the case of drop-casting, the spherical nature is retained. However, the spin-coating case reveals that the µG is pushed towards the surface. The shown experimental results on PEG do indicate a slight directional tilt of the µGs in comparison to the results on bare glass. In order to exclude the possibility that this tilt is introduced by washing off the substrates from any residuals before the addition of the blinking buffer, additional testing was required. The testing substrates were washed off by pipetting water in different directions onto to the substrate. The water was always pipetted onto the standing substrate from above, the directionality was introduced by rotating the substrate for each new measurement. This was done in order to investigate if the direction of the water flow introduced by washing of the residuals with water, would allow to control the direction of the tilt which the adsorbed µGs display.

All images taken on PEG resulted in a slight tilt of the µG with completely random directionality, completely unrelated to the direction of the water flow introduced in the washing process. It can therefore be concluded that the phenomenon of the slight µG tilt happens randomly and towards all directions, it will therefore not be further discussed in the next paragraphs.

iii) FOCTS

The FOCTS measurements discussed in section 3.2.1, exhibited the strongest fried-egg conformation. This effect was also pronounced in simulations and could be explained due to the strong polymer-substrate interactions, as the substrate is strongly hydrophobic in regard to the measured contact angle. The experimental results for the different deposition methods of µGs on FOCSTS are depicted Fig. 3-9 and allow for a comparison with previous results.

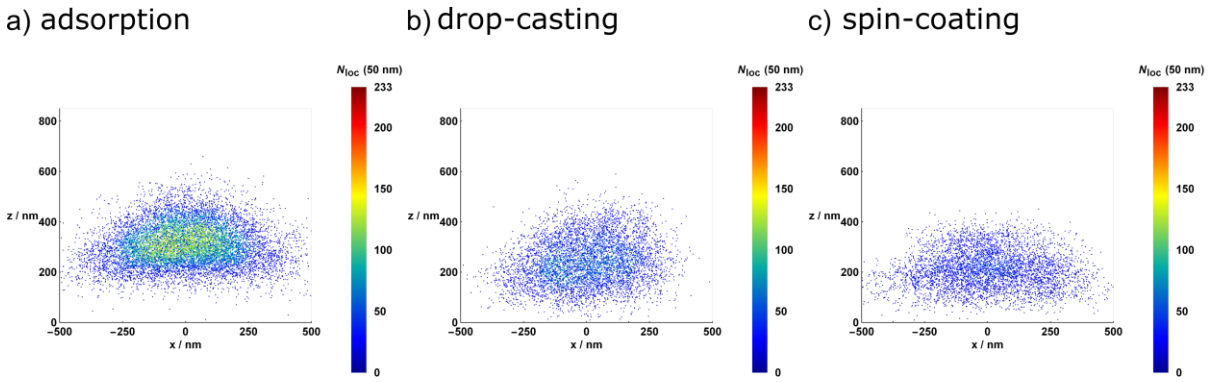

Fig. 3-9: 3D dSTORM measurements of one pNIPMAM µGs on an FOCTS substrate. The deposition method varies from (a)-(c) as follows: (a) adsorption, (b) drop-casting, (c) spin-coating.

The visual analysis of the SRFM results on FOCTS reveal a strong adsorption of the µG to the surface. The fried-egg conformation is especially visible in the cases of adsorption (a) and spin-coating (b). Due to a stronger interaction of the µG with the hydrophobic surface, the contact area is larger than imaged on the reference system (glass). Noticeably, in the cases of glass and PEG, there was no significant attachment of the µG to the surface after adsorption. However, in the case of FOCTS, adsorption in combination with molecular interaction, seems to induce strong spreading of the µG. This behavior can be explained by the amphiphobic characteristics of FOCTS.(Wong, Corrales et al. 2020) This means that even though FOCTS does not interact strongly with neither hydrophilic nor hydrophobic systems, it prefers the interaction with the polymer in comparison to that with water. The µG therefore takes a surfactant-like role, reducing the water-substrate interactions by increasing its contact area to the fluorinated substrate and thereby shielding the water from the substrate.

In order to further understand the behavior of µGs upon different deposition methods, computer simulations conducted by the group of Prof. I. Potemkin (Physics Department, Lomonosov Moscow State University) will be discussed in the next section.

3.2.4. Computer-simulated microgels after deposition

As already mentioned, most computer-simulated results reporting the investigation of µGs at the surface, neglect the presence of evaporating solvent during deposition. Commonly, the adsorption of a µG to the solid support is simulated in the continuous presence of a solvent. This matches the experimental setup of “adsorption” which was investigated in the previous section. Such a simulation does not account for the evaporation of the solvent which takes place upon deposition via e.g. drop-casting or spin-coating. As the results from the previous section have shown, the deposition method and therefore the degree and speed of evaporation, do influence the adsorption process and thereby the conformation of the µG at the surface. In order to compare computer-simulated results with experimentally acquired results, the evaporation of the solvent must be incorporated to the theoretical model. Therefore, molecular dynamics (MD) simulations of single µGs were performed by Andrey Rudov (research group of Igor Potemkin at Moscow State University). In these simulations, in a first step, single µGs surrounded by water were adsorbed on three surfaces of varying hydrophilicity (FOCTS, glass, PEG) as depicted in Fig. 3-10. The analogue situation in terms of experiments would translate to the deposition of a droplet of µG solution onto the substrate, before adsorption of the µGs and also before evaporation of the solvent. In this situation, the single µGs would still reside within the droplet and, at the same time, the solvent (which is the main component of the droplet) would start to evaporate into the surrounding. This would, after a specific amount of time, lead to the complete evaporation of the solvent from the droplet and to the adsorption of the µGs to the surface. The simulated situation, before adsorption of the µG, is represented in Fig. 3-10. The evaporating droplet which hosts the µG is referred to as “water droplet”, whereas the evaporated solvent from the droplet into the surrounding of the µG is referred to as “vapor”.

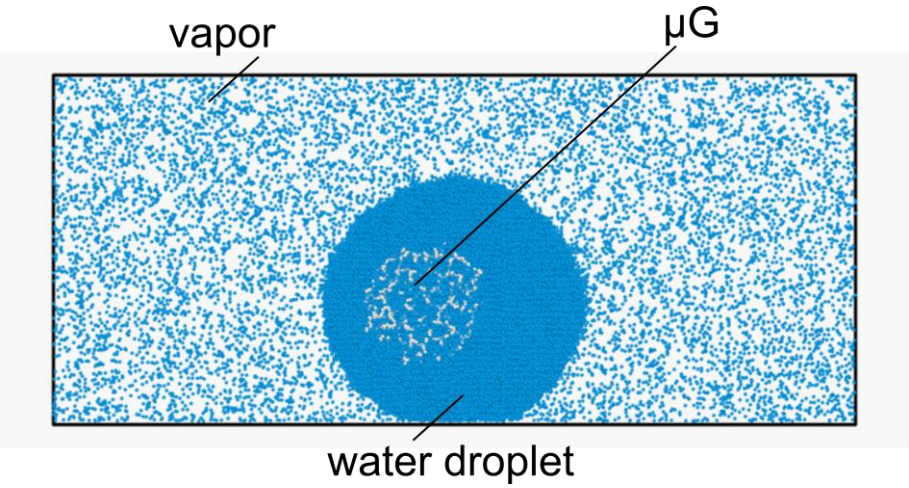

Fig. 3-10: Simulation snapshot of the initial system: droplet with µG ("water droplet") deposited on a substrate, before the adsorption of the single µG to the interface. The droplet is surrounded by vapor which forms due to evaporation of the solvent.

The challenge of the presented computer-simulations consists in tuning specific parameters to mimic different evaporation effects during spin-coating and during drop-casting. The parameters, that can be tuned in simulations, are the interaction parameters ε, which can be derived from combining the Finitely Extensible Nonlinear Elastic (FENE) potential and the Lennard-Jones potential. In this approach, the interaction between µG segments, water molecules and the particles forming the solid wall are set via the interaction energies ε_{ij}. Specifically, this means the interaction between (i) the µG ("*M*") and the water/vapor ("*W*"), ε_{MW}, (ii) between the water and the surface ("*S*"), ε_{WS} and (iii) between the µG and the surface, ε_{MS}. The interaction energies ε_{MW}, ε_{WW} and ε_{MM} were calculated using the Lennard-Jones relation. The µG-water interaction ε_{MW} (with $\varepsilon_{MW} = 1\,\varepsilon$ for the swollen state) was deduced from the previously calculated water-water interactions (with $\varepsilon_{WW} = 1\,\varepsilon$) and the µG-µG interactions (with $\varepsilon_{MM} = 0.275\,\varepsilon$). The next two steps consisted of (a) deriving the water-substrate interactions based on experimentally acquired contact angles and (b) of deriving the µG-substrate interactions.

a) Estimation of the water-substrate interactions ε_{WS}

The interaction parameters of a pure water droplet with the different surfaces were estimated without the presence of a µG. Here, the interaction energy between the water beads building up the droplet, and the substrate were varied. To estimate the interaction energies, a correlation with experimentally acquired values was used.

The contact angle θ of a pure water droplet was used for the estimation of the interaction energy between the droplet and the surface. The contact angle θ was analyzed as a function of the surface/liquid interaction parameter ε_{WS}. Using the experimentally measured contact angles depicted in Fig. 3-11, it was possible to calculate the interaction parameters being ε_{WS} ~ 1.7 ε; 2.75 ε and 3.25 ε for FOCTS, glass and PEG, respectively.

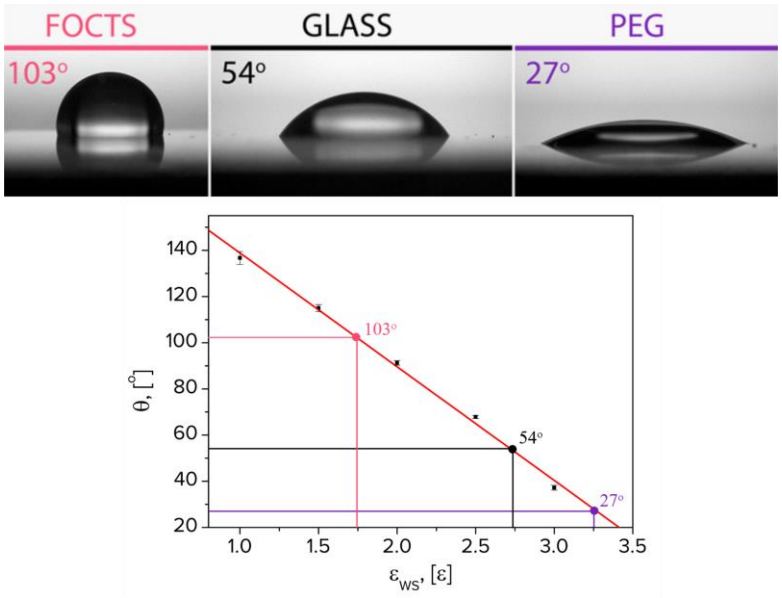

Fig. 3-11: Images of the contact angles of a 5 µL water droplet on the different surfaces. The interaction energies ε_{WS} between water and substrate were calculated with the experimental contact angles. Diagram provided by Andrey Rudov.

The above figure provides a relationship between contact angle and interaction energy. This relationship is the basis for the estimation of the interaction parameters between µG and substrate in the next step (b), were the contact angle of the simulated µGs will be deduced from a calculated volume ratio on the different surfaces. The relationship depicted in Fig. 3-11 can then be used for the estimation of the interaction energies from the obtained contact angles.

b) Estimation of the interaction parameters between µG and substrate

The next step consisted in identifying the interaction parameters between the different substrates and the µG segments through the estimation of the interaction energy ε_{MS} for the three different cases adsorption, drop-casting and spin-coating. The experimental deposition of a single µG for the cases of adsorption, drop-casting and spin-coating was imaged using fluorescence microscopy as described in section 3.2.3.

The calculated volume ratios from all three experiments were incorporated in simulations to estimate the interaction parameters for the three different cases, while still neglecting the evaporation of the solvent. The evaporation is not yet considered in this step, to be able to interpret the effect of evaporation in the next simulation step. The spreading degree of the µGs was estimated based on its surface points fitted with the LSQR approximation explained in section 3.2.2. A sphere cap was fitted around the positions of the µG beads, approximating the shape of the µG on the surface. This procedure resulted in a volume ratio between 0 and 1 as previously described in Fig. 3-5. The volume ratios for the simulated data is represented in Fig. 3-12.

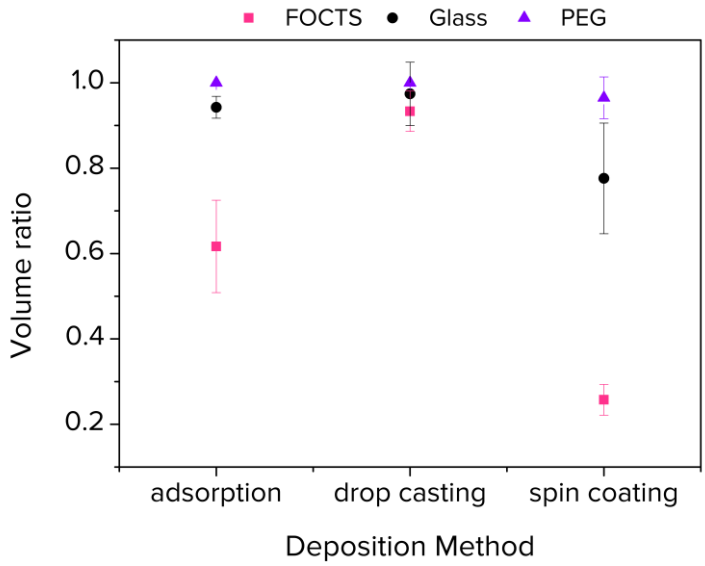

Fig. 3-12: Volume ratio of the fitted sphere cap to its ideal sphere volume for three different deposition methods (adsorption, dropcasting, spincoating) of pNIPMAM-µGs onto three different surfaces of varying hydrophilicity: FOCTS (squares), glass (circles) and PEG (triangles). Diagram provided by Andrey Rudov.

It was found that at low ε_{MS} the µG retains its spherical shape which gives a volume ratio of 1. Meanwhile, the increase of the interaction energy results in a decrease of the ratio to zero (see Fig. 3-13) which corresponds to the fried-egg conformation. It is assumed that the driest system with the least amount of solvent is represented by the spin-coated case as schematically depicted in

Fig. 3-13. The volume ratio can be converted into a contact angle, which describes the contact of the fitted sphere cap to the surface. Matching the results extracted from the diagrams in Fig. 3-12 and

Fig. 3-13, the interaction values ε_{MS} of the simulated µGs after deposition were obtained.

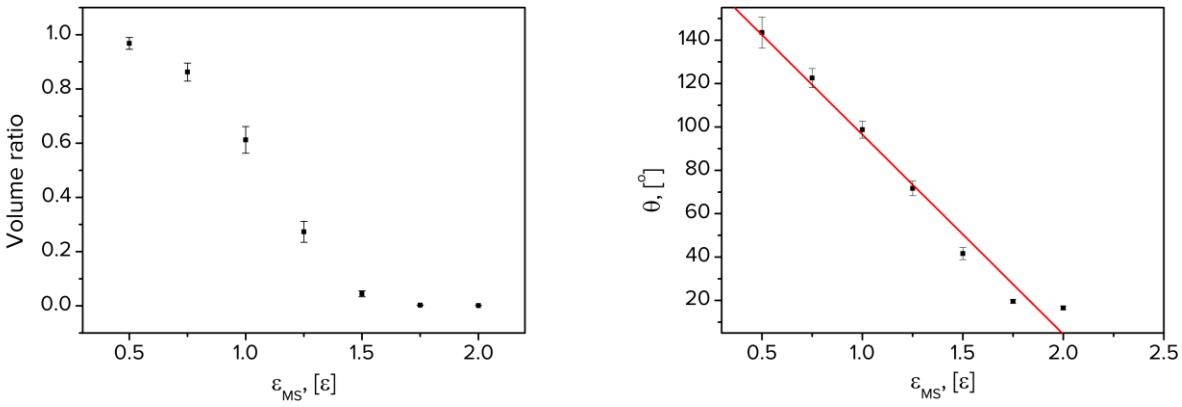

Fig. 3-13: Relation between the contact angle θ and the interaction energy ε (right diagram). The contact angle can be deduced from the ratio of the volume of the fitted sphere cap to its ideal sphere volume (left diagram).

The resulting interaction energies are summarized in table Fig. 3-1.

Table 3-1: Final results for the interactions energies between µG and the different substrates. These values allow to calculate the final equilibrium structures. For all surfaces the interaction energies of the water-water, µG-µG, and µG-water interactions were calculated resulting in $\varepsilon_{MW} = \varepsilon_{WW} = 1\,\varepsilon$ *and* $\varepsilon_{MM} = 0.275\,\varepsilon$.

Interaction Energy	FOTS	Glass	PEG
ε_{MS}	$1.7\,\varepsilon$	$2.75\,\varepsilon$	3.25
ε_{WS}	$1.75\,\varepsilon$	$0.85\,\varepsilon$	$0.5\,\varepsilon$

After having calculated the different interaction energies, it was finally possible to include these values for the computer simulation of the µGs at the different surfaces upon evaporation. The three deposition methods, adsorption, drop-casting and spin-coating, are schematically depicted in Fig. 3-14 To calculate the solvent evaporation for the three cases at different surfaces, a single µG was simulated with the calculated interaction energies within the water droplet, as depicted in Fig. 3-10. After 10^7 time steps of equilibration, the investigation of the evaporation of the solvent from the droplet was started. The equilibrium structure, before evaporation, depicts the “adsorption” case shown in Fig. 3-15. For all three experiments, the temperature of the substrate as well as the ambient temperature was kept constant. For the cases of drop-casting and spin-coating, the difference in the vapor pressure close to the

droplets surface and the ambient (partial) pressure of the vapor far away from the droplet drives a diffusive flux, leading to evaporation of the droplet.

Among different techniques in MD allowing to simulate the droplet evaporation process, we used the following method. We removed water vapor beads, i.e. molecules, from the system to shift the balance between condensation and evaporation. The rate of droplet evaporation was controlled by the number of removed particles and the removal frequency. Experimentally, one molecule was removed every 10, 100, and 1000 time steps. The spin-coating process approximates the removal of one molecule every 10 time steps, whereas the drop-casting process is approximated by the removal of one molecule every 1000 time steps. These numbers do not claim an accurate prediction of the experimental evaporation processes. However, they represent the idea of a much faster evaporation in case of spin-coating compared to that of drop-casting. The different µG conformations after deposition at the surface are related to the different amounts of water that are left after evaporation within the µG.

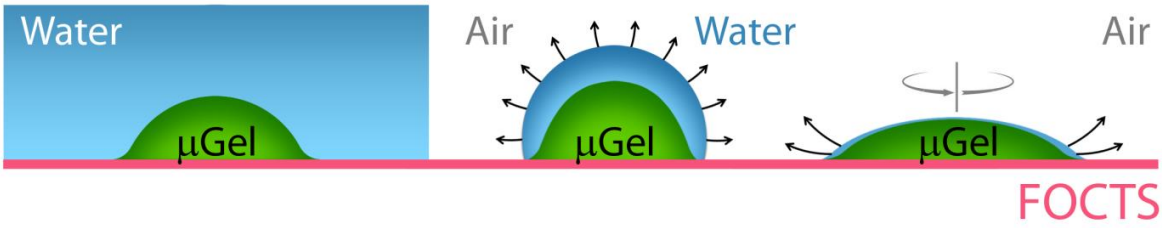

Fig. 3-14: Scheme of µG spreading behavior on the FOCTS modified surface depending on the different deposition methods: adsorption, dropcasting and spincoating.

The two cases that are easiest to compare with experimental SRFM results are the case of adsorption and the case of spin-coating. This is due to the fact that the equilibrium structure before evaporation refers to the adsorbed case, whereas in the spin-coating case the evaporation rate is comparably fast leading to a completely dry and collapsed µG. The resulting µG conformations from simulations and experiments at the interface (depicted in

Fig. 3-15) are in accordance with each other. As already discussed in the previous section, the experimental results for the adsorption case on FOCTS were surprising, as a strong fried-egg conformation was formed. The computer simulations show the same behavior in this case. This confirms the theoretical explanation that the µG takes on a surfactant-like role, shielding the fluorinated surface from the solvent. It should be noted that the equilibrium structures, that are the result of the computer simulations, do not completely reflect the experimental images

in the case of spin-coating. The simulated case would match the experimental situation immediately after the spin-coating process. But, in order to perform dSTORM measurements the sample has to be rehydrated with a buffer solution.

This rehydrated sample is imaged in the SRFM results. However, the accordance between the obtained results clearly show that the conformation taken during or after the deposition, does also define the conformation after rehydration.

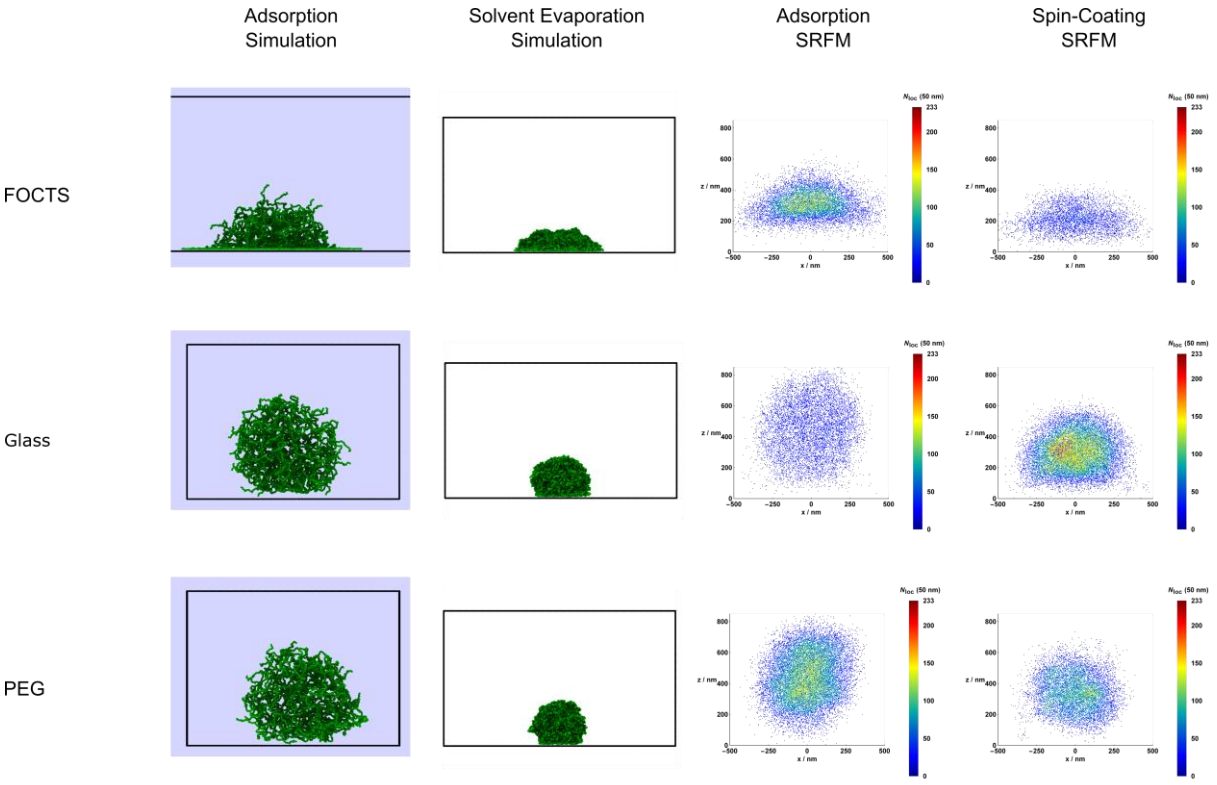

Fig. 3-15: Simulated µG equilibrium structures in the adsorbed case (water) and after complete evaporation (air).

3.2.5. Visualization of 3D SRFM data

The representation of the SRFM results in this chapter highlight the importance of the appropriate visualization tools for this type of data. Unfortunately, open source state of the art visualization software like *Visual Servoing Platform* (ViSP) (El Beheiry and Dahan 2013) have mainly been developed for the biomedical community and therefore do not fit the requirements for the analysis of µG data. The idea reported by the ViSP developers consists of overcoming challenges including the efficient handling of millions of individual localizations, the description of localization precisions in three dimensions and the incorporation of intuitive depth cues,

multichannel compatibilities and 3D quantitative features. (El Beheiry and Dahan 2013) Despite the fact, that ViSP is a great step towards visualizing 3D data, its main problems derive from the poor performance of the general usability and user-interface of the software.

It is furthermore not possible to intuitively adapt the 3D rotation angles of the field of view, which in most cases leads to a spatially distorted visualization of the box plot and the axes. Finally, the output results in terms of images and videos are not sufficiently flexible in order to analyze µG data. A detailed description of the state-of-the art visualization tools can be found in the supporting information of this chapter, see section 8.1. In order to circumvent time-intensive and unsuitable image analysis, a new Mathematica-based analysis tool was developed as part of this dissertation. The developed open-source software µBerry is capable of performing necessary processing steps to create high-quality images and videos of individual µGs. For ease of use, a graphical user interface was created which allows to enter all necessary information to the program and to give the user control over type and format of the output. A detailed explanation, as well as the user manual can be found in the supporting information of this chapter, see 8.1.1. As an example, the most basic µBerry output will be presented here.

Fig. 3-16 depicts the investigated pNIPMAM µG on an FOCTS substrate after adsorption. The µG is visualized in 3D from a viewing angle above the µG, as well as in 2D (y/x, z/x and z/y planes) to allow for a complete interpretation of the data. Finally, it can be stated that the implementation of µBerry as a visualization tool for 3D µG data significantly improves the workflow.

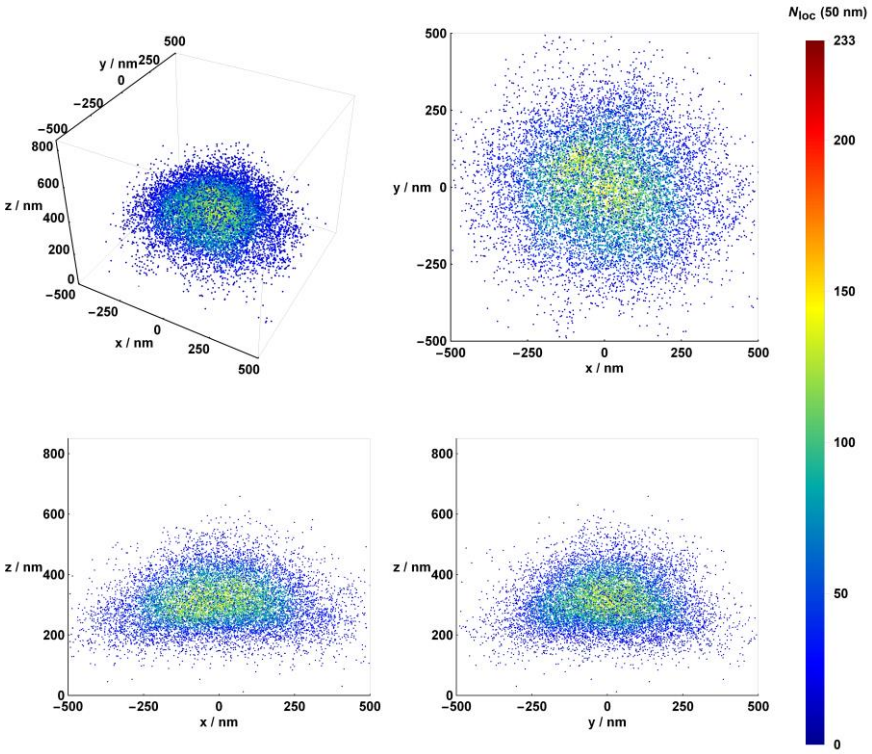

Fig. 3-16: Example of the µBerry output, including a 3D visualization from a viewpoint above the µG and three 2D visualization along y/x, z/x and z/y.

3.3. Summary and outlook

The results presented in this chapter were motivated by the development of a lithographic method explained in chapter 4. Through this lithographic approach, µGs are immobilized on a surface pattern through DNA-hybridization. To do so, it is important that the µGs retain their native spherical conformation and therefore the question on an appropriate surface functionalization was raised. In this chapter, it was shown that the answer to this question implies a fundamental understanding of the interactions between the µG and the solid interface. It was found that the deformation behavior of µGs also depends on the surface hydrophilicity and the sample preparation method. In the case of the investigated pNIPMAM µGs, three surface coatings – being a fluorinated surface, a PEG-ylated surface and a hydrophobic (ODS) surface – were analyzed. The evaluation of the results clarified that the spherical shape of the µG is maintained as long as the solid interface mimics the solvent properties. This suggests that in the presented case, the deposition on a hydrophilic PEG surface retains the spherical µG structure. The two other remaining surfaces ODS and FOCTS can be regarded as hydrophobic from a physical point of view.

The contact of the two surfaces with the polymer chains of the µG is more favorable than the one with water. In other words, the sub-chains adsorb to the surface to minimize unfavorable surface-water contacts leading to a fried-egg conformation of the µG. The µG deformation was furthermore investigated upon different deposition methods (i) adsorption from solution, (ii) drop-casting and (iii) spin-coating. It was shown that when the µG is deposited through adsorption from solution on a PEG substrate, the native, spherical shape is entirely retained. This is because no solvent evaporation takes place in this scenario and the µG is surrounded by solvent at all times. Interestingly, it was found that the case of adsorption on a fluorinated substrate leads to a fried-egg conformation. This is because the µG takes on a surfactant-like role shielding the fluorinated surface from the solvent. Even though SRFM methods like dSTORM provide valuable information on the µG conformation at the interface, it was demonstrated that the validation of these findings by means of computer simulations is of great importance to understand the undergoing molecular processes. Furthermore, the analysis of the µG shape through a parametrization process which is independent from the data acquisition method, has proven to be a valuable tool to compare µG data from different sources. Finally, the development of the Mathematica-based image analysis tool µBerry allows for an appropriate visualization of the acquired 3D SRFM data superior to previous solutions. New visualization possibilities include rotating videos, density build-ups and slicing through the µG.

This project is an example for a variety of disciplines coming together to elucidate fundamental processes. In future work, the combination of computer simulations based on theoretical models, with experimental data will become even more important. Furthermore, the inclusion of experts from the image analysis community will allow to automatically evaluate the obtained data with state-of-the art algorithms. One point of criticism with respect to the presented sphere fitting approach is, that microgels have no defined / discrete surface, that would allow for the definition of a clear sphere boundary. Nevertheless, this approach still serves as a relevant preliminary example that depicts how important it is to develop methods that make the acquired data comparable regardless of the acquisition method. Finally, this chapter has shown that it is of great importance to understand the fundamental processes at the interface before developing applications at that interface. µGs are highly complex constructs which makes predictions of their behavior in a certain chemical or physical environment extremely difficult. The findings on the hydrophilic surface functionalization benefit the lithographic approach that is described in the next chapter.

4. Lithographic approach to immobilize microgels via hybridization

This chapter builds on the fundamental findings discussed in the previous chapter and focus on the development of a lithographic process towards the immobilization of µGs to the solid support. Relevant theoretical background for this chapter can be found in the theoretical background section of this dissertation. This project mainly builds on foundations of c-EBL (see 2.2.1), photolithography with photolabile protecting group (PPG) (see 2.2.2) and DNA (see 2.4) and µG systems (see 2.3). In section 4.1 the motivation for the development of a surface-bound µG system, as well as an overview of the existing approaches is outlined. Furthermore, a general approach of the joint lithographic process will be presented. The discussion of the results in section 4.2 includes the analysis of each step towards the generation of a surface-bound µG system. Finally, a summary of the presented results as well as an outlook for future research will be given in section 4.3.The research presented in this chapter is embedded in project A6 as part of the CRC for functional µGs and µG systems. Within this framework, this project represents an ongoing cooperation between the research groups of Prof. Ulrich Simon (Institute of Inorganic Chemistry, RWTH Aachen University) and Prof. Dominik Wöll (Institute of Physical Chemistry, RWTH Aachen University). The main cooperation partner in this project was Dr. Sabine Eisold, former Ph.D. student in the Simon-laboratory. Her investigations on the DNA-functionalization of µG systems are of great importance for the final immobilization of µGs at the solid support via DNA hybridization.(Eisold 2018) She furthermore reported a method for the hybridization of DNA-functionalized µGs to gold nanoparticles decorated with the complementary DNA strand. Additionally, her investigations show that it is possible to release the µGs from the solid support - represented by the AuNP - by heating the system above the melting temperature T_m of the DNA double strand.(Eisold 2018) These results serve as preliminary experiments for the controlled hybridization of µGs to the patterned surface and the subsequent release from the individual spots.

The experiments presented in this chapter were supported by Pia Lenssen (Research group of Prof. Dominik Wöll) as part of her bachelor thesis and research assignment in her master's program in chemistry at RWTH Aachen University.

4.1. Introduction

While a large part of µG research has so far been concentrated on µG suspensions and their applications, there is increasing interest in surface-bound µG systems.(Nyström and Malmsten 2016) The investigation of stimuli-responsive surface structures and the control of their properties represents a growing field in soft condensed matter research, life sciences and material science. The overall goal of designing new responsive and switchable surfaces requires detailed knowledge on the underlaying complex interfacial processes.(Wellert, Richter et al. 2015) In this field, surface modification approaches range from physisorption, with and without covalent attachment, to spin coating, wrinkling, and other strategies for induced assembly.(Nayak and Lyon 2005, Burmistrova, Steitz et al. 2010, Wellert, Richter et al. 2015, Nyström and Malmsten 2016) In order to incorporate structural complexity to the immobilization of µGs at the solid support, methods like charge-induced self-assembly (Lu and Drechsler 2009), photolithography (Chen, Kawazoe et al. 2007) and microcontact printing (Peng, Zhao et al. 2013, Li, Kappl et al. 2019) have been reported. The introduction of structural complexity allows for new applications in the above-mentioned fields and represents a crucial step for the development of devices. The previous chapter was dedicated to the adsorption behavior of µGs at different solid supports. The impact of the surface hydrophilicity, as well as the deposition method, was presented. When discussing the immobilization of objects like µGs at the solid-liquid interface, it is crucial to differentiate between classical deposition methods like spin-coating and drop-casting and binding via chemical interaction forces. Clearly, drop-casting and spin-coating do not provide any structural direction of the deposition. In other words, these methods do not allow to realize a structured deposition in a specific pattern without a chemical modification of the surface. In this chapter, the knowledge gained in the previously presented studies is used to introduce structural complexity to optimize the deposition of µGs to the solid support. Thereby, the focus was laid on the covalent binding of µGs to specific spots at a patterned surface. One limitation of the mentioned patterning-methods such as microcontact printing or photolithography consist in the size of the pattern and thereby the length scale of the structural complexity of the deposition.

Classical photolithographic approaches for instance, will always be restricted to the diffraction limit of light (see section 2.1), limiting the patterns to a size of several hundred nm. This shows that still today, one of the most important challenges in the field of µG immobilization, involves the control of the length scale, which is especially important in fields like the semi-conductor industry. As already introduced in the theoretical background section of this dissertation (see section 2.2.1), nano lithography is a commonly used technique to create nanoscopic surface patterns. The aim of this chapter is to present a new approach which combines the previously introduced c-EBL method with classical photolithography using PPG (see section 2.2.2). The combination of these two methods has several advantages. First, c-EBL allows to write smaller spots than classical photolithography. As the De-Broglie wavelength of an electron is smaller than that of a photon, the resolution of electron beam lithography can be pushed far below 10 nm.(Vieu, Carcenac et al. 2000) This means that in theory it is possible to immobilize a single object in the nm-range, e.g. a small µG, to one c-EBL spot. The overall goal of this approach involves the immobilization of µGs to the surface - via DNA-hybridization - onto nanoscopic spots that are part of a pattern fabricated using c-EBL (see Fig. 4-1).

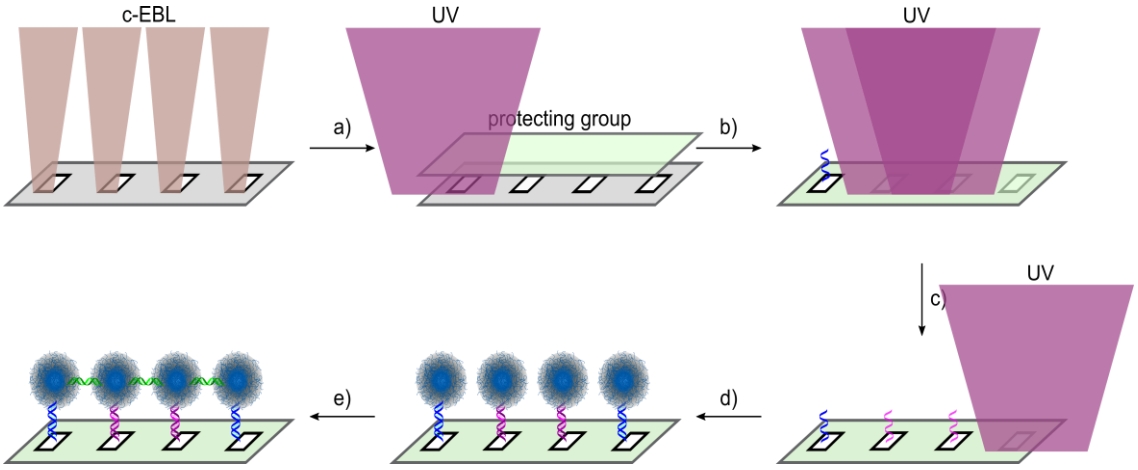

Fig. 4-1 Schematic process of a directed µG immobilization to the solid interface using a combination of c-EBL and photolithography. After c-EBL, the spots within the pattern are reacted with a photolabile protecting group (a). After deprotection (b), sDNA can selectively be bound to the spots (c,d). The immobilization of sDNA is followed by the hybridization of DNA-functionalized µGs to the sDNA on the surface (d) resulting in super-structures (e).

In a first step, a surface pattern is written using c-EBL. The spots marked in white in Fig. 4-1 can be designed in the nanometer range, due to the high resolution of EBL. The spots are then reacted with PPGs which afterwards can be selectively deprotected using a focused UV-laser.

However, the physical limitation of the UV-laser is an important factor during deprotection, as it is not possible to selectively address single c-EBL spots if the spot size of the UV laser surpasses the distance between the c-EBL written spots, see Fig. 4-1.

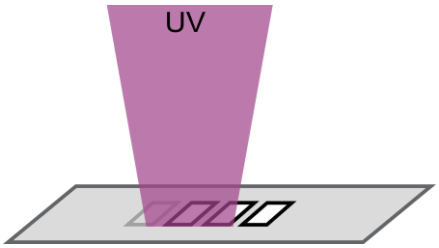

Fig. 4-2: The combination of c-EBL and photolithography reaches its physical limitations when the size of the laser spot surpasses the distance between the c-EBL written spots.

The important advantage of combining c-EBL with photolithography in this approach is that on the one hand it is possible to write c-EBL spots with sizes in the nm-range, which would not be possible using only photolithography. On the other hand, the introduction of the photolithographic method allows for the flexibility to chemically address these c-EBL spots with different systems, like e.g. with sDNA. As long as the coordinates of the c-EBL spot can be addressed with e.g. a piezo table, the photolithographic approach can be repeated for numerous cycles on the same substrate. As shown in the overall procedure, after photochemical deprotection of the spots, a functionalization with sDNA can take place. The immobilized sDNA serves as chemical anchor point at the surface allowing for the hybridization of a complementary DNA strand. In the presented case, µGs are functionalized with this complementary DNA strands in order to be immobilized via hybridization of the complementary strand with the sDNA at the substrate. This technique allows for the creation of super-structures, as depicted in Fig. 4-1e. The fact that µGs have a stimuli-responsive behavior, allows to address them with appropriate triggers being e.g. temperature, specific pH or wavelength. Once immobilized, it is therefore possible to control the swelling/collapse of specific µGs at the surface. These final stimuli-responsive super-structures allow for applications in the field of actuators like nano-scaled peristaltic pumps or micro reactors. Final applications are highly flexible as it is possible to immobilize different µGs with e.g. different VPTTs to specific spots within a pattern while addressing them through individual stimuli. The respective chemical path is displayed in Scheme 4-1 and will function as a reference throughout the step by step discussion of the individual surface modifications in section 3.2.

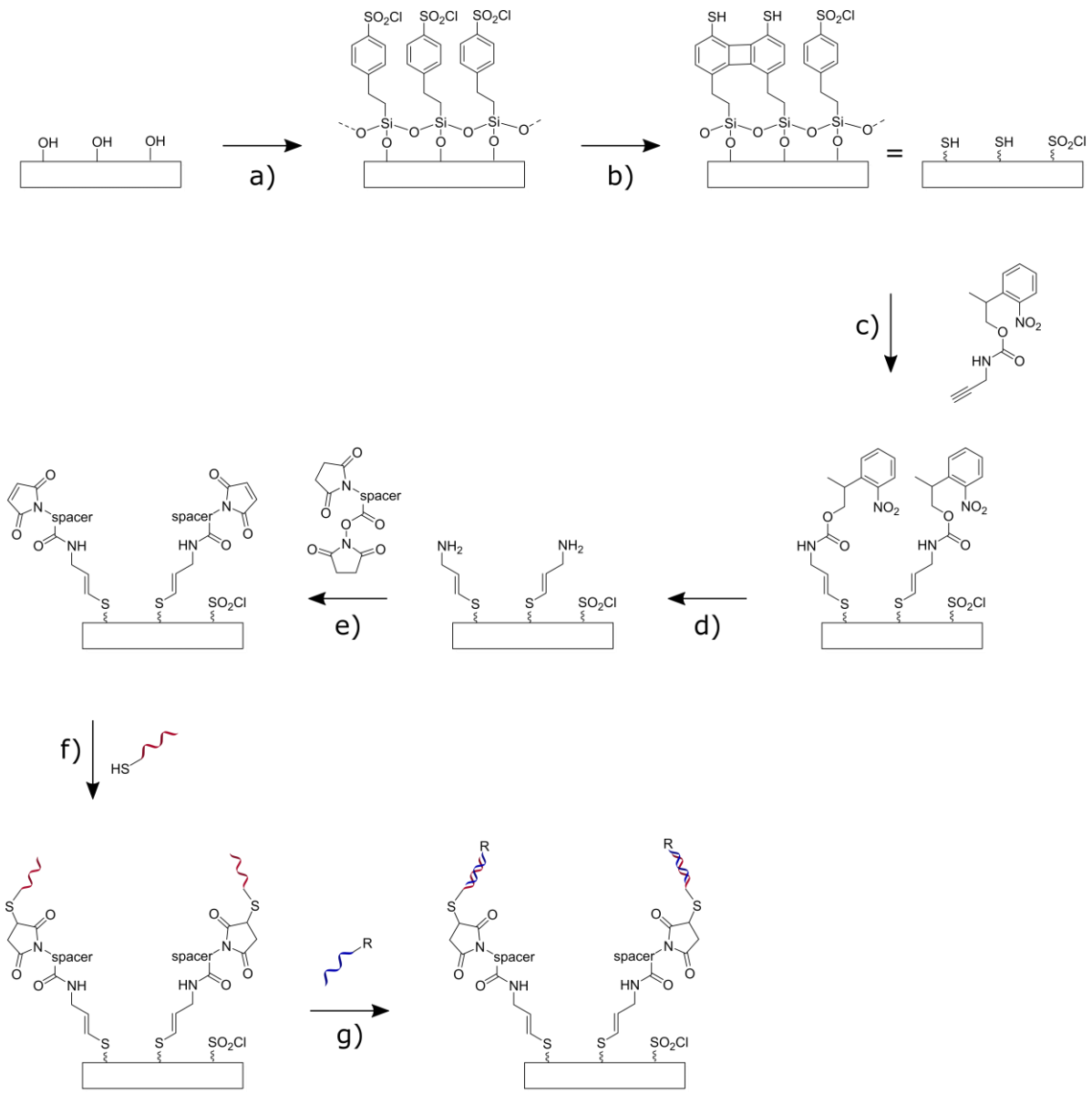

Scheme 4-1: Chemical path of the joint c-EBL and photolithography approach to create complex surface-bound µG structures. In the first step the plasma-cleaned surface is silanized resulting in sulfonyl-chloride functionalities at the surface (a). The sulfonyl-chloride is then site-specifically reduced to thiols by means of c-EBL (b). The thiols are selectively labeled with a photolabile protecting reagent via a thiol-yne reaction (c). The deprotection of the protecting group leaves specific spots with an amine functionality (d). The amine groups can be further reacted with a spacer (e). The maleimide end of the spacer can be used to selectively couple thiol-functionalized DNA molecules via thiol-maleimide "click" chemistry (f). Finally, the immobilized sDNA can be hybridized with a compatible DNA strand (g). The immobilization of µGs takes place as depicted in (g) with µG=R.

4.2. Results and discussion

This section describes the development of the lithographic process. First, the experimental challenges that arise when combining c-EBL and photolithography will be explained in section 4.2.1. The overall goal of building a µG bound system will be addressed in two sub-projects (i) the development of an DNA chip through the combination of c-EBL and photolithography, outlined in sections 4.2.2 to 4.2.4. and (ii) the immobilization of DNA-functionalized µGs to surface-bound sDNA, described in section 4.2.5.

4.2.1. Detecting c-EBL structures in optical microscopes

One of the main challenges regarding the combination of c-EBL and photolithography stems from the fabrication of the c-EBL pattern in an electron microscopy set-up. Photolithography and all fluorescence-based experiments are performed and monitored using an optical microscope. Unfortunately, the c-EBL pattern itself is not detectable in the bright-field mode of an optical microscope. Even though the (thiol-) pattern is visualized via labeling with a fluorescent (maleimide-functionalized) dye in most experiments, the remaining challenge is its localization. The size of the pattern that is used for preliminary experiments is only 40 x 40 µm, an area that has to be found on a 24 x 50 mm coverslip. I introduced the idea of incorporating a marker system created with a focused ion beam (FIB) device, in my master thesis.(Hoppe Alvarez 2017) This marker system (see Fig. 4-3) is visible in both setups without fluorescent dyes and provides a common coordinate system for both electron and optical microscopy.

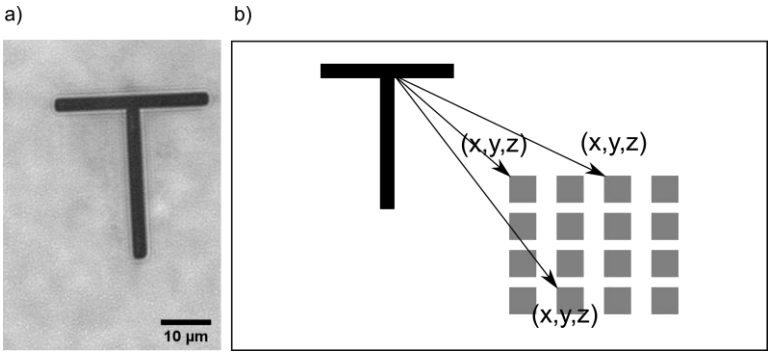

Fig. 4-3: FIB structure visible in both electron microscopy and optical microscopy, imaged in the brightfield mode of an optical microscope (a).(Hoppe Alvarez 2017) The FIB structure serves as coordinate system or reference when writing the c-EBL pattern. This allows to provide a list of x,y,z-coordinates for each spot within the pattern (b). The spots can then be selectively addressed in the optical microscope using an automized piezo table, even though they are not visible.

I also introduced an algorithm that allows for the automated recognition of the pattern, which is linked to the piezo table of the optical microscope.(Hoppe Alvarez 2017) This procedure is needed when specific spots within the pattern have to be addressed individually in the photolithography step. It has to be noted that the FIB procedure itself is an elaborate and costly process, performed by the group of Prof. Mayer (Gemeinschaftslabor für Elektronenmikroskopie, RWTH Aachen University). Therefore, in most experiments presented in this chapter, the FIB method is not employed. Instead, a simple scratch mark in proximity of the pattern has proven to work as simple and cost-efficient method to find the pattern in the optical microscope. The “L” shaped scratch mark is inscribed by hand using a diamond cutter on the bare substrate before the c-EBL procedure is conducted. As the scratch mark is visible in both setups, the pattern is written in proximity of the end points of the “L” shape.

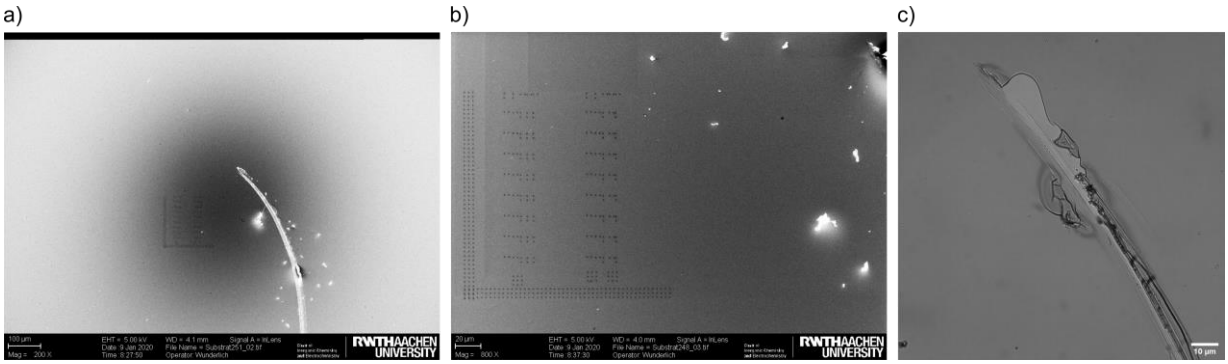

Fig. 4-4: Images (a) and (b) represent SEM images taken directly after the c-EBL procedure. The pattern (b) is always placed at the end points of the “L” shaped scratch-mark. The c-EBL procedure was entirely conducted by the laboratory technician Birgit Hahn (IAC). Image (c) was taken in the brightfield mode of an optical microscope. The endpoint of the scratch-mark is clearly visible in the optical microscope allowing to estimate the position of the pattern.

The SEM images with both the visible mark and the visible pattern can then be used for guidance while finding the pattern in the brightfield mode of the optical microscope. Of course, this procedure is only applicable to localize the whole pattern and does not allow to address single spots. The endpoint of the “L”-shaped scratch-mark is depicted in a SEM image (a) in Fig. 4-4. The c-EBL pattern as wells as residuals from the scratch surface are depicted in the SEM image (b) of the same figure. The end point of the scratch-mark is clearly visible in the brightfield mode (image (c)) of an optical microscope, allowing to estimate the position of the pattern.

4.2.2. Protection via thiol-yne reaction

For the c-EBL method employed in this project, first a self-assembled monolayer (SAM) has to be fabricated consisting of 2-(4-chloro-sulfonylphenyl)ethylsilane. This experimental method was described by Schaal et al.(Schaal and Simon 2013) As described in section 2.2.1, ITO substrates are used in these type of experiments in order to incorporate a conductive layer which avoids charging effects and would lead to a decrease in resolution.(Schaal and Simon 2013) ITO substrates furthermore have the advantage to provide optical transparency, which is crucial for further investigations with optical microscopy. As depicted in Scheme 4-2, the electron beam selectively reduces the SAM to thiols creating a surface pattern.

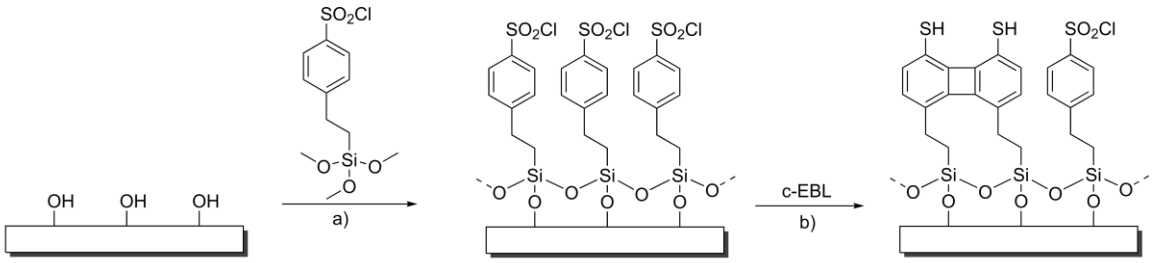

Scheme 4-2 Selective reduction of a SAM, consisting of 2-(4-chloro-sulfonylphenyl)ethylsilane (a, b), to thiols (c). The thiols form the spots within the c-EBL pattern.

The corresponding SEM image of such a pattern is exemplarily shown in Fig. 4-5. The pattern consists of a square of 20 x 20 spots each with the dimension of 1 µm x 1 µm. The dosage of the electron beam is 5 kV.

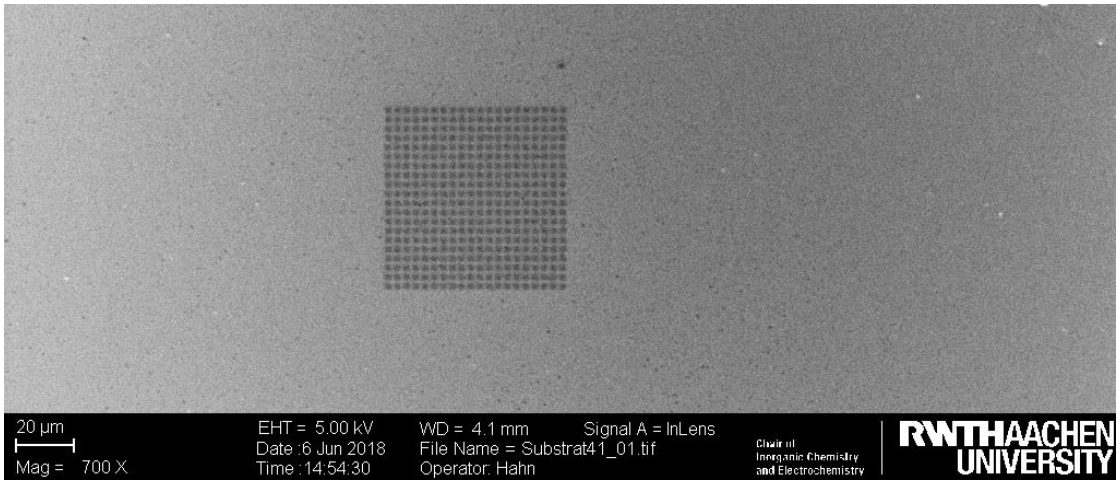

Fig. 4-5 SEM image of the c-EBL pattern. The light background consists of the remaining sulfonyl chlorides, whereas the dark spots depict the reduced species (thiols). The c-EBL procedure was entirely conducted by the laboratory technician Birgit Hahn (IAC).

To combine c-EBL and photolithography, it is important to ensure the successful protection of the pattern. Therefore, an NPPOC derivative is chosen as a suitable PPG. The compound was first synthesized by the author of this dissertation in her master thesis.(Hoppe Alvarez 2017) The advantages of this type of protecting groups were already discussed in section 2.2.2. The photolabile protecting group is designed with an alkyne functionality to react in a thiol-yne reaction to the thiols at the surface (spots). Furthermore, the compound leaves a free amine functionality at the surface after photochemical deprotection (see blue label in Scheme 4-3). In previous work in solution, it was shown that the thiol-yne reaction is successful when conducted under alkaline condition. NMR analysis revealed that the reaction works best using NaOH as a base.(Hoppe Alvarez 2017)

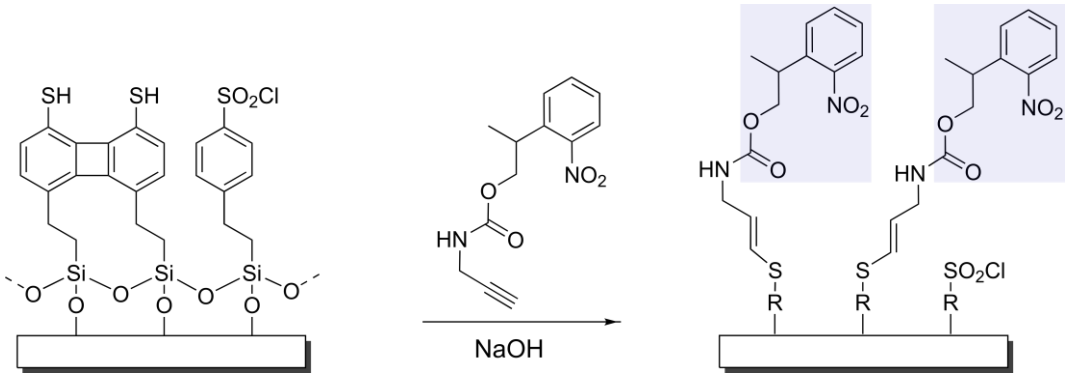

Scheme 4-3 Thiol-yne reaction of the reduced thiols (c-EBL pattern) with the photolabile protecting group 2-(4-chloro-sulfonylphenyl)ethylsilane. The blue-highlighted parts are cleaved in the following step employing an UV laser.

Based on the preceding experiments, the challenge consists of adapting these conditions to the surface system depicted in Scheme 4-3. Surface chemistry is known to strongly differ from experiments in bulk due to a variety of factors. Surface chemistry is commonly performed by incubating the reaction solution on the surface for a specific amount of time. Dust particles or other artefacts on the surface can impede the surface reaction as the target molecules can be blocked by these objects. Furthermore, incubation-times can be longer than the reaction-time in bulk, as the binding event of two reactants is statistically less favorable than in bulk. Unfortunately, longer incubation times always bare the risk of drying out the reaction solution on the surface and therefore lead to the random formation of multi-layers which cannot be used for future reaction steps. Surface reactions are commonly analyzed using contact angle measurements with a water droplet.(Lester 1961, Cras, Rowe-Taitt et al. 1999) The reaction of the thiols within the pattern with the PPG lead to a higher surface hydrophilicity after the protection. The increase in hydrophilicity can mainly be explained through the addition of the nitro group and the carbamate function. In the presented case, contact angle measurements turn out to be experimentally challenging, as the reaction does only take place at the micron-sized spots within the pattern. It is therefore not feasible to place a water droplet in a contact angle measurement on a single spot to investigate the surface hydrophilicity in this small area. In order to still acquire quantitative information on the change in contact angle upon surface protection, a silanized surface with a thiol monolayer was synthesized according to Scheme 4-4. The concentration of the protecting group was increased in order to monitor the turnover of the thiol-groups. The theoretical expectations should result in a decreasing contact angle, as more thiols are reacted and subsequently the surface gets more hydrophilic.

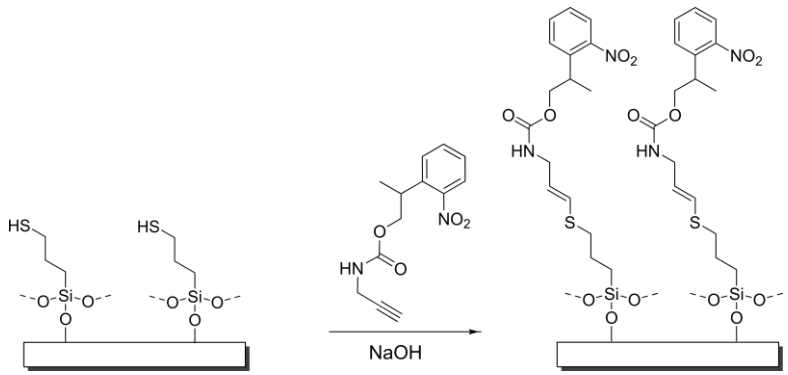

Scheme 4-4:Thiol-yne reaction of a thiol-monolayer with a photolabile protecting group. The thiol-monolayer mimics the thiol spots resulting from the c-EBL pattern. The thiol monolayer allows to monitor the reaction by means of contact angle measurements.

For the presented results depicted in Fig. 4-6, the ratio of the PPG and NaOH was maintained at 1:1 at all times. As expected, an increase in the concentration of the protecting group leads to lower contact angles and thus to a more hydrophilic surface. This preliminary experiment can be interpreted as a qualitative confirmation of the successful thiol-yne reaction at the surface. Fig. 4-6 illustrates a strong drop in the contact angle from 44° to 34° after the surface reaction with a protecting group concentration of 1 mmol L^{-1}. Further increase of the concentration does not significantly influence the contact angle, as its stays low, indicating a hydrophilic surface. This leads to the conclusion that a minimum concentration of 1 mmol L^{-1} is necessary to protect a thiol-monolayer with the chosen protecting group.

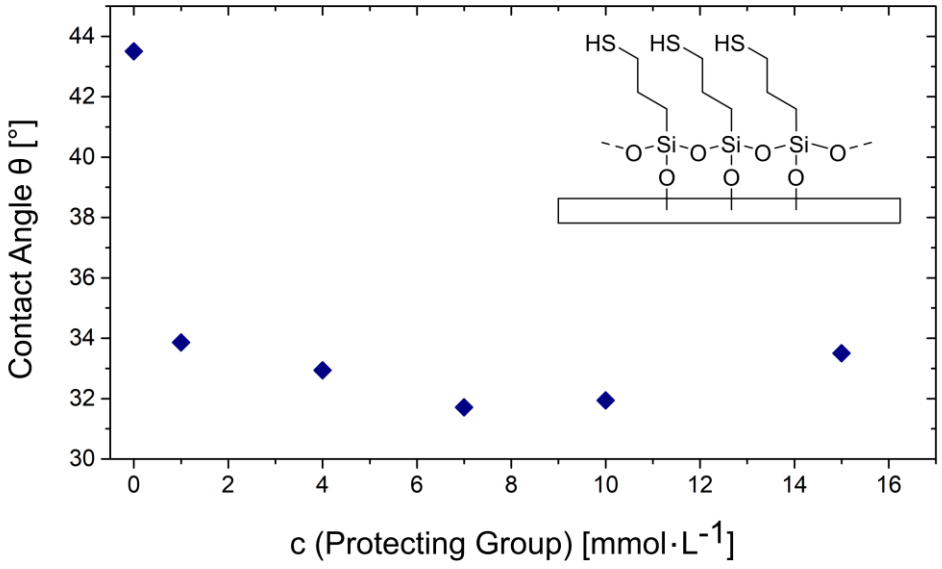

Fig. 4-6 Dependency of the surface hydrophilicity on the concentration of the photolabile protecting group used for the the thiol-yne reaction. The reaction was performed on a substrate functionalized with a thiol monolayer (see Scheme 4-4) and subsequently the contact angle measurements were performed. The surface reaction leads to a decrease of the contact angle and thus an increase in the surface hydrophilicity.

The preliminary experiments on the surface with a thiol monolayer have shown that the in-vitro reaction is reproducible at the solid-liquid interface. In a second step the thiol-yne reaction has to be optimized on the patterned substrates. In order to evaluate this reaction, the non-functionalized thiol groups were quantified reacting them with a maleimide-functionalized dye (Atto 565). Subsequent read-out of the fluorescence intensity revealed if the protection of the thiols was successful or not. The successful reaction would ideally not result in any fluorescent signal (see Scheme 4-5). It must be noted that this evaluation assumes the absence of unspecific binding events.

Therefore, a faint pattern can still represent a successful thiol-yne reaction. Furthermore, an inverted pattern, meaning less fluorescence on the spots in comparison to the background, is also possible. This would indicate that the unspecific binding events of the fluorescent dye are more likely to happen in the unprotected background than on the protected spots. The following three reaction parameters were analyzed: (a) the incubation time of the PPG, (b) the pH value concerning the controlled addition of NaOH and (c) the optimum concentration of the photolabile protecting group. All experiments were conducted in TIRF mode which has the advantage of reducing the background fluorescence and is optimal for the detection of fluorescent signals at or near the surface (see section 2.1.3).

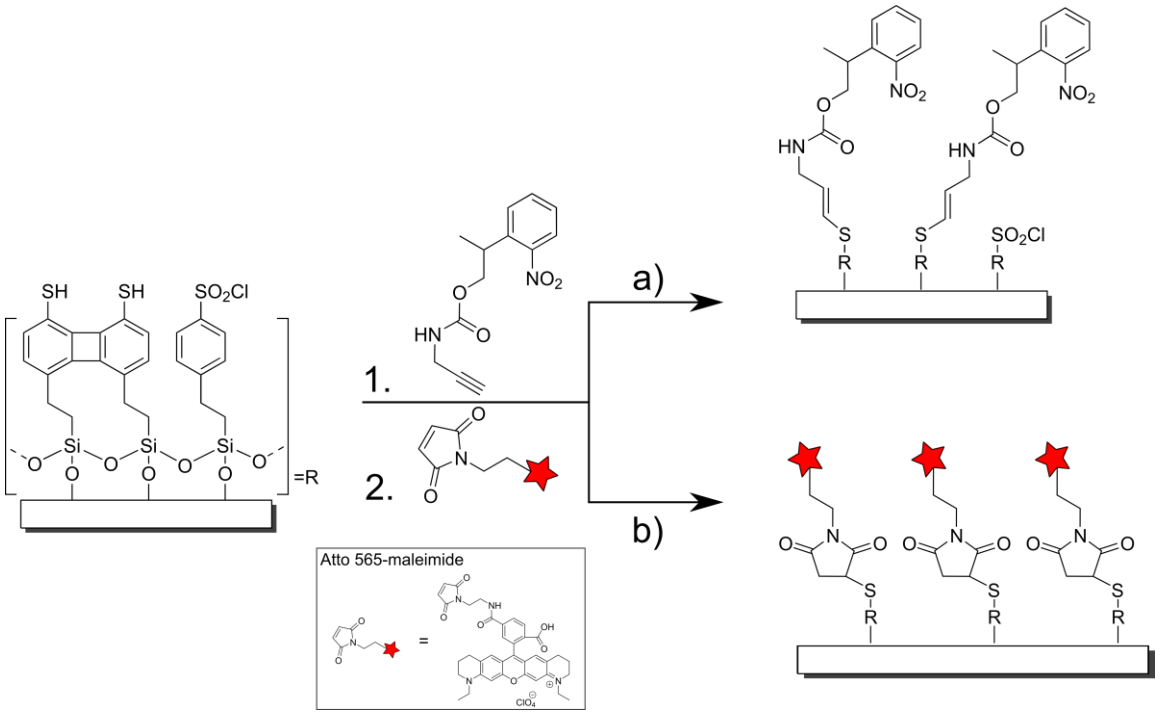

Scheme 4-5: After the supposed protection of the pattern with a photolabile protecting group, a maleimide-functionalized fluorescent dye (Atto-565) was reacted to the surface in a second step. (a) If the protection of the pattern was successful, no fluorescence should be detectable. (b) If the protection was unsuccessful, the thiol-functions are still available and will thus react with the maleimide-dye. This results in a fluorescing pattern.

As expected, the ideal cases resulting in an inverted pattern or no fluorescence at all – after a successful protection – could not be observed for all measurements. Therefore, the decrease in fluorescence intensity of the pattern was investigated depending on the different parameters in order to find the optimum conditions. Again, the decrease in fluorescence is related to a lower number of reactive thiols, which is directly linked to the successful protection of this species. For each parameter variation experiment, the fluorescence of the faint surface pattern was analyzed.

A histogram, representing the photon count in dependence of the fluorescence intensity, was extracted from a specific area of each pattern and the mean value of the intensity was later used for comparison. The histogram represents the photon counts depending on the fluorescent intensity. For each measurement the histogram was taken of an equally sized area. To consider possible inhomogeneities of the laser profile, the histogram area was always taken at the same illumination conditions. This analysis procedure is exemplarily depicted in Fig. 4-7. The remaining analyzes can be found in the supplementary information in section 8.2 (see S.I. 8-23).

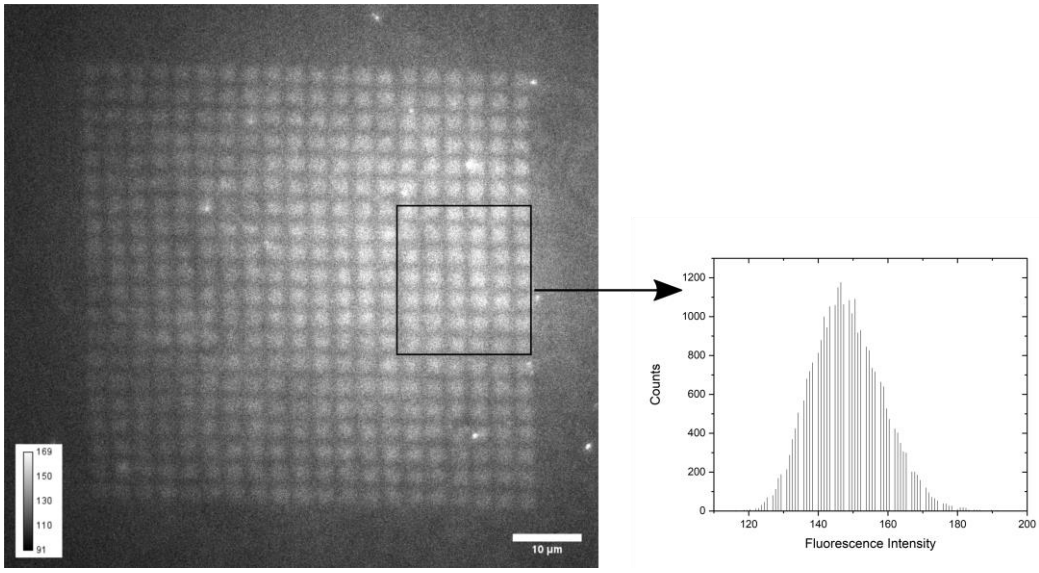

Fig. 4-7: Fluorescence of the pattern after protection due to incomplete conversion of the thiols with the protection group. The histogram represents the photon counts per fluorescent intensity value. For each measurement, the histogram of an equally sized area was taken and the mean value of the intensity was later used for comparison with other measurements. This measurement was adapted from the Bachelor thesis of Pia Lenßen.

(a) Incubation time

The incubation time of the photolabile protecting group was tested with a 1:1 ratio of the protecting group and NaOH. A comparison between 1.5 h and 68 h of incubation with the reaction solution, revealed a low and almost constant fluorescence intensity of the pattern. After 1.5 h of incubation, the mean fluorescence intensity value was 555. After 68 h of incubation the mean fluorescence intensity extracted from the pattern had a value of 539 counts under the same conditions. This reveals an almost insignificant decrease. Due to the assumption that the thiol-yne reaction is already terminated after 1.5 h, all following experiments were conducted accordingly.

(b) Variation of the NaOH concentration

The variation of the NaOH concentration was tested between 1 mmol·L^{-1} and 25 mmol·L^{-1}. The ratio between NaOH and the protecting group was maintained at 1:1. The evaluation of the intensity profiles of the surface pattern is depicted in Fig. 4-8. The fluorescence intensity of the pattern decreases strongly until an NaOH concentration of 10 mmol·L^{-1} is reached at a pH of 10. Afterwards, the fluorescence intensity of the pattern increases again. The strong decrease in the fluorescence clearly depicts a higher turnover of the thiols with an increase of the concentration of NaOH. This behavior is in accordance with theoretical expectations, as the thiol-yne reaction takes place under Michael-addition conditions.(Lowe 2014) Once the optimum pH-value is reached, the theoretical expectations would have suggested a constant fluorescence intensity of the pattern. One possible explanation for the less successful protection of the pattern at higher NaOH concentrations is that the more basic conditions influence the PPG. One possibility which is controversially discussed in literature is the hydrolysis of the carbamate function of the photolabile protecting group under alkaline conditions.(Dittert and Higuchi 1963)

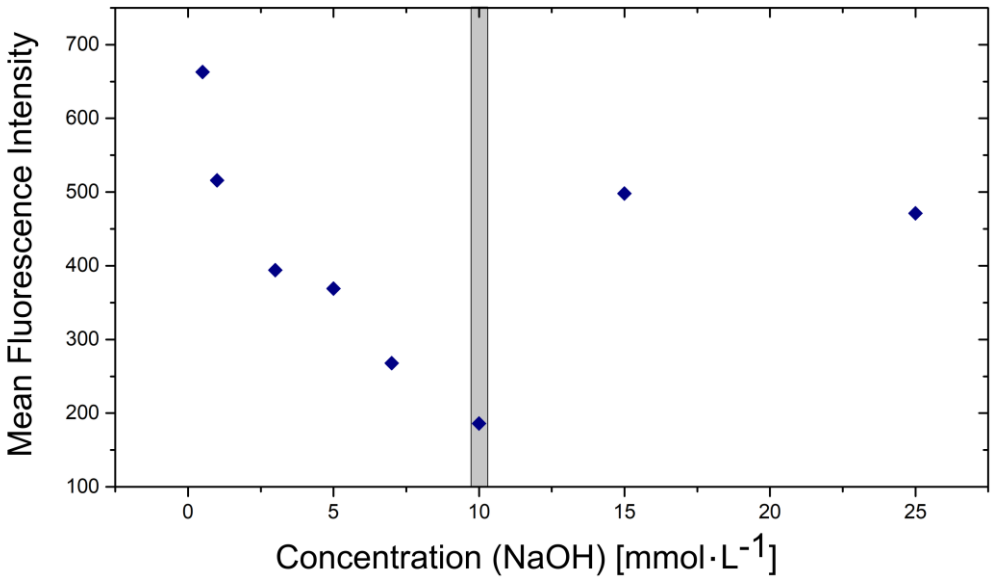

Fig. 4-8: Dependency of the thiol-yne reaction on the pH value. The remaining fluorescence after protection and subsequent functionalization with a labeled dye is depicted. The ratio of the protecting group and NaOH is 1:1. The lowest fluorescence intensity and therefore the maximum protection of the pattern is measured at c(NaOH)=10 mmol·L^{-1}, pH=10. This diagram was adapted from the Bachelor thesis of Pia Lenßen.

The stability of the photolabile protecting group was investigated under alkaline conditions using UV/VIS spectroscopy and NMR spectroscopy (see section 8.2.3 in the supporting information of this chapter). These investigations resulted in controversial results, as the UV/VIS spectrum did change under alkaline conditions, although the NMR results did not reveal a change in the chemical composition. As the alkaline conditions do not interfere with the protection of the pattern at an NaOH concentration of 10 mmol L^{-1} (pH=10), they were not further investigated.

(c) Concentration of the protecting group

As the second parameter, the concentration of the PPG was varied at an optimum pH value of pH=10. The concentration was increased from 1 mmol·L^{-1} to 20 mmol L^{-1}. In case of the preliminary contact angle measurements on the thiol-monolayer (see Fig. 4-9), an increase of the protecting group concentration above 1 mmol L^{-1} did not lead to a strong change in the surface hydrophilicity. In contrast to these experiments, the mean fluorescence intensity of the pattern drops significantly until the lowest value is reached at a protecting group concentration of 13 mmol L^{-1} (see Fig. 4-9). The increase of the concentration above the optimum value does not lead to a saturation but to an increase of the mean fluorescence of the pattern. As in the previously discussed similar behavior after the increase of the NaOH concentration, it could be possible that a molecular change of the protecting group leads to a decrease of the protection quality. As this behavior is not relevant at a concentration of 13 mmol L^{-1}, this is the concentration that was used for future experiments.

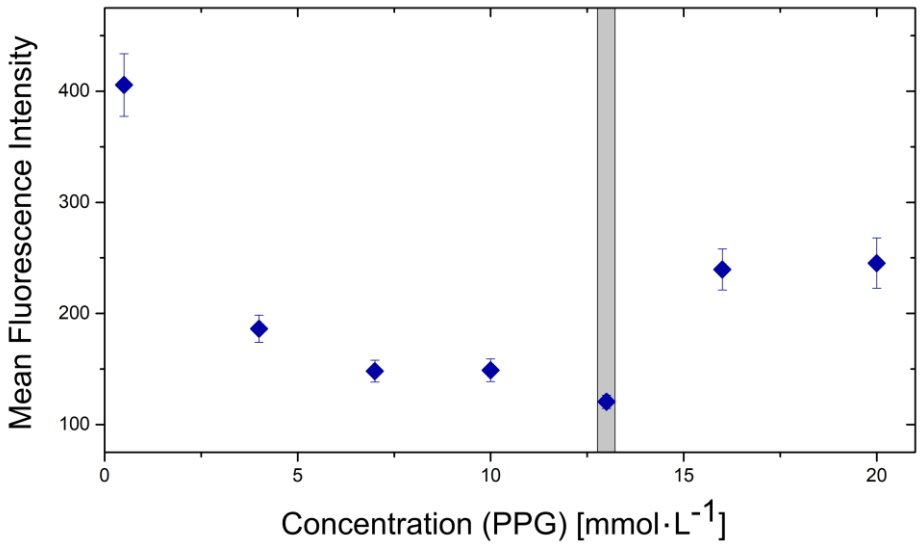

Fig. 4-9: Dependency of the thiol-yne reaction during variation of the concentration of the protecting group at a constant pH of 10. The remaining mean fluorescence of the pattern after protection and subsequent functionalization with a labeled dye is depicted. The lowest fluorescence intensity (and therefore the maximum protection of the pattern) is measured at c(Protecting Group)=13 mmol·L^{-1}. This diagram was adapted from the Bachelor thesis of Pia Lenßen.

Summarizing the findings, the transition from the thiol-yne reaction in bulk, to the solid-liquid interface was successful. Since the protection does only take place at the c-EBL spots, the usual surface analysis via contact angle measurements was not possible. The surface modification with a thiol monolayer served as preliminary system which allowed to verify the successful thiol-yne reaction at the surface through contact angle measurements. The influence of the incubation time as well as the pH value and the concentration of protecting group were monitored with conventional fluorescence microscopy in TIRF mode. Therefore, the supposedly protected thiol spots were incubated with maleimide functionalized fluorescent dye. Hence, in case of a successful protection of the spots no fluorescent signal should be detectable in an ideal case. Mainly due to unspecific binding events, it was found that even in cases of a successful protection, a faint pattern was still visible. Therefore, the mean fluorescence of the pattern was used as a reference value for comparison between the measurements. The ideal parameters for a successful protection of the thiol pattern include an incubation time of 1.5 h, the control of the pH value with NaOH until pH=10 is reached and a concentration of the protecting group of c=13 mmol L^{-1}. An inverted pattern with the protected spots is depicted in Fig. 4-10. The diffraction rings visible on the pattern stem from an artifact at the surface and are not related to the protection of the pattern.

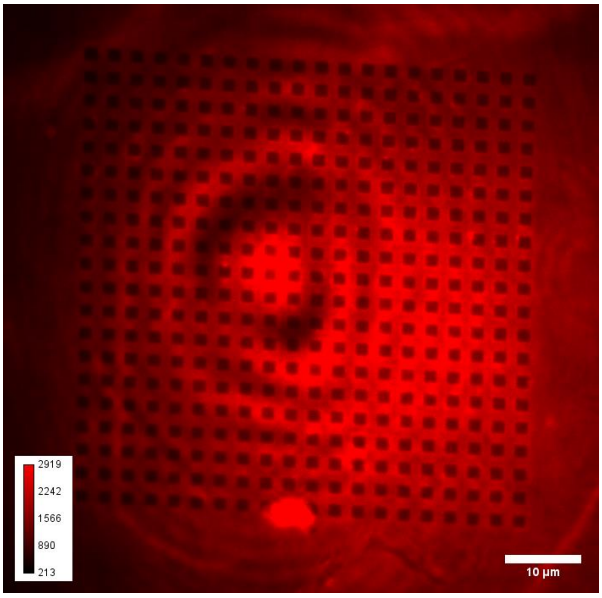

Fig. 4-10: Protected pattern via thiol-yne reaction. After protection, the substrate was incubated with a maleimide functionalized dye. Due to the successful protection of the thiol-spots the dye molecules cannot react to the pattern. The background fluorescence is due to unspecific binding of the dye to the background. This image was measured by Pia Lenßen as part of her Bachelor thesis.

4.2.3. Immobilization of sDNA

The successful functionalization of the thiol spots with the protecting group was followed by the deprotection of the pattern with UV-light as presented in step (d) of the general Scheme 4-1. The success of the deprotection can be verified with the subsequent immobilization of a fluorescently labeled linker to the deprotected amine function at the surface, see step (e) in the overall Scheme 4-1. A suitable linker must have an NHS-ester functionality at one end to bind to the deprotected amine on the surface and a maleimide functionality at the other end to bind to the fluorescently labeled thiol-terminated DNA strand. In case of an unsuccessful deprotection, the linker molecule cannot bind to the surface and therefore the c-EBL pattern could not be imaged using fluorescence microscopy, see Scheme 4-6.

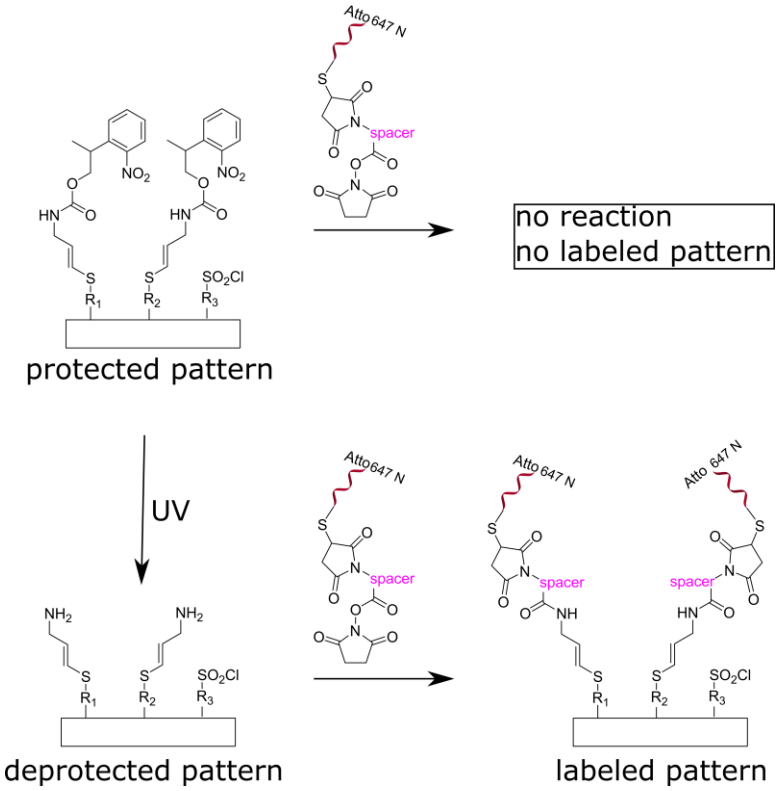

Scheme 4-6: The deprotected pattern is reacted with a linker molecule, functionalized with fluorescently labeled DNA. In case of an unsuccessful deprotection, the linker could not be immobilized at the surface and thus the pattern would not be visible through fluorescence microscopy.

Two different linker candidates, with varying spacer molecules, were compared after 10 minutes of irradiation with UV light of λ=365 nm and an optical output of 200 mW/cm^2. The position of the spacer molecules is marked in pink in Scheme 4-6. As depicted in Fig. 4-11, two linker candidates, SMCC[1] and SMPB[2], were compared to each other. Both linkers were functionalized with an Atto-647N labeled thiol DNA (DNA-3-Atto-SH[3]), see Fig. 4-11. Fluorescence microscopy was performed in TIRF mode at a laser wavelength of 640 nm and an exposure time of 10 ms. All settings were kept equal for both linker candidates in order to ensure the comparability of the results.

[1]Succinimidyl-4-(p-maleimidophenyl)butyrate
[2]Succinimidyl-4-(N-maleimidomethyl)cyclohexane-1-carboxylate
[3]Atto 647N - CGC ATT CAG GAT AAA AAA AAA A - 3'SH

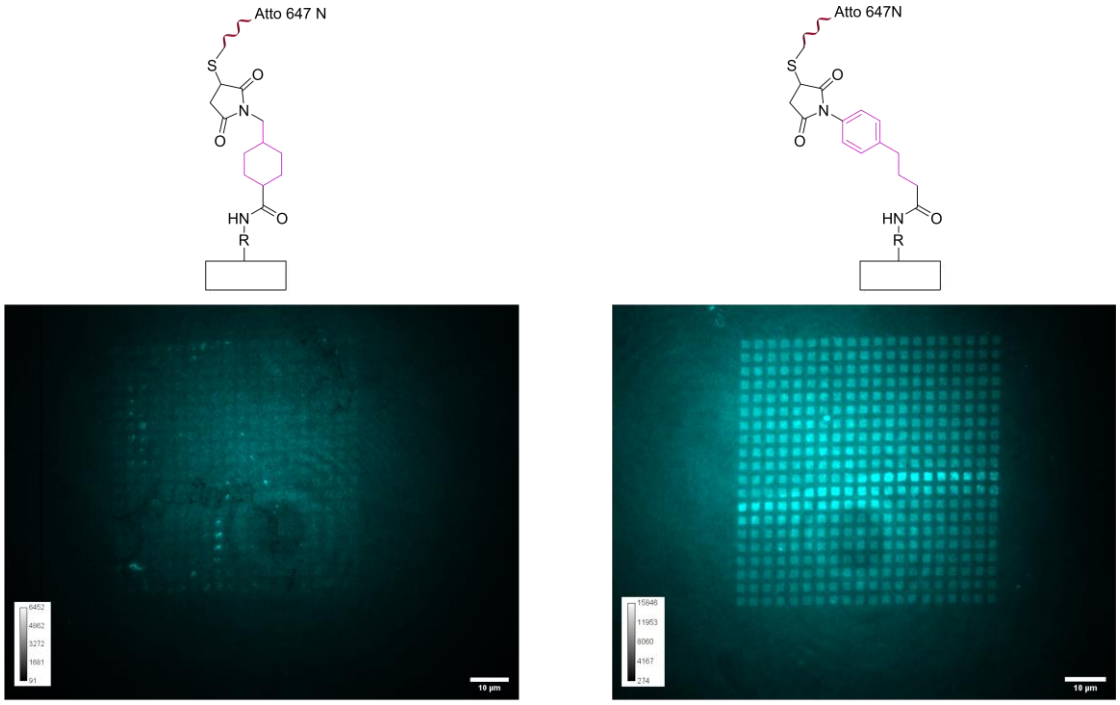

Fig. 4-11: Pattern functionalization at the free amine after deprotection with UV light. Two linker candidates, SMCC and SMPB, were bound to the pattern for comparison. Both linkers are functionalized with an Atto647N-labeled thiol-DNA. Images are taken in TIRF mode with a 561 nm laser.

The resulting fluorescence microscopy images show that the c-EBL pattern is visible in both cases. However, the pattern quality is much better in the case of SMPB, while the single spots appear as very faint in the case of SMCC. The reason for the difference in the pattern quality could either lie in the reaction conditions at the surface or in the reaction between linker and thiol-DNA. As a result, from the comparison between the two linker candidate, SMPB was used for all subsequent experiments.

4.2.4. Hybridization

In order to hybridize sDNA-functionalized molecules to the surface, a non-fluorescent, thiol-terminated sDNA, DNA-4-SH[4], was linked to the SMPB linker. The complementary DNA strand, DNA-3-Alexa[5], was labeled with an Alexa 647 dye and hybridized to the immobilized DNA (see section 7.2.6). The incubation time for the hybridization was set to 8 hours. After incubation, the substrate was thoroughly washed with autoclaved water to ensure the surface was cleaned from any salt residuals. Fluorescence microscopy was performed in TIRF mode at a laser wavelength of 640 nm and an exposure time of 50 ms. The fluorescent pattern Fig. 4-12 represents the successful hybridization reaction at the surface.

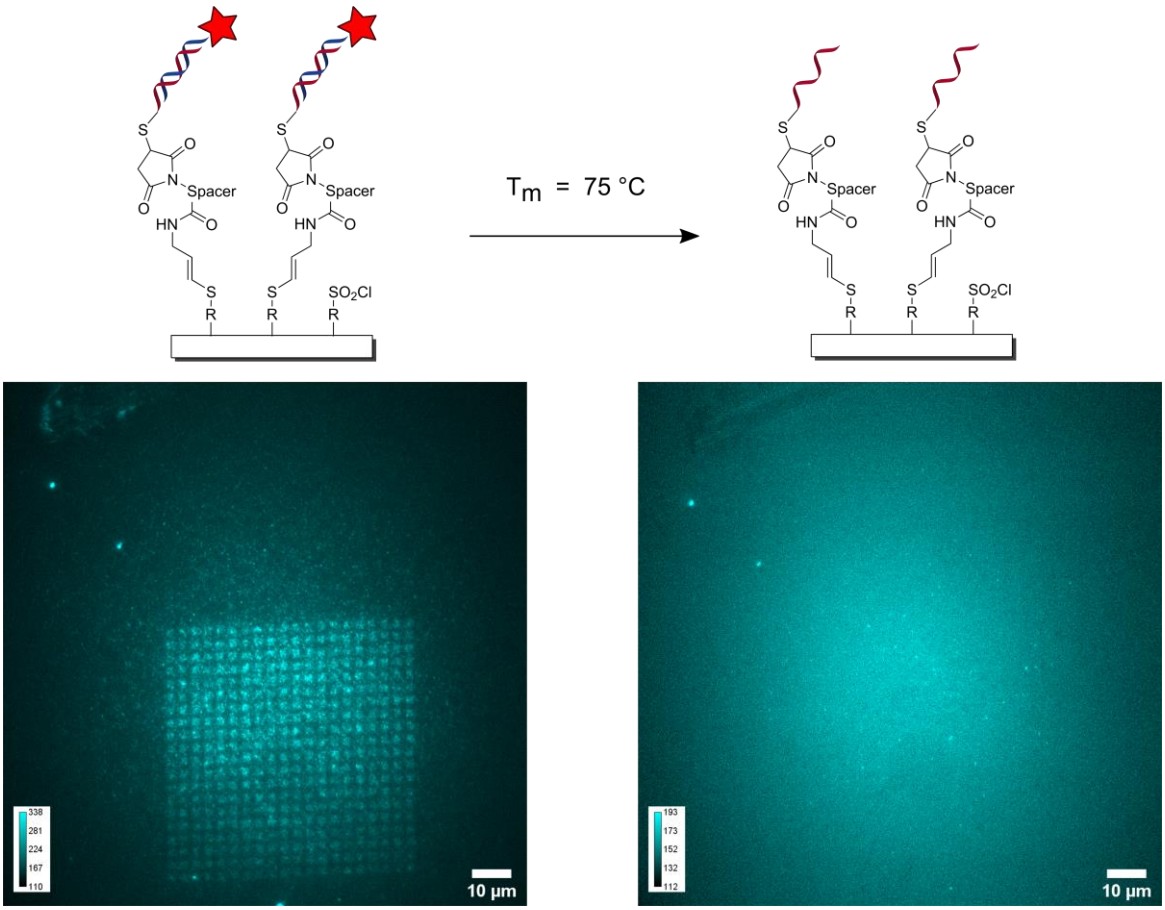

Fig. 4-12 Successful hybridization of a fluorescently labeled DNA strand to the immobilized sDNA on the surface. After melting at 75 °C, dehybridization leads to the vanishing of the pattern.

[4]ATC CTG AAT GCG AAA AAA AAA A – 3' SH
[5]CGC ATT CAG GAT AAA AAA AAA A -3' Alexa 647

In order to verify the reversibility of the hybridization experiment and therefore melt the hybridized strands, the substrate was removed from the microscope to heat the system. For the melting process, the substrate was positioned in a phosphate-buffered saline (PBS) buffer environment and heated in a water bath to 75 °C (see section 7.2.6). After purification, the substrate was imaged again under the exact same microscopy settings as for the hybridization experiment. As depicted in Fig. 4-12, after heating up the system above the melting temperature, the pattern was vanished and was not visible anymore. A scratch mark that was placed as described in section 4.2.1, as well as the two bright fluorescent spots on the upper left side of both images, ensured that the same area as before could be imaged.

4.2.5.Structured deposition of µGs

The necessity of understanding the spreading behavior of µGs at surfaces of different hydrophilicities derived from the question on how to maintain the natural spherical shape once the µGs are immobilized at the spots. It is therefore evident, that the research questions motivating chapters 3 and 4 of this dissertation co-evolved together and both motivated and impacted each other. The results presented in chapter 3 clearly revealed that a hydrophilic PEG surface allows to maintain the spherical shape of the µGs. Therefore, to ensure the natural shape is maintained after hybridization of the µGs to the pattern, the SO_2Cl-background was functionalized with an amine terminated PEG brush (for preparation, see section 7.2.3). The first attempt to hybridize DNA-functionalized µGs to the surface pattern with the PEG background were designed without the previously presented photolithography steps. Instead, the same pNIPMAM µGs used in chapter 3 were reacted with 1,4 dithioerythritol (DTT) in order to reduce the disulfite-groups of the µG to thiols. The µGs were afterwards reacted with maleimide-functionalized DNA, DNA4Mal[6].

[6]5’-ATC CTG AAT CGC Maleimide

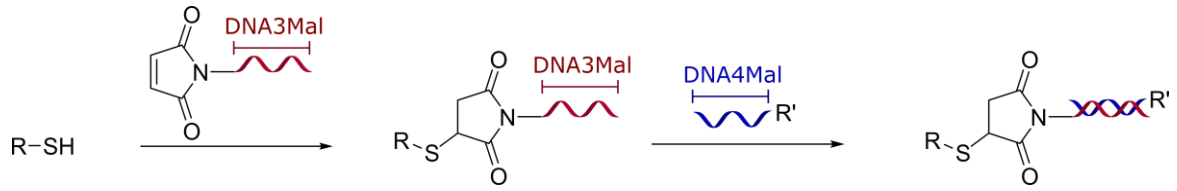

Scheme 4-7: Reaction path for the immobilization of DNA functionalized µGs (R') without the previously described photolithography steps. The c-EBL pattern consisting of thiols is directly reacted with maleimide functionalized sDNA (DNA3Mal). The immobilized strands can then be hybridized to the complementary strand (DNA4Mal).

In order to compensate for the difference in length between the sDNA and the PEG brushes, we elongated the DNA sequence by introducing two additional spacer molecules to the system. To do so, the surface was first incubated with DNA3Mal[7]. Spacer 1[8] was then hybridized to the immobilized DNA3Mal after 6 h of incubation. Spacer 2[9] was subsequently hybridized to Spacer 1 after an incubation time of 6 h. Finally, the DNA4Mal-functionalized µGs were hybridized to spacer 2 at the surface, see Fig. 4-13. This approach did not allow us to address individual spots but serves as proof of concept for the hybridization of DNA-functionalized µGs to immobilized strands at the surface

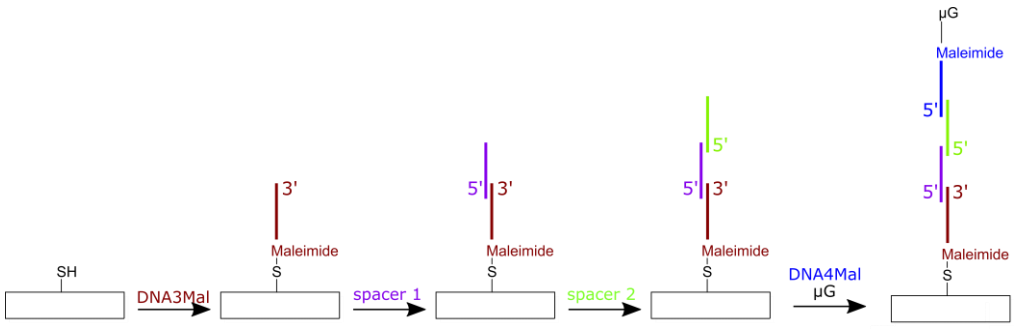

Fig. 4-13: Schematic overview of the necessary steps to immobilize pNIPMAM µGs to the surface. The thiol spots at the surface were first incubated with DNA3Mal. Spacer 1 was then hybridized to the immobilized DNA3Mal after 6 h of incubation. Spacer 2 was subsequently hybridized to Spacer 1 after an incubation time of 6 h. Finally, the DNA functionalized µGs were hybridized to spacer 2 at the surface.

[7]CGC ATT CAG GAT AAA AAA AAA A-3'Maleimide
[8]ATC CTG AAT GCG AAG CGC GGC GGG AGT GGT GGT TAC GCG CAG CGT GAC CGC TAC ACT TGC CAG CGC CCT AGC GCC CGC TCC TTT CGC TTT CTT CCC TTC CTT TCT CGC CAC GTT CGC C
[9]GCA CCC CCG CAT TCA GGA TGC CGG CGA ACG TGG CGA GAA AGG AAG GGA AGA AAG CGA AAG GAG CGG GCG CTA GGG CGC TGG CAA GTG TAG CGG TCA CGC TGC GCG TAA CCA CCA CTC CCG CCG CG

The DNA-functionalized µGs were synthesized by Dr. Sabine Eisold as part of her dissertation.(Eisold 2018) The final pattern was investigated using fluorescence microsocopy in TIRF mode, with a laser wavelength of 640 nm and an exposure time of 50 ms. This presented approach did not lead to any detectable fluorescence of the pattern during the microscopy experiment. The most probable explanation for the unsuccessful immobilization experiment leads back to the different length scales of the individual components. Even though we tried to compensate for the difference in length between the sDNA and the PEG brushes by adding spacer 1 and spacer 2, the visual description in Fig. 4-13 is unfortunately a very simplified presentation of the situation which can lead – and in this case has probably led – to false assumptions. The initial idea of the molecular DNA/spacer construction as a rigid rod which holds itself upwards in a 90° angle from the surface, did not work experimentally. The PEG brushes, with a molecular weight of 5000 g/mol have a length of ~50 nm while it is most likely that the DNA/spacer construction was flattened out and therefore the DNA anchor points were not in reachable distance for DNA-functionalized µG. It is probable that the height of the polymer brushes in the background and the immobilized DNA-stands at the spots create a nanoscopic surface topology resulting in indentations. This could then lead to an effect that is schematically depicted in Fig. 4-14. In this scenario, the µG would not fit into the indentation and the hybridization would therefore be sterically hindered. Two possibilities allow for the circumvention of this size effect. Both are schematically presented in Fig. 4-14. One possibility consists in repeating the experiment using the same substrates with the PEG 5000 brushes, but with smaller µGs. Another possibility, using the same µGs as in the preliminary experiment, consists of synthesizing substrates with shorter PEG-brushes. We chose to synthesize smaller pNIPMAM µGs with a R_h of 190 nm, the sample preparation is described in section 7.2.8. The synthesis of theses µGs was conducted by Rebecca Hengsbach and Niklas Lothman (IAC; RWTH Aachen University).

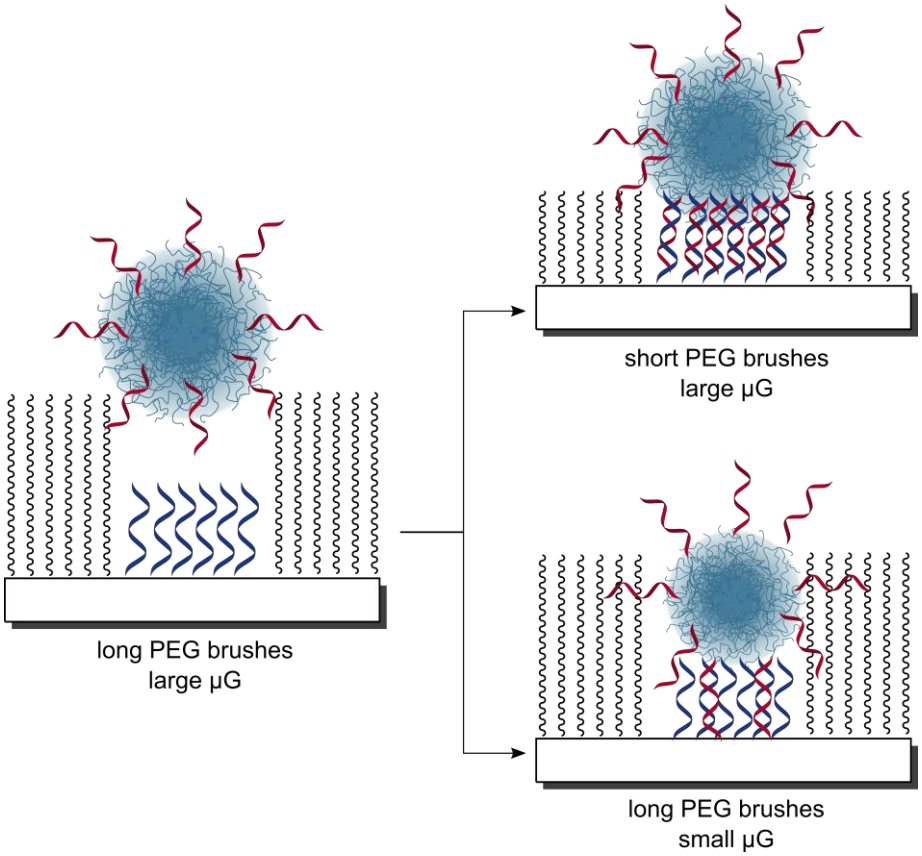

Fig. 4-14: Schematic explanation of the relevant size effect for the immobilization of DNA-functionalized µGs to sDNA on the surface. Blue and red curly lines represent the complementary DNA strands, the black curled lines represent the PEG brushes.

It should be noted that labeled sDNA is expensive and should therefore not be used without preliminary experiments. We therefore performed a prove of concept experiment without the labeling step. The newly synthesized pNIPMAM µGs were prepared as previously explained for the larger µGs. Reduction with DTT allowed for the functionalization of the µGs with DNA4Mal. In this case, the preliminary measurement consisted in imaging the immobilized, but unlabeled, µGs in the brightfield mode. The successful immobilization and verification of the experiment imaged in the transmission mode of an optical microscope is depicted in the supplementary information (see figure S.I. 8-30). As the preliminary experiment showed that the immobilization of the smaller µGs was successful, the next step consisted in hybridizing the complementary labeled DNA3Alexa to the immobilized µGs at the surface. The resulting fluorescence images are depicted in Fig. 4-15.

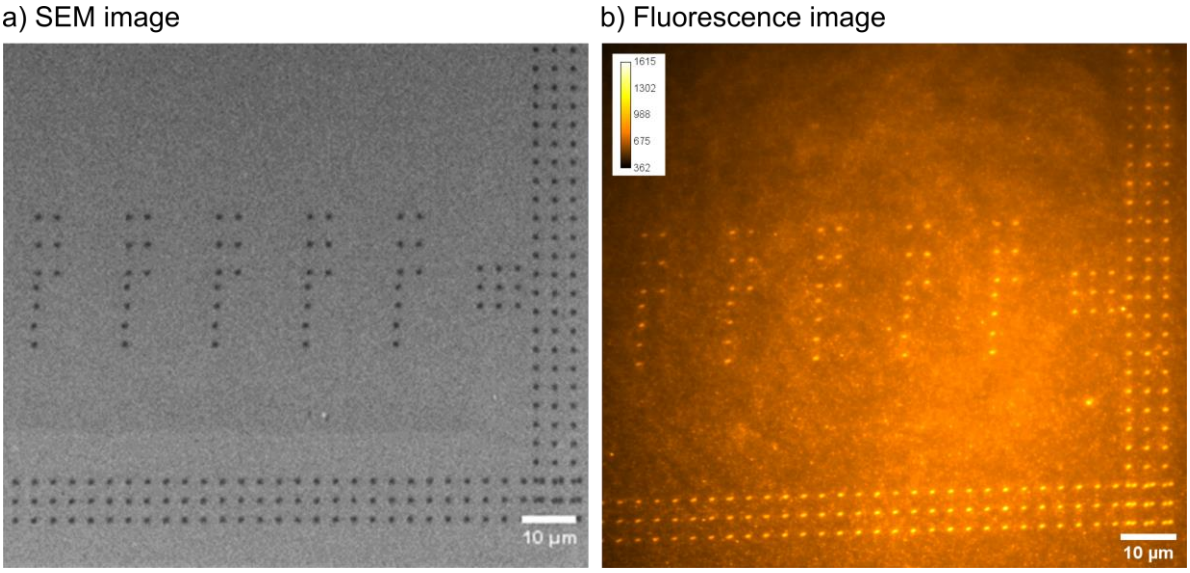

Fig. 4-15: Structured deposition of DNA-functionalized µGs (R_h = 190 nm). (a) c-EBL pattern after the writing process in SEM mode. (b) Immobilized µGs through hybridization to the DNA strands at the pattern. The image was taken in TIRF mode using a 640 nm laser.

Image (a) represents the SEM image directly after the pattern was written using c-EBL. Image (b) shows the same image section as in the SEM image, but after functionalization of the background with PEG brushes and after immobilization of the µGs to the spots. The immobilized and labeled µGs are clearly visible in the fluorescence image. With this experiment, the primary goal of immobilizing DNA-functionalized µGs to a structured surface is achieved. Future investigations will include experiments on the second possibility suggested in Fig. 4-14 concerning the previously used larger µGs with shorter PEG brushes. Furthermore, it will be important to perform super-resolution fluorescence microscopy of the immobilized µGs to verify if the spherical shape is in fact maintained through the PEG brushes, as it was shown on the PEG monolayer in chapter 3.

4.3. Summary and outlook

The basic idea of the research presented in this chapter consisted of combining c-EBL and photolithography to enable the hybridization of DNA-functionalized µGs on a structured surface. The important advantage of combining c-EBL with photolithography in this approach is that on the one hand it is possible to write c-EBL spots in the nm-range, which would not be possible using only photolithography. On the other hand, the introduction of the photolithographic method allows for the flexibility to chemically address these c-EBL spots with different systems, like e.g. with sDNA. This project was feasible due the framework of the CRC 985 allowing to combine different fields of expertise in project A6. The research on this topic took a time frame of three years, resulting in two sub projects that will go hand in hand in future work. The seven-step process, depicted in Scheme 4-1, involves the production of a SAM, the c-EBL process, the protection and deprotection of the pattern as well as the incorporation of a linker and finally the immobilization and subsequent hybridization steps. The experimental routine starting from the preparation of the glass substrate to the hybridized system, took exactly one week. It was possible to combine the c-EBL method with the photolithographic approach through the selective functionalization of the pattern with a PPG (see section 4.2.2). This allowed for the deprotection of the pattern using UV light and the subsequent immobilization of sDNA to the spots (see 4.2.3). The final step of the joint lithographic method resulted in the successful hybridization of the complementary strand to the surface (see 4.2.4). The hybridization of DNA-functionalized µGs to a surface pattern with immobilized sDNA at the single spots was conducted without the photolithographic steps. The maleimide-functionalized sDNA was directly functionalized to the thiol-spots, allowing for a much less time-consuming sample preparation.

The second part of the project, that had the aim to immobilize DNA-functionalized µGs at the surface, was combined with the fundamental results discussed in chapter 3. The SO_2Cl, creating the unmodified surface background, was therefore reacted with PEG brushes in order to ensure the spherical shape of the µGs once they were immobilized to the pattern. The impact of the different length scales was intensely studied resulting in an experimental change to smaller µG-systems. This was important in order to ensure that the hybridization was not sterically hindered. Finally, the hybridization of DNA-functionalized µGs to the pattern was successful and could be monitored and verified using TIRF microscopy. It should be noted that for both sub-projects, one of the experimental challenges that had to be compensated for consisted in the fact that the pattern itself is only visible in the electron microscope and not visible in the optical microscope (see section 4.2.1).

Furthermore, as the different steps of the surface functionalization were mainly focused on the pattern itself, commonly used verification methods like contact angle measurements were not conductible. The successful surface modifications had to be monitored using fluorescence microscopy methods with the downside of having to deal with unspecific binding events on all surfaces. Overall, the two main results demonstrate that both, the combined lithographic approach, as well as the hybridization experiments do work individually. An important next step will consist of merging the two sub-projects together, which will allow for the possibility to address single spots individually. Another important step includes the reduction of the spotsize to investigate the limitations of this approach. It would furthermore be interesting to perform super-resolution fluorescence microscopy measurements in order to verify that the spherical shape of the µGs is indeed maintained as predicted according to the findings in chapter 3. The immobilized µGs are more than half the size of the µGs that were investigated in the previous chapter. It could therefore be possible that the number of localizations resulting from dSTORM experiments will be lower. DNA-based point accumulation for imaging in nanoscale topography (DNA-PAINT) (Iinuma, Ke et al. 2014) could in this case result in better quality images.

5. Immobilization of stretched DNA inside thermos-responsive hydrogels

This section provides an insight into a new experimental method that allows to immobilize and analyze DNA molecules in a linearized conformation. This project has derived from a cooperation between the groups of Prof. Dr. Weinhold (Institute of Organic Chemistry, RWTH Aachen University) and Prof. Dr. Wöll (Institute of Physical Chemistry, RWTH Aachen University). The idea of combining the biochemical expertise provided by the Weinhold laboratory with the expertise on bio-hybrid polymer systems and surface modifications - presented in the previous chapters - had the goal to challenge the cost-intensive state of the art DNA stretching methods. DNA stretching is of great importance when it comes to epigenetic analysis or the identification of structural variations causing diseases. The procedure presented in this work is experimentally simple and cost-efficient in comparison to existing technologies in the field of DNA-stretching. The inventive step in this new procedure has led to a pending process-patent application (dt.: deutsche Prioritätsanmeldung eines Verfahrenspatentes) registered by RWTH Aachen University and the inventors Prof. Dr. Dominik Wöll, Prof. Dr. Elmar Weinhold, Felix Gularek and the author of this dissertation, Laura R. Hoppe Alvarez. The patent application with the German title “Verfahren zum Strecken eines Nukleinsäuremoleküls” was registered on July 22, 2019 with the registration number DE 10 2019 119 782.1. The preparation of the DNA samples was mainly performed by Felix Gularek, Ph.D candidate in the research group of Prof. Dr. Elmar Weinhold, while the microscopic part as well as the stretching of the DNA in the gel was performed by the author of this work. The experiments on the optimization of the ideal stretching conditions and the associated automated analysis were partly conducted by Lars Pritzlaff as part of a research assignment in his master’s program in chemistry at RWTH Aachen University. The entire research assignment was designed and consistently supervised by the author of this dissertation.

5.1. Introduction

In the past few decades the scientific field of deoxyribonucleic acid (DNA) analysis took a rapid development.(Shendure, Balasubramanian et al. 2017) In 1989, the Human Genome Project was started with the ambitious goal to extract the entire DNA sequence of the human genome within 15 years.(Watson 1990) During this time span techniques were developed, that allowed the project to be finished by 2001 with a cost of 300 Mio. US$, which was less than expected.(Lander, Linton et al. 2001, Metzker 2010) Today, analyzing an entire human genome by next generation sequencing methods costs around 1000 US$.(Shendure, Balasubramanian et al. 2017) The obtained information provides an insight on the genotype of patients. The information encoded in the genome is directly connected to phenotypical features.(Johannsen 1911) New medical applications like sequencing, allow to retrace diseases to certain alleles of genes or other single nucleotide polymorphisms.(Altshuler, Daly et al. 2008) For the evaluation of larger mutations like insertion, deletion, inversion and copy number variants, methods that provide larger range information are more suitable.(Neely, Deen et al. 2011) With DNA mapping, the displacement of genes and the copy number of sequences are directly accessible, whereas with sequencing only small segments are analyzed in one piece which must be assembled to longer sequences afterwards. In this assembly repeated sequences cause problems when larger than the investigated segments. Therefore, diseases like facioscapulohumeral muscular dystrophy (FSHD) that are based on a copy number variant of tandem repeats are genetically better traceable by DNA mapping.(Tsumagari, Chen et al. 2010) The longer range of DNA mapping is enabled by DNA barcoding, where short sequences of e.g. 4 or 6 bp are marked with reporter groups. This way, labels that are several hundred bp apart from each other can be recognized instead of single nucleotides. Additionally, epigenetic information can be traced by an appropriate labeling design as the labels are introduced sequence specifically.(Levy-Sakin, Grunwald et al. 2014) When the labeled sequences match the sequences that are occupied by epigenetic marks, these positions cannot be labeled anymore and the labeling equals a query of the modifications.(Sharim, Grunwald et al. 2019) One of the most important epigenetic modifications is the methylation of CpG dinucleotides. Aberrant CpG methylation of specific genomic regions is associated with cancer.(Sharma, Kelly et al. 2010) In this context DNA mapping provides a possibility for early cancer detection and prevention. A crucial step that enables the reading of the barcode is the stretching of labeled DNA strands to an extend that allows for the differentiation of the different labels and the possibility to assign them to specific positions.

Commercially available products use manufactured nanoscale channels in combination with an exterior force of an electric field or hydrodynamic flow (see section 2.5.7).(Lam, Hastie et al. 2012) The DNA strands are forced into the channels and are stretched there, since their degree of freedom is limited by the diameter of the nano channel. On the one hand, the advantages of this method lie in the high throughput and large DNA strand lengths.(Lam, Hastie et al. 2012) On the other hand, the method is expensive due to the investment in devices like the Saphyr system which is distributed by the company binano genomics. Nano channel devices are priced around several 100,000 $ with single chips costing more than 1000 $ each. A commonly used method in research laboratories is DNA combing (see section 2.5.8). Here, DNA strands are stretched on modified, solid glass or polymer surfaces.(Michalet, Ekong et al. 1997, Neely, Deen et al. 2011) The surface modification with positively charged silanes provides anchor points for the negatively charged DNA strands. Due to the interplay of a forced fluidic flow and the ionic attachment to the surface, the DNA is linearized and stretched. The flow can be achieved e.g. by capillary forces or by microfluidic devices.(Wu, Jeffet et al. 2018) Advantages of DNA combing lie in a simple experimental design and a good overstretching quality.(Liu, Wang et al. 2004, Wu, Jeffet et al. 2018) On the other hand, DNA combing is limited by the restricted strand length of approximately 50 kbp that can be stretched. Furthermore, the stretching ratio is not always uniform neither for different strands nor for different regions on the same strand.(Wu, Jeffet et al. 2018) We presented an alternative method to stretch DNA strands. In this new method, DNA strands are linearized by incubating a flat thermo-responsive hydrogel with a drop of DNA solution on top of it at elevated temperatures. Thereby, the hydrogel accomplishes different purposes at once. First, the hydrogel provides a large surface area which enables a high solvent evaporation. Since the drop containing DNA solution represents a reservoir of solvent, a hydrodynamic flow from the drop to the hydrogel's surface is achieved. Secondly, the hydrogel contains a channel-like polymer network forcing the DNA strands to be linearized when carried through the hydrogel with the flow. This effect is amplified by exceeding the VPTT of the thermo-responsive hydrogel as the polymer collapses and forms a closer-meshed network.(Backes, Krause et al. 2017) Finally, after full consumption of the drop of DNA solution, the hydrogel is dried and stays tightly meshed, fixating the DNA in its entropically unfavorable linear conformation and enabling analysis by means of fluorescence microscopy.

5.2. Results and discussion

In this study, the parameters of DNA modification and purification (see 5.2.3), hydrogel preparation and analysis with fluorescence microscopy were optimized to an applicable level for short DNA strands of about 40 kbp. T7 phage DNA was used and modified with a fluorophore by two different types of DNA methyltransferases (MTases), namely M.TaqI and M.BseCI. Their respective specific recognition sequences are 4 and 6 bp long which allows for different labeling densities. The strand contours were stained with the fluorophore YOYO-1®, which is varied in its concentration (see 5.2.8). After applying the DNA to the hydrogel, different DNA concentrations and drop volumes were screened (see 5.2.5). For the hydrogel itself, different thicknesses and gel diameters were tested (see 5.2.4). The method of drying was varied as well described in section 5.2.6. After optimizing these parameters, images were recorded and analyzed with automated analysis methods that cover several steps (see 5.2.12). First, the entire image processing for single images and composite images. Secondly, the complex recognition of DNA strands in the images was executed. Subsequently, further analysis was conducted including strand length statistics and a comparison of the found barcode patterns to calculated ones. The results established a basis on which further studies with respect to medical application shall be built.

5.2.1. General concept and approach

As a result of the combination of the author's expertise in biohybrid polymer systems at interfaces and the cooperation partner's knowledge in DNA mapping and optical DNA-mapping, investigations on the behavior of long DNA molecules within gel-systems were studied for biomedical applications. These investigations let to a new method for DNA stretching, which is a crucial step in the DNA mapping process. In this section, this technique for DNA stretching is introduced, which has potential to exhibit multiple advantages over previous methods (see 2.5.6) ranging from low cost to a high strand-linearization quality. The overall goal of the project consists of delivering a method that enables fast, cheap and reliable DNA stretching for DNA mapping and epigenetic analysis.The matrix used for DNA stretching consists of a thermo-responsive hydrogel which is covalently bound to a glass substrate. For the synthesis of this hydrogel (see 7.3.5), a stock solution containing the monomer NIPAM, the crosslinker N,N'-Methylenebisacrylamide (MBA) and a photo initiator, all solved in dimethylsulfoxide (DMSO), are deposited between a glass substrate and a round coverslip (see Fig. 5-1).

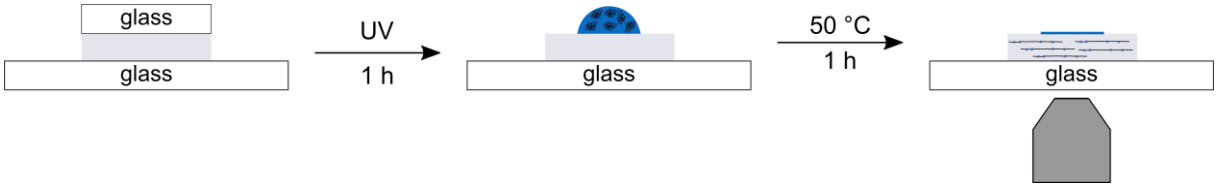

Fig. 5-1: Experimental procedure for DNA stretching in hydrogels. The pNIPAM hydrogel is polymerized between two glass-slide via UV-initiation. A drop of DNA-solution is dropcasted on the polymerized hydrogel film. The substrate is then left to dry at a temperature of 50 °C leaving linearized DNA strands in the gel.

The glass substrate was modified with a silane functionalized with a monomer unit. By irradiation of the solution with UV light the free-radical terpolymerization was conducted according to section 7.3.5. After formation of a PNIPAM hydrogel film that is covalently bound to the glass substrate, the circular coverslip at the top could be subsequently removed. The DMSO was substituted with water. Simultaneously, a DNA solution was prepared that contains target DNA that was sequence-specifically alkylated with a TAMRA containing cofactor by a DNA MTase. Subsequently, the modified DNA solution was purified from excess fluorophores and stained with YOYO-1®. Finally, a drop of the DNA containing solution was put on top of the hydrogel to allow diffusion into the gel. In the following crucial step, the stimuli-responsive collapse of the hydrogel is triggered by thermal treatment through incubation at elevated temperatures above VPTT with the aim of stretching the DNA inside the hydrogel. Afterwards, the sample was analyzed by means of fluorescence microscopy with a spinning disk confocal fluorescence microscope (see 2.1.2). The entire DNA strands and the labeled sequences were imaged separately with different laser wavelengths. The goal of this investigation consisted of the search for experimental parameters that allow further analysis of the stretched DNA strands obtained by fluorescence microscopy, including the comparison of the TAMRA label positions to the theoretically expected label positions of the target DNA. The system was optimized by systematic variation of parameters that include the DNA preparation, as well as the hydrogel preparation. For the DNA part, a crucial factor was the purification from excess fluorescent cofactors. It was found that the agarose plug purification (APP) (section 5.2.3) was best suitable as purification method. Another parameter, that was important for the evaluation of the images, was the fluorophore label density. Here, two densities were compared that were based on the recognition sequences of the MTases M.TaqI with a 4 bp sequence and M.BseCI with a 6 bp sequence. The numbers of produced labels on the used T7 phage DNA were 111 and 3, respectively, on a theoretical B-DNA contour length of 13.6 µm (section 5.2.7).

In addition, the ratio of YOYO-1® staining fluorophore to the amount of base pairs was varied to ensure homogeneous intercalation along the DNA strands (section 5.2.8). Furthermore, the volume of the drop of DNA solution deposited on the hydrogel and the concentration of the included DNA was optimized (section 5.2.5). Furthermore, the hydrogel preparation, the thickness (section 5.2.4) and the diameter (section 5.2.9) were varied. The set of optimized parameters resulted in linearized DNA strands allowing for evaluation through optical mapping. The arising task of the image analysis is presented in the appendix of this chapter (section 8.3.1). To enable a high analysis throughput, the evaluation was automated by usage of a set of Python programs which were developed as part of this investigation. It includes the processing of the fluorescence microscopy images, as well as the composition of relating images, which combine the two laser wavelength channels used. Furthermore, a pattern recognition algorithm was developed, which enables the automated detection of linearized DNA strands in the fluorescence microscopy images. Additionally, a histogram was created, that illustrates the distribution of DNA strand lengths. Finally, the intensity profiles of labels along the DNA strands were obtained. The identified strands were compared to T7 phage DNA by fitting their intensity profiles to theoretical ones, that were calculated from the nucleobase sequence of the target DNA. The key results of the optimization were then summarized in the conclusion (section 5.3) followed by a short outlook in the same section.

5.2.2. Optimization of the experimental parameters

The basic preparation of the silanized substrates, as well as the synthesis of the hydrogel is similar for all optimization steps. Each parameter variation described in this chapter represents one deviation from the main preparation protocol. Therefore, the basic protocol will be described in this paragraph and the specific variations are outlined in the respective paragraphs. The substrates are synthesized by pipetting a drop of NIPAM polymerization solution containing NIPAM, BIS and the photoinitiator (preparation see 7.3.5 in the experimental section) onto the cleaned and subsequently silanized surface. The solution is then covered with a Ø10 mm coverslip. The hydrogel is exposed to UV light (λ=254 and 266 nm) for 1 h from the top. After irradiation, the coverslips are removed, and the substrates are stored in MilliQ water over night. The finished hydrogels are left to air-dry for 16 h. Afterwards, the hydrogel is incubated at 50 °C before a drop of the DNA-solution is pipetted onto the hydrogel.

The system is incubated at 50 °C for 1 h before imaging on a spinning disk confocal microscope. The intercalating agent YOYO-1® is imaged with a 488 nm laser and the AdoYnTAMRA labels are imaged with a 561 nm laser, with an exposure time of 50 ms.

5.2.3. Effects of the agarose plug purification on the quality of the microscopy images

After the DNA strands had been labeled with AdoYnTAMRA (see chemical structure in section 2.5.4), it was necessary to purify the DNA containing initial solution from excess fluorophore molecules. Without purification, a high signal in the background overlaying the DNA strands was detected. This hindered the differentiation between label fluorophores and free fluorophores. For this investigation, the commonly used APP method was performed. The exact procedure of the APP is described in section 7.3.4. An agarose solution was prepared by solving the low melting temperature agarose TE buffer, while incubating at 75 °C for 1 h. The unpurified DNA solution and the agarose solution were incubated at 43 °C for 10 min. Both solutions were mixed thoroughly with same volume fractions. The mixed solution was transferred into disposable plug molds and cooled at 6 °C for 1 h. The plugs were washed six times by incubating them at room temperature on a shaker at 100 rpm for at least 6 hours per wash cycle. The plugs were centrifuged in a micro test tube and incubated at 75 °C for 15 min. After incubating them at 43 °C for 15 min, β-agarase was added and they were incubated at 43 °C for 1 h. They were cooled to 6 °C for 15 min. Proteinase K was added and the mixture was incubated at 43 °C for 1 h. For the test of the purification quality, APP was applied to λ phage DNA which was labeled with M.TaqI. The resulting overlaid fluorescent microscopy images in Fig. 5-2 reveals that – as desired – the major part of fluorophores is located on the DNA strands whereas only few of them lie between the strands.

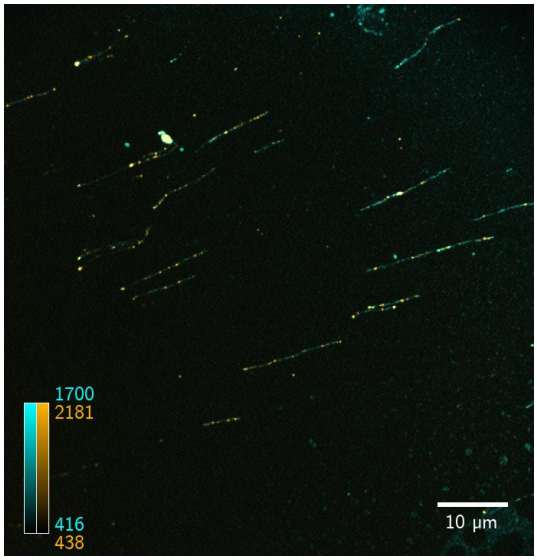

Fig. 5-2: Fluorescence microscopy image of λ phage DNA strands stretched in hydrogels. The strands were labeled with AdoYnTamra and purified from excess fluorophores by APP with a new protocol (see section 7.3.4). The strands were intercalated with YOYO-1®.

This gives a hint that the newly applied purification protocol works well for removing excess (labeling) fluorophores from the DNA solution. Therefore, this method was applied for all following series that contain labeled DNA. The remaining unassigned signals may result either from not removed cofactor molecules or from auto-fluorescent behavior of the hydrogel. The origin of those signals will play an important role in section 5.2.7. The test of the purification method is the only one that was conducted with λ phage DNA. For all following variations T7 phage DNA was used.

5.2.4. Variations of the hydrogel thickness

The thickness of the hydrogel is an important parameter to control the behavior of the DNA strands in the hydrogel medium. It affects the theoretical concentration of the DNA as the same amount of substance is applied to a different volume of hydrogel. Additionally, the imaged DNA strands are expected to be immobilized at the interface between hydrogel and glass surface. An increased thickness of the hydrogel implies a longer diffusion path for the DNA molecules from the top of the hydrogel to the imaged plane. Both aspects will have an effect on the density of the imaged DNA strands as well as on the orientation and stretching behavior of the strands. The mentioned effects are examined in this section. The thickness of the hydrogels was varied experimentally by changing the volume of the polymerization stem solution (see section 7.3.5).

The volume of the NIPAM polymerization solution applied to the surface was varied between i) 1 µl, ii) 2 µL and iii) 3 µL. The thickness was proportional to volume with the cross-sectional area as proportionality constant. The hydrogel volumes of 1, 2 and 3 µL correspond to a measured height of the drop-casted polymerization solution onto the substrate of 13, 25 or 38 µm, respectively. An exemplary fluorescence microscopy image is depicted in Fig. 5-3 visualizing the effect of the different hydrogel thicknesses. Clear differences in the stretching behavior and concentration can be observed. The hydrogel prepared with a stem solution volume of 1 µL leads to no visible stretching results. The DNA strands are rather closely coiled and only few connection lines between coils can be recognized. Those lines are not stretched but curled. While these images include only intercalated but unlabeled DNA, images of labeled strands would not be suitable for any barcoding or profiling analysis. The hydrogel with a preparation volume of 2 µL reveals a better stretching quality. The amount of line shaped strands outweighs the coiled strands by far. However, the lines themselves are not completely straight and, more importantly, they overlay each other in a way that individual strands are not distinguishable. The DNA in the thickest hydrogel of this series looks similar to the one with intermediate thickness with the difference that individual strands are observable. Using labeled T7 phage DNA should allow for the label-fluorophores to be well assignable to the strands which would enable further analysis of the label positions or the intensity profiles along the strands. All hydrogels in the following sections with a diameter of 10 mm were prepared with 3 µL of polymerization stem solution.

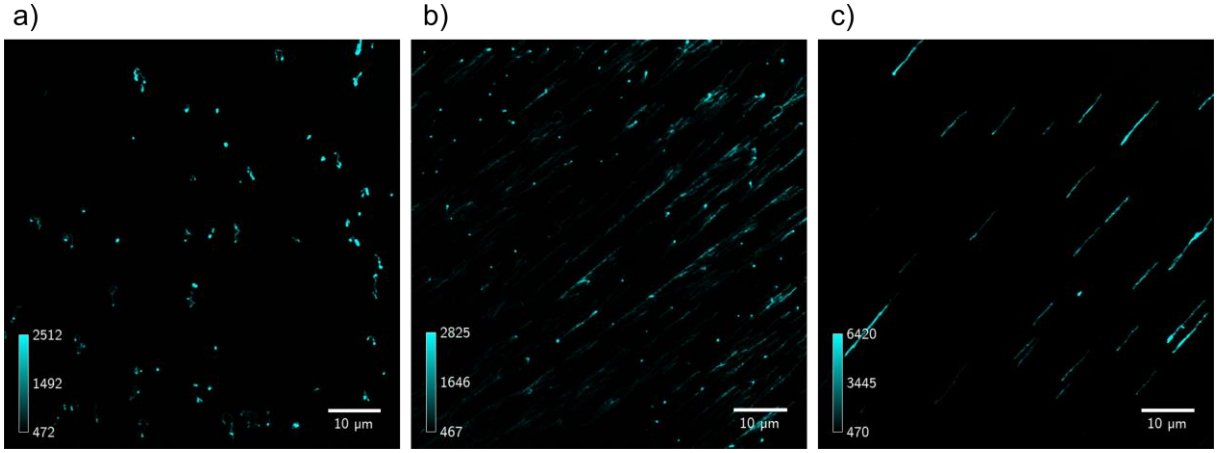

Fig. 5-3: Fluorescence microscopy images in the intercalation channel of T7 phage DNA strands stretched in hydrogels of different thicknesses. Hydrogels were prepared with 1 µL (a), 2 µL (b) and 3 µL (c) of polymerization stem solution. The strands were intercalated with YOYO-1®.

The difference in the stretching results upon varying gel thicknesses, could be due to a decreased transmission of UV light when polymerizing the hydrogel. During the hydrogel preparation, the UV lamp is placed on top of the substrate and the light is thus directed onto the sample from above. Lambert Beer's law describes the relation between absorbance *A*, transmission *T*, the molar decadic absorption coefficient ε , the concentration *c* and the layer-thickness *L*, as depicted in equation (14).

$$A = -\log_{10}\frac{I}{I_o} = -\log_{10} T = \varepsilon c L$$
$$T = 10^{-(\varepsilon c L)} \qquad (14)$$

Although the absorption coefficient of the photoinitiator (2-hydroxy-2-methylpropiophenone) was not measured in DMSO, a literature value of ε = 8000 L mol^{-1} cm^{-1} in water (Brautzsch, Kerzig et al. 2016) was used for calculations. The transmission was calculated according to Lambert Beer's law with a concentration of *c* = 0,05 mol L^{-1}, for layer-thicknesses between 0 and 60 µm, see Fig. 5-4.

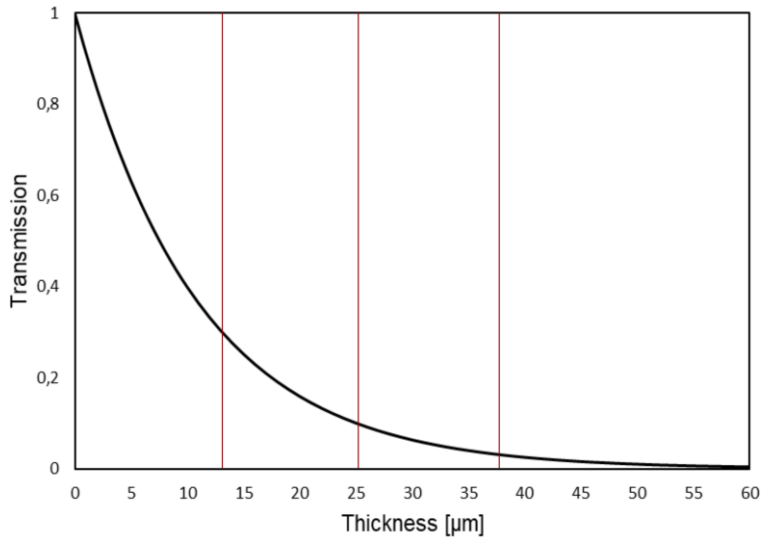

Fig. 5-4: Diagram of the layer-thickness dependent transmission behavior according to Lambert Beer's law. The three hydrogel thicknesses that were synthesized are marked in red at 13 µm, 25 µm and 38 µm. The best stretching of the DNA molecules was achieved at a layer-thickness of 38 µm.

The dependency of the transmission of light from the layer thickness of the gel shows a strong decrease towards higher thicknesses. The best stretching results of DNA molecules were achieved at a hydrogel thickness of 38 µm. At this value, the transmission is already strongly decreased, which means that most of the light is not able to reach the lower hydrogel regions.

Due to this effect, the quality of polymerization and therefore the characteristics within one hydrogel vary, apparently leading to a positive effect for DNA stretching in thicker gels. As this chapter is focused on finding the optimum conditions for the stretching of DNA molecules in hydrogels, the effect of the light transmission during polymerization was not further analyzed. Future studies will include a more detailed understanding on the impact of the transmission of UV light during polymerization and the related stretching of DNA molecules.

5.2.5. Variation of the DNA concentration in and the volume of the applied drops

The global and local concentration of DNA strands in the hydrogel and the imaged plane plays a major role for the suitability of the produced fluorescence microscopy images for further analysis. Therefore, the DNA concentration in the applied drop and its volume represent two key parameters that must be controlled. The variation series regarding the DNA concentration were carried out with unlabeled T7 phage DNA. Three different mass concentrations of DNA were tested. A solution of unlabeled T7 phage DNA (1ng μL^{-1}) and YOYO-1® (1.53 µmol L^{-1}) in 1x TE buffer was incubated at 37 °C for 16 h. The solution was subsequently diluted in water to i) 5 pg μL^{-1}, ii) 25 pg μL^{-1} and iii) 50 pg μL^{-1}. Representative fluorescence microscopy images for the three different concentrations are depicted in Fig. 5-5. The sample with a concentration of 5 pg μL^{-1} results in no observable stretched DNA strands. The bright dots can be interpreted as coiled DNA strands. Those strands are not suitable for further analysis in optical mapping.

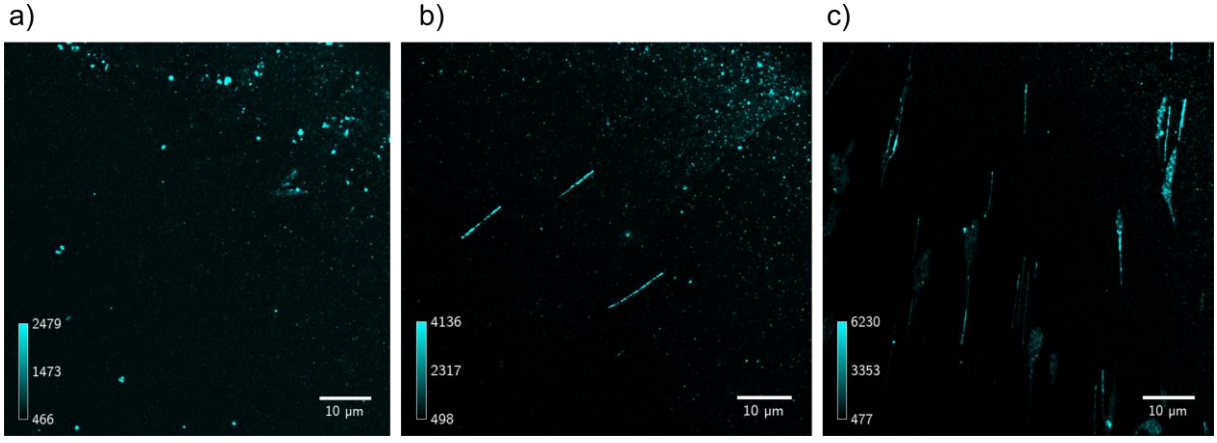

Fig. 5-5: Fluorescence microscopy images in the intercalation channel of T7 phage DNA strands stretched in hydrogels. The DNA concentration in the applied drops is 5 pg μL^{-1} (a), 25 pg μL^{-1} (b) and 50 pg μL^{-1} (c). The strands were intercalated with YOYO-1®.

At concentrations of 25 pg μL^{-1}, several non-overlaying, individual DNA strands can be identified. The problematic aspect of these images lies in the high signal of the background that does not originate from DNA strands but from other sources. The most promising results are obtained for the sample with a concentration of 50 pg μL^{-1}. Many stretched individual strands can be observed while there appears to be much less signal in the background. The DNA strands are well distinguishable enabling further analysis of the length statistics and intensity profiles in case of labeled DNA. In all subsequent experiments, a DNA concentration of 50 pg μL^{-1} was chosen. For the background signal different origins seem possible. Since the fluorescence intensity of YOYO-1® increases multiple orders of magnitude when it is intercalated to DNA, free YOYO-1® molecules are very unlikely to be the origin of the background signal. It is more likely that the YOYO-1® molecules are intercalated in small DNA fragments or that the YOYO-1® fluorescence is also enhanced by an interaction with components from the hydrogel matrix itself. Since the increase in fluorescence within the DNA molecules is based on intercalation and therefore stacking, the photo initiator with its aromatic system may also affect the fluorescence of YOYO-1®. However, the influence of the polymer network on the fluorescence of YOYO-1® was not examined. Drops of different volumes were also applied with unlabeled T7 phage DNA. The 1 µL and 10 µL volumes are compared to each other. Representative fluorescence microscopy images are depicted in Fig. 5-6. For a drop volume of 1 no individual DNA strands were visible. All observable strands overlay with other strands and form longer lines or grafted structures. This makes the assignment of labels to defined strands impossible and therefore those images are not suitable for further analysis. The reason for the clustered appearance of DNA for a small drop volume may be the limited distance that the strands are able to cover: The smaller the drop, which acts as a liquid reservoir, the shorter the time in which a flow induced by evaporation occurs and subsequently the shorter the distance the strands can cover. For a drop volume of 10 µL the DNA strands are distributed in a way, that individual strands are observable. All strands are stretched and within one image they are oriented in the same direction. The background displays no disturbing signal. The strands are perfectly suitable for further analysis since all labels would be assignable to the corresponding strand. For following variations including labeled DNA a drop volume of 10 µL is chosen.

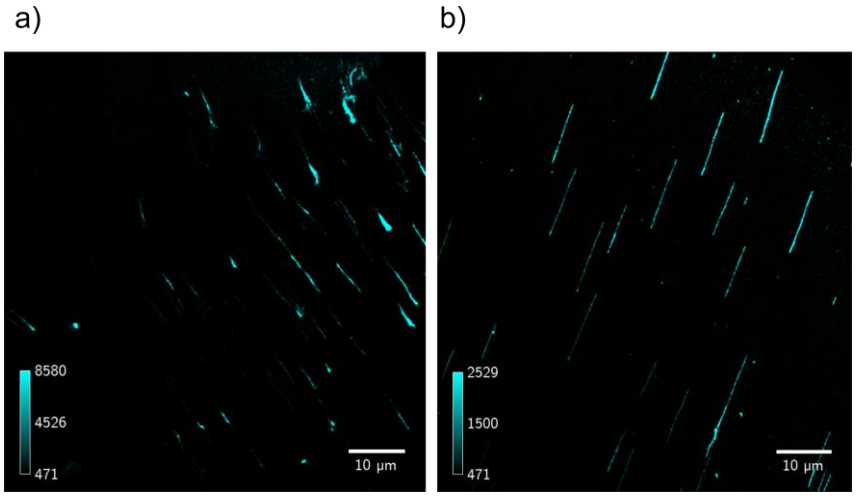

Fig. 5-6: Fluorescence microscopy images in the intercalation channel of T7 phage DNA strands stretched in hydrogels. The volume of the DNA containing drop is a) 1 µL or b) 10 µL. The strands were intercalated with YOYO-1®.

5.2.6. Variation of the drying approach

The most important step for the presented DNA-stretching approach consists of evaporating the solvent from the hydrogel which induces a flow due to evaporation. The speed of evaporation depends on temperature as well as on pressure. In all previous experiments the drying was achieved by heating the hydrogel for 1 h. The exact procedures can be found in section 7.3.5. In this section the application of vacuum to the incubated substrate is compared to the control experiment with thermal treatment. After the placement of the DNA droplet, the substrates were placed in a desiccator and vacuum was applied to the system for 1 h. One representative fluorescence microscopy image for each of the two drying approaches is depicted in Fig. 5-7. After drying at reduced pressure, no stretched DNA strands are observable. The spots that probably consist of or at least contain DNA molecules are either dot-shaped or broad coil structures. Since the shape of the DNA differs from the previously observed stretched or non-stretched strands, drying of the hydrogel by evacuation does not seem to be suitable for DNA stretching. The control experiment with thermally treated hydrogels results in images including stretched DNA strands. For all following experiments the reduced pressure method is neglected, and thermal treatment is applied.

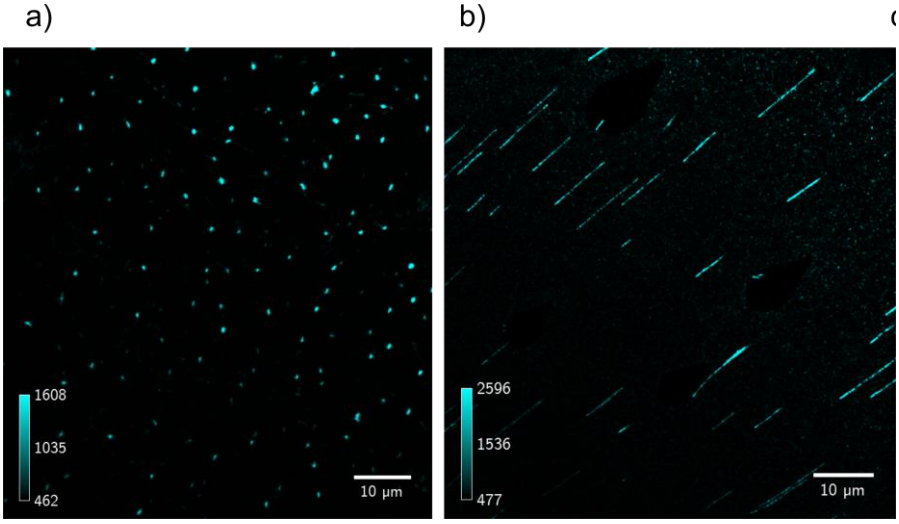

Fig. 5-7: Fluorescence microscopy images in the intercalation channel of T7 phage DNA strands stretched in hydrogels. (a) depicts a hydrogel dried by evacuation, (b) depicts a thermal treated hydrogel. The strands were intercalated with YOYO-1®.

5.2.7. Variation of the label density

For the analysis of the genetic information provided by the strands the DNA has to be labeled with a fluorophore as described in section 2.5.3. The density of the labels, i.e. the amount of labels relative to the amount of bp, can be controlled by the choice of the labeling enzyme. The density for randomly distributed bp can be estimated to one label for every 4N bp, where N is the number of bp in the recognition sequence of the MTase. But since every MTase has its own specific sequence and the DNA strands are not made of randomly arranged bp, the exact label density may differ. The label density is important for the evaluation as it determines whether it is possible to resolve the labels conventional optical microscopy or not. This is feasible only when the distance between two labels is above the diffraction limit of the microscope. In case of a shorter distance an alternative lies in recording an intensity profile along each strand and comparing it to an expected, calculated prole. We compared two labeling enzymes: M.TaqI with the recognition sequence TCGA which results in 111 labels for T7 phage DNA with 39937 bp.(Dunn, Studier et al. 1983) and M.BseCI modifies the 3 positions with the recognition sequence ATCGAT. This enzyme labels with a sufficiently large distance to enable the observation of the exact positions using conventional fluorescence microscopy. For M.TaqI modified T7 phage DNA, the distance between most labels is too small and an analysis by comparison of intensity profiles is expected to be the only option.

T7 phage DNA (50.0 ng µL-1) was mixed with a) M.TaqI (1.00 eq. per TCGA, 0.213 µM) or with b) M.BseCI (20.0 eq. per ATCGAT, 0.115 µM) and AdoYnTAMRA (10 µM) in 1x NEB4 buffer or 1x BseCI buffer, respectively. The M.TaqI containing mixture was incubated at 65 °C for 1 h and the M.BseCI containing mixture was incubated at 55 °C for 1 h. Fig. 5-8 depicts an example of overlaid fluorescence microscopy images of T7 phage DNA labeled by M.TaqI and M.BseCI. The image for the M.TaqI labeled DNA illustrates that all labels can be clearly assigned to their related strands. Within one strand, the signals of many labels seem to overlay. Thus, individual positions of the labels cannot be obtained. However, the resulting image is suitable for a comparison of the measured intensity profiles with calculated ones. This approach is followed in the next sections.

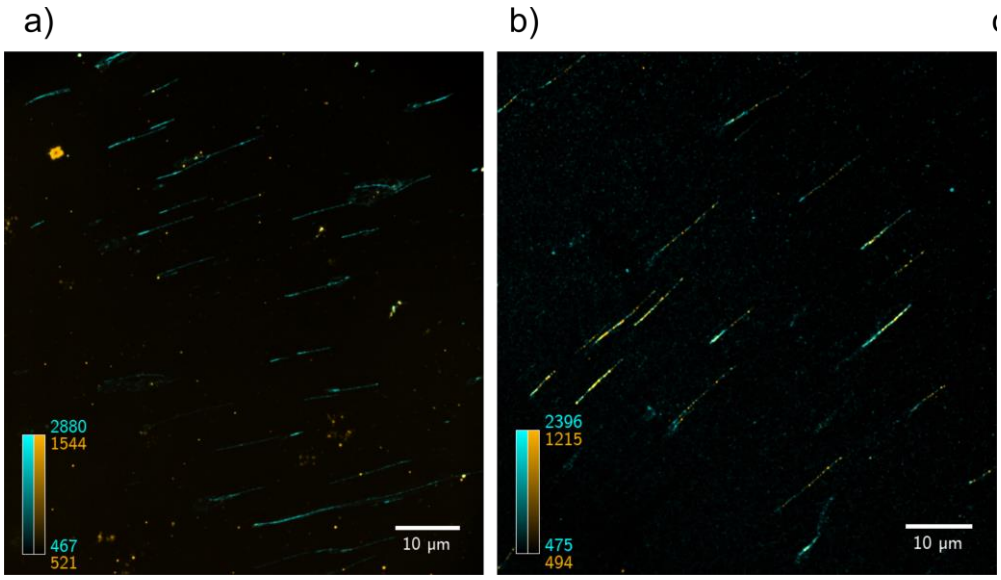

Fig. 5-8: Overlaid fluorescence microscopy images of T7 phage DNA strands stretched in hydrogels. The strands were intercalated with YOYO-1® and labeled with AdoYn-TAMRA by a) M.BseCI and b) M.TaqI, respectively.

The overlaid image of the DNA labeled with M.BseCI depicts well distinguishable strands. While some of the labels seem to be well assignable to the corresponding strands, there are also many labels that are not assignable and are located in areas without strands. This may be due to cofactor molecules that remain even after the APP. Since the ratio of excess fluorophores to covalently bound labels is much higher than for the high density labeled DNA, the wrong assignment of free fluorophores to strands due to local proximity carries much more weight. A quantitative analysis is only feasible, if this error is prevented by reducing the free fluorophores in the hydrogel. In the presented work, the analysis of the strands will be carried out comparing intensity profiles and not by the evaluation of individual label positions.

5.2.8. Variation of the staining concentration

The evaluation of the intensity profiles requires a uniform stretching ratio along each strand to ensure reliable results. Since YOYO-1® intercalates between the nucleobases of the DNA strands, it affects the stretching ratio. A problem might occur if there is not enough YOYO-1® present to fill the entire strand as the fluorophore molecules prefer some specific nucleobase arrangements over others.(Rye, Yue et al. 1992, Hirons, Fawcett et al. 1994) When the intercalator does not cover the entire strand, some parts including many of the preferred arrangements are more overstretched than other parts. This stretching ratio inhomogeneity has to be prevented. To gain an insight on the needed staining concentration, three different YOYO-1® concentrations were tested. The concentrations translate to the ratios of YOYO-1® to the number of bp, being: a) 0.02 bp^{-1}, b) 0.1 bp^{-1} and c) 1.0 bp^{-1}. In the case of the highest concentration there is one equivalent of YOYO-1® for each bp in the solution. A solution of unlabeled T7 phage DNA (2.5 ng μL^{-1}) and YOYO-1® (1.91 µL) in 1x TE buffer was incubated at 37 °C for 16 h. The three YOYO-1® solutions had the following concentrations: a) 20 µM, b) 2 µM and c) 0.4 µM. The solution was subsequently diluted in water and the system was incubated at 50 °C for 1 h before imaging on a spinning disk confocal microscope. YOYO-1® was imaged with a 488 nm laser.

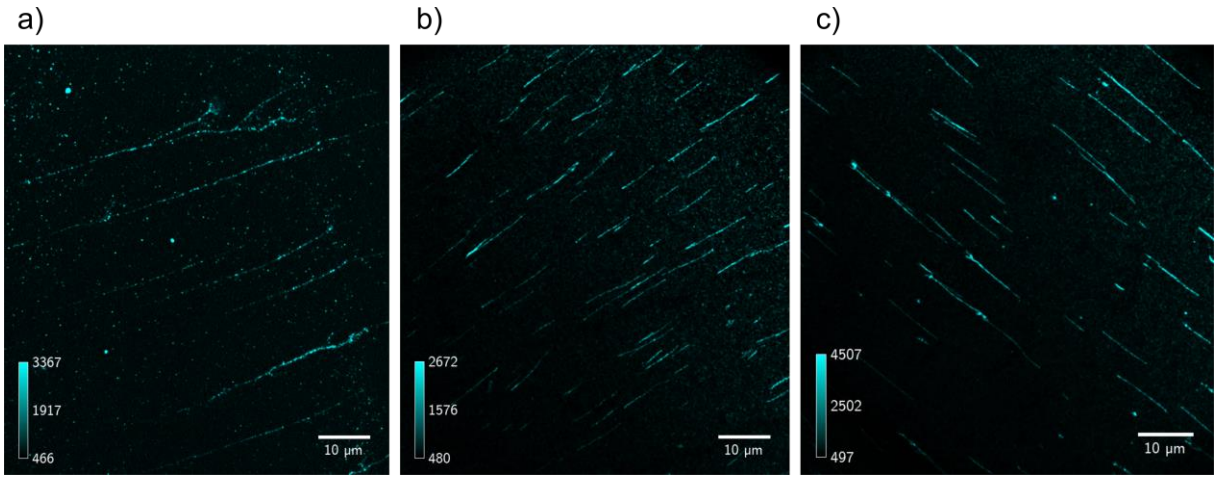

Fig. 5-9: Fluorescence microscopy images in the intercalation channel of T7 phage DNA strands stretched in hydrogels. The strands were intercalated with YOYO-1® in different concentrations being (a) 0.02 bp^{-1}, (b) 0.1 bp^{-1} and (c) 1.0 bp^{-1}.

The measured fluorescence microscopy images visualizing the investigated staining concentration are depicted in Fig. 5-9. At a concentration of 0.02 bp^{-1} clear gaps between highly intercalated parts of the DNA strands can be observed.

At a concentration of 0.1 bp^{-1} the gaps become less distinct, but still observable. Only for a concentration of 1.0 bp-1, the strands seem to be homogeneously intercalated by YOYO-1® as they only appear sparsely. In this case a homogeneous stretching ratio distribution is expected. Since this behavior is favored, the following experiments were carried out with a staining concentration of 1.0 bp-1.

5.2.9. Increase of the hydrogel diameter

The expected mechanism of the stretching process is based on a pulling effect on the DNA molecules in the gel. The radial pull on the DNA is expected to origin from the evaporation of the solvent out of the hydrogel through the hydrogel surface. This leads to the assumption that an increased surface area may result in more evaporated solvent per time and therefore a stronger pulling effect. Following this idea, the stretching ratio, shape and orientation should be improved. To examine the effect of the hydrogel surface on the stretching behavior, the hydrogel diameter was increased from previously used 10 mm to 22 mm. This corresponds to a 384% increase of the surface area. The remaining parameters were chosen according to the optimized ones from the previous variation series, see Table 5-1. The resulting fluorescence images are depicted in Fig. 5-10.

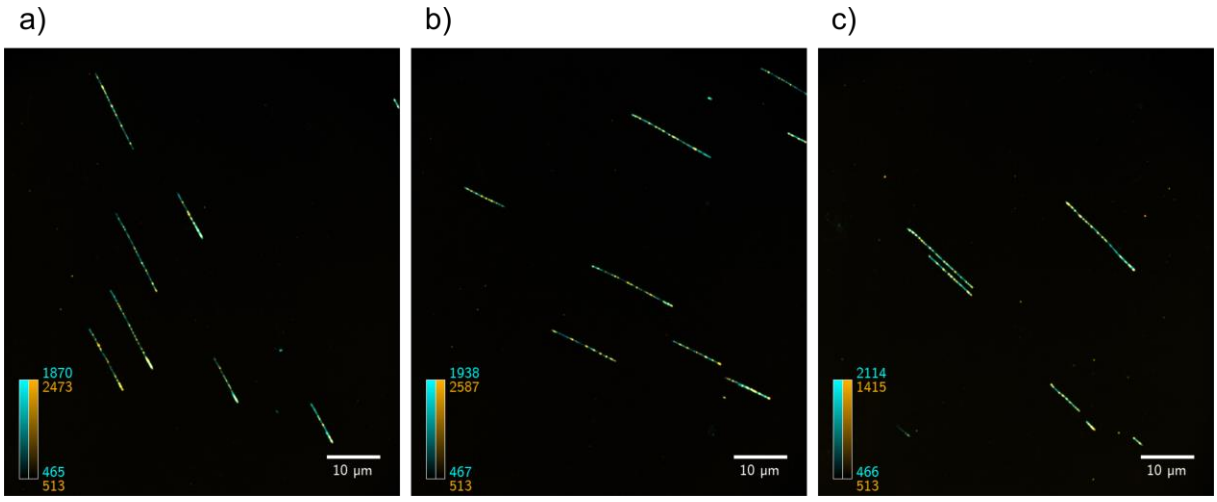

Fig. 5-10: Overlaid fluorescence microscopy images of T7 phage DNA strands stretched in hydrogels with a diameter of 22 mm. The strands were intercalated with YOYO-1® and labeled with AdoYnTAMRA by M.TaqI.

Fig. 5-10 shows three overlaid exemplary fluorescence microscopy images. For all of the images stretching of the DNA strands was obtained. Such a quality of the stretching was not found in any previous experiment.

All strands are shaped in perfectly straight lines while having the same directional orientation. The labels are located on top of the lines and are well assignable to the relating strand. Only very few signals of the fluorophores are situated between the strands. These images are perfectly suitable for further analysis.

5.2.10. Summarized optimal parameters for DNA stretching

With the increase of the hydrogel diameter from 10 to 22 mm the final step – towards evaluable DNA molecules for optical DNA mapping – is performed. The DNA strands are linearly stretched and follow a uniform orientation. The AdoYnTAMRA labels are clearly assignable to the relating strands and only few signals are observed in the background. The summarized experimental condition to acquire the desired stretching quality are listed in Table 5-1.

Table 5-1: Optimized experimental parameters for DNA stretching in pNIPAM hydrogels.

Parameter	Optimization result
purification method	APP
hydrogel thickness	38 µm
DNA concentration in applied drop	50 pg μL^{-1}
volume of applied drop	10 µL
drying method	Thermal treatment
label density	111 $(39937\ bp)^{-1}$ (by M.TaqI)
hydrogel diameter	22 mm

5.2.11. Analysis of the key results

The optimized parameters enabling optical mapping, were obtained with the parameters shown in section 5.2.10. A total of 22 overlaid images provide the foundation for further analysis which is performed automatically by a python program which was developed in this work. Detailed information on the analysis software can be found in the appendix of this chapter (see section 8.3.1).

Besides the image processing the python script includes the pattern recognition algorithm for DNA strands, the evaluation of the strand length distribution and the comparison of measured intensity profiles to a calculated profile which is based on the expected label positions. Each of these steps is covered in one of the following sections.

5.2.12. Recognition of DNA strands

The pattern recognition algorithm was used to analyze 22 overlaid fluorescence microscopy images containing individual DNA strands. For each image, the algorithm finds the strands, assigns an ID to each strand and frames it. The exact procedure is described in section 8.3.1. The strand analysis of the previous results shown in Fig. 5-10 (section 5.2.9), are depicted in Fig. 5-11.

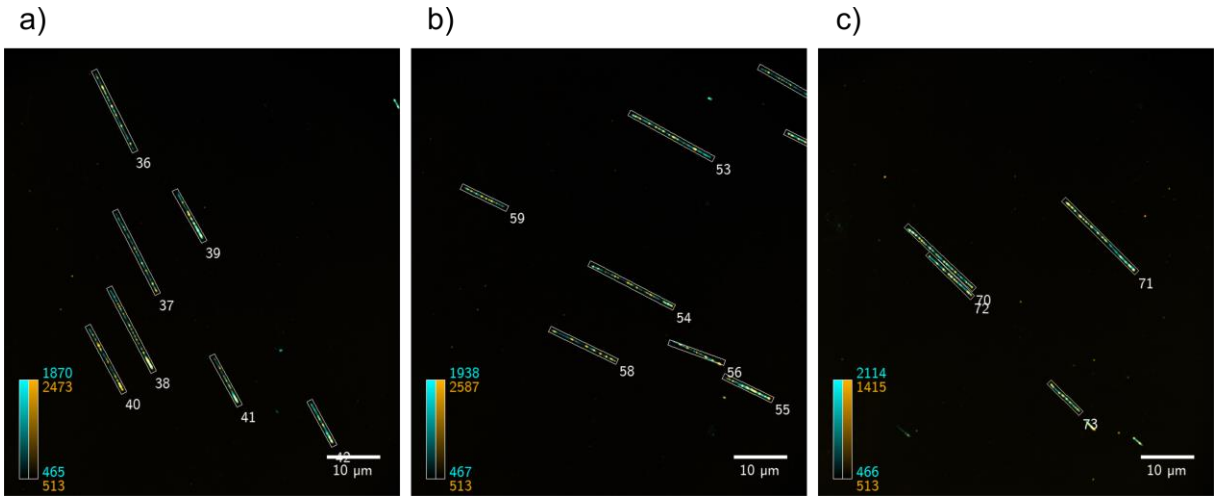

Fig. 5-11: Overlaid fluorescence microscopy images of T7 phage DNA strands stretched in hydrogels with a diameter of 22 mm. The strands were intercalated with YOYO-1® and labeled with AdoYnTAMRA by M.TaqI. An ID is assigned to each strand.

The DNA strands are recognized and highlighted with a frame. In all 22 analyzed images 105 intact strands with a minimum length of 2 µm were recognized. This does not include overlapping strands or strands that exceed the borders of the image.

5.2.13. DNA strand length distribution

The expected length of T7 phage DNA can be calculated by multiplying the number of base pairs (39937 bp (Dunn, Studier et al. 1983)) with the distance between two base pairs in the natural B-form (0.34 nm (Watson and Crick 1953)). Assuming the DNA to be stretched but not overstretched, i.e. the stretching ratio is 1.0, each strand has a calculated length of 13.6 µm. The 105 recognized strands are used for the analysis of the strand length statistics. The measured lengths of all those strands are illustrated in a histogram in Fig. 5-12.

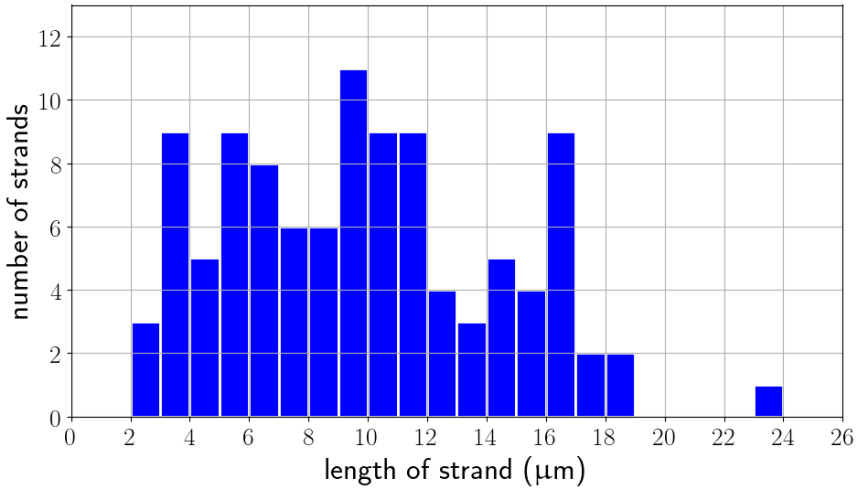

Fig. 5-12: Distribution of strand DNA strand lengths measured in the 22 mm hydrogel plotted as a histogram with 1 µm bins.

The expected length of 13.6 µm lays in the bin from 13 to 14 µm, which is a relative minimum in the histogram. This minimum divides the distribution into a part with 81 strands shorter than 13.6 µm and another part with 24 strands longer than 13.6 µm. There are two main reasons for strands appearing shorter than expected in the images. The first one can be explained by the strands not being entire T7 phage DNA strands but rather fragments of it. The fragmentation may be due to shear forces that are present during the preparation, e.g. while pipetting. In addition, shear forces in the hydrogel due to the evaporation force could be another possibility. The second reason lies in the ends of the strands folding back and overlaying themselves. This is observable in Fig. 5-13, where the contrast of the example image is adjusted only linearly with the result of overlaying ends being observable. All strands have the folded back ends on the same side. They all point towards the radial center of stretching.

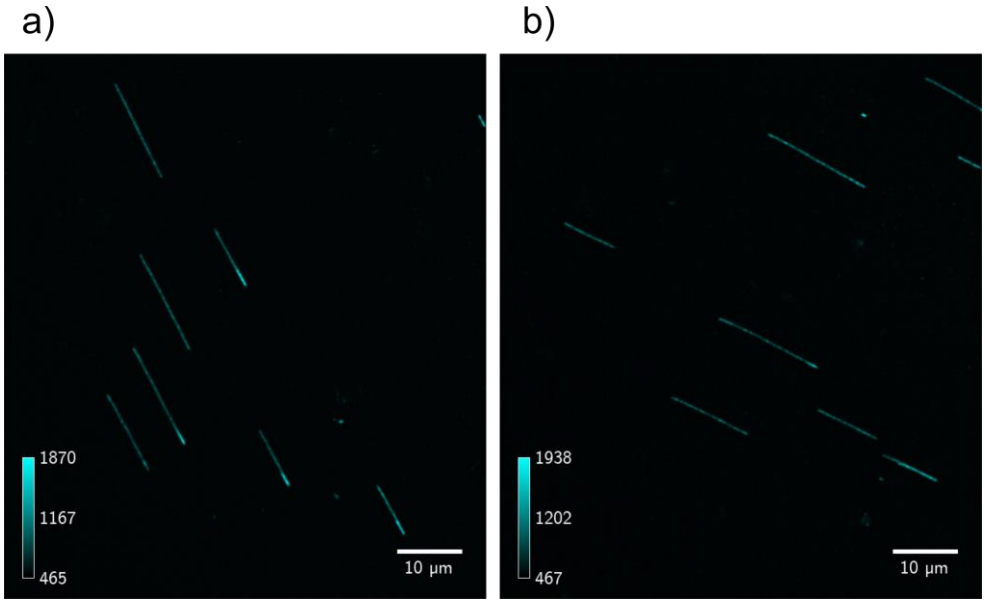

Fig. 5-13: Fluorescence microscopy images in the intercalation channel of T7 phage DNA strands stretched in 22 mm hydrogels. The strands were intercalated with YOYO-1®. The contrast is adjusted linearly. Folded back ends appear brighter than non-overlapped strands. The radial center of stretching is located at the bottom right outside of the images.

The DNA strands longer than 13.6 µm are assumed to be complete or nearly complete and not folded back. The reason for the strands being longer than expected lies in the overstretching. A stretching ratio greater than 1.0 may be due to widening of the DNA by intercalation of YOYO-1® (Wu, Jeffet et al. 2018) or due to overstretching by the pulling forces that affect the strands in the hydrogel. Since the totality of the strands is not known, the stretching ratio cannot be estimated from the strand length distribution in a reasonable manner. Nonetheless, the stretching ratio can be determined by the analysis of the labels and their intensity profiles along the strands.

5.2.14. Intensity profiles and fitting

For the analysis of the intensity profiles the 24 strands with a length above 13.6 µm were chosen. The intensity profiles were obtained as described in section 8.3.1. They are compared to their respective theoretical profile that is calculated from the expected label positions by adding Gaussians with a variable height and width which are located at the position of the label (figure S.I. 8-38, section 8.3.1). All of the measured profiles are compared to the theoretical prole by fitting it to the data.

The fitting parameters are the intensity I_0 and standard deviation σ of each Gaussian, the stretching ratio r_s and the displacement of the starting point x_0 of the strand. An example fit for the profile of strand 36 in Fig. 5-11 is depicted in S.I. 8-40 in the appendix of this chapter. There are two main criteria for a fit to be accepted as reasonable. First, the Gaussian shape is surveyed. If the standard deviation of the Gaussian exceeds a value of 0.2, then the fit does not mirror the real optics. Second, for positions with very low intensities in the calculated profile a relatively high signal in the data is not explicable. In both cases the fits are discarded. Under these conditions 16 out of 24 fits produce reasonable parameters. The stretching ratio is averaged over all fits and a value of 1.28 ± 0.05 is obtained. The stretching ratio of 1.28 indicates an overstretching of the strand by 28% compared to the expected length of B-DNA. In order to explain the overstretching two reasons seem conceivable. First, the overstretching may be due to the evaporation pull that is also responsible for the linearization of the DNA strands. A higher pulling force could result in a higher stretching ratio. However, a second explanation might be the intercalation of YOYO-1® between the bases which widens the strands. In general, a higher stretching ratio is favored as it increases the distance between two covalently bound fluorophores. Therefore, the signals of the fluorophores can be better distinguished from each other and the resolution with respect to the labels is enhanced. A stretching ratio of 1.28 lays between the non-overstretched B-DNA with a stretching ratio of 1.0 and the overstretching commonly observed for combing methods which ranges up to 1.7. (Wu, Jeffet et al. 2018) The low standard deviation of only 0.05 indicates that the different strands are stretched uniformly. It suggests that the pull force affecting the DNA is similar throughout all the regions of the hydrogel which contain stretched DNA. This indicates a high comparability and a high controllability of the stretching process. These are key factors for the reproducible parallelizability of the analysis. Nonetheless, the low standard deviation is not to be mistaken as evidence for a uniform stretching ratio within each strand. This has to be evaluated with other methods like a DNA ruler which has equidistant labels located on the strand like Wu et al. (Wu, Jeffet et al. 2018) used in their work. For this type of strand, the distances and stretching ratios between two adjacent labels can be obtained. This results in local stretching ratios for small enough but resolvable distances. The investigations of the local stretching ratio with DNA ruler molecules may be conducted in further studies.

5.3. Conclusion and outlook

This presented investigations on a new DNA stretching method for optical DNA mapping result from a successful cooperation between the Wöll-laboratory and the Weinhold-laboratory at RWTH Aachen University. The findings were published in form of a patent application that is under revision since July 2019. Technical stretching of DNA molecules is crucial when it comes to the analysis of genetic structural variations or epigenetic information. In both cases, methods like optical mapping allow to encode this information and elucidate severe diseases like FSHM or cancer. The idea of stretching DNA molecules in thermo-responsive hydrogels is driven by the necessity of facilitating cost-intensive and experimentally challenging state of the art methods like DNA combing or nano channel technologies. The main goal of optimizing and automating the entire DNA stretching process was successful. The presented experimental parameters result in homogenously linearized DNA strands containing sequence-specific labels that can be visualized using standard fluorescence microscope. The automated analysis in form of a python program allows for the recognition of single DNA strands and the subsequent in-line evaluation of the intensity profiles of the labeled strands. In a first step, the experimental parameters concerning the DNA solution, hydrogel properties and drying method were analyzed. The suitability of the APP for the removal of excess labeling fluorophores was verified. In addition, T7 phage DNA was labeled with the fluorescent cofactor AdoYnTAMRA with the alkyl transferring enzyme M.TaqI. This enzyme provided a better ratio of label-fluorophores to excess-fluorophores compared to M.BseCI. The intercalating reagent YOYO-1® was used to stain the entire DNA strands and its ratio was varied resulting in an optimal value of 1.0 bp^{-1}. Furthermore, the DNA concentration and the volume of the drop of DNA solution applied to the hydrogel were optimized to 50 pg μL^{-1} and 10 µL, respectively. For the hydrogel thickness 38 µm proved to be the optimum value. Finally, the increase in the hydrogel diameter from 10 to 22 mm improved the quality of DNA strand linearization in a way, that enabled further image analysis. The results obtained with these parameters seem to compete with known methods like DNA combing or nanochannel approaches and they fuel expectations for future bio-medical application. For this purpose, a Python program in several parts was developed. It covers the image processing from the multi-frame raw data acquired with fluorescence microscopy to colored images with adjusted contrast. It combines the data obtained from two different wavelength channels that image either the entire strands or

selectively the labels. After the image processing part, the data analysis starts with the pattern recognition. Here, an algorithm was developed, that finds all linearized strands in the images. The length of these strands is obtained as well as the label intensities along each strand. The lengths serve in a statistical manner, whereas the intensity profiles are used for further analysis. Both, strand length and intensity profile are compared to a theoretical profile that is calculated from the known nucleobase sequence of T7 phage DNA. In a fitting procedure the accordance is probed and for matching strands the overstretching, quantified by the stretching ratio is evaluated. A stretching ratio of 1.28±0.05 was determined as an average over 16 analyzed intensity profiles. This ratio emphasizes the high potential of the method. On the one hand, the strands are slightly overstretched, which simplifies the differentiation between single labels that overlay each other due to a distance lower than the Abbe diffraction limit. On the other hand, the low standard deviation highlights the high homogeneity of stretching throughout the hydrogel. This promotes the reproducibility and comparability of the results obtained by the investigated DNA stretching methods. Future works will build on the achieved results. Different monomers, even those forming non-thermo-responsive hydrogels, may be tested. To enable high throughput for the investigations, the automation should be further promoted. Beside the analysis, the measurement may be automated as well. This can be realized by a program that controls the piezo table of the microscope, the microscope focus, the laser and the capturing settings. In this way, the samples could be scanned entirely without any bias by the researcher in little time. Another great improvement would consist of the determination of exact label positions instead of intensity profiles. It would open new possibilities for the comparison between observed label barcodes and databases of known DNA sequences from viruses, bacteria, plants, animals and even human beings. In order to enable the determination of label positions maintaining high label densities, the implementation of super-resolution fluorescence microscopy to the examined system is necessary. Challenges lie in the dried state of the hydrogel after immobilization of the DNA, which is compatible with only few super-resolution techniques. The development of a working system would represent a milestone in further studies. In order to estimate the limitations of the presented method, human DNA has to be tested. Thereby it is important to ensure that the DNA molecules stay intact and do not break during preparation (e.g. pipetting). The possibility to analyze genomic DNA with fragments of several 100 kbp would define a new breaking point in DNA stretching. Once it is possible to analyze genomic DNA, it will be important to compare the obtained experimental data with medical, genomic databases. This will allow preliminary studies on e.g. DNA probes with well reported genetic diseases like FSHD. All in all, this work provides the starting point for the development of a new DNA stretching technique. Suitable experimental

parameters were found and a program for automated analysis was developed. Based on these findings, the technique can be improved in further studies.

The investigations shall include the screening of further parameters, the advancement of automation, the introduction of super-resolution fluorescence microscopy and the usage of longer genomic DNA from human beings. The development of the presented DNA stretching technique is a step towards possible medical applications in diagnosis of diseases that are based on genetics like FSHD or that are accompanied by epigenetic changes like some types of cancer.

6. Summary and outlook

The presented results in this dissertation were obtained within the framework of the CRC 985 for functional µGs and µG systems. In a first project within the CRC; the deformation behavior of pNIPMAM µGs was investigated upon the surface hydrophilicity. The deformation at the solid-liquid interface was observed by means of dSTORM as a 3D super-resolution fluorescence microscopy technique. The obtained results revealed that the native, spherical µG shape is retained in the case of a hydrophilic (PEG) surface, whereas the so-called fried-egg conformation is observed at hydrophobic surfaces. The obtained results were supported by computer-simulations conducted by the cooperation partners within the CRC. It was deduced, that the reason for the low contact area of the µG at a hydrophilic surface is due to the fact this surface mimics a solvent-like system and therefore prevents strong interactions at the interface. Although the conducted DPD simulations and the experimental analysis provide consistent results, it was found that the comparison between the results could only be done visually, by eye. Therefore, a parametrization approach was introduced that allows for the comparison of the µG shape regardless of the acquisition method of the data. This approach fits a sphere cap around the 3D point cloud data, approximating the shape of the µG on the surface. Subsequently, the ratio of the volume of the fitted sphere cap to the volume of the hole fitted sphere is taken, which results in a scalar between zero and one. In addition to the analysis of the deformation behavior of µGs on surfaces of different hydrophilicity, the deformation was also analyzed according to the preparation methods. Therefore, the common laboratory techniques spin-coating, drop-casting and adsorption from solution were compared and evaluated. It was found that the effect of solvent evaporation plays a significant role in the final conformation of the µG at the solid interface. As the state of the art analysis software for 3D microscopy data is mainly targeted for biomedical applications, the analysis of µG data was found to be time-consuming and bound to a low-quality output. Therefore, a new Mathematica based image analysis software was developed which allows for the analysis of µG data in form of images or videos. The new software is published as an open source software for the community allowing for e.g. rotating videos, density build-ups or image slicing through the gel.

In a second project, a new method for the targeted surface immobilization of µGs onto surface patterns was developed within the SFB. A combination of c-EBL and photolithography was carried out in cooperation with the project partners from the field of inorganic chemistry. A seven-step process depicted in Scheme 4-1 involves the production of a SAM, the c-EBL process, the protection and deprotection of the pattern as well as the incorporation of a linker and finally the immobilization and subsequent hybridization steps. The experimental routine starting from the preparation of the glass substrate to the hybridized system takes exactly one week. Because of the time-intense sample preparation it was decided to branch the general project into two parts which should be combined in future work. The hybridization of DNA-functionalized µGs to a surface pattern with immobilized sDNA at the single spots was therefore conducted without the photolithographic steps. It was shown that DNA-functionalized µGs can be hybridized to immobilized strands by hybridization. All in all, the two main results show that the combined lithographic approach, as well as the hybridization experiments do work separately. One of the important next steps will consist of reuniting the two sub-projects back together. The combination of both results would allow for the possibility to address single spots individually. Another important step includes the reduction of the spot-size to investigate the limitations of this approach. It would furthermore be interesting to perform super-resolution fluorescence microscopy measurements in order to verify that the spherical shape of the µGs is indeed being maintained, as predicted according to the findings in chapter 3. The immobilized µGs are more than half the radius and thus one eights of the volume of the µGs that were investigated in the previous chapter. It could, therefore, be possible that the number of localizations resulting from the dSTORM experiments will turn out to be rather low. Potentially, DNA-PAINT could in this case result in better quality images.

The presented research on biohybrid polymer systems gave rise to a cooperation with the organic chemistry department. A new method was developed, allowing for the stretching of DNA molecules in thermo-responsive hydrogels. The characteristic DNA barcode can then be analyzed using fluorescence techniques, further allowing the investigation of (epi-)genetic information that can cause structural variations or diseases like cancer. The newly developed method was registered in form of a patent which is pending at the moment of the submission of this dissertation. As part of the cooperation, a Python-bases image analysis software was developed to automatically identify the linearized DNA strands using a pattern recognition algorithm. Furthermore, the automated analysis of the intensity profiles of the characteristic DNA-barcode gives rise to applications in the biomedical field.

Future work will build on the achieved results. Different monomers, even those forming non thermo-responsive hydrogels, may be tested. Another great improvement would consist of the determination of exact label positions instead of intensity profiles.

It would open new possibilities for the comparison between observed label barcodes and databases of known DNA sequences from viruses, bacteria, plants, animals and even human beings. In order to enable the determination of label positions maintaining high label densities, the implementation of super-resolution fluorescence microscopy to the examined system is necessary. In order to estimate the limitations of the presented method, human DNA has to be tested. Thereby it is important to ensure that the DNA molecules stay intact. The possibility to analyze genomic DNA with fragments of several 100 kbp would define a new breaking point in DNA stretching. Once it is possible to analyze genomic DNA, it will be important to compare the obtained experimental data with medical, genomic databases. This will allow preliminary studies on e.g. DNA probes with well reported genetic diseases like FSHD. The different projects presented in this dissertation clearly show that the field of crosslinked polymers at the solid-liquid is of great importance in different communities. The fundamental finding on the spreading behavior of µGs could e.g. directly be implemented in the new lithographic approach to immobilize µGs at a surface pattern. Furthermore, biomedical applications like new method to stretch DNA-molecules in thermo-responsive hydrogels, would not be possible without the fundamental insights gained from the other projects concerning the surface modification and the polymeric behavior at the solid support. Furthermore, fluorescence microscopy techniques were used throughout all the presented projects in the different chapters. Even though it is a straight-forward technique providing structural information, it was shown that the automation of data analysis is of growing importance. Therefore, it is important for future work to combine modern imaging techniques with state-of-the-art image processing methods. The new step of incorporating modern image analysis will give rise to fundamentally new insights and applications in the field of 3D analysis of experimental data.

7. Methods and experimental

This chapter includes methods and experimental information associated to the chapters 3, 4 and 5. The experimental procedures belonging to chapter 3, µGs at the solid interface, are described in section 7.1. The relevant experimental parts for chapter 4, lithographic approach to immobilize µGs at the solid support, are depicted in chapter 7.2. Finally, the information corresponding to chapter 5, immobilization of DNA molecules in hydrogels, are summarized in chapter 7.3. Instruments that were used in all projects are summarized here:

Plasma cleaning

For plasma cleaning, a Zepto system from Diener Electronic was provided by the group of Prof. Dr. Ulrich Simon (Inorganic Chemistry, RWTH Aachen University).

Fluorescence microscopy

TIRF mode: Commercial inverted microscope (Nikon Eclipse Ti-E). Fluorescence was collected with a 100×/1.40 NA oil immersion objective (HP PLAN, Nikon) and imaged on a CMOS camera (Photometrics, PRIME 95B) with 640 nm laser (Toptica iBeam smart 640CD) with a theoretical laser power of 200 mW. For 3D localization, the DH-PSF method described in section 2.1.6 was implemented using a double Helix SPINDLE^{TM} module.

Spinning disk mode: Spinning disk confocal fluorescence microscope VisiScope Confocal-CSUX1 with Nikon Ti and Andor EMCCD camera was used.

Contact angle measurements

For the contact angle measurements, a system provided by the group of Prof. Dr. Ulrich Simon (Inorganic Chemistry, RWTH Aachen University) was used. The setup included an adjustable table, a syringe and a camera. The images were evaluated by the “Drop Analysis – LB-ADSA” plugin (Medical Imaging Group, Swiss Federal Institute of Technology in Lausanne) for ImageJ (National Institutes of Health, USA).

7.1. Experimental section chapter 3

Section 7.1 includes the experimental procedure for the synthesis and functionalization of pNIPMAM µGS used in chapter 3, as well as the detailed procedures for the different surface modifications (7.1.2), contact angle measurements (0) and the preparation of the different deposition methods (7.1.4).

The investigated microgels in chapter 3 where imaged on a commercial inverted microscope (Nikon Eclipse Ti-E). Fluorescence was collected with a 100×/1.40 NA oil immersion objective (HP PLAN, Nikon) and imaged on a CMOS camera (Photometrics, PRIME 95B). To measure the fluorescence microscopy images, a 640 nm laser (Toptica iBeam smart 640CD) with a theoretical laser power of 200 mW and a measured laser power of 60 mW at the objective, which was used at max. 9% of the laser power.

For 3D localization, the DH-PSF method described in section 2.1.6 was implemented using a double Helix SPINDLE^{TM} module

7.1.1. Synthesis and functionalization of the pNIPMAM microgels

The synthesis of the pNIPMAM µGs was carried out in ultrapure (ELGA Purelab Plus system from ELGA LabWater). The used chemicals were purchase from commercial source without further purification.The µGs were synthesized via a modified precipitation polymerization. (Berndt and Richtering 2003)

N,N'-Bis(acryloyl)-cystamine (BAC) was used as the comonomer. (Gaulding, Smith et al. 2012) N-isopropylmethacrylamine (NIPMAM, 5.113 g, 40.2 mmol, Sigma-Aldrich, 99%), BAC (0.163 g, 0.626 mmol ,Alfa Aesar, 98%) and cetrimonium bromide (CTAB, 13 mg, 0.035 mmol, Sigma-Aldrich, ≥96%) were dissolved in H_2O (270 mL). As initiator, V50 (sigma-Aldrich, 99%, 0.164 g, 0.605 mmol in 30 mL H2O) was used. After 45 min under Ar atmosphere, the monomer mixture was heated up to 70 °C and the initiator was added. After 3.5 h the mixture was stirred overnight at room temperature. For purification, the µGs were filtered through glass wool and washed with H_2O (centrifugation, 3 x 25 krpm, 1.5 h). The µGs were characterized via dynamic light scattering (DLS, Zetasizer ZS, Malvern). Their z-averaged 1.6 ±0.2 µm with a polydispersity index (DPI) of ~1. Above the VPTT of 42 °C, the µGs collapsed to 470 ±5 nm with a PDI of 0.04 (see Fig. 7-1)

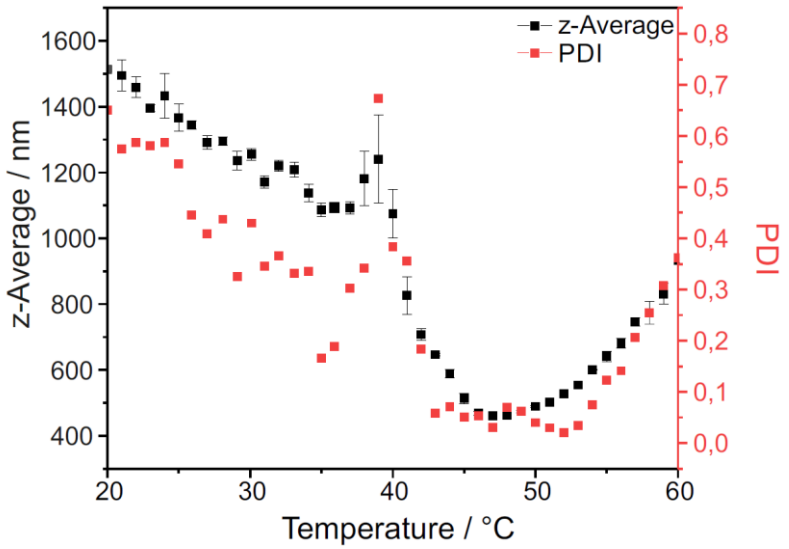

Fig. 7-1: Temperature dependent DLS measurement of the pNIPMAM-µGs in H_2O. The z-average is plotted with its corresponding PDI in dependency of the temperature.This measurement was conducted by Dr. Sabine Eisold who also provided this figure.

7.1.2. Surface modification

FOCTS

The modification with Trichloro(1H,1H,2H,2H-peruorooctyl)silane (FOCTS) was performed by gas phase silanization with 3-Aminopropyltriethoxysilan (APTES) based on a published procedure.(Gilles, Winter et al. 2012) The glass slides were cleaned with acetone (Sigma-Aldrich) and isopropanol (Merck) in an ultrasonic bath for 3 min. Each step was repeated 2 times. The samples were dried in a N_2 stream and activated with O_2 plasma (Pico, electronic Diener Plasma Surface Technology, 200 W, 1.4 mbar, 2 min). The substrates were exposed to the vapor of FOCTS in a glass desiccator (Ar air, 45 mbar, 1.5 h) in a glovebox.

ODS

For the functionalization with ODS, the procedure for silanization with APTES reported by Nath et al. (Nath and Chilkoti 2004) was modified. Prior to the functionalization, the substrates were cleaned by boiling in $NH_3/H_2O_2/H_2O$ (1:1:3, v/v/v), and stored overnight in isopropanol saturated with KOH. The next day substrates were put into a HCl/MeOH (1:1, v/v) mixture for 30 min. After washing with H_2O, the substrates were dried at 60 °C overnight. The silane was dissolved in EtOH (5 vol%) and the glass substrates were dipped in this mixture for 20 min. Afterwards they were washed 2 x with CH_2Cl_2 and 3 x with EtOH and, subsequently, stored at 120 °C overnight.

PEG

The substrates were cleaned and functionalized in the same way as the ODS substrates, but with 2-(4-Chlorosulfonylphenyl)ethyltrimethoxysilane (FOCTS, Acros 50% in CH_2Cl_2). For the preparation of the PEG solution, 1000.33 mg of polyethylene glycol amine (PEG, Sigma-Aldrich, M_W~5000 g mol.1) were dissolved in H_2O (10 mL), and an appropriate amount of Na_2CO_3 in H_2O (30 mL) was added to adjust the pH value to 10-11. The substrates were incubated with this mixture for 90 min. Afterwards they were stored in aqueous HCl (pH 2) for 5 min and washed with H_2O.

7.1.3. Contact angle measurements

The contact angle measurements were performed with a homemade contact angle measurement system. Droplets of 5 L of ultrapure water were used and the images were processed with the plug-in Drop analysis - LB-ADSA for ImageJ. The images are shown in Figure Fig.7-2.

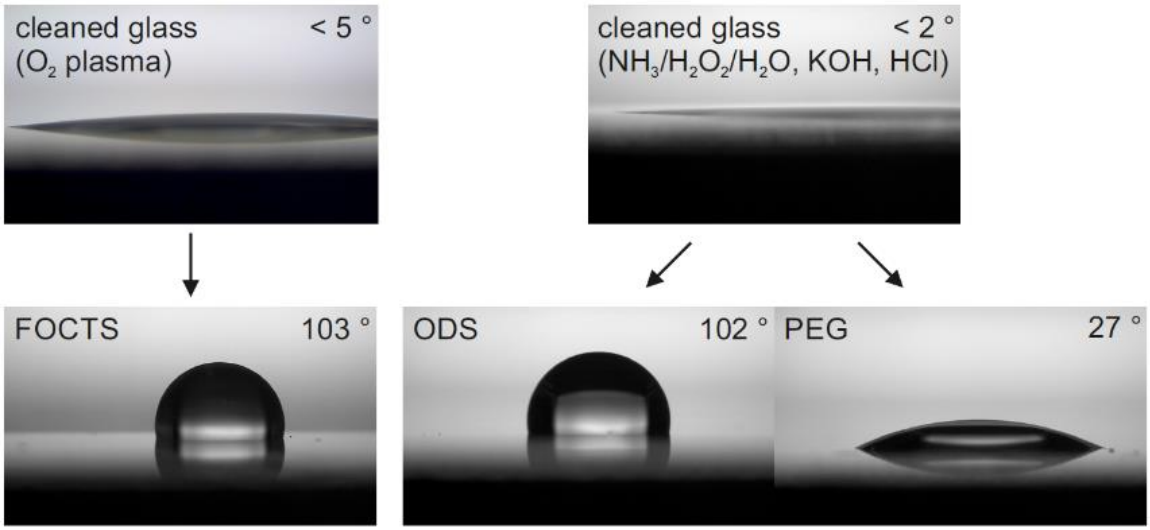

Fig.7-2: Images of 5 µL water droplets on the different surfaces for the determination of the contact angle.

7.1.4. Sample preparation for different deposition methods

For spin-coating, 20 µL of the sample solution were spin-coated (Laurell Technologies Incorporated, Model: WS-650MZ-23NPPB) onto the substrate at 4000 rpm. The sample volume was always applied onto the rotating substrate. In the case of drop-casting, a drop of 2 µL in volume was placed onto the substrate and left to dry for one hour at room temperature. The third investigated deposition method consisted of an adsorption experiment. This means that in contrast to the other two presented methods, the sample is never left to dry and the µGs are always surrounded by solvent. Therefore a droplet of 10 µL in volume was deposited onto the substrate and covered afterwards in order to prevent strong evaporation of the solvent. The adsorption of the µGs to the substrate was observed after 15 minutes of incubation time. This monitored live in the brightfield mode of an optical microscope. The substrate was then washed twice with 1 mL of Milli-Q water. In this case it was crucial to immediately apply the blinking buffer for the 3D d-STORM measurements, in order to guarantee that no drying effects take place at the solid-liquid interface.

7.2. Experimental Section chapter 4

Section 7.2 belongs to the results discussed in section 4 regarding the development of a lithographic process. Therefore, the experimental procedures of the different surface modifications steps are described in sections 7.2.1 to 7.2.7. The final hybridization of the DNA-functionalized µG to the sDNA at the surface is described in section 7.2.8.

The investigated surface reaction in chapter 4 where imaged on a commercial inverted microscope (Nikon Eclipse Ti-E). Fluorescence was collected with a 100×/1.40 NA oil immersion objective (HP PLAN, Nikon) and imaged on a CMOS camera (Photometrics, PRIME 95B). To measure the fluorescence microscopy image, a 640 nm laser (Toptica iBeam smart 640CD) with a theoretical laser power of 200 mW. Surface reactions were always carried out it quasi-TIRF mode.(Whelan and Bell 2015)

7.2.1. Silanization and c-EBL

For the silanization the substrates were first cleaned in 1% hellmanex solution for three days and then washed with ultrapure water and dried under N_2. The substrates were then cleaned in O_2 plasma for 900 s at 100 W. In the next step, the substrates were incubated in 5 % silane solution for 15 minutes and then stored over night at 120 °C. Note that in the case of the homogeneous thiol layer, the silane solution refers to (3-mercapto)-trimethoxysilane in ethanol. In the case of ITO substrates, the silane solution refers to 2-(4-chlorosulfonylbenzene)-trimethoxysilane in ethanol.

The pattern fabrication via c-EBL is performed in the Simon-Lab (Institute of Inorganic Chemistry, RWTH Aachen University). The responsible lab-technician is Birgit Hahn. The c-EBL routine is conducted according to Schaal et al.(Schaal and Simon 2013) The c-EBL experiments were carried out with two different systems from RAITH. First, an Elphy Plus system (software version 4) was used. For a higher positioning accuracy, a precision table (NMT 20 from Klocke Nanotechnik) was used instead of the actual sample stage used.(Schaal and Simon 2013) Additionally, an e-Line system (software version 5 and 6) was used.

7.2.2. Thiol-yne reaction

The thiol-yne reaction was performed on the patterned substrates. The reaction was conducted in absolute ethanol. The NaOH and protecting group concentrations were adjusted to have a 1:1 ratio. All stock solutions have a concentration of 0.1 $molL^{-1}$ in absolute ethanol. For the reaction, the patterned substrates were incubated in a falcon tube or a rolled rim bottle, each filled with 15 mL of the reaction medium. The containers were covered with aluminum foil to protect the systems from UV ligt. The substrates were incubated in a solution of 2-(4-chloro-sulfonylphenyl)ethylsilane (13 mM) and NaOH (10 mM) in ethanol for 1.5 hours. After incubation, the substrates were washed with ethanol, then ultrapure water and afterwards dried with N_2.

7.2.3.Peg-ylation of the background

Prior to the functionalization, the substrates were cleaned by boiling in $NH_3/H_2O_2/H_2O$ (1:1:3, v/v/v), and stored overnight in isopropanol saturated with KOH. The next day, the substrates were put into a HCl/MeOH (1:1, v/v) mixture for 30 min. After washing with H_2O, the substrates were dried at 60 °C overnight. For the preparation of the PEG solution, 1000.33 mg of polyethylene glycol amine (PEG, Sigma-Aldrich, M_W~5000 g mol.1) were dissolved in H_2O (10 mL), and Na_2CO_3 in H_2O (30 mL) was added to adjust the pH value to 10-11. The substrates were incubated with this mixture for 90 min. Afterwards they were stored in aqueous HCl (pH 2) for 5 min and washed with H_2O.

7.2.4. Linker immobilization

The reaction condition for both linker systems i.e. succinimidyl-4-(p-maleimidophenyl)butyrate, SMPB and succimidyl-4-(N-maleimidomethyl)cyclohexane-1-carboxylate, SMCC were performed accordingly. The reagent was diluted to a concentration of 10 mM in dimethyl sulfoxide (DMSO). The ITO substrates with the deprotected pattern were incubated with the linker solution for 1 hour, then washed twice with DMSO and autoclaved water in a 1:1 ratio. Finally, the substrates were washed with pure autoclaved water. The surface was dried with N_2.

7.2.5. DNA immobilization

For direct labeling of the deprotected pattern, a fluorescently labeled sDNA (Atto 647N - CGC ATT CAG GAT AAA AAA AAA A - 3' SH) is reacted to the maleimide-function of the linker. For hybridization experiments, first an unlabeled sDNA (ATC CTG AAT GCG AAA AAA AAA A - 3' SH) is reacted to the same maleimide function of the linker. In both cases, 0.1mM DNA solution in water is diluted to 0.01mM with a PBS buffer system (10mM NaCl, 1mM sodium dihydrogen phosphate). A 5-10 µL drop of the diluted DNA solution is positioned on each pattern and incubated for 100 minutes.

7.2.6. DNA hybridization and de-hybridization

A fluorescently labeled sDNA solution (CGC ATT CAG GAT AAA AAA AAA A - 3' Alexa 647) is diluted as described in the above section (DNA immobilization). This sDNA is complementary to the non-fluorescent species ((ATC CTG AAT GCG AAA AAA AAA A - 3' SH). The ITO substrates with the pattern facing upwards are put in a chamber filled with autoclaved water. The substrates are incubated for 8 h, then washed with autoclaved water and dried with N_2.

For de-hybridization the substrate is positioned in a Falcon® tube filled with PBS buer (10mM NaCl, 1mM sodium dihydrogen phosphate), which is heated in a water bath to 75 °C. Afterwards the substrate is washed with autoclaved water and dried with N_2.

7.2.7. Synthesis of the DNA-functionalized microgels

The synthesis of the DNA functionalized µGs was performed by Rebecca Hengsbach and Niklas Lothmann (IAC, RWTH Aachen University). Synthesis instructions were taken after the synthesis instructions of Alex Oppermann (IPC, RWTH Aachen University).

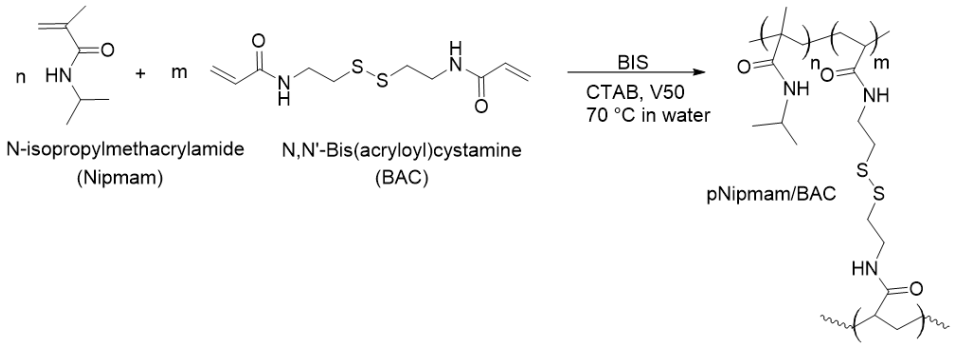

Scheme 7-1: Schematic of the synthesis of pNIPMAM µGs for immobilization at the pattern. The µGs will be functionalized with DNA in the next step. This schematic was provided by Rebecca Hengsbach (IAC, RWTH Aachen).

The general route for a 140mM Poly(N-isopropylmethacrylamide) core synthesis is illustrated in Scheme 7-1. A 270 mL aqueous solution of NIPMAM (92 mol%), BAC (1.5 mol%), BIS (3 mol%) and CTAB (0.06 mol%) in bi-distilled H_2O was prepared. Additionally, a second 30 mL solution of the initiator V50 (1.6 mol%) in bi-distilled H_2O was prepared. Both solutions were degassed with N_2 for 45 minutes. The monomer mixture was then added to the reaction flask and preheated to 70 °C under constant N_2 atmosphere. After reaching the reaction temperature, the initiator solution was added, the clouding of the reaction solution indicated the nucleation process. After stirring the system for 3.5 h at 70°C with 250 rpm, the reaction was cooled overnight. The next day, the reaction solution was filtered through glass wool to remove aggregated particles. The turbid white dispersion was then centrifuged three times at 25000 RPM for 1.5 h for purification. Characterization was done by means of DLS (R_h =190 ± 1 nm).

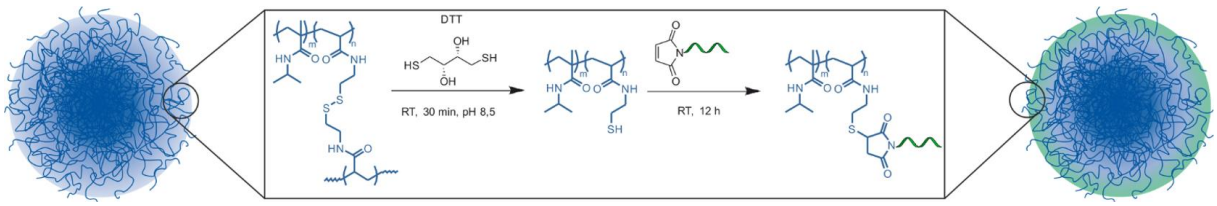

Scheme 7-2: DNA-Functionalization of pNIPMAM µGs. Scheme is provided by Rebecca Hengsbach and Dr. Sabine Eisold (IAC RWTH Aachen University).

The experimental conditions are adapted from the dissertation of Dr. Sabine Eisold.(Eisold 2018) The functionalization with maleimide-terminated DNA was performed according to Scheme 7-2. A first resdispersion of the above synthesized pNIPMAM µGs (5 mg) in H2O (0.5 mL, pH 8.5) is followed by the addition of 1,4-Dithioerythrit (DTT) (in H_2O, 0.1 M, pH 8.5).

The reaction mixture was left for 30 min. The µGs were purified through centrifugation (5.5 krpm, 10 min) and where subsequently washed 3 times before being redispersed in H_2O (1 mL, pH 7.4). DNA4-Mal (50 µL, 0.1 mM, see Table 7-1) where added and the reaction mixture was shacked overnight. Afterwards, the DNA-functionalized µGs were centrifuged (5.5 krpm, 10 min) for purification and redispersed in H_2O (pH 7.4).

7.2.8. Microgel hybridization to the pattern

After standard preparation of the c-EBL substrates according to 7.2.1, the thiol pattern is functionalized with DNA3Mal (see Table 7-1) with a buffer (5 mM Tris HCl, 10 mM MgCl2, 1 mM EDTA, 0.05 vol% Tween20). Afterwards, Spacer 1 (10 µM, 150 µL, see Table 7-1)) was incubated for 6h for successful hybridization to DNA3Mal (see Table 7-1)). Spacer 2 (10 µM, 150 µL, see Table 7-1) was incubated for 6 h for successful hybridization to Spacer 1 (see Table 7-1). The µG dispersion (150 µL) synthesized according to 7.2.7 was incubated for 6 h for µG immobilization.

Table 7-1: Used base-sequences with their acronym in this experimental section.

A Molecules	Sequence
DNA3Mal	CGC ATT CAG GAT AAA AAA AAA A - 3' Maleimide
DNA4Mal	5'-ATC CTG AAT GCG Maleimide
Spacer 1	ATC CTG AAT GCG AAG CGC GGC GGG AGT GGT GGT TAC GCG CAG CGT GAC CGC TAC ACT TGC CAG CGC CCT AGC GCC CGC TCC TTT CGC TTT CTT CCC TTC CTT TCT CGC CAC GTT CGC C
Spacer 2	GCA CCC CCG CAT TCA GGA TGC CGG CGA ACG TGG CGA GAA AGG AAG GGA AGA AAG CGA AAG GAG CGG GCG CTA GGG CGC TGG CAA GTG TAG CGG TCA CGC TGC GCG TAA CCA CCA CTC CCG CCG CG

7.3. Experimental section chapter 5

Chapter 7.3 provides information on the experimental procedures that are necessary in order to stretch DNA molecules in hydrogels. This includes the general information on chemicals used for the DNA-stretching procedure (see 7.3.1).

Subsequently the agarose gel electrophoresis (7.3.2), as well as the DNA preparation (7.3.3), the agarose plug purification (7.3.4) and the preparation of the hydrogel (7.3.5) is described in detail.

For all fluorescence microscopy measurements, the spinning disk confocal fluorescence microscope VisiScope Confocal-CSUX1 with Nikon Ti and Andor EMCCD camera was used.

7.3.1. Chemicals and buffering systems

The used water was either purified by a combination of Millipore Elix 3 with a downstream Milli-Q Academic system (σ = 0:055 µS cm^{-1}) or by a membraPure Astacus^2 system (σ = 0.055 µS cm^{-1}). The chemicals that were used during this project are listed in Table 7-2.

Table 7-2: Overview of the used chemicals for DNA stretching.

Chemicals	Purity	Supplier
acetone	99 %	VWR chemicals
AdoYnTAMRA		Felix Gularek (RWTH)
agarose		Sigma Life Science
SeaPlaque® agarose		Lonza
argon	4.8	Westfalen AG
bromophenol blue		SERVA
dimethyl sulfoxide (DMSO)	99.7 %	Acros Organics
dithiothreitol (DTT)		GERBU
ethylenediaminetetraacetic acid (EDTA)	99.2 %	GERBU
GelRed®		Biotium
glycerol	99.5 %	GERBU
2-hydroxy-2 mehtylpropiophenone	97 %	Aldrich Chemistry
M.BseCI		Kerstin Glensk (RWTH)
M.TaqI		Kerstin Glensk (RWTH)
magnesium acetate	99 %	Sigma Life Science
2-mercaptoethanol (β -ME)	99 %	Sigma Life Science
N,N'-methylenebis(acrylamide) (MBA)	99 %	Sigma-Aldrich
N-isopropylacrylamide (NIPAM)	97 %	Aldirch Chemistry
oxygen	5.0	Westfalen AG
potassium acetate	99.0 %	Fluka
2-propanol	98 %	VWR chemicals
proteinase K		Qiagen
R.ClaI		New England Biolabs
R.TaqI		Thermo Fisher Scientific
T7 phage DNA		BIORON
3-(trimethoxysilyl)propyl acrylate	92 %	Aldrich Chemistry
TRIS acetate		Sigma Life Science
TRIS-HCl	99.0 %	GERBU
YOYO-1® (DiYo-1)	99.89 %	AAT Bioquest
β - -agarase I		New England Biolabs
β - agarase I bu_er		New England Biolabs
λ phage DNA		Thermo Fisher Scientific

Different aqueous buffering systems were used in combination with the DNA preparation:

- 1x TE buffer (10 mM TRIS-HCl, 1 mM EDTA, pH 8.0)
- 1x NEB4 buffer (50 mM potassium acetate, 20 mM TRIS acetate, 10 mM magnesium acetate, 1 mM DTT, pH 7.9)
- 1x BseCl buffer (10 mM TRIS-HCl,10 mM EDTA, 2 mM β-ME, pH 7.4)
- 6x loading buffer (30 % glycerol, 0.25 % bromophenol blue)
- 0.5x TBE buffer (45 mM TRIS-HCl, 45 mM boric acid, 10 mM EDTA)

7.3.2. Agarose gel electrophoresis

An agarose gel was prepared by solving agarose (0.21 g, 0.7 wt.%) and GelRed® (3 µL, 10,000x in simmering 0.5x TBE buffer (30 mL). The mixture was cured in an electrophoresis cast with an inserted comb to form the wells. After curing, the chamber was filled with 0.5x TBE buffer. The sample solutions that should be analyzed were mixed with 6x loading buffer (20 % of sample volume). They were pipetted into the wells. A voltage of 90 V was applied, and the gel ran for 45 min. The gel was evaluated by irradiation with UV light (λ = 312 nm) to display the DNA bands. An image of the bands was taken. **Restriction Modification Assay**: To evaluate the DNA modification, one restriction solution was prepared for each used MTase. For the modification by M.TaqI the restriction enzyme R.TaqI (0.33 U μL^{-1}) was solved in NEB4 buffer (1x). For the DNA modifed by M.BseCI the restriction enzyme R.ClaI (0.33 U μL^{-1}) was solved in NEB4 buffer (1x). An additional restriction solution of NEB4 buffer (1x) without an REase was prepared. A reference sample with the target DNA (50.0 ng μL^{-1}) was prepared. All of the DNA containing samples (5 µL) were mixed with both the respective restriction solution (7.5 µL) and the reference restriction solution (7.5 µL). The solutions containing R.TaqI or M.TaqI modified DNA were incubated at 65 °C for 1 h. The remaining solutions were incubated at 37 °C for 1 h. Proteinase K (700 mAU μL^{-1}, 1 µL) was added to all of the mixtures. They were thoroughly mixed and incubated at 37 °C for 30 min. 6x loading buffer (2.5 µL) was added to each solution, they were thoroughly mixed, and an agarose gel electrophoresis was proceeded with each of the mixtures (6.4 µL each, 100 ng DNA). **Quantification Test**: To quantify the DNA concentration in a purified sample a quantification test was performed. Reference solutions were prepared containing the double, same, and half concentration of target DNA. The sample solution (10 µL) and all reference solutions (10 µL) were mixed thoroughly with 6x loading buffer (2 µL).

An agarose gel electrophoresis was executed with 4.8 µL of each mixture. The exposure time for the image was adjusted with the result that no pixel was overexposed. By comparison of the integrals over the DNA bands of the sample and the references the DNA concentration in the sample was estimated.

7.3.3. DNA preparation

Modification of λ Phage DNA with AdoYnTAMRA by M.TaqI

λ phage DNA (50.0 ng μL^{-1}) was mixed with M.TaqI (1.00 eq. per TCGA, 0.189 µM) and AdoYnTAMRA (10 µM) in 1x NEB4 buffer. The mixture was incubated at 65 °C for 1 h. **Restriction Modification Assay**: Full protection, see Fig. 7-3 a).

Modification of T7 Phage DNA with AdoYnTAMRA by M.TaqI or M.BseCI

T7 phage DNA (50.0 ng μL^{-1}) was mixed with M.TaqI (1.00 eq. per TCGA, 0.213 µM) or M.BseCI (20.0 eq. per ATCGAT, 0.115 µM) and AdoYnTAMRA (10 µM) in 1x NEB4 buffer or 1x BseCI buffer, respectively. The M.TaqI containing mixture was incubated at 65 °C for 1 h and the M.BseCI containing one was incubated at 55 °C for 1 h. **Restriction Modification Assay:** Full protection for M.TaqI, partly restriction for M.BseCI, see Fig. 7-3 b).

7.3.4. Agarose plug purification

A 2 wt.% agarose solution was prepared by solving the low melting temperature agarose (10 mg) in 1x TE buffer (500 µL) while incubating at 75 °C for 1 h. The unpurified DNA solution and the agarose solution were incubated at 43 °C for 10 min. They were mixed thoroughly with same volume fractions. The mixed solution was transferred into disposable plug molds and cooled at 6 °C for 1 h. The plugs were washed six times by incubating them in TE buffer (1x, 50 mL) at 25 °C on a shaker at 100 rpm for at least 6 hours per wash cycle. After each cycle the buffer solution was exchanged. After the last cycle the buffer was removed. The plugs were centrifuged in a micro test tube and incubated at 75 °C for 15 min. After incubating them at 43 °C for another 15 min, β-agarase I (4 µL) was added and they were incubated at 43 °C for 1 h. They were cooled to 6 °C for 15 min. Proteinase K (700 mAU μL^{-1}, 2 µL) was added and the mixture was incubated at 43 °C for 1 h. **Quantification Test**: 11.5 ng μL^{-1} for M.TaqI labeled T7 phage DNA, 9.5 ng μL^{-1} for M.BseCI labeled T7 phage DNA, see Fig. 7-3 c).

7.3.5. Preparation of the pNIPAM hydrogels

Cleaning of the Glass Substrates: Rectangular glass substrates (Marienfeld, High Precision Microscope Cover Glasses, 24x50 mm, No.1.5H) were cleaned by ultrasonication consecutively in water, acetone and 2-propanol for 5 min each. Circular cover slips (10 mm; 22 mm) were cleaned the same way and stored in 2-propanol. The glass substrates were plasma cleaned for 1000 s at 100 W and an O_2 pressure of 0.44 mbar.

Silanization of the Glass Substrates: The glass substrates were put in a desiccator without desiccant. An evaporating dish with 3-(trimethoxysilyl)propyl acrylate (100 µL) was juxtaposed to the substrates. The desiccator was evaporated for 15 min. The vacuum was kept for 2 h. After the evaporating dish had been removed, the desiccator was evacuated for 1 h. The glass substrates were stored light-tightly in argon atmosphere at ambient pressure. A reaction scheme for the silanization is given in Scheme 7-3.

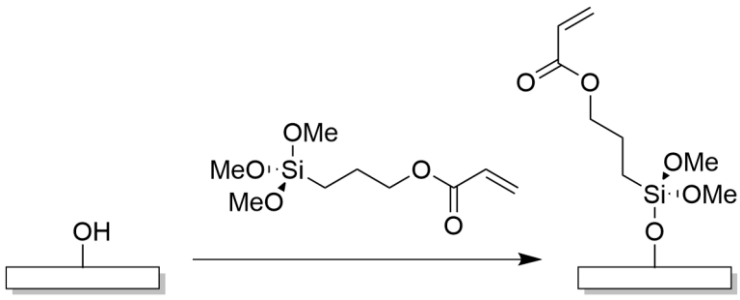

Scheme 7-3: Modification of the plasma-cleaned glass surface with the silane 3-(trimethoxysilyl)propyl acrylate. Contact angle: 46° ± 4° (Biggs et al.(Biggs, Edmondson et al. 2015): 47° ± 2°)

Polymerization of the pNIPAM hydrogels

A polymerization solution containing the monomer NIPAM (2.56 M, 100 eq.%), the crosslinker MBA (50.2 mM, 1.96 eq.%) and the photoinitiator 2-hydroxy-2-methylpropiophenone (49.9 mM, 1.94 eq.%) in DMSO was prepared. For each hydrogel a drop of polymerization solution (for 10 mm cover slips: 1.0 µL; 2.0 µL; 3.0 µL; for 22 mm: 14.5 µL) was pipetted on a glass substrate and covered with a cover slip (10 mm or 22 mm diameter).

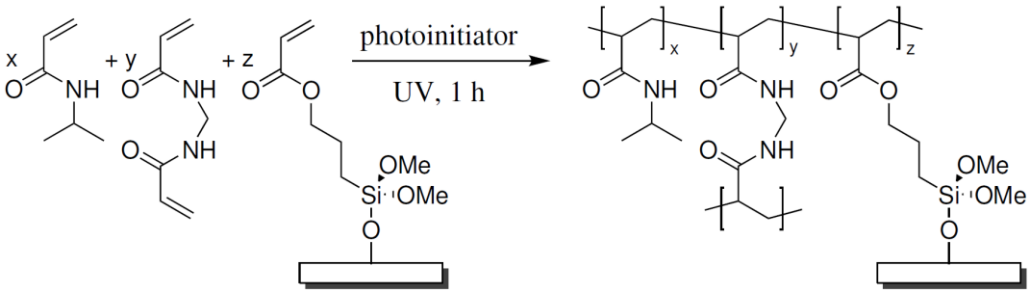

Scheme 7-4: Free radical Terpolymerization of NIPAM, MBA and the end groups of the surface bound silane.

The free-radical terpolymerization was started by exposing the samples to UV light ($\lambda_{short\text{-}wave}$= 254 nm and $\lambda_{long\ wave}$ = 366 nm) for 1 h. Crosslinked and surface bound PNIPAM hydrogels were obtained. The cover slip was removed, and the hydrogel was stored in water (50 mL) for at least 16 h. The hydrogel was air dried for at least 16 h.

Thermal Treatment of Loaded Hydrogels

The hydrogel was incubated at 50 °C for 5 min. A drop of the target DNA containing solution (10 µL; 5 µL; 1 µL) was pipetted onto the hydrogel. The system was incubated at 50 °C for 1 h.

7.3.6. Restriction modification assays and quantification test

Restriction modification assays belonging to section 7.3.3 as well as the quantification test belonging to 7.3.4 are depicted in Fig. 7-3.

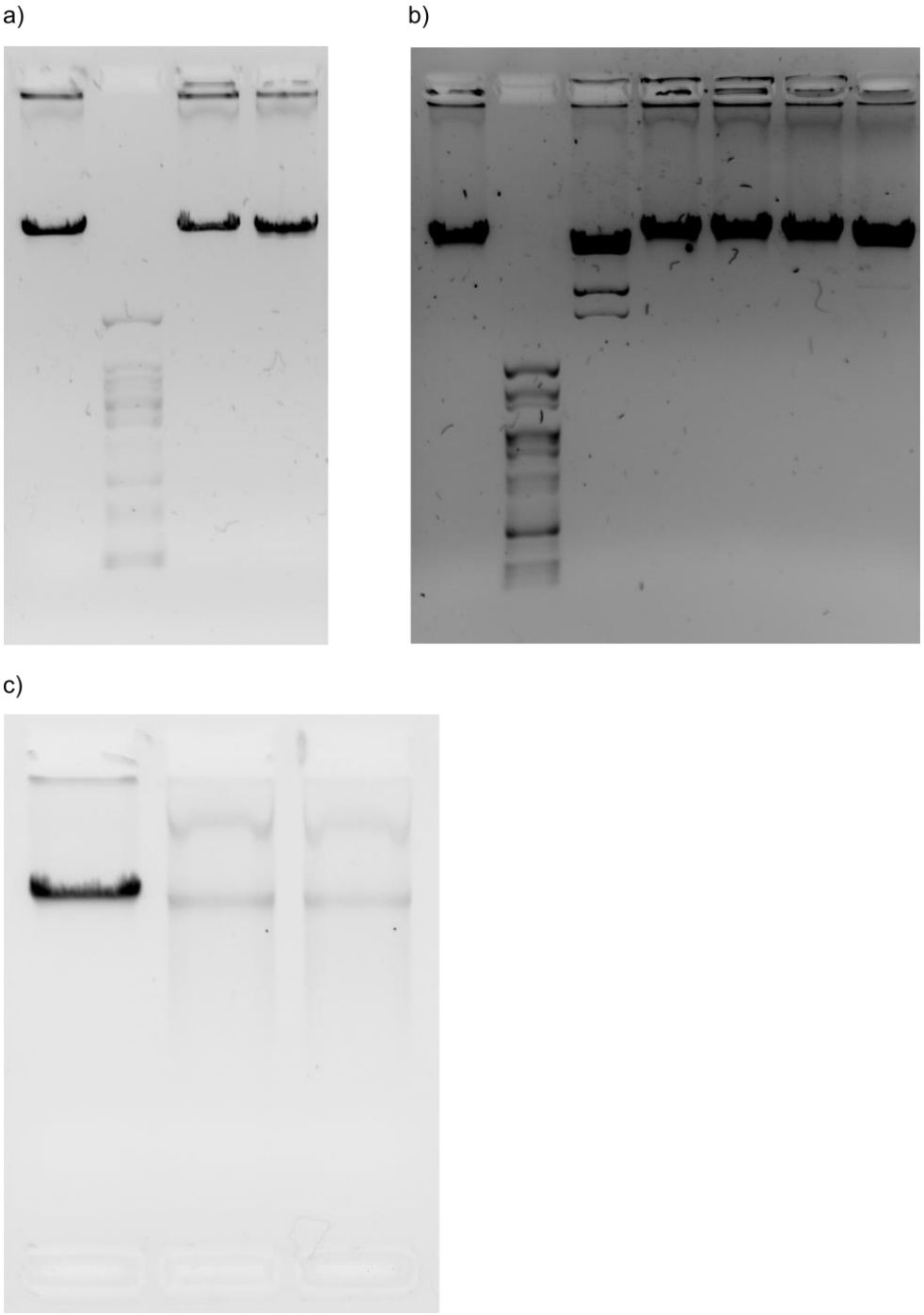

*Fig. 7-3: Restricion Modication Assay of λ phage DNA. Lanes from left to right refer to 1) reference DNA with restriction enzyme, 2) reference DNA without restriction enzyme, 3) M.TaqI labeled DNA with restriction enzyme and 4) M.TaqI labeled DNA without restriction enzyme **(a)**, belonging to section 7.3.3; Restricion Modifcation Assay of T7 phage DNA. Lanes from left to right refer to 1) reference DNA without restriction enzyme, 2) reference DNA with R.TaqI, 3) reference DNA with R.BseCI, 4) M.TaqI labeled DNA without restriction enzyme, 5) M.TaqI labeled DNA with R.TaqI, 6) M.BseCI labeled DNA without restriction enzyme and 7) M.BseCI labeled **(b)**, belonging to section 7.3.3., Quantification test of T7 phage DNA. Lanes from left to right refer to 1) reference DNA with 25 ng µL , 2) M.TaqI labeled DNA and 3) M.BseCl labeled DNA **(c)**, belonging to 7.3.4.*

8. Supplementary information

This chapter includes the supplementary information associated to the chapters 3, 4 and 5. Section 8.1, associated to chapter 3 mainly provides additional information on the visualization software µBerry. Section 8.2 is focused on adding information to the different surface modification steps presented in chapter 4. Finally, a detailed description of the automated analysis software for the DNA-stretching approach presented in chapter 5, will be given in section 8.3.

8.1. Supporting information chapter 3

This section provides information on the visualization tool µBerry. A general introduction to the state of the art software will be given before introducing the different components of µBerry, Finally the user manual is also added to the supplementary information.

8.1.1. 3D Visualization software µBerry

Introduction

Super-resolution fluorescence microscopy is a powerful tool to acquire detailed structural information of the investigated samples. This work has given an overview on the importance of choosing the right super-resolution experiment, as well as the appropriate optical tools to increase the image quality. Furthermore, it was shown that 3D-data can be acquired implementing techniques like a DH-PSF to acquire the z-information. As complex as the experimental execution of super-resolution microscopy may be, it is important to not underestimate the effort that is required for the analysis and visualization of the acquired data-set. In this section, an overview of the state-of-the art software tools will be given, before the introduction of µBerry, a software that was developed as part of this work to visualize 3D point cloud data.

One of the most important software tools – if not the most important tool – in scientific image analysis is the open source program ImageJ. The development of ImageJ started over 25 years ago at the national health institute (NIH),(Schneider, Rasband et al. 2012) being the primary agency of the United States government responsible for biomedical and public health research. Up to today, the development and the extensions that are provided are highly community-driven and allow for complex analysis especially of fluorescence microscopy data in the biomedical field.

An important ImageJ plug-in for the analysis of SRFM data is the ThunderSTORM addition. ThunderSTORM is an open-source, interactive and modular tool in ImageJ designed for automated processing, analysis and visualization of data acquired by single-molecule localization microscopy methods such as PALM and (d)STORM.(Ovesný, Křížek et al. 2014) Sub-diffraction localization of molecules is accomplished by computing the centroid of local neighborhoods, by a radial symmetry approach,(Parthasarathy 2012) or by fitting a suitable PSF model using standard or weighted non-linear least-squares methods, or using maximum-likelihood estimation (Mortensen, Churchman et al. 2010).(Ovesný, Křížek et al. 2014) If none of the above localization methods is selected, the approximate localizations from the previous step will be used. The uncertainty of the localization of molecules is calculated according to Thompson et al. (Thompson, Larson et al. 2002) or according to Quan et al.(Quan, Zeng et al. 2010) if EMCCD cameras are used.(Ovesný, Křížek et al. 2014) The summarized localizations can be directly visualized in the ImageJ software. The 2D-dSTORM data of pNIPMAM µGs on a glass surface is exemplarily depicted in S.I. 8-1.

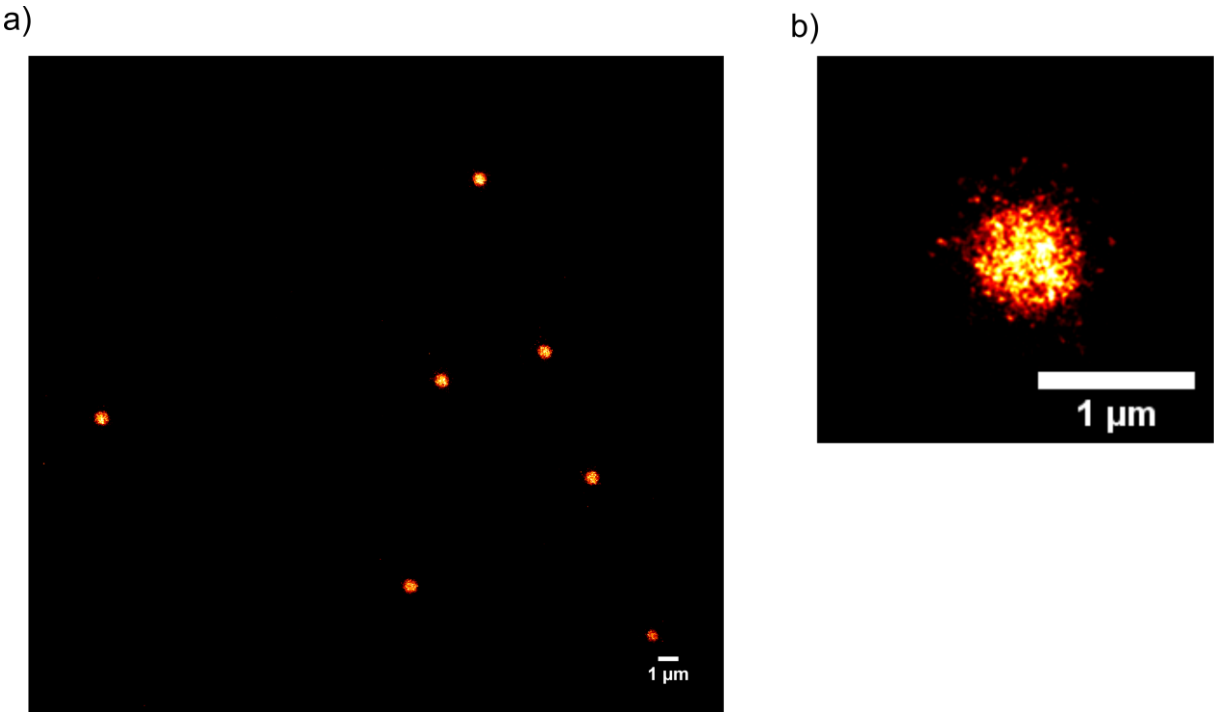

S.I. 8-1: 2D SRFM data of pNIPMAM µGs at a glass substrate acquired with the dSTORM method. Three sets of 20000 frames were acquired experimentally and analyzed using the ThunderSTORM plug-in of the ImageJ software. The visualization including the color scheme and the scale-bar was done using the conventional ImageJ tools.

The analysis of 3D SRFM data acquired with a DH-PSF can also be directly performed in ImageJ after the implementation of the 3DTRAX™ plug-in. It is GUI-based software, implemented as a Fiji (ImageJ) plugin, optimized for use with the Double Helix SPINDLE® imaging system. The software enables calibration data analysis of 3D data acquired using the SPINDLE module. 3DTRAX offers localization for 3D super-resolution reconstruction and particle tracking.

Even though the 3DTRAX software is crucial tool to analyze the acquired data, it is not yet suitable to adequately visualize 3D point cloud data like that generated when imaging µGs. In 2013, Beheiry et al. reported on their new 3D visualization software ViSP. The idea was to overcome challenges including the efficient handling of millions of individual localizations; the description of localization precisions in three dimensions; and the incorporation of intuitive depth cues, multichannel compatibilities and 3D quantitative features.(El Beheiry and Dahan 2013) Despite the fact, that ViSP is a great step towards visualizing 3D data, it has to be stated that it was found not to be challenging for handling 3D µG data. Unfortunately, the main problems derive from the poor performance of the general usability and user-interface of the software. It is not possible to intuitively adapt the 3D rotation angles of the field of view, which in most cases leads to a spatially distorted visualization of the box plot and the axes, see S.I. 8-2. The image below exemplarily depicts eight µGs that have been imaged using the 3D-

dSTORM technique. The data was analyzed using the 3DTRAX software in ImageJ. The resulting localizations were fed to the ViSP software in the form of a *x,y,z,i,f*-matrix where *x,y,z* represent the positions in the respective axes, *i* is the intensity information and *f* represents the frame-number in which the emitter was localized.

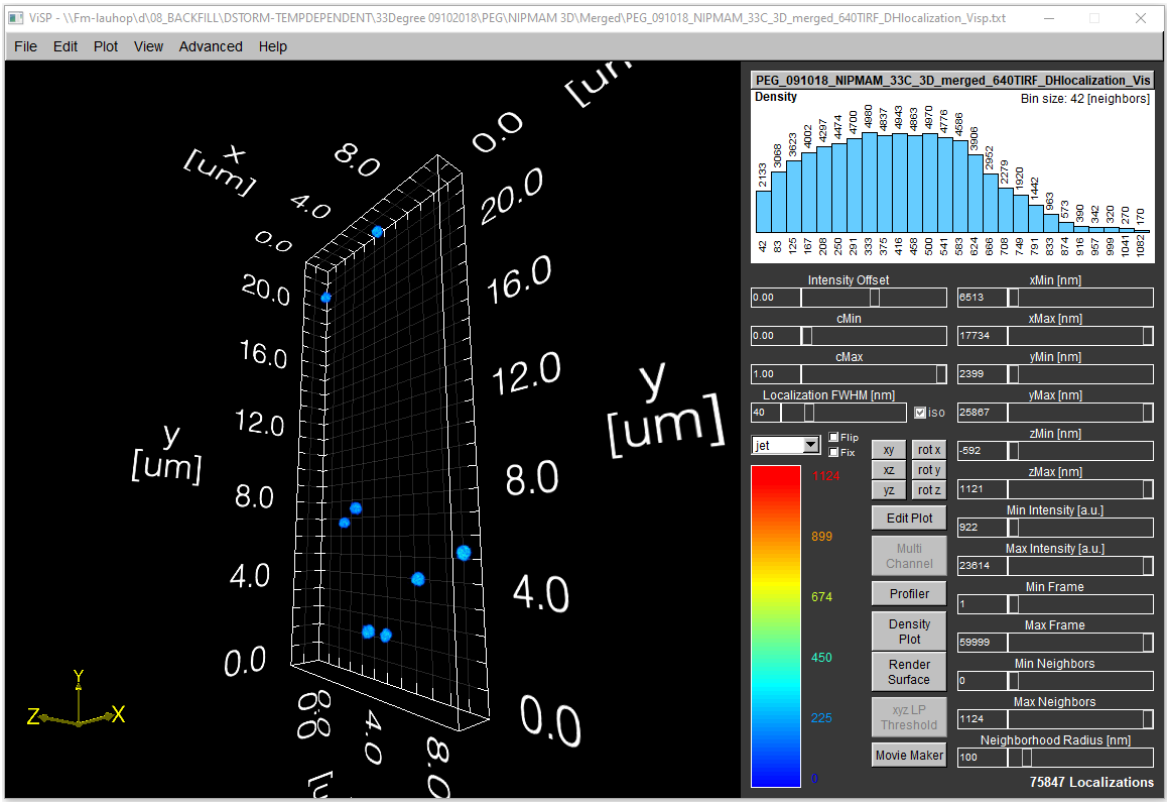

S.I. 8-2: Screenshot of the 3D visualization software ViSP. The field of view shows eight pNIPMAM µGs marked in blue in a distorted box plot. The distortion of the box plot and the axis-scaling is due to the limited options of handling the rotation of the image. On the right side the user-interface is depicted.

The single µGs have to be cropped out of the summarized image in ViSP in order to be analyzed individually. Unfortunately, the cropping is not implemented properly and has to be readjusted by hand until the cropped section is represented as desired, see S.I. 8-3. The x, y and z sliders denominated with “xMin, xMax, yMin, yMax, zMin, zMax” have the function to adjust the limits of the boxplot and therefore the visualized localizations as well as the scaling of the axes. The minimum and maximum setting points of the sliders do only function until a specific limit that not related to the boundaries of the visualized probe and therefore not understandable to the user. A work-around the poorly working sliders seems to be the possibility to enter the slider position as a number and therefore enabling the setting of the correct box positions.

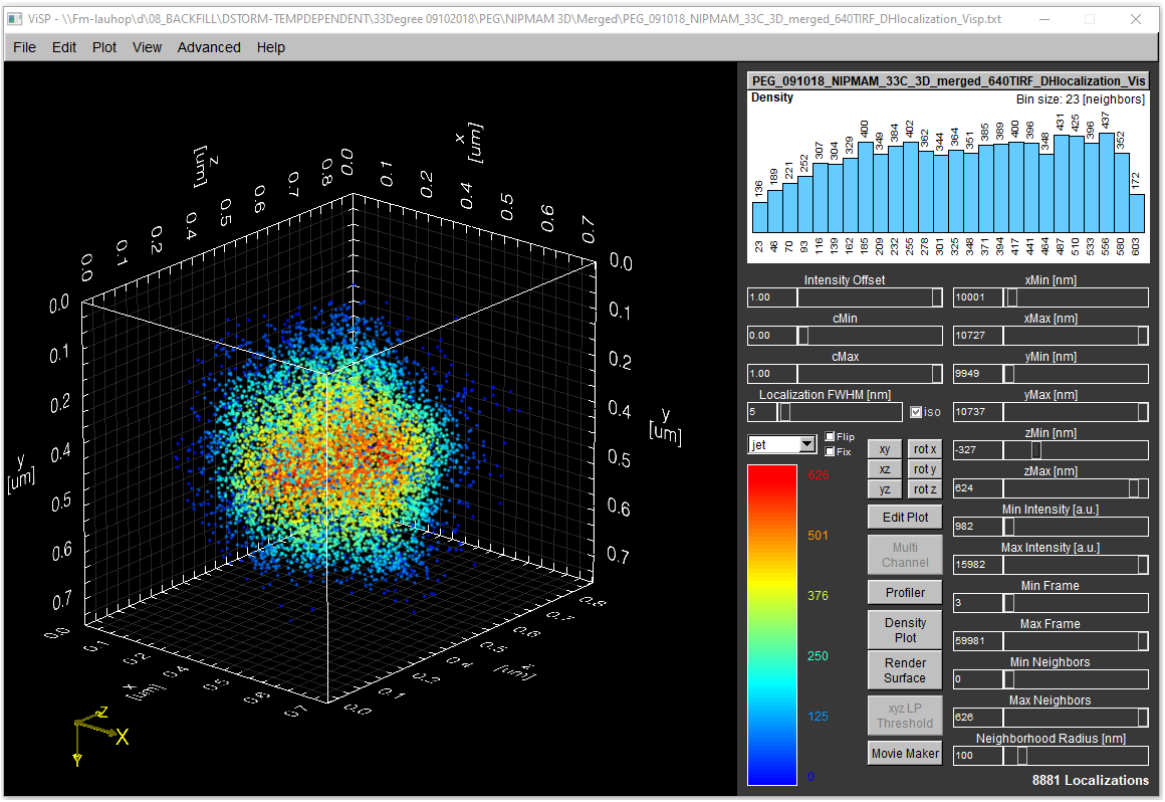

S.I. 8-3: Screenshot of the 3D visualization software ViSP. The field of view shows one cropped pNIPMAM µG marked in blue in a distorted box plot. The color bar refers to the labeling density defined as the number of surrounding localizations in a radius of 50 nm.

ViSP does not only allow to export images but also allows for the generation of 3D videos. In this case one of the output possibilities which is important when showing 3D data, is the possibility of showing the object rotating around one axis.

The output formats of ViSP are ".3D" for images and ".TIF" for videos. These formats are not easily linked with presentation software like e.g. PowerPoint (Microsoft). Therefore another data transformation step in another program is required to acquire the data in the desired format like .PNG (transformation e.g. with ImageJ) or .MP4 (transformation e.g. with handbrake).

The launch of ViSP definitely has opened new possibilities for visualizing 3D (microscopy) data. It is a free software tool that allows for the general analysis of point cloud data. The limitations -especially in terms of its usability- on the other hand also indicate that it is difficult to provide one solution for the different scientific communities. For the case of µG analysis, the requirements for visualizations are different from what can be provided by ViSP.

Software

The Mathematica code for µBerry was developed int. al. as part of a research assignment of Simon Schog (B.Sc.) supervised by the author of this dissertation. µBerry is a Mathematica-based visualization software capable of performing necessary processing steps to create high-quality images and videos of individual µGs. For ease of use, a graphical user interface was created to enter all necessary information for the program and to give the user control over the output's type and format. In the following, the possible outputs from µBerry will be explained.

Images

The most basic output of µBerry are images of the µGs in both 2D and 3D. There are three 2D images of the µG, with an observation angle in the xy face, the xz face, and the yz face, as well as one 3D image of the µG. Additionally, a composite image of the previously mentioned images is created, S.I. 8-4. Especially, when the visualization medium of choice is an image and not a video, it is important to include images from different directional perspectives to fully cover the shape of the µG from all angles. In order to maximize the gain in information from a single measurement, the output of µBerry always includes a color function. The color function is used to color the individual localizations and introduce a fourth dimension into the output. By default, the color function is a jet-like color function used to visualize the localization density defined as the number of surrounding localizations in a radius of 50 nm.

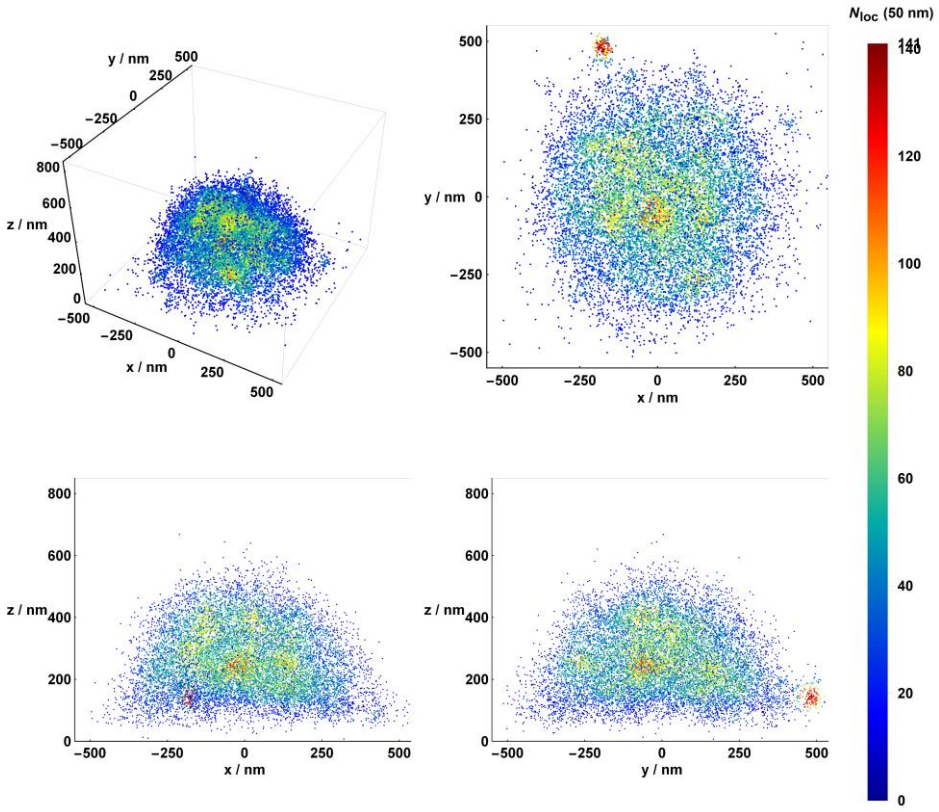

S.I. 8-4: Composite image of a µG containing a three-dimensional image (upper left), the xy face (upper right), the xz face (lower left), and the yz face (lower right).

Slices

The image of a 3D point cloud as a whole can bare misleading information or -more likely- not show all the relevant information. Especially in the case of µGs, which are soft matter objects with a heterogenous density distribution, it can be important to visualize or enhance specific parts. Therefore, µBerry allows to create stacks of images cutting the µG into slices along the three axes, see S.I. 8-5. The user has control over the width of the slices to optimize the images depending on the size and number of localizations of their µGs. The text above the image, indicating the minimum and maximum coordinates of the current slice, is an optional element and can be excluded from the output. While normal images capture the overall shape of a µG, they do not provide much information about the internal structure of the µGs because of overlapping points in the image. The slices were created to circumvent this problem by splitting the µG into clearly defined sections with easily accessible internal structures.

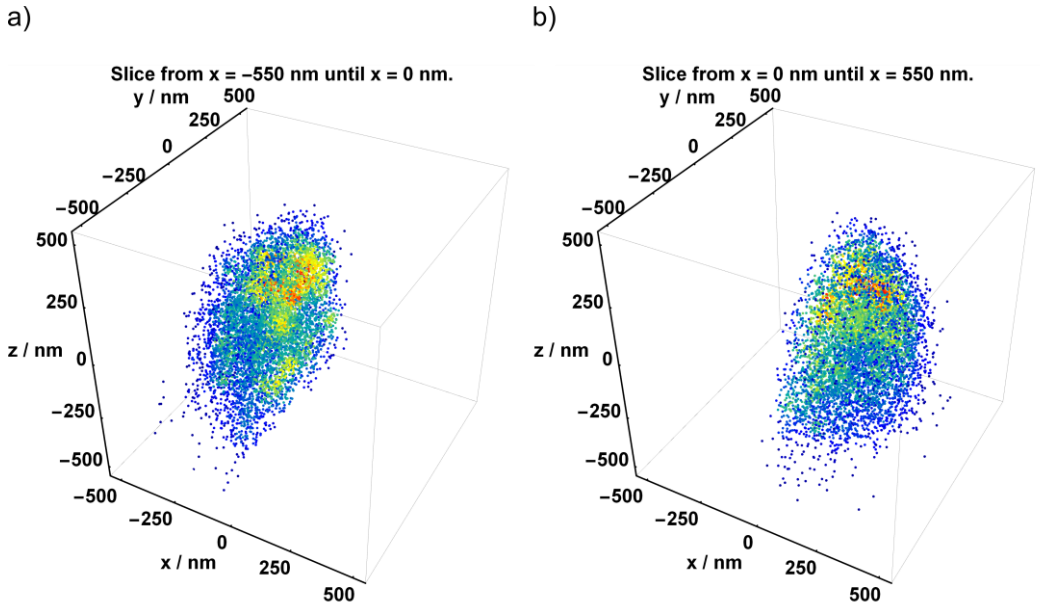

S.I. 8-5: Slices of a defined diameter of a µG along the x-axis, cutting the µG in half. The diameter of the slices and respectively the amount of slices through the object can be previously defined in the user-interface of µBerry

Videos

The visualization of 3D data is best done using videos, as this allows to show the 3D objects from different angles and perspectives. µBerry provides several types of default video options, allowing for a detailed view of the 3D structure or internal structures of the µGs. It should be noted, that the video options shown in this work can only be depicted in the form of images. As the basic option, rotation videos can be created in µBerry showing the µG rotating around the three axes, see S.I. 8-6. This allows for a better understanding of the three-dimensional structure of the entire gel and to show parts of the µG in more detail (e.g. the deformed bottom side or back) which under normal circumstances are not directly visible. The user can control the speed of the rotation by changing the rotation increment between the frames.

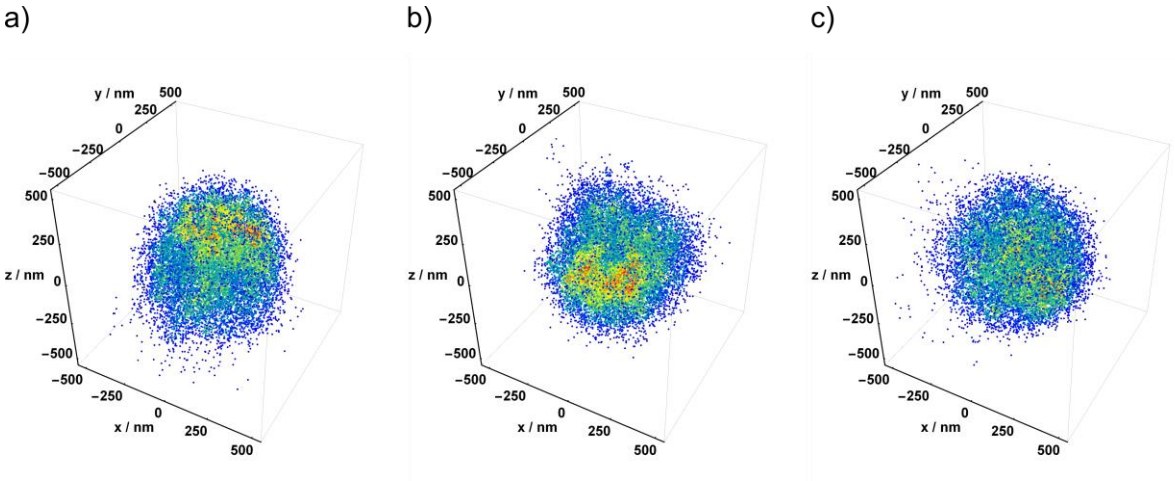

S.I. 8-6: Still images of a video in which a µG rotates around the x-axis. The user can control the speed of the rotation by changing the rotation increment between the frames. The axis of rotation is also chosen in the user interface of µBerry.

The second video option in µBerry consists of an invisible plane moving along the axes, while the parts already passed by the plane vanish in the background. Afterwards, this process is reverted and the µG is built up again. The user has control over the speed with which the plane moves along the axes. By gradually cutting away the µG from one end, the internal localizations are slowly revealed. This allows for a better visualization of internal structures, such localization density maxima or minima.

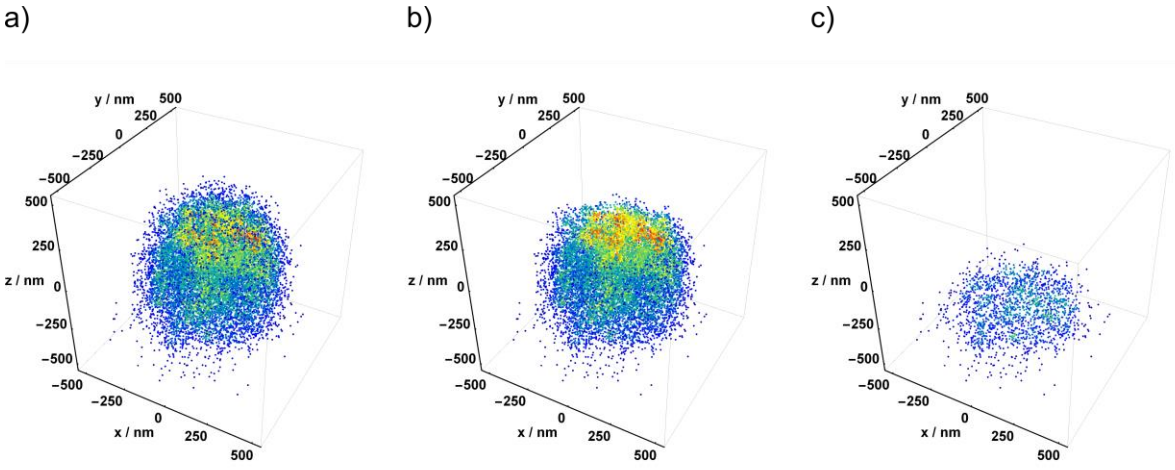

Fig. 8-1: Still images of a video in which a µG is built up as a plane of a specific diameter moves through the gel along the z-axis. The speed of the plane moving through the object as well as the axis along which the plane moves, can be set in the user interface.

The third type of video incorporates two invisible planes with a fixed distance move along the axes and cut away all points above/below the upper/lower plane. This leaves a single slice of the µG, which travels through the entire object once and then returns to the starting position, see S.I. 8-7. The user has control over the thickness of the slice and the speed at which it

moves along the axes. The difference to the previous video is that this video features only a slice of the µG instead of a build-up of the whole gel. Therefore, there are no additional localizations except for the current slice, which greatly enhances the contrast for an even clearer image of the internal structures.

a) b) c)

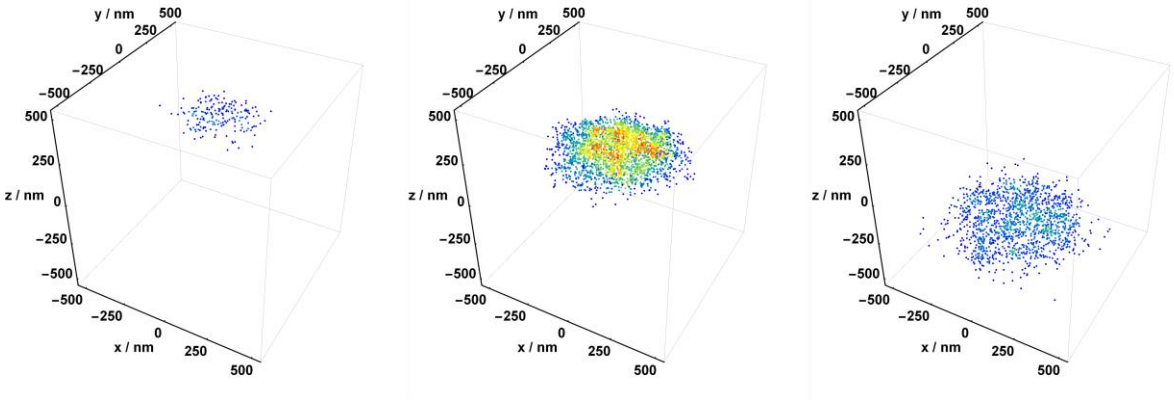

S.I. 8-7: Still images of a video representing the "walking slice" option in which only a slice of a specific diameter moves through the µG along the z-axis. The speed of the slice moving through the object as well as the axis along which it moves, can be set in the user interface.

In the last type of video, the µG is slowly build up from the maximum in labeling density to the least dense localizations while rotating around the z axis, see S.I. 8-8. The user has control over the speed of the rotation and µBerry will automatically adjust the number of new localizations per frame to completely build up the µG after one full rotation. This allows for a better visualization of the distribution of localization densities within the µG and the symmetry of the distribution.

a) b) c)

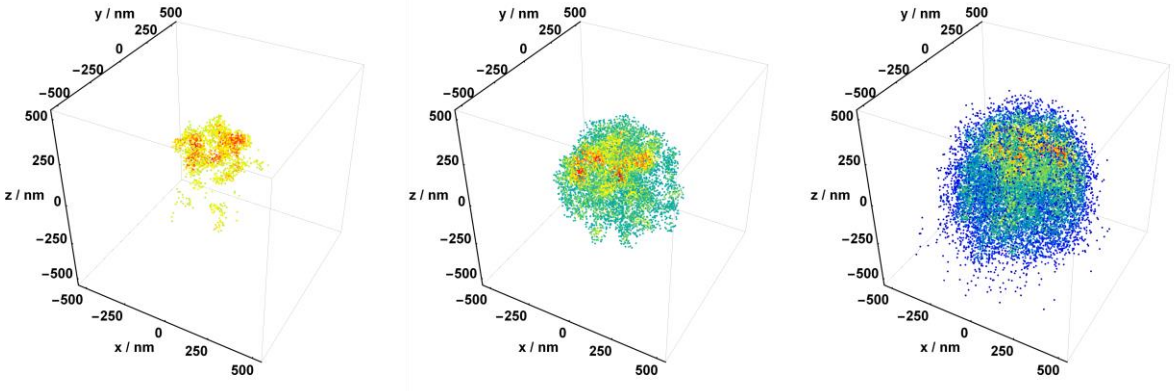

S.I. 8-8: Still images of a video in which a µG rotates around the z-axis while it is built up from the densest points to the least dense points.

Radial distribution

The software µBerry provides the option to generate plots of the normalized radial distribution of localizations. This is done by dividing the µG into spherical shells of identical thickness and counting the localizations within each shell. To normalize the data, the total number of localizations per shell is divided by the volume of the shell. µBerry creates plots for each individual µG, as well as a plot containing distributions for all µGs, and a plot containing distributions for all µGs as well as the average distribution across all µG, see S.I. 8-9. Additionally, µBerry has the option to export a file containing the data points to plot the distributions in other programs. The user can control the thickness of the shells and the maximum radial distance for the plot. Radial distributions can be used to study the location of the fluorescent dye molecules within the µG. As dyes are often bound via comonomers, this information could be used to characterize the radial composition of µGs.

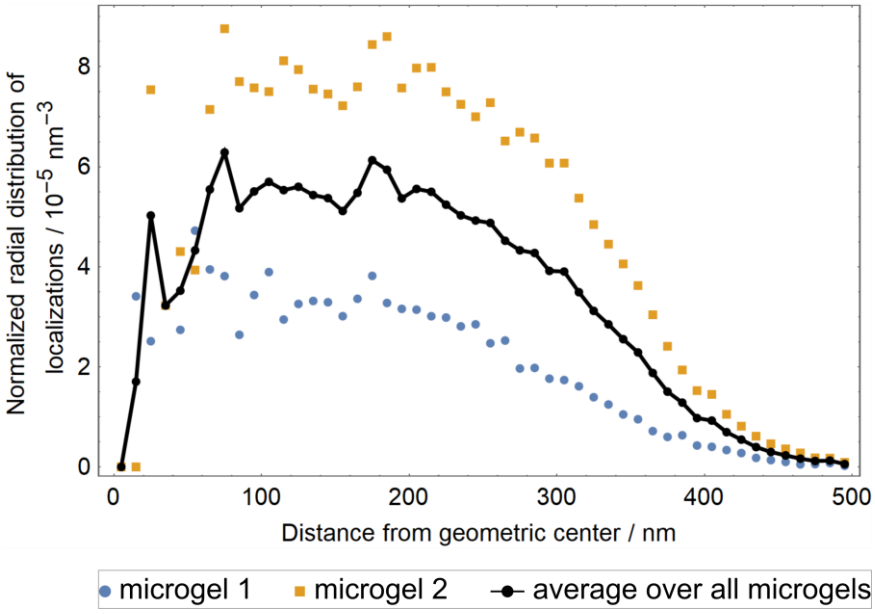

S.I. 8-9: Normalized radial distribution of localizations for two µGs, as well as the average distribution over the two gels.

Additional options

By default, µBerry includes a color bar indicating the labeling density in every output. This option can be turned off as depicted in S.I. 8-10, e.g. when multiple images are to be shown next to each other. This way the user doesn't have to manually crop the images containing the color bars as it is the case for programs like ViSP.

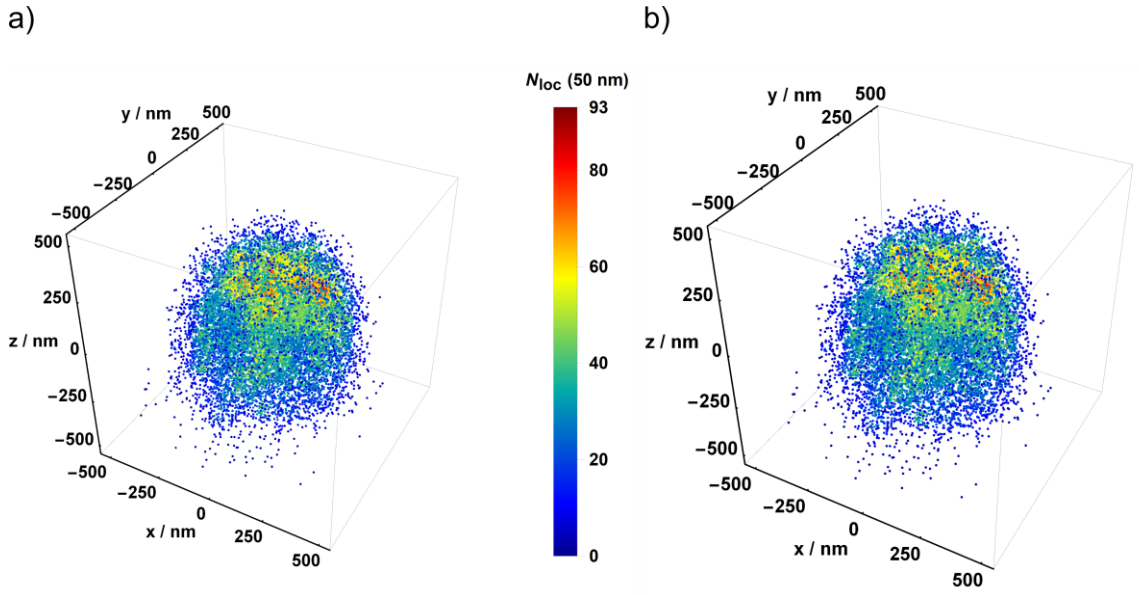

S.I. 8-10: Three-dimensional image of a µG containing a color bar and of a µG without color bar. The color bar indicates the labeling density represented by the number of localizations in a default radius (50 nm).

The user can choose the option to include circles in the 2D images, indicating the hydrodynamic radius of the µGs, see S.I. 8-11.

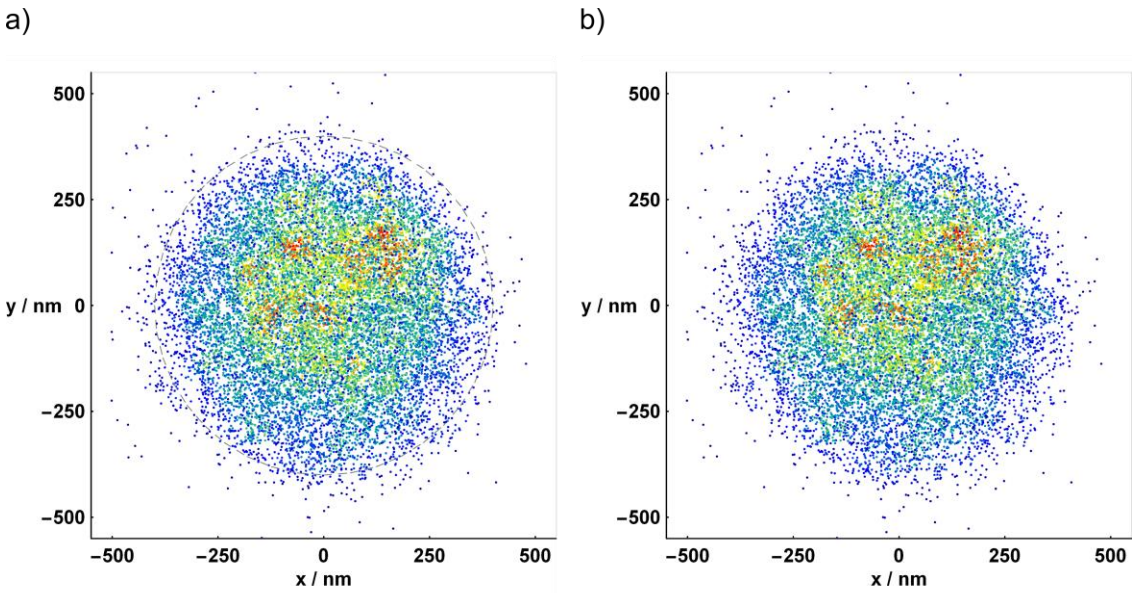

S.I. 8-11: Image of the xy-face of an exemplary µG surrounded by a circle indicating the hydrodynamic radius (a); image of the xy-face of an exemplary µG without the indication of the hydrodynamic radius.

Additionally, the user has the possibility to freely choose any combination of font and background colors which can be beneficial for data presentations depending on the lighting of the room, see S.I. 8-12

a) b)

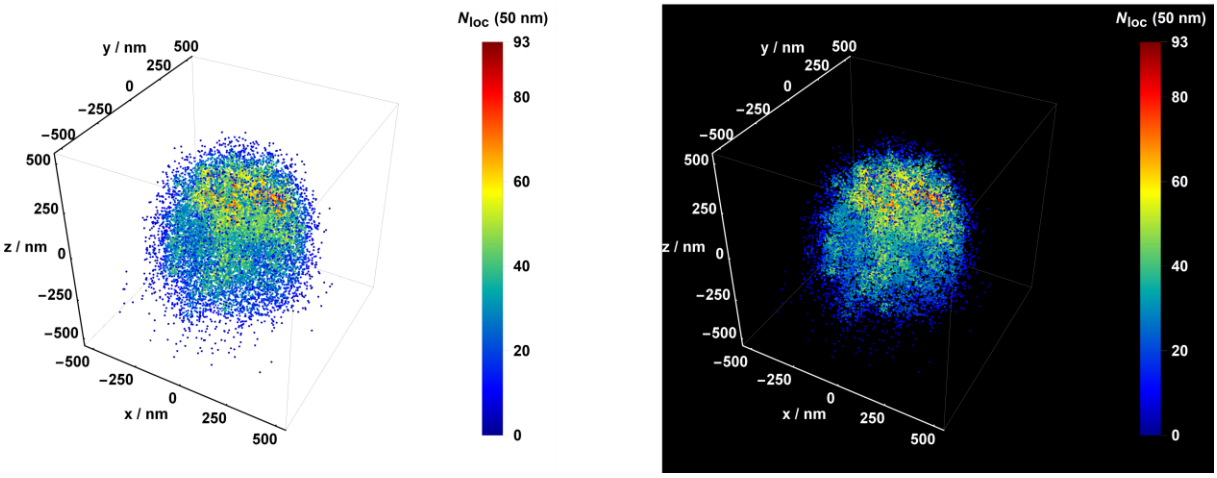

S.I. 8-12: Images of the same µG with different font and background colors. This option can be beneficial depending on the lighting of the room in which the data is presented.

In cases of µG data containing a large amount of stray points with very low localization density, it may be beneficial to filter these points out. For this purpose, µBerry has an option to filter out any point below a minimum value which the user can set, see S.I. 8-13. By default, this option is turned off in order to avoid data manipulation.

a) b)

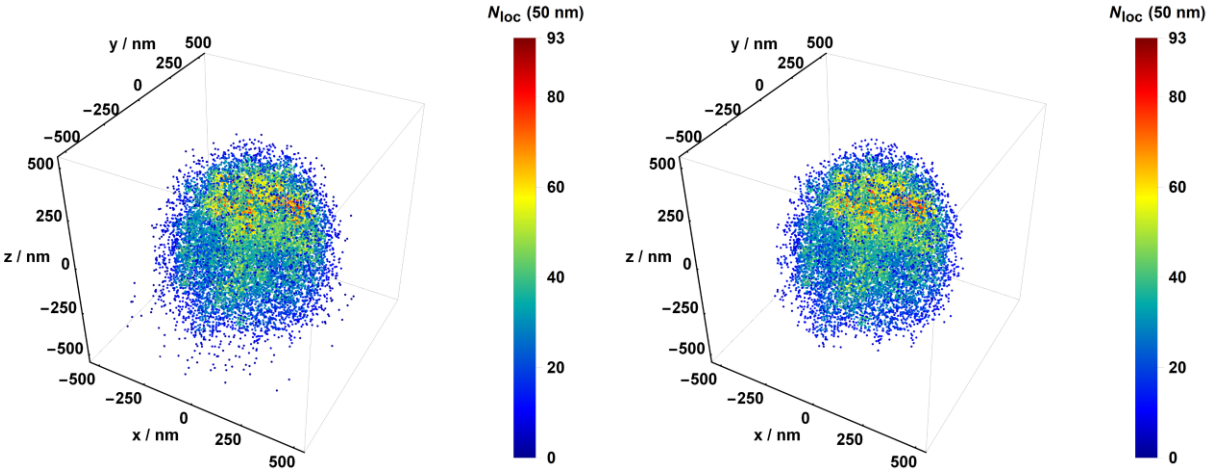

S.I. 8-13: Images of the same µG without filtering stray points (a) and after filtering out all points with localization density smaller than 5 (b).

The color function does not necessarily have to be linked to the labeling density. Therefore, µBerry provides the possibility configurate custom color functions and color bars, see S.I. 8-14.

Color functions can be created by entering pairs of one color and one numerical value associated with this color. µBerry automatically creates a gradient between two colors to create the complete custom color function with smooth color transitions. Additionally, the user has control over the interval of the color bar's labels as well as over the text displayed above the color bar. This feature allows µBerry to be used for the visualization of a variety of additional information, such as the polarity of the localizations.

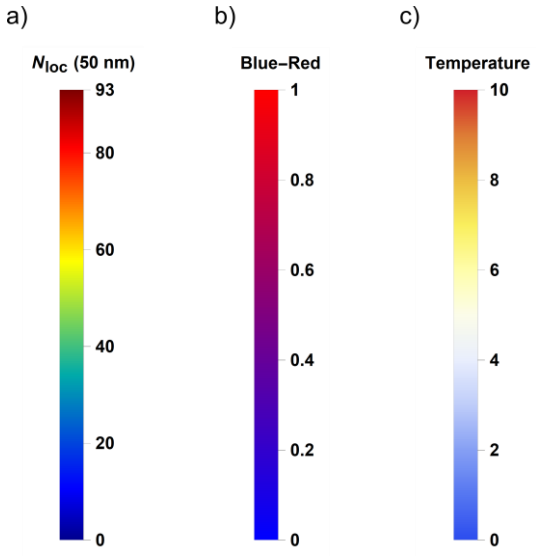

S.I. 8-14: Images of possible color functions. Standard jet-like color function used for density plots (a), custom color function ranging from blue over purple to red (b), custom temperature color function ranging from blue over white to red (c).

Outlook on the future development of µBerry

The development of the µBerry software was tailored to analyze 3D point cloud data of µG systems. It was developed due to the necessity to analyze and present structural information in a uniform and reliable manner. Even though, µBerry has immensely facilitated the way of presenting data, it still is in a preliminary state that has high potential for improvement. This improvement can only be achieved by teaming up with experts in the field of image analysis.

At the moment the analysis of data sets of single µGs is only possible after the already explained cropping procedure in ViSP, see S.I. 8-2 and S.I. 8-3. The challenges regarding the reliability and the limited usability of the ViSP software were the main reason to start the development of µBerry. It is therefore crucial to replace the cropping step with an appropriate solution within µBerry itself.

This project will be driven forward due to a new cooperation with the group of Dorit Merhof at the institute of imaging and computer vision of RWTH Aachen University. In a preliminary experiment, a cluster analysis employing a kernel density estimator(Botev, Grotowski et al.

2010) was ran over several data sets consisting of all µGs imaged in the field of view in one dSTORM experiment. It was shown that µG point clouds can be identified as local clusters of points, by computing the point density and then extracting the bounding boxes around the local maxima of the point density, see S.I. 8-15.

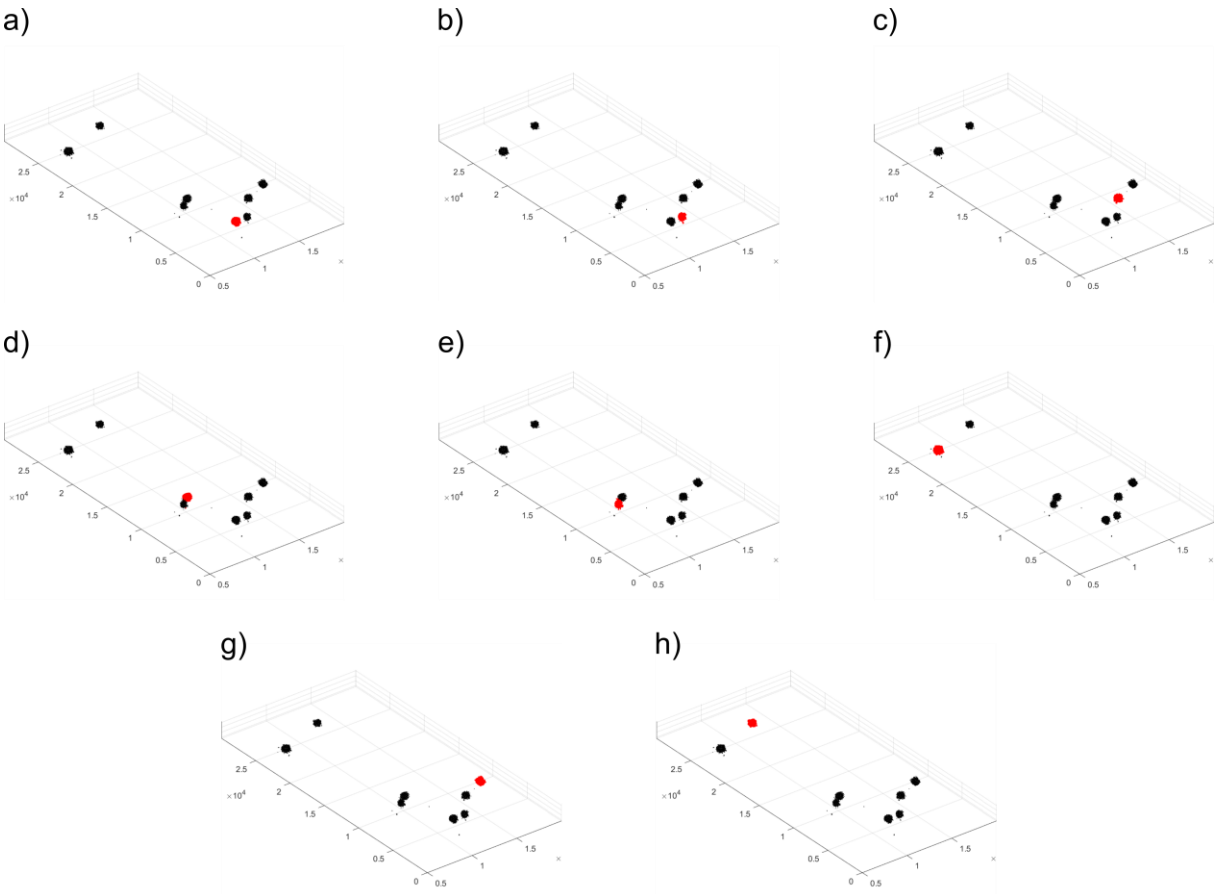

S.I. 8-15: Matlab-based cluster analysis of 3D point cloud data of pNIPMAM µGson a PEG surface. The point clusters (marked in red) are identified with a kernel density estimator.(Botev, Grotowski et al. 2010) Images a)-h) clearly show that he individual µG can be differentiated from each other, this is even possible in cases where two µGs are in close proximity (d, e).

The cluster analysis was performed on the µG data shown in chapter 3 and published in 2019.(Hoppe Alvarez, Eisold et al. 2019) As it is exemplarily shown in S.I. 8-15, the red highlighted µGs represent the individual clusters. The cluster analysis was successful on all remaining surfaces being ODS and FOCTS. It should be noted that the clustering method has its limitations in cases of very high background signal. As a rule of thumb, it was possible to estimate that if the individual µGs were not differentiable by eye, the accuracy of the cluster analysis would also decrease. The preliminary cluster analysis was implemented in a MatLab routine and will be included to the µBerry software in the future.

µBerry manual

1. **Before starting**

   Before starting the program, check the following points:

   - Verify that Mathematica is installed on the computer you are using and that you have access to the Mathematica notebook **µBerry.nb**.
   - An image called **Logo.png** should be located in the same directory as the notebook.
   - If you want to make videos using µBerry, you need the program **ffmpeg.exe**. It should come with the notebook but is otherwise downloadable for free.
   - Your input data files should be saved in a directory called **Input** located in your main directory.

2. **Program**

   2.1 General information

If you have checked the above points, you can now use the program.

Open the notebook in Mathematica and start it by pressing Shift + Enter. Make sure that you have selected the notebook (by simply left-clicking somewhere in the code); otherwise, the code won't run.

Alternatively, you could start the program by selecting **Evaluation** from the top menu and then selecting **Evaluate cells**.

Once started, the program will produce a user interface (UI).

Fill in all the data that is necessary for your desired output (everything else which is not needed should be grayed out and inactive) and press the **OK** button.

The program will now run and create your output. The speed of the program is (naturally) dependent on the number and size of your input files and the desired resolution of the output files.

When first starting the program, you should consider using low resolution for the output files and deselect the option to include slices and videos in your output to increase speed. This will also give you the opportunity to check whether your input and the plotting parameters are correct and the output is to your liking.

If so, increase the resolution and choose all the output options you want. As long as the Mathematica notebook isn't closed (or forcefully shut down), your input in the UI is saved. Thus, if you want to change parameters after a run, it saves you a lot of time.

If you want to shut down the program at any point, select **Evaluation** in the top menu and then choose **Quit kernel** (last option), followed by **local**. Please note that µBerry will automatically create directories for your output in your main directory. If these directories already exist, their contents will be deleted before each run! Especially for the videos, this feature is mandatory - so if you have already created data that you want to keep, do not forget to save it to a secure location!

2.2 General tab

As for all tabs, the blanks are already filled with a selection of commonly used information, this is colored in light grey. You can use this for guidance.

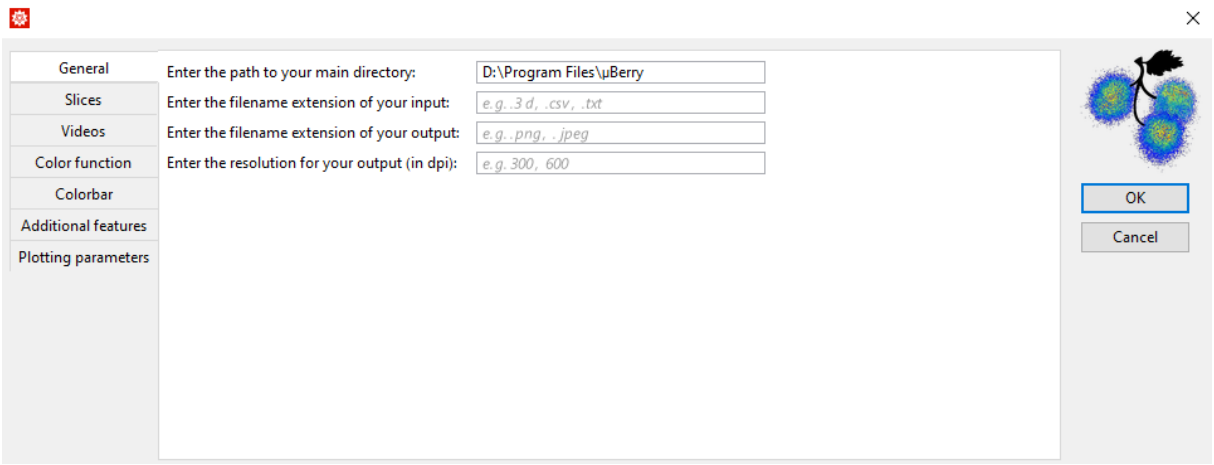

S.I. 8-16: General tab of the user interface in µBerry.

The General tab of the UI is supposed to be the most straightforward of all the tabs included in µBerry.

The path of your main directory can be simply copied from Windows Explorer; otherwise, you can of course enter it yourself.

Make sure to use backslashes (“\”) in the path! The filename extensions should contain the dot (“.”) followed by the extension. For input files, “.3d” and “.csv” are recommendet. For output files, you can only choose the filename extension of images (“.png”, .”jpeg”, “etc.”). All videos created with µBerry will be exported as .mp4 - if you need a different format, you have to convert it yourself.

2.3 Slices tab

As for all tabs, the blanks are already filled with a selection of commonly used information, you can use this for guidance.

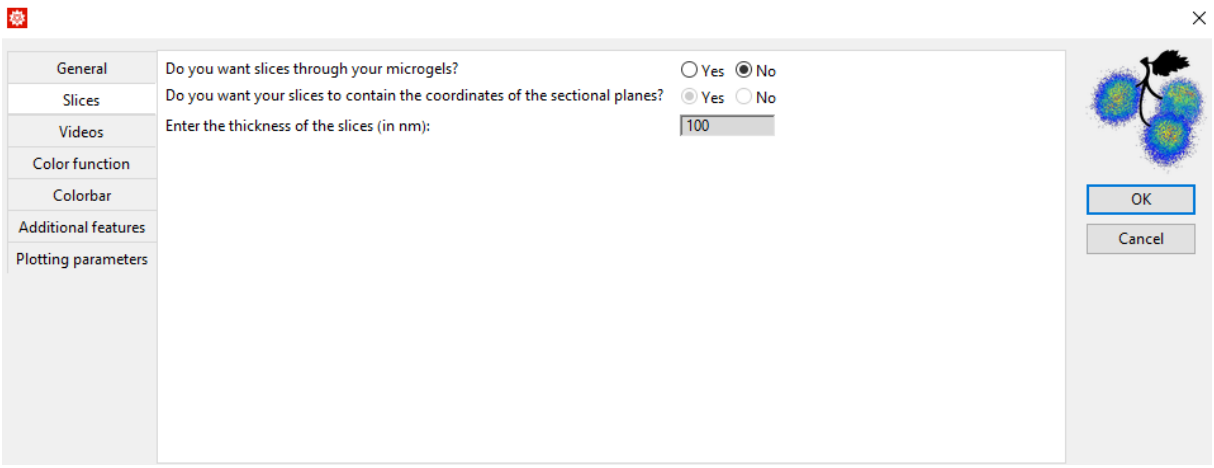

S.I. 8-17: Slices tab of the user interface. The default value for the slices is 100 nm, which can be changed according to the desired output.

If you want your output to contain slices through your µGs, choose yes. By default, the program starts with no selected. If you chose yes, you have to enter the thickness of your slices (in nm). In most cases, a slice thickness of 100 nm is sufficient. Additionally, you can choose an option to add the coordinates of the current slice to the image.

2.4 Videos tab

As for all tabs, the blanks are already filled with a selection of commonly used information, this should be used as guidance.

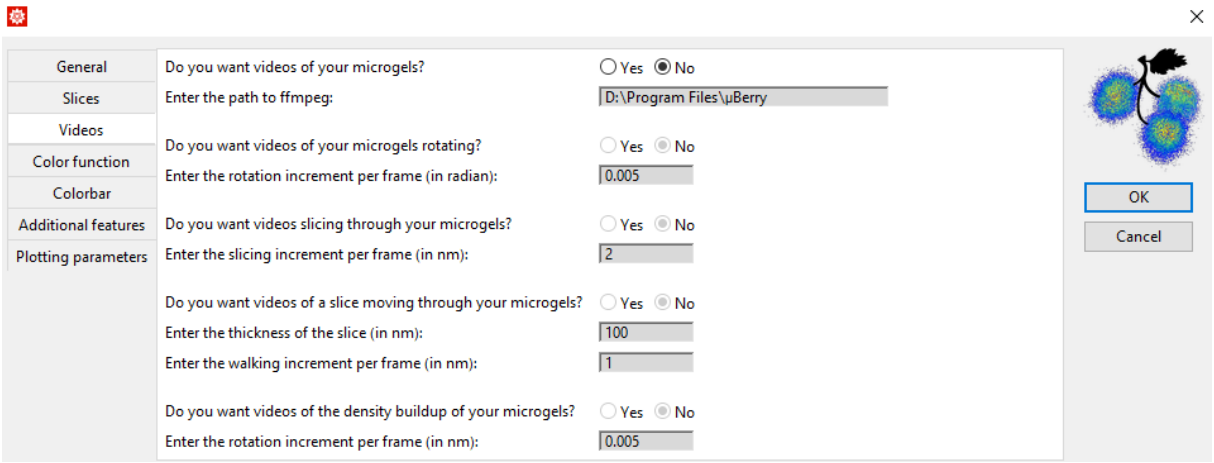

S.I. 8-18: Slices tab including default settings which can be changed according to the desired output.

If you want your output to contain videos of your µGs, choose yes. Since videos are very time consuming (in comparison to simple images or slices), you can choose which types of videos you want in your output.

If you net videos of your µGs rotating around the x, y, and z axes, choose **yes** and enter the rotation increment in **radian per frame**. The µGs will always make one full rotation (360° or 2π).

The example videos which come with the manual were made with an increment of 0.005 rad per frame.

If you need your output to contain videos slicing through your µGs along the x, y, and z axes, choose **yes** and enter the slice increment in **nm per frame**. The video will always slice through the entire µG and then return the µG on the way back.

The example videos which come with the manual were made with an increment of 2 nm per frame.

If you need your output to contain videos of a single slice walking through your µGs along the x, y, and z axes, choose **yes** and enter the thickness of the slice **in nm** and the walking increment in **nm per frame**. The slice will walk through the µGs twice.

The example videos which come with the manual were made with a slice thickness of 100 nm and a walking increment of 2 nm per frame.

If you need your output to contain a video of the µG being built up from the densest points, choose **yes** and enter the rotation increment in **radian per frame**. The µG will always make one full rotation around the z axis and complete the buildup with the last frame.

The example video which comes with the manual was made with a rotation increment of 0.005 rad per frame.

Since Mathematica itself produces pure quality videos for this purpose, the program **ffmpeg** is used instead. This means that the individual frames of the video are created in Mathematica, while the video itself is reconstructed with ffmpeg. This step is done automatically but represents the most time-consuming part of the µBerry-routine! Usually, depending on the input parameters, the videos construction takes 5 min per video.

2.5 Color function tab

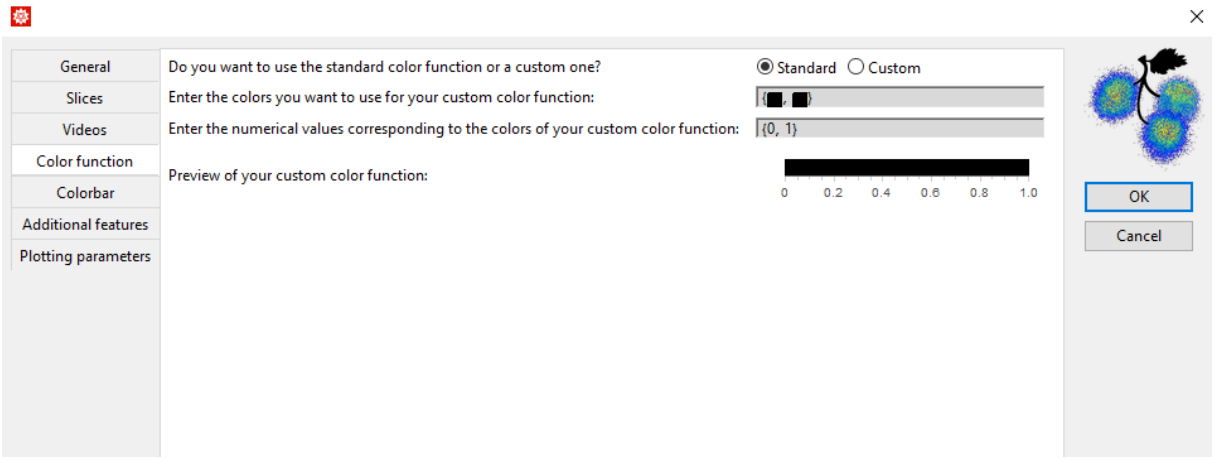

S.I. 8-19: Color function tab of the user interface where the jet-like color function is programmed in the default settings.

By default, µBerry operates in density mode and uses a jet like color function for the graphics. In the case that a different color function is needed, other color bars can be chosen.

To make nwe color function, two lists have to be entered: (1) a list of colors to be used in the color function and (2) a list of numbers corresponding to the colors. Lists in Mathematica have to be written in brackets { } and individual elements of the lists are separated by commas. As an example, a completely black color function is loaded by default.

There are multiple ways in which colors can be specified in Mathematica:

- The easiest way is to simple use the name of common colors like Blue, Red, Yellow, Green, etc. Please note that these colors always have to start with a capital letter!
- Of course RGB codes can also be entered as colors. **Write RGBColor[red, green, blue]** to add the color. Please note that Mathematica does not operate with the usual range of 0-255, but with the range of 0-1. Instead of adding the RGB codes of the desired color, it is also possible to add the hexadecimal code (**also using RGBColors[ ]**). Please note that the code has to be in **""**.
- Mathematica also has a vast number of named colors and color functions which are free to use. Choose Palettes from **the top menu**, then **Color schemes** to access a list of colors directly in Mathematica. You should use an empty notebook to do this because Mathematica lets you import the color from the menu directly into the code. This way, you do not accidentally add code where

it does not belong. To use color functions as the basis of your color, write **ColorData[Color Scheme in "", number]** to get a specific color (e.g. **ColorData["Rainbow", 1]** will produce the color at the numerical value 1 of the color scheme Rainbow).

The UI contains a preview of the color function that is entered. This means you can check whether the selected function is to your liking and alter the color function without having to make the output. Please note that the preview is updated only every time you switch objects like text boxes or radio buttons. Additionally, once you have entered the color specifications and change objects, Mathematica should transform your code into little squares in the color you have chosen. In case you have made a wrong input for the color function, the preview will turn dark red / brown color. This usually means that the number of colors and numbers does not match.

2.6 Color bar tab

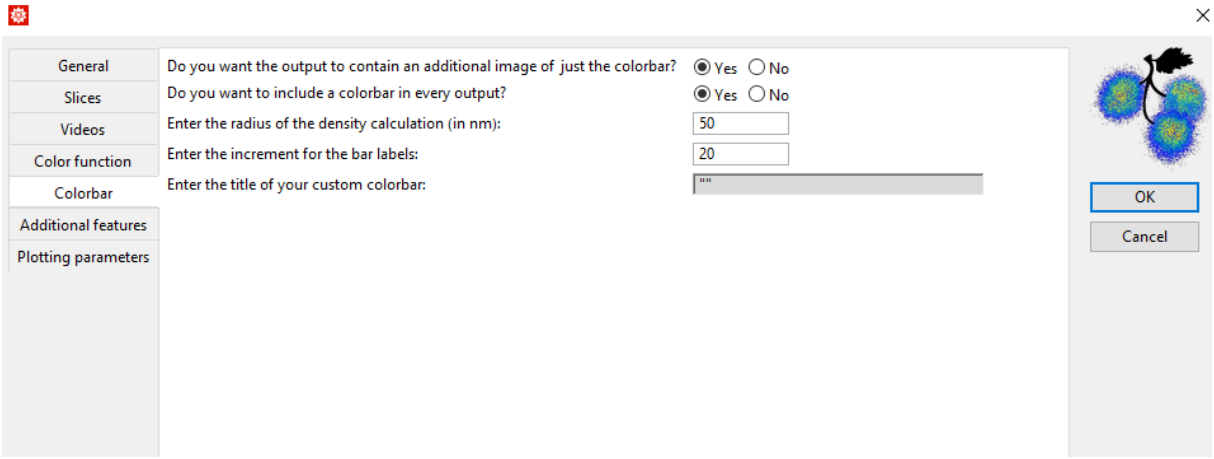

S.I. 8-20: Colorbar tab in the user interface of µBerry including default setting for the radius of the density calculation and the increment for the bar labels.

If the output should contain an additional image of just the color bar, choose yes. It will be saved in the directory **Images**. By default, this option is selected.

If you need every single image / video to contain the color bar, choose yes.

If no is chosen, only the grids will have the color bar, as they use a slightly different colorbar.

If you the standard color function was choesen, you have to enter the radius of your density calculation in nm. This information is needed for the correct title of the color bar. Additionally, this value will be taken for the calculation of the density (if needed, see below). No matter

which kind of color function you have chosen, you have to enter the increment for the bar labels.

The color bar will always have a label at its minimum and maximum value and additional labels depending on the increment that was chosen. In the case of a density color function, you will have to guess a first value (as you most likely don't know the maximum density) and then correct the increment in a second run. If you have chosen a custom color function, you have to enter the title of the color bar:

1. If the title is a simple word / phrase, just enter it as a string (in **""**).

2. If the title ha bold or italic elements, use **Style[string, Bold / Italic]**.

3. If the title contains superscript or subscript elements, use **ToString[Superscript[normal string, superscript string]**, **StandardForm]** (or Subscript...)

4. Strings can be connected to each other by using **<>**.

2.7 Additional features tab

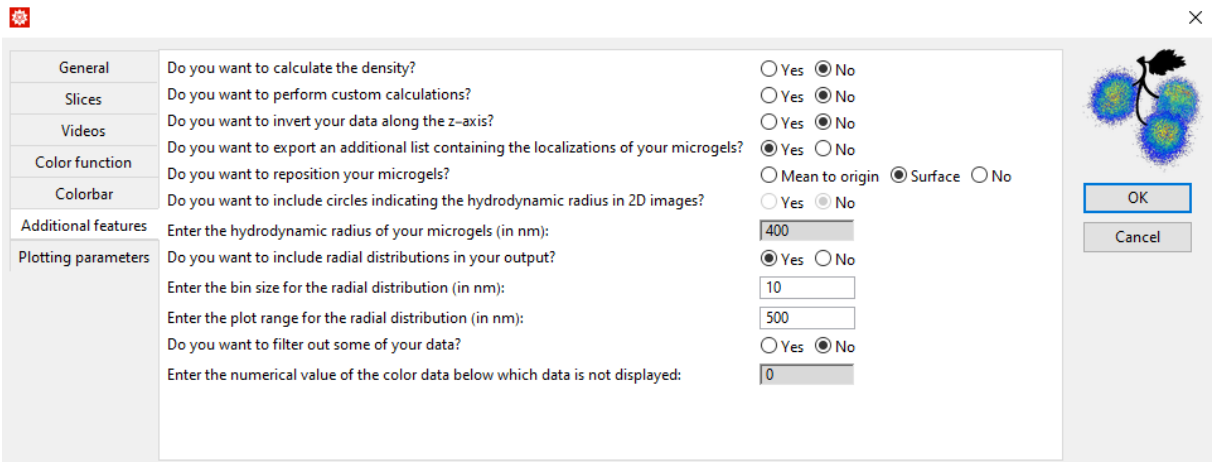

S.I. 8-21: Additional features tab of the user interface of µBerry including default settings for the bin size of the hydrodynamic radius, radial distribution, the plot range for the radial distribution. These settings can be changed according to the input data.

In case the data density was not already, you can do so with this program. The density calculation takes time (a data set containing roughly 15,000 data points takes roughly 2-3 minutes).

If you this option in chosen, the program will automatically export .csv files containing the input data and the calculated densities to a directory called **Density** in your main directory. This way, you will not have to do the calculation again in the future.

In case you want to perform your own calculations, you can choose yes. In this case, you have to manually add code to the program to make your calculations. In the standard code, there is an empty if condition which you can fill with your code (press **CTRL + f** to search for **(* Custom calculations *)** to find it.

- At this point of the program, the µG data is stored in a list called **data**. To access individual µGs in the list, **use data[[# of µG]]**. Please note that the first element of a Mathematica list is indexed as 1 and not as 0, as is common in other languages.
- If you want to access parts of a µG's data, use **data[[# of µG]][[# of row, # of column]].** Instead of entering a number, you can also use **All** to select all rows / columns. For example, **[[All, 3]]** will select the entire third column (meaning all z values). If you want to access multiple adjacent elements, use **number ;; number**, e.g. **[[1, 1;;3]]** will select the first three entries (x, y, and z coordinates) of the first point.
- Most likely, you want to perform the calculations in a loop for all your µGs and a for loop would be the standard choice for this in many languages. Do NOT do this in Mathematica as for-loops are very slow and prone to bugs! Instead, use a **do-loop** (which is basically the same as a for-loop but works more reliably in Mathematica). Do-loops are entered as **Do[commands, {iteration variable, min value, max value}]**. If you want to use more than one command in the loop, seperate them by using semicolons.
- **After each line of code, you should always include a semicolon.** Otherwise, Mathematica will print everything you do in the notebook which dramatically decreases speed.
- Simple calculations like adding, subtracting, multiplying, and dividing are performed using **+, -, *, and /**. You can also combine them with **=** to automatically apply the operation to the variable, e.g. variable ***= 2** is the same as variable = variable * 2.
- If you want to use **if conditions**, write **If[condition, true, false, neither]**. The options false and neither are optional; only true has to be added (although it can be left empty). If you want to select only certain parts of your data, you can use **Select[list, condition]**. The condition in this case has to be followed by an additional **&!** If you want to access certain numbers of your list, you can use **#[[number]]**. For example, the condition **#[[3]] => 0 &** will select all entries of the list whose z coordinate is larger or equal to 0. If multiple conditions have to be true, combine them using **&&**. If one true condition out of a group of conditions is sufficient, you can use **||**.
- If you want to sort your list, you can use **SortBy[list, condition]**. In this case, the condition should be one entered **as #[[# of column]] &**. Depending on how you want your list to be ordered (ascending or descending), you may have to add a **-** before the condition (as a simple workaround).

- If you need additional commands for your custom calculation, you can use the online resources of Mathematica. Mathematica has explanations (with examples) for virtually any command and there are many great tips in online forums etc. Alternatively, you could try going through the code of µBerry. There are many operations which cannot be discussed here in detail and which may be useful for you. In general, the code has comments to explain how certain commands work and why they are used.

If you want your data to be inverted along the z axis, choose yes.

In general, the program allows you to position the µG in 3Different ways. If you choose **origin**, the µG is shifted to the origin of the coordinate system.

If you choose **surface**, the µG is shifted to the origin of the coordinate system and then it is shifted along the z axis to only positive z values.

If you choose **no**, the µGs aren't moved at all.

Depending on which choice you make here, you have to enter different plotting parameters (see below).

In case you have chosen to reposition your µGs to the origin, you have the option to include circles in your 2D images (xy face, xz face, and yz face). These circles indicate the hydrodynamic radius which you have to enter (in nm).

µBerry also comes with the option to filter out data according to the fourth column (and the fourth column only!).

If you choose **yes**, you can enter the minimum numerical value of the data points that need to have to be displayed. This option might be useful to remove stray data points with e.g. low density to make better images. For obvious reasons, this option is turned off by default and should be used with caution.

2.8 Plotting parameters tab

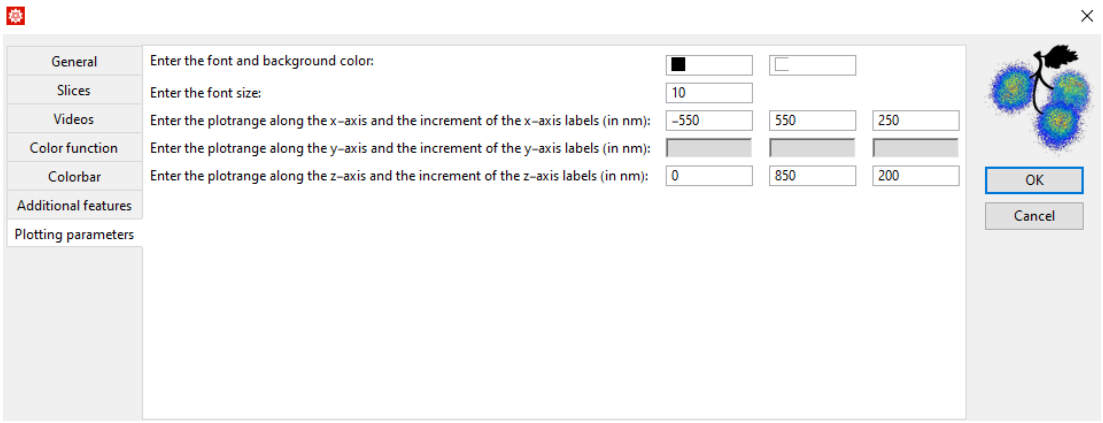

S.I. 8-22: Plotting parameters tab of the user interface of µBerry including default values fpr the plotting parameter of a µG of ~1 µm in diameter. The values can be adjusted according to the sample.

The last tab contains information needed to plot the data. Different fonts and background colors can be imaged for the images (see above for information about colors in Mathematica).

By default, the background is set to transparent (None). The font size of the image can be changed by entering the value. By default, the font size is 10. If a much larger font size is chosen, the labels will unfortunately start overlapping.

Depending on which positioning method was chosen previously, the following data has to be entered:

- If **origin** was chosen, the program will create a cube around the µG. The minimum and the maximum coordinate along the x axis have to be entered which should still be displayed in the images (as the size of the cube). Additionally, the increment for the axis labels have to be entered. 0 will always be labelled! Since a cube has identical sides, only the labels for one side have to be entered.
- If **surface** was chosen, the program will create a square prism around the µG. For this, you have the minimum and maximum coordinate along x (which will also be used for the y axis) and the minimum and maximum coordinate along z have to be enterd. Each axis has to be given different increments
- If **no** was chosen, the program will create a cuboid around the µG and the minimum and maximum coordinates as well as the labelling increments for each axis individually have to be entered.

8.2. Supporting information chapter 4

This chapter includes the supporting information corresponding to chapter 4, lithographic approach to immobilize µGs via hybridization. First, the additional microscopy data for the evaluation of the thiol-yne reaction will be provided in section 8.2.1. The optimization of the incubation time used for section 4.2.3) is described in section 8.2.2. Section 8.2.3. provides the analysis of the influence of alkaline condition on the photolabile protective group and finally, the visualization of the c-EBL pattern in transmission mode is described in 8.2.4.

8.2.1. Analysis of the thiol-yne reaction

Here, the monitoring process of the protection reaction of the pattern (see section 4.2.2), is presented. Due to the uncompleted conversion of the thiols with the protection group, the faint pattern can be analyzed. Each histogram represents the photon counts depending on the fluorescent intensity. For each measurement, the histogram was taken of an equally sized area. and the mean value of the intensity was later used for comparison with other measurements. Each measurement represents a protection with a varying concentration of the protecting group (pH=10).

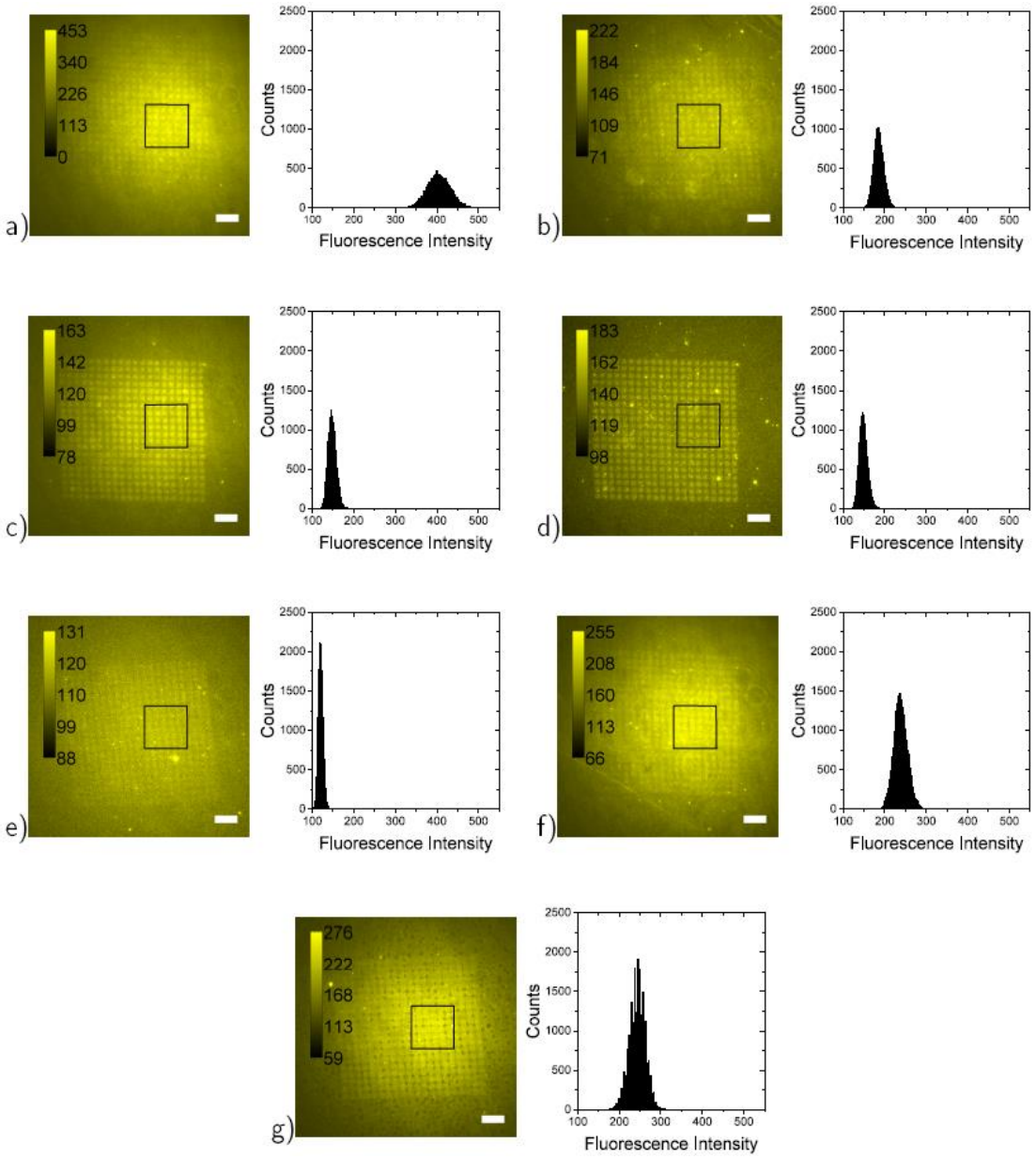

S.I. 8-23: The different protecting group concentrations are 0.5 mmol L-1 (a), 4 mmol L-1 (b), 7 mmol L-1 (c), 10 mmol L-1 (e), 13 mmol L-1 (f), 16 mmol L-1 (f), 20 mmol L-1 (g).). The scale bars refer to 10 µm. The measurements were performed by Pia Lenßen as part of her Bachelor thesis.

After the ideal PPG concentration of 13 mmol L^{-1} was found, the incubation times for this concentration were varied. Again, the measurements were analyzed taking the mean fluorescence intensity of the faint pattern.

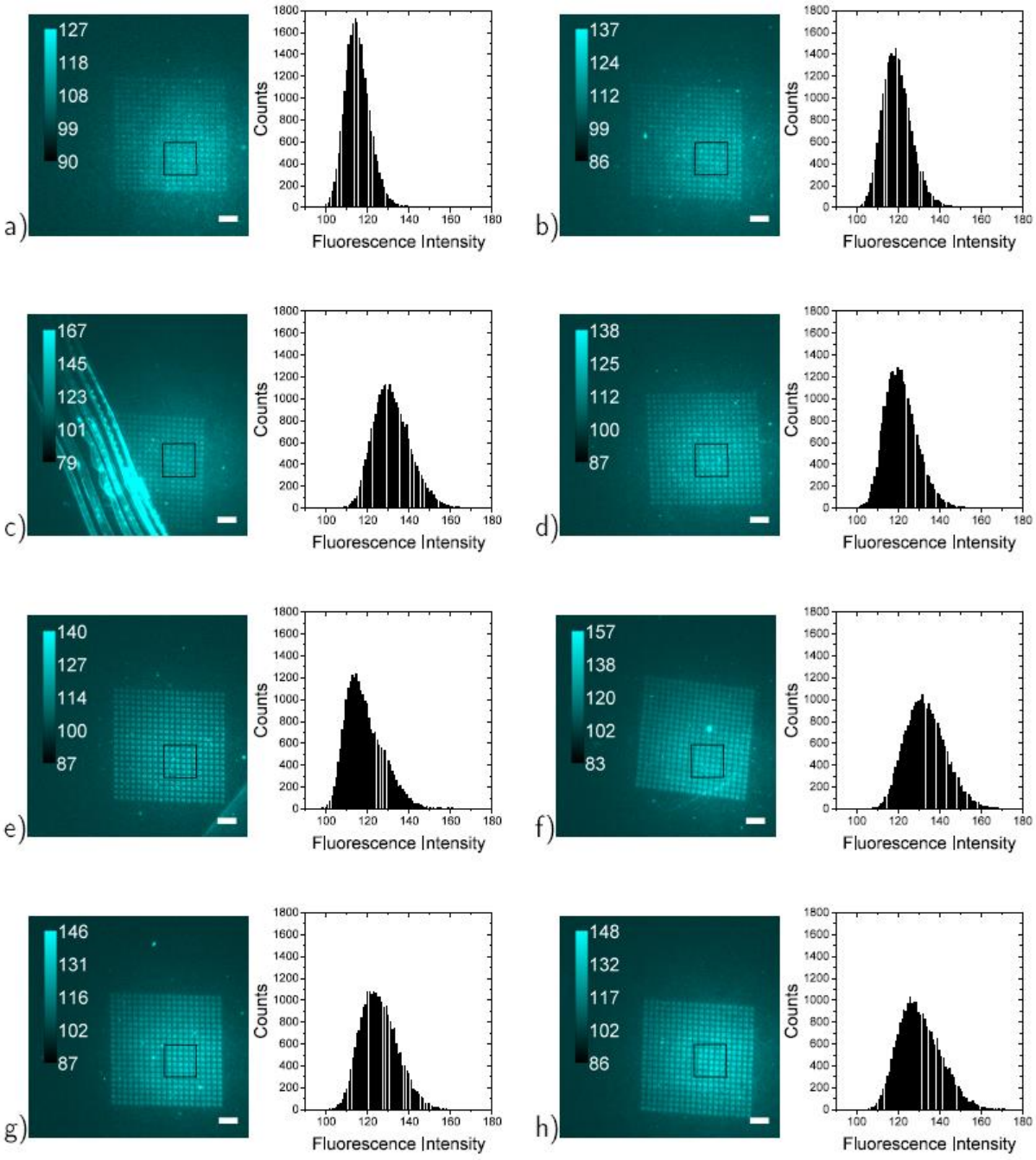

S.I. 8-24: The different protecting group incubation time are no exposure (a), 10 s (b), 30 s (c), 1 min (e), 2 min (f), 3 min (f), 5 min (g), 10 min (h). The scale bars refer to 10 µm. The measurements were performed by Pia Lenßen as part of her Bachelor thesis.

8.2.2. Optimization of the incubation time of the sDNA

In order to optimize the complete functionalization of the thiols (spots) at the surface (see section 4.2.3), the incubation time of the DNA-functionalized linker has to be adjusted. Therefore, a thiol-DNA-SMPB solution was incubated on the deprotected, patterned surface for 80, 100, 120 and 150 minutes.

The pattern definition appears to be related to the quality of the DNA immobilization. It should be noted that a high quality in this case refers mainly to sharp spot edges and homogenous fluorescence of the pattern. This is based on the idea that for increasing incubation times, the immobilization density increases up to a specific point at which all thiols are reacted. The pattern quality is then expected to decrease and result in blurriness due to the formation of multilayers and an increase in unspecific binding events.

The comparison of the fluorescently labeled sDNA-functionalized pattern is depicted in figure S.I. 8-25.

After and incubation time of 80 minutes, the fluorescence is homogenous and the pattern is clearly visible even though the spot edges are not sharp.

After 100 minutes of incubation time the fluorescence of the pattern is still homogenous, but now the spot edges are clearly defined and can be classified as sharp.

After 120 and 150 minutes of incubation time a decrease in fluorescence can be observed. The single spots become more blurred in comparison to the sample previous sample.

As a conclusion, for all subsequent experiments the thiol-DNA-SMPB solution was incubated on the deprotected, patterned surface for 100 minutes.

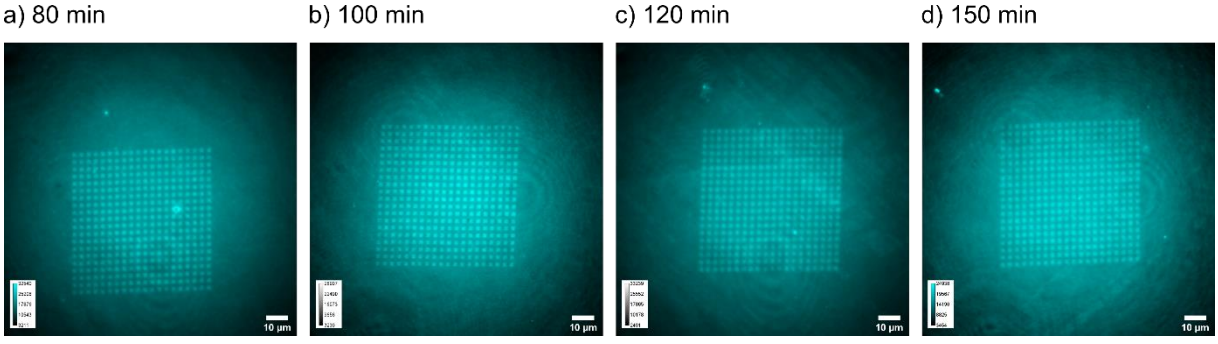

S.I. 8-25: Optimization of the incubation time of the sDNA reaction to a SMPB linker at the deprotected surface. The pattern is visualized by sDNA labeled with Atto 565. The fluoresce images are taken in TIRF mode to reduce background fluorescence.

8.2.3. Influence of alkaline condition on the PPG

The analysis of the influence of the alkaline conditions (section 4.2.2) given through the addition of NaOH were analyzed with UV/VIS spectroscopy as well as with NMR spectroscopy.

a) UV/VIS measurements

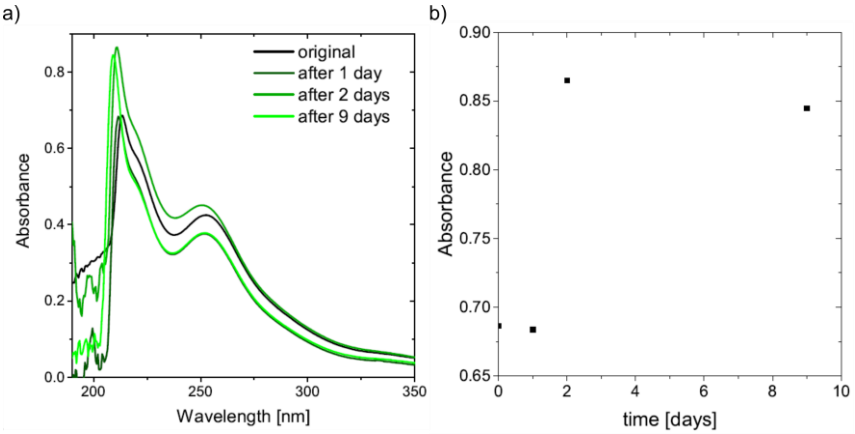

S.I. 8-26: UV/VIS spectra of the photolabile protecting group with NaOH in ethanol (a). The vial with the reaction solution was stored for a total of nine days and measured after the first, second and ninth day. Maximum absorbance of the four curves depicted in (a) against the measuring time (b).

The UV/VIS spectra of the protecting group in ethanol with the addition of NaOH clearly show a spectral change in the presented diagrams in S.I. 8-26. On the one hand the maximum absorbance peak increases with time, on the other hand a wavelength shift of the position of this peak can be detected. The changes in the UV/VIS spectra indicate that the protecting group is indeed affected by the alkaline conditions. In order to further analyze these changes NMR measurements were conducted.

b) NMR measurements

To substantiate the results acquired with the previously shown UV-VIS measurements, suitable proton NMR experiments were performed. For this purpose, the photolabile protecting group was solved in deuterated methanol, as this has similar properties to ethanol, which is used within the thiol-yne reaction. S.I. 8-27 shows the simulated 1H-proton NMR for the protecting group with the theoretically assigned protons to the respective peaks. This theoretical spectrum is used as a reference for the experimentally measured spectrum of the protecting group without any additions (see S.I. 8-28). Figure 18 displays the spectrum of the original protecting group.

In contrast to the predicted spectrum, a clear split-up of the aromatic peaks (protons 1, 2, 3 and 6) and the methyl peak (proton 13) as well as small multipletts in the range of 3.3-3.8 ppm

can be seen. It is known for molecules with stereogenic centers that for R/S-configurations the chemical shift of surrounding nuclei can be different.(Jennings 1975, Buist, Marecak et al. 1995) In regard to this information and the circumstance, that the protecting group has a stereogenic center in position 7, the split up of the peaks can be directly related to the chirality of the molecule. Due to the integral ratio of 1 : 0.11 for equal groups it is assumed, that the protecting group is a non-racemic mixture of the two possible configurations.

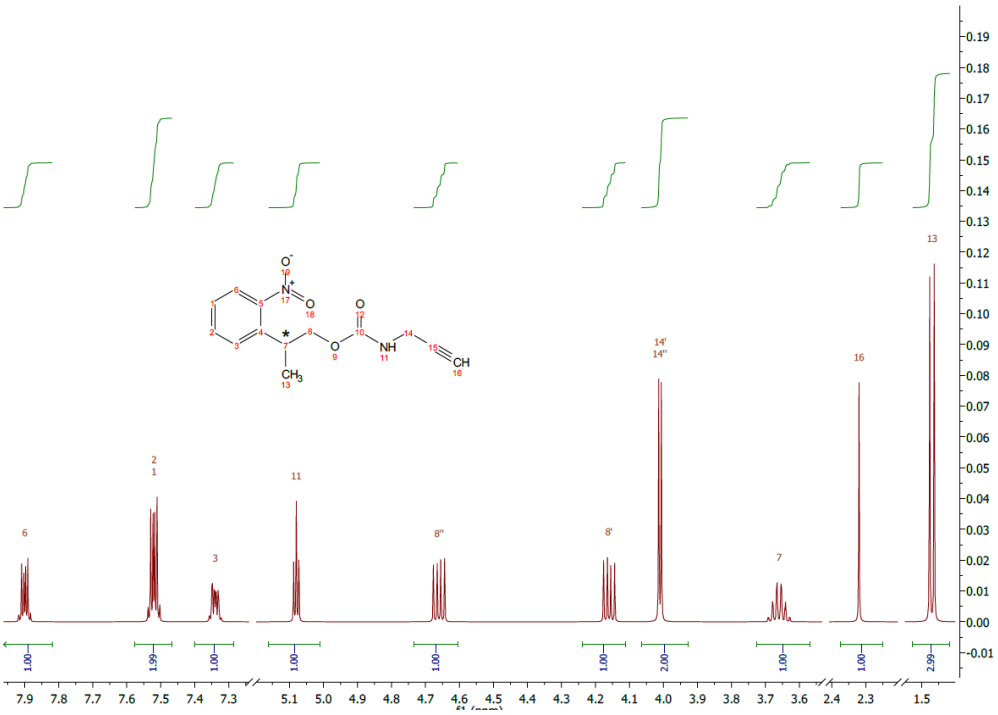

S.I. 8-27: Predicted NMR spectrum of the photolabile protecting group. The spectrum was predicted using the Mestrelab software Mestrenova.

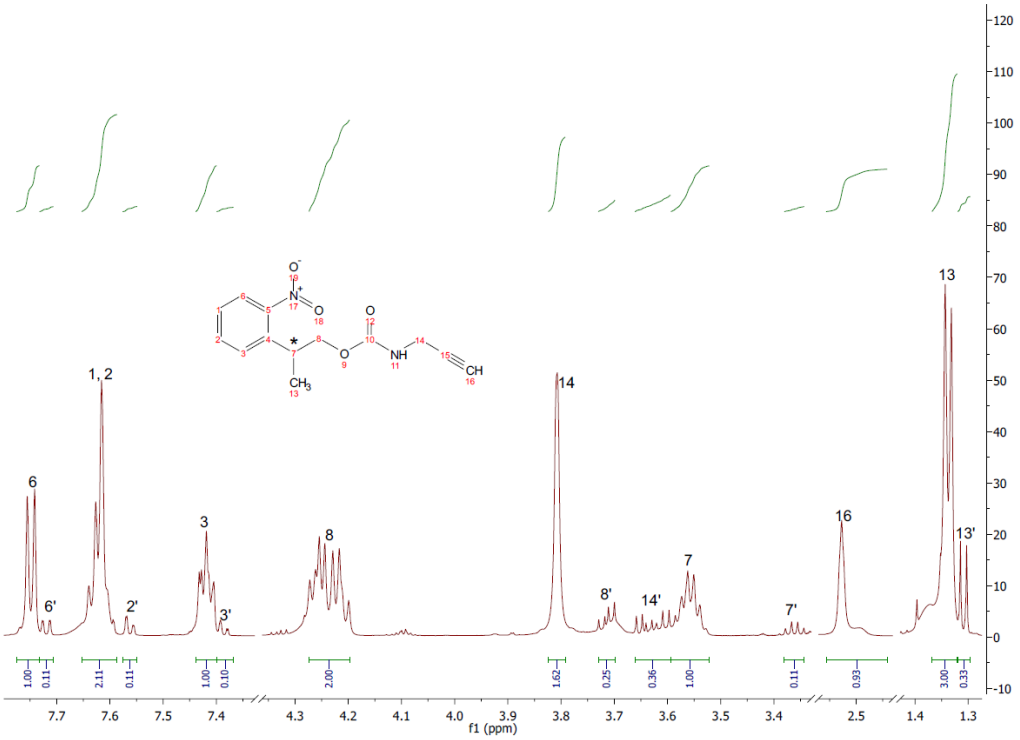

S.I. 8-28: ^{1}H-NMR spectrum (600 MHz) of the photolabile protecting group in deuterated methanol with the assigned protons.

Four spectra are displayed in S.I. 8-29 depicting (a) the original sample of the photolabile protecting group, (b) the same sample illuminated with ambient light for eight days, (c) the spectrum of a mixture of the protecting group with NaOH and (d) the same sample as c) after eight days, which revealed spectrum d). The only difference between spectra a) and b) lies in the decrease of peak 16, which is related to the slightly acidic proton of the terminal alkyne. This change is ascribed to an exchange of this proton with deuterium of the solvent. The more deuterium is introduced, the weaker the signal at this position.

The comparison of spectrum c) and d) reveals a change of the chemical shift of each peak to lower values referred to the methyl peak of the solvent. Furthermore, the peak of the acidic proton 16 disappears, which can be ascribed to a faster exchange of this proton with deuterium in presence of NaOH. An abstraction of the proton on this position seems inconceivable because NaOH provides not enough base strength.(Cram 1965) A significant change from spectrum c) to d) is the convergence of the peak areas of the two molecule configurations. An explanation for this convergence is the racemization of the stereogenic center induced by NaOH. A complete racemization leads to equal signal intensities for both configurations. Basing on the NMR experiments, it is probable, that the protecting group is stable against ambient light and is racemized by the influence of NaOH. Contradicting, the UV/VIS experiments lead to the conclusion that the influence of NaOH, has an impact on the molecular

structure. It is stated that there is a change in the protecting group which can be detected by UV/VIS but not by NMR spectroscopy, due to differences in the measuring sensitivity. Further NMR experiments with higher exposure times to NaOH might give indication about the occurring processes. Meanwhile, it is assumed that the influence on the protecting group are negligible in terms of practical applications. Therefore, the process towards the project goal described in section 7.2.2 is not hindered by the addition of NaOH at a pH of 10.

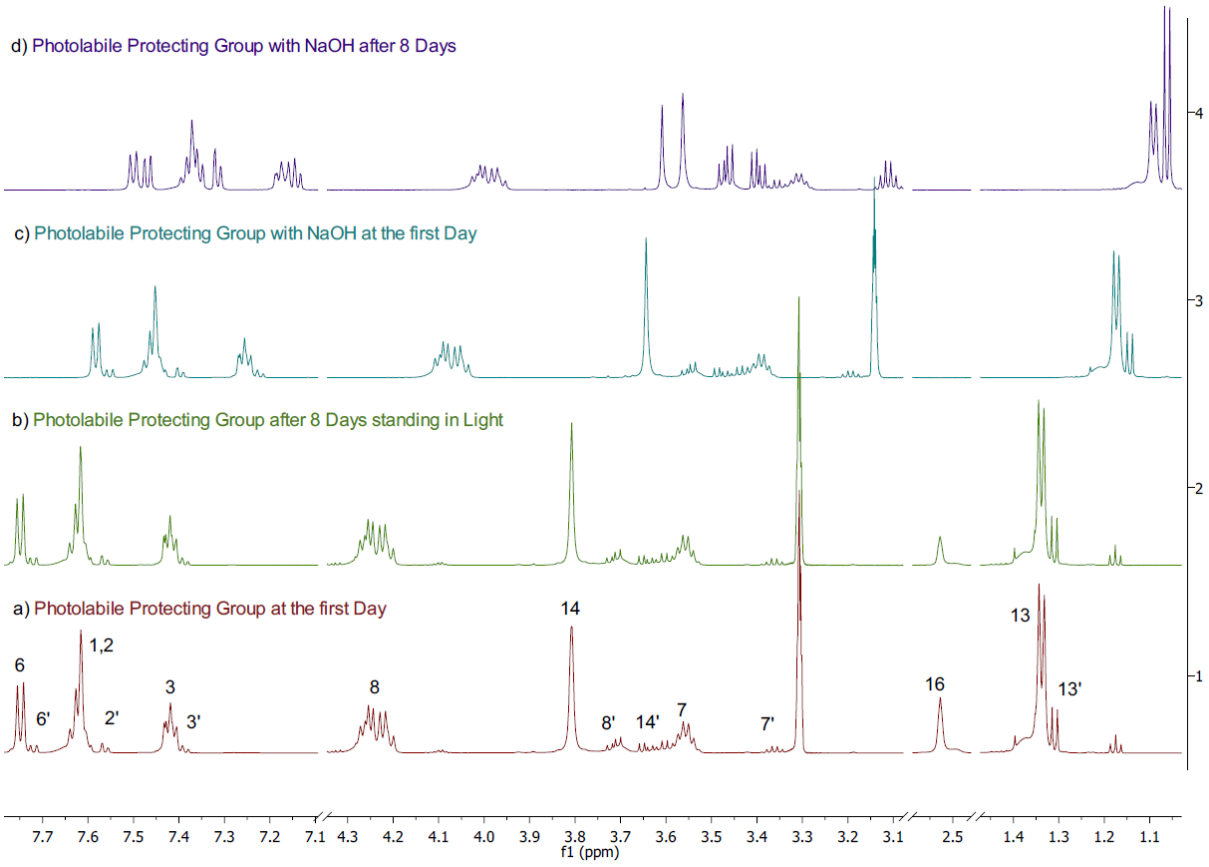

S.I. 8-29: ^{1}H-NMR spectrum (600 MHz) of the photolabile protecting group at the first day without any exterior effect (a), after 8 days without protection from ambient light (b), after one day of exposure to NaOH (c) and after eight days of exposure to NaOH (d)

8.2.4. Visualization of c-EBL pattern in transmission mode

The smaller pNIPMAM µGs employed for the second attempt of immobilization have a R_h of 190 nm. The prove of concept was performed by hybridizing the µGs to the immobilized stands at the surface without a subsequent labeling step with the complementary, labeled DNA.

the preliminary measurement presented here consisted in imaging the unlabeled µGs in brightfield mode. In case of a successful immobilization, the pattern should already be visible in the transmission mode without the need of fluorescence microscopy.

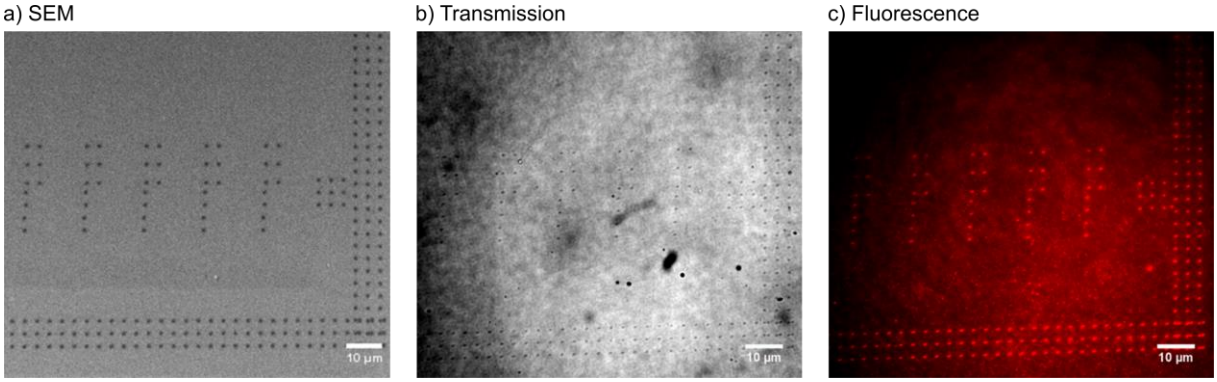

S.I. 8-30: Structured deposition of DNA-functionalized µGs (R_h = 190 nm). The left image shows the c-EBL pattern after the writing process in SEM mode (a). The middle image shows the immobilized µGs in transmission mode (d) and the right image shows the immobilized µGs after hybridization to the DNA strands at the pattern (c). Image (c) was taken in TIRF mode using a 640 nm laser.

8.3. Supporting information chapter 5

This section provides the step by step explanation of the automated image processing script and the analysis script employed in chapter 5.

8.3.1. Automated image processing and analysis by a python script

In order to enable the analysis of large data sets it is crucial to automate all processes that follow the measurements. This includes each step from image processing to DNA strand recognition and length measurement up to the analysis of the intensity profiles. In previous studies these different steps were performed using multiple programs. One example is the images analysis in ImageJ (Wayne Rasband, National Institutes of Health, US) either by a macro or even manually if optimal contrast adjustment is needed. Previously, the cooperation partners in this project performed the analysis of intensity profiles mapping the strands by hand. The intensity profiles were obtained using the according function in ImageJ. The comparison of the experimental intensity profile was manually compared to a theoretical intensity profile in Excel (Microsoft).

The above described procedure is not suitable to analyze large data sets in an acceptable time span. Therefore, one of the goals in this projects consisted in the consolidation of the different analysis functions in a single automated program. For this purpose, the programming language Python (Python Software Foundation) was chosen due to its flexibility and its user number in the scientific community. In the following sections the general concept of the program implemented for this study is introduced and each part of the program is presented and explained with an example.

8.3.2. General concept

The Python program can be divided in three parts depending on the intended output of each part. The task and the process of every part of the program is illustrated in S.I. 8-16.

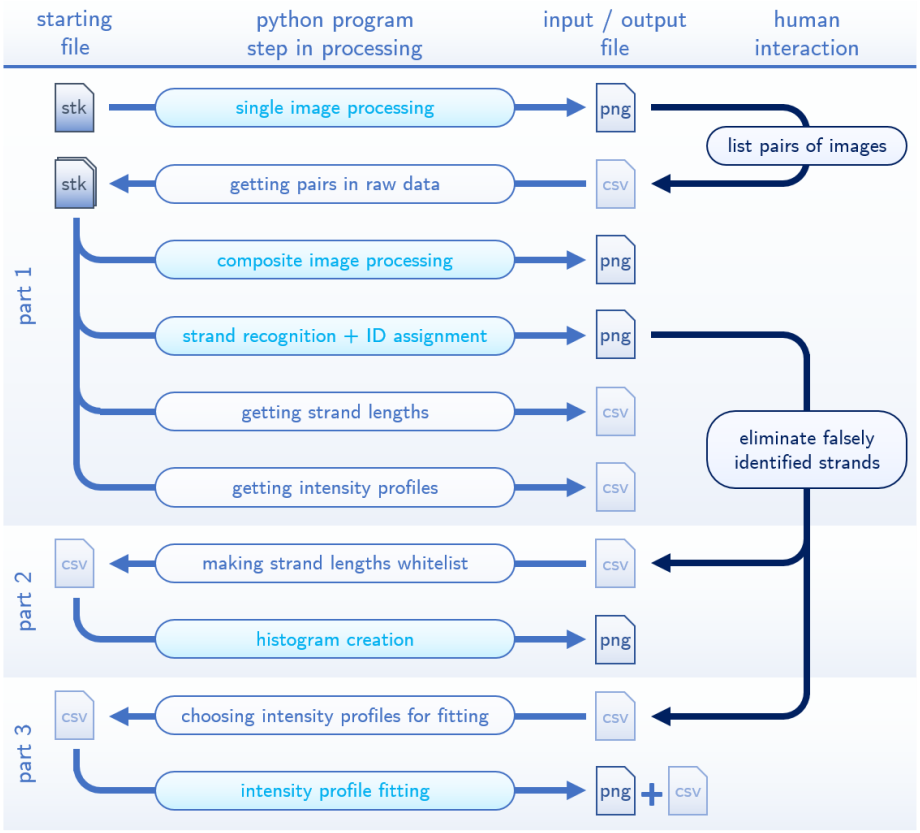

S.I. 8-31: Illustration of the image processing program in form of a flow chart. The program is divided in parts 1-3.

In the first step of part 1, the raw microscopic data is processed. The obtained images have a 16-bit format depicting the fluorescent intensity represented as the gray-scale value in dependence of the x- and y-coordinates. Each file contains several frames that were acquired consecutively imaging the same region. For each file, all frames are processed to a single image representing the brightness-encoded intensity of the signal in dependence of the two-dimensional position. Therefore, this image illustrates only one wavelength channel. Hence, it only contains the fluorophore intercalated DNA strands or the sequence specific labels.

After deciding manually which images contain the same region of the hydrogel, the second step of the part 1 is executed. Here, the corresponding images are combined and processed in a way that illustrates the affiliation of the labels to the DNA strands. Each of the two wavelength channels is represented by an individual color. Additional to the composite image processing, the second step of part 1 includes the crucial step of recognizing the strands.

A pattern recognition algorithm finds the strands and assigns an individual ID to them. Furthermore, the strand length is obtained for each strand. If a strand exceeds a particular minimum length, the intensity profile along the strand is determined. In a manual verification step, falsely identified strands can be eliminated by submitting them to a blacklist. By executing the second part of the program, a histogram of the strand lengths is created, excluding the previously blacklisted strands. The third part of the program covers the analysis of the intensity profiles along the DNA strands including a fit of a calculated profile to the data. All these steps are conducted for all images within one folder, where the folder represents the measured sample. It is possible to use a loop to repeat the entire processing and analysis for multiple folders in one single run. The decision about what folders shall be analyzed can be input by a file that must be named “config.csv” file. This includes further options like e.g. the definition of the colors for the output images. The entire procedure takes place in different sub-folders of one root folder, which will be referred to as `root/` in this report. The three parts of the Python program are located in the folder `root/python_program/` together with the configuration file. All raw data files of one sample are saved in the directory `root/raw_data/”sample_name”/`, where `“sample_name”` depends on the measured hydrogel. The processed images of the sample are located in `root/processed_images/”sample_name”/`, while all further analysis results including the strand length histogram and intensity profiles are saved in `root/analysis/”sample_name”/`. The entire folder structure is illustrated in S.I. 8-32

.

```
root/
    phython_program/
        HydroStretch-1-ImageProcessing.py
        HydroStretch-2-LengthStats.py
        HydroStretch-3-FitProfiles.py
        config.csv
    raw_data/
        "sample_name"/
            "raw images" (.tif, .stk)
    processes_images/
        "sample_name"/
            images_PNGs/
                "single channel images" (.png)
            composite_PNGs/
                "composite_strands_PNGs"
            composite_strands_PNGs/
                "composite images with strand IDs" (.png)
    analysis/
        "sample_name"/
            relating_images.csv
            length_distribution.csv
            length distribution blacklist.csv
            length_distribution_clean.csv
            length_distribution.png
            intensity_profiles/
                "intensity profiles" (.csv)
            theoretical_profile.png
            intensity_profile_fits/
                fit_images_meta.csv
                "intensity profile plots with fits" (.png)
```

S.I. 8-32: Structure of the directories and files that are part of the processing and analysis with the Python programs. The different type of files are color-coded as follow: Pink: python programs, brown: raw data, blue: manual input, green: output files.

8.3.3. Input via configuration file

There are a variety of input parameters that can be defined separately in the tabular configuration file. The first column contains the descriptions of the parameters whose values are defined in the second column. In the beginning of the input file it is defined whether only one or more than one folder shall be included. Then, the name of the folder or -in case of multiple folders- the common name root is requested. To recognize the multiple-layer images as stacks instead of movies, the usually used number of frames for each wavelength channel has to be stated along with the number of frames that shall be included in the processing. Furthermore, the colors for the intensity in both wavelength channels and for brightfield images as well as the associated color of the scale bar is requested. The colors used to plot and fit the intensity profiles can be customized as well. In addition, some thresholds and parameters for the analysis can be set. The entire configuration file is illustrated in S.I. 8-33.

Header	Settings			Descripton	Input Values
Folder_Mode	Single_Folder			here you can say, which folders shall be processed	options:"Folder_Root", "Folder"
Folder_Root	sample_root			only if "Folder_Root" is chosen	string, that all wanted folders start with
Folder_Name	sample_name			only if "Folder" is chosen	exact string of the folder name
Colors	Blue	Green	Red	colors for the processed images	floats between 0 and 1
Brightfield	1.00	1.00	1.00		
488	1.00	1.00	0.00		
561	0.00	0.70	1.00		
Scale Colors	Blue	Green	Red	colors for the scale bar in processed images	floats between 0 and 1
Brightfield	0.00	0.50	1.00		
488	1.00	1.00	1.00		
561	1.00	1.00	1.00		
Merging Alpha	Alpha			weighting factors for merging the two color channels	floats between 0 and 1
488	0.70				
561	1.00				
Frames in Stacks	Raw	Evaluate		Raw: number of frames in stacks of one coordinate	integers
488	10	10		Evaluate: number of frames with the best signal to noise	
561	200	100		that shall be used for averaging	
Binary Threshold Parameter	0.15			parameter for thresholding to binary image, threshold	floats between 0 and 1
				lays at parameter postion between min and max pixel	
Hough Lines Parameters	Values			Paramters for Hough Lines Transform	integers
rho	1			distance resolution in pixels of the Hough grid	
theta	1			angular resolution in degrees of the Hough grid	
threshold	20			minimum number of votes (intersections in Hough grid cell)	
min line length	20			minimum number of pixels making up a line	
max line gap	10			maximum gap in pixels between connectable line segments	
Grouping to Strands	Values			Parameters to group lines to strands	integers
Distance between Lines	5			maximum distance in pixels to belong to the same strand	
Angle between Lines	5			maximum angle in degrees to belong to the same strand	
Maximal Angular Divergence	15			Strands with bigger divergence are eliminated	integer
Frame Halfwidth	5			Half width of frame around strands in pixels	integer
Profiling Threshold Distance	13.6			minimum distance to be profiled	float
Width of one Pixel	0.10833			to convert pixel to µm and reverse	float
Histogram Settings	Values			Settings to Customize the Histogram	
Background Color	white			and the Intensity Profiles	valid string
Foreground Color	black				valid string
Hist Color	blue				valid string
Tick Size	20				integer
x/y Label Size	24				integer
Intensity Profile Settings	Values			Settings to Customize the Intensity Profiles	
Profile Color	blue				valid string
Fit Color	red				valid string
Margin Color	orange				valid string
Legend Size	16				integer
Fitting Settings	Values			Settings for the Fit	
Signal Treshold	0.05			to determine the fitting region, value is ralative intensity	float between 0 and 1
Sigma	0.1				float
Stretching Guess	1				float

S.I. 8-33: Illustration of the setting possibilities in the configuration file used as input for the Python programs.

8.3.4. Single image processing

In the first step of the part 1 of the program, the images taken in each wavelength channel are processed. This includes averaging frames in cases in which the image is a stack consisting of many frames, as well as contrast adjustment, coloring and adding scale bar and calibration bar. The entire process is depicted in an example in S.I. 8-34.

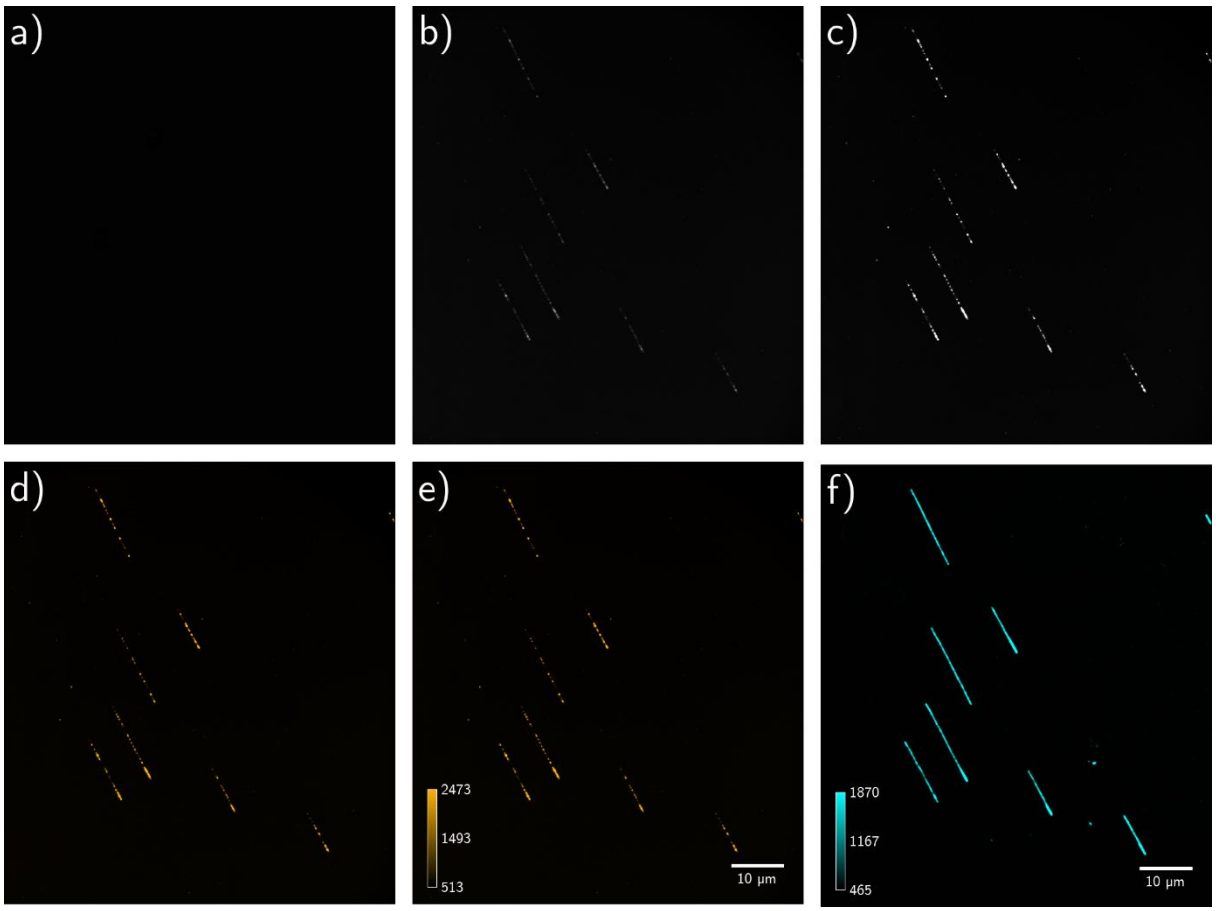

S.I. 8-34: An example image in the 561 nm channel through the entire processing chain. After averaging (a), linear contrast enhancement (b), sigmoidal contrast enhancement (c), coloring (d) and adding scale and calibration bar (e). The corresponding image in the 488 nm channel is depicted in (f).

Once an image le is loaded to the program, the image processing begins. The first step consists of deciding which format the file has. In case of a .TIFF file including a single frame image, no averaging has to be conducted. However, in case of an .STK file consisting of multiple frames two contents are possible. Either the frames belong to a movie acquired while moving to different x- and y-positions of the sample (STK movie) or all frames were acquired

at the same position of the sample to enable averaging over a longer time (STK image). The number of frames serves as a criterion for deciding between STK images and movies, since each wavelength channel has its own constant number of frames in STK images. This way an STK file recorded in the 561 nm channel containing 200 frames is identified as STK image and all frames are averaged for further processing. In the 488 nm channel STK images consist of 10 individual frames. The conditions that apply for averaging depend on the laser wavelength due to the possibilities to focus before capturing. In the 488 nm channel bleaching of the fluorophores is not critical as there is enough substance and only the shape of the strands has to be recognizable. The focus is adjusted prior to the capturing and all 10 frames are averaged. In contrast, bleaching of the labels in the 561 nm channel is very critical for further analysis since every single fluorophore molecule labels a sequence specific position. Therefore, the focus is adjusted manually while capturing and some frames are not in focus. In order to sort them out a criterion similar to the commonly used signal/noise ratio is defined and calculated for every frame. The gray-scale value of the brightest spot of the frame is divided by the average gray-scale value of the frame. The 100 frames with the highest ratio are averaged to a single frame image. STK files that contain movies are not processed any further. Subsequently, the contrast is adjusted linearly. This means, that the highest gray-scale value from the averaged image is set to be 255 which is the highest value for 8-bit images. The lowest gray-scale value is set to 0. The remaining values are adjusted linearly. In some images the strands are not perfectly distinguishable from the background after this contrast enhancement. Therefore, a second step of contrast adjustment is applied which is non-linear. By utilizing a sigmoidal function, the gray-scale values are shifted to the extremes. The differences between lower and higher signal regions are enhanced. The sigmoidal function is displayed in S.I. 8-35.

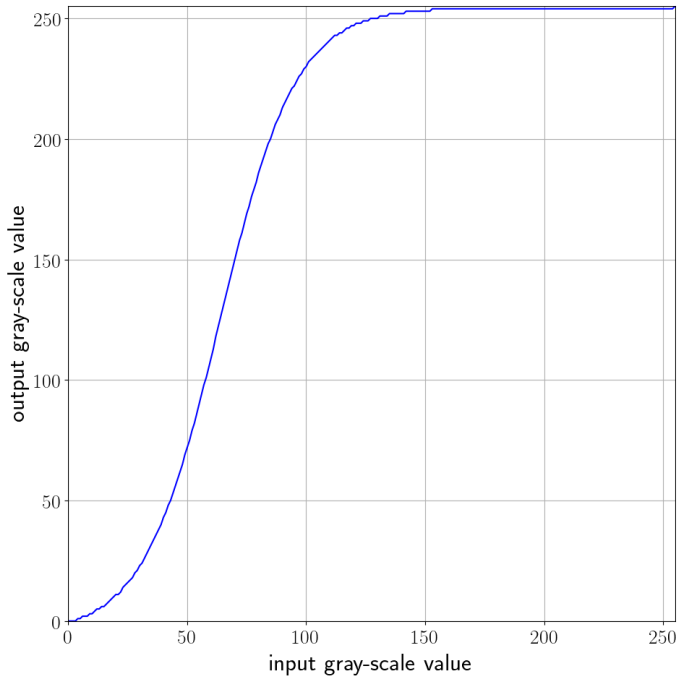

S.I. 8-35: Plot of the sigmoidal function used for the non-linear contrast adjustment.

One color for each wavelength channel is defined int the configuration file as the RGB color model . For each of the three primary colors red, green and blue, the gray-scale image is multiplied by the corresponding color factor between 0 and 1. The three-color channels are combined to one image.

Finally, the scale and calibration bars are added. The color of these elements can be controlled with the configuration file as well. For the 10 µm scale bar the distance of one pixel has to be entered to the configuration file. The corresponding number of pixels is calculated and the scale bar is placed in the lower right part of the image. For the calibration bar a color gradient is created in the lower left part of the image. Next to the bar the maximum and minimum gray-scale values of the original, averaged image are displayed. These values correspond to the intensities that were measured by the EMCCD. The images (e) and (f) of the image series in figure S.I. 8-34 illustrate the final result for both used laser wavelengths.

8.3.5. Composite image processing

Before acquired images of the two wavelength channels can be combined, they have to be assigned to each other manually. The previous step of the program created a CSV table with 488 and 561 as headers where the image IDs can be entered. Afterwards the second step of

the first program reads that table and repeats the composite image processing for every pair of images. The processing starts with averaging and contrast enhancement as described for the single image processing in S.I. 8-34. Subsequently, the two adjusted images are added to each other. The weighting factors for the addition are constituted by the configuration file. The scale bar is added in the same way as for single wavelength images. The calibration bar includes a color gradient as well as maximum and minimum gray-scale values for both wavelength channels. An example composite image is depicted in S.I. 8-36.

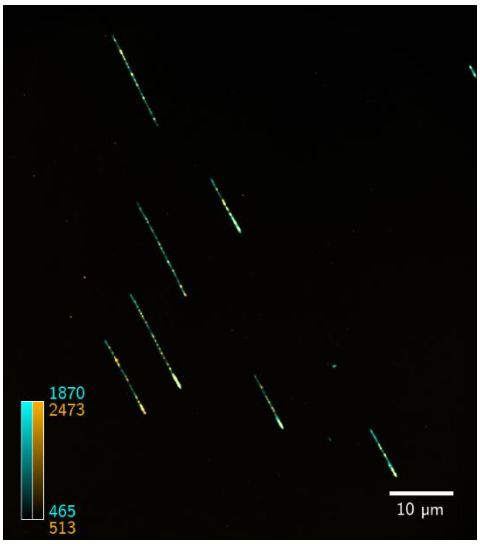

S.I. 8-36: Example composite uorescence microscopy image. The signals of the TAMRA labels acquired in the 561 nm channel (orange) overlay the entire DNA strands stained with YOYO-1® and imaged in the 488 nm channel (blue).

8.3.6. Pattern recognition for DNA strands

The recognition algorithm for DNA strands is included in the second step of the first program, as it is also performed for each pair of images. In addition to the contrast adjustments described in the previous section, a proportional contrast enhancement is conducted for both images. This means, that the maximum gray-scale value is set to 255 and the remaining values are adjusted proportionally. The proportional contrast image of the 488 nm channel serves as a starting point for the pattern recognition algorithm. The entire pattern recognition algorithm starting from an example image is illustrated in figure S.I. 8-37.

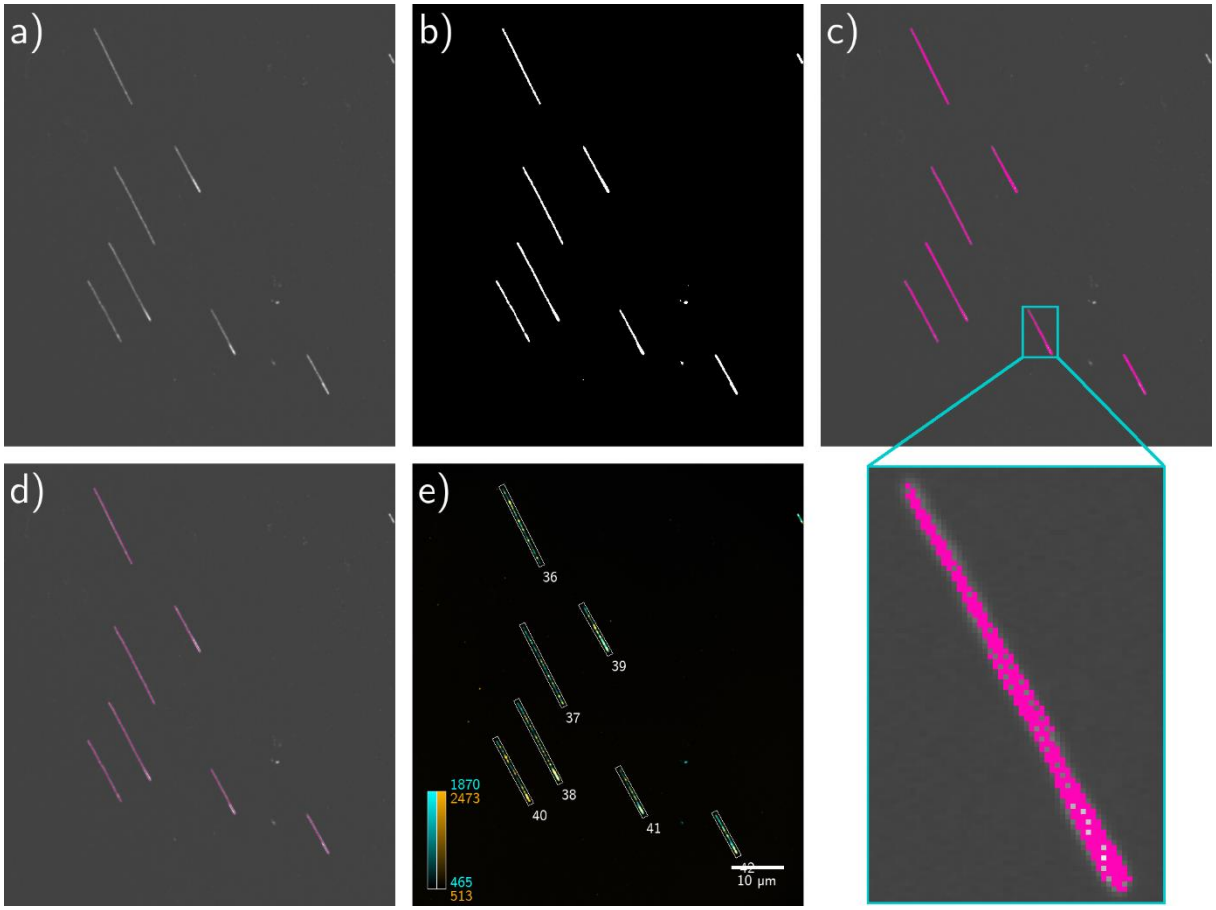

S.I. 8-37: An example image in the 488 nm channel with proportional contrast (a), after binarization (b), Hough lines algorithm (c), grouping the lines (d) and highlighting the strands in the composite image (e). The magnified region reveals several overlaying lines.

Initially, the image is binarized. All pixels with gray-scale values below a threshold are set to 0. The remaining ones are set to 255. The threshold is a weighted mean of the minimum and the maximum value, where the weighting factors are 0.85 and 0.15, respectively. The weighting can be changed in the configuration file.

Subsequently, the probabilistic Hough line transform(Hough 1962, Duda and Hart 1972) is executed on the binarized image. The transform is implemented in the OpenCV package for Python. The input parameters for the algorithm can be adjusted in the configuration file. The output includes all recognized edges in the image. Therefore, the algorithm does not directly recognize the DNA strands but their transitions to the background are identified as edges. Furthermore, recognized line segments overlay each other in many cases. In order to extract the strands from the line segments, a number of additional steps are necessary. First, the lines are assigned to groups where each group represents one strand. For this purpose, the distances and angles between all pairs of lines are measured. In case of both values remaining below a respective threshold set in the configuration file, the line segments are grouped. In the

beginning, one group is created for each line. Afterwards, these groups are merged resulting in only one group per strand.

Secondly, a line segment describing the DNA strand has to be extracted from each group of line segments. In order to obtain the straight (line) describing the strand, a fit is performed. The fit function can represent all possible straights that intersect the image in dependence of two parameters. The minimized value in the fit is the sum of all squared perpendicular distances between the end points of all line segments and the straight that is fitted. In order to determine the end points of the strand on the found straight, all end points of the line segments are projected on the straight perpendicularly. The outermost points define the end points of the strand.

When reviewing all recognized strands some obviously wrong strands can be identified including large impurities without a defined shape. Those spots tend to consist of multiple overlaying strands which is of advantage in order to eliminate them. First, the average orientation of the strands is determined. Secondly, the strands with a difference to the average orientation over a threshold from the configuration file are detected. For all of those strands it is tested whether they intersect with further strands. All strands that differ too much in orientation or that intersect one of those strands are eliminated. The result of this step is a list of all strands that were recognized by the algorithm. For each strand, the x- and y-coordinates of both end points, the length and the orientation are stored.

After recognizing all strands in an image, they are highlighted in the composite images from by frames. In addition, an ID is assigned to each strand. The IDs are consecutive for different images of the same sample, see image (d) and (e) in figure S.I. 8-37.

8.3.7. Strand length distribution

The list of strands serves as a starting point for the strand length distribution. For each strand the strand ID, the IDs of the 488 nm channel and 561 nm channel images and the strand length in µm are exported in a common CSV file during the second step of the first part of the program. In a manual step the images with recognized strands can be reviewed and strands that were recognized falsely, with wrong orientation or that protrude out of the image can be determined and entered to a blacklist CSV file. All those strands will be excluded from the strand length statistics. Once the two CSV files are created, the second program can be executed. It creates another CSV file that only includes strands which are not blacklisted. Their lengths are illustrated in a histogram. In that histogram the number of strands that have a length in the

same range of 1 µm are plotted versus the length. The histogram that is produced for the key measurement is depicted in Fig. 5-12 in section 5.2.13.

8.3.8. Intensity profile fitting

In the last step of the first program the intensity profile is determined for each strand that has a length above a threshold that can be set in the configuration file. The image from the 561 nm channel with proportional contrast adjustment serves as a starting point for obtaining the profiles. For this purpose, the end points of each strand are marked in this image. A continuous line of pixels between these points is received. For each pixel the distance to the first pixel is stored in µm. The gray-scale value of each pixel is stored as well. For each of the strands the lists of gray-scale values and distances are saved as a CSV file.

In the third program the obtained intensity profiles are analyzed by fitting a calculated profile to the data. This is conducted for all intensity profiles that were received from the first program excluding those belonging to strands that were blacklisted before. First of all, a fit function has to be defined. In this approach the function is calculated from the theoretical positions of the labeled sequences by summing up one gaussian for each position. All gaussians are assumed to have the same shape and area. This is reasonable since for an ideal system all fluorophores should exhibit the same characteristics and should therefore lead to the same intensity. In addition, it is beneficial for the fit as only two parameters, the gaussian prefactor I_0 and the standard deviation σ, have to be fitted. The development of this function is illustrated in figure S.I. 8-38. The orange diamond shaped dots mark the label positions on an arbitrary example strand. The single molecule intensities are represented by the blue dotted gaussians, while the full calculated profile represented by the red line is obtained as the sum of those gaussians. In order to fit this function to the experimental intensity profiles, two more parameters have to be considered. On the one hand the analyzed profile of the real strand may not begin at 0 resulting in a fit function that has to be shifted to the beginning of the strand. This is conducted by a shifting parameter x_0. This can have the effect that the real strand may be overstretched. This is considered by a stretching ratio factor r_s. An inverse profile is accessed by a negative stretching ratio.

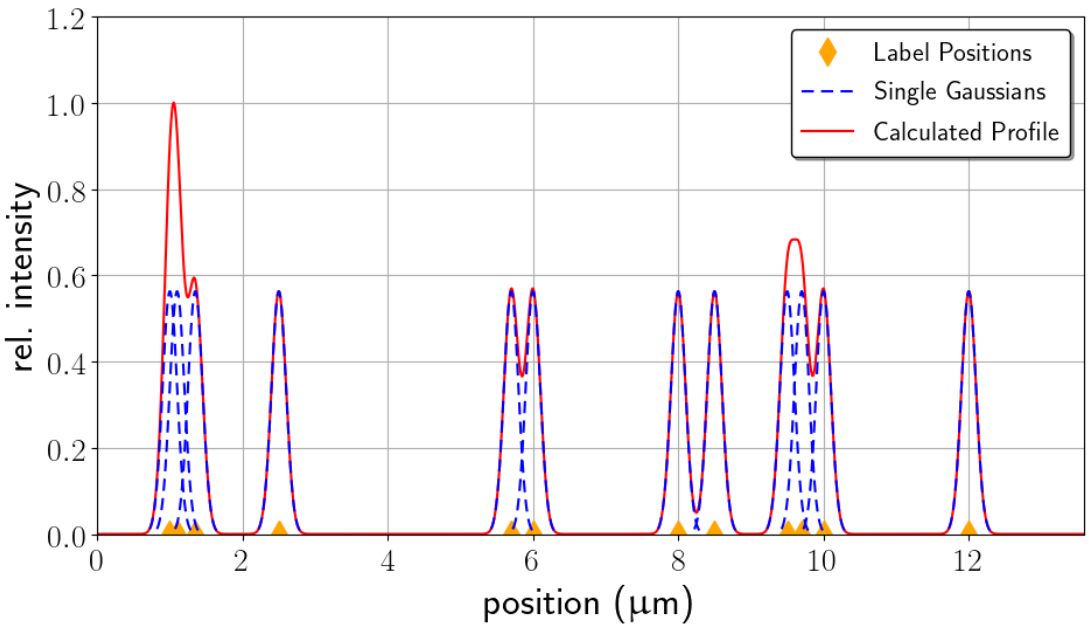

S.I. 8-38: Schematic of the development of the theoretical intensity profile for usage as a fit function by an arbitrary example. The orange diamonds mark the label positions, the blue dotted lines represent their gaussian intensities and the red line visualizes the sum as the theoretical profile.

After the fit function is defined, the least squares fit is executed for each non-blacklisted profile. All intensity profiles are analyzed in a loop one after the other. For each profile the values for the spatial and intensity coordinates are read. A base line correction is proceeded by subtracting the minimum intensity from the entire data set. All intensities are normalized to relative intensities resulting in the highest value equaling 1. In the next step, the margins of the fit are defined. The region of the fit begins at the first position with a relative intensity over a threshold and ends at the last position that fulfills this condition. The threshold can be set in the configuration file. Since the intensity profiles have many maxima and minima, the fit is not excessively stable. Therefore, a good set of initial conditions has to be chosen. To obtain the best possible result, six different sets of initial conditions are tried and the best one by means of the lowest sum of error squares is used. For all of the attempts the initial σ is input via the configuration file. The initial I_0 is received from the normalization of the calculated profile with the set σ. The sign of the stretching ratio is varied. Three attempts are based on each of the two orientations, forward and inverse. In the first attempt for each variation it is assumed that the fit region mirrors the entire strand. In this case, the stretching ratio is calculated as the ratio of the region width to the B-DNA contour length. The initial shifting parameter x_0 is set to the beginning or end of the of the fit region for the forward or inverse orientation, respectively. The remaining four attempts are executed with a fixed stretching ratio that is controlled in the

configuration file. The function is then aligned to the beginning or the end of the fitting range for both, forward and inverse orientation, which makes four possible alignments in total. All initial guesses are visualized in figure S.I. 8-39 . The parameters resulting from the best fit are kept for further analysis.

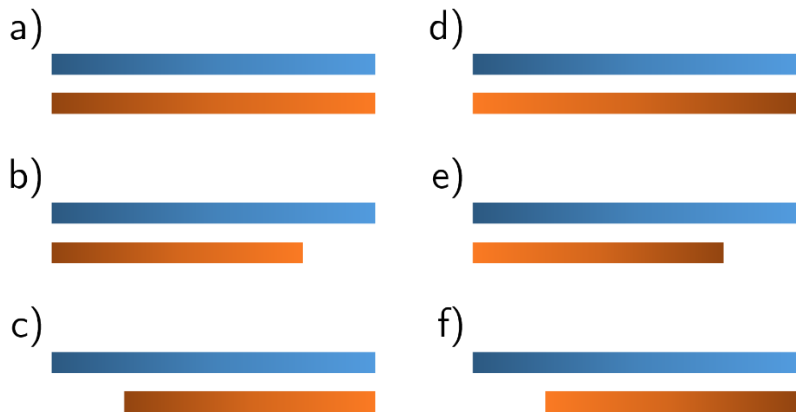

S.I. 8-39: The blue boxes represent the experimental intensity profiles, while the orange boxes represent the profiles produced by the fit function with different initial guesses. (a) - (c) depict forward orientations of the fit function, while (d) – (f) depict reverse orientations. In (a) and (d) the fit profiles are overstretched, in (b), (c), (e) and (f) they are aligned to one end.

For each of the intensity profiles a plot of the data and the theoretical profile calculated with the fitted parameters in the marked range is created. The fitting process is illustrated in figure S.I. 8-40 (a)-(d). An example result is depicted in figure S.I. 8-40 (e). The fitted parameters for all analyzed profiles are exported in form of a CSV file. In a manual step the unreasonable fits can be eliminated. A fit is regarded as unreasonable if one of the following two conditions apply. First, the standard deviation σ of the gaussians is too high. That means that the gaussians are too broad to mirror the real intensity profile. The threshold used for the results of this study is stated in section 5.2.14. Secondly, there is significant intensity at a position in the data where the fitted profile has a minimum at near zero intensity. Since this is a hint for a displaced fit, those fits can also be discarded. From the remaining, reasonable fits the absolute values of the stretching ratio are used to calculate an average stretching ratio $\overline{r_s}$ and the corresponding standard deviation Δr_s .

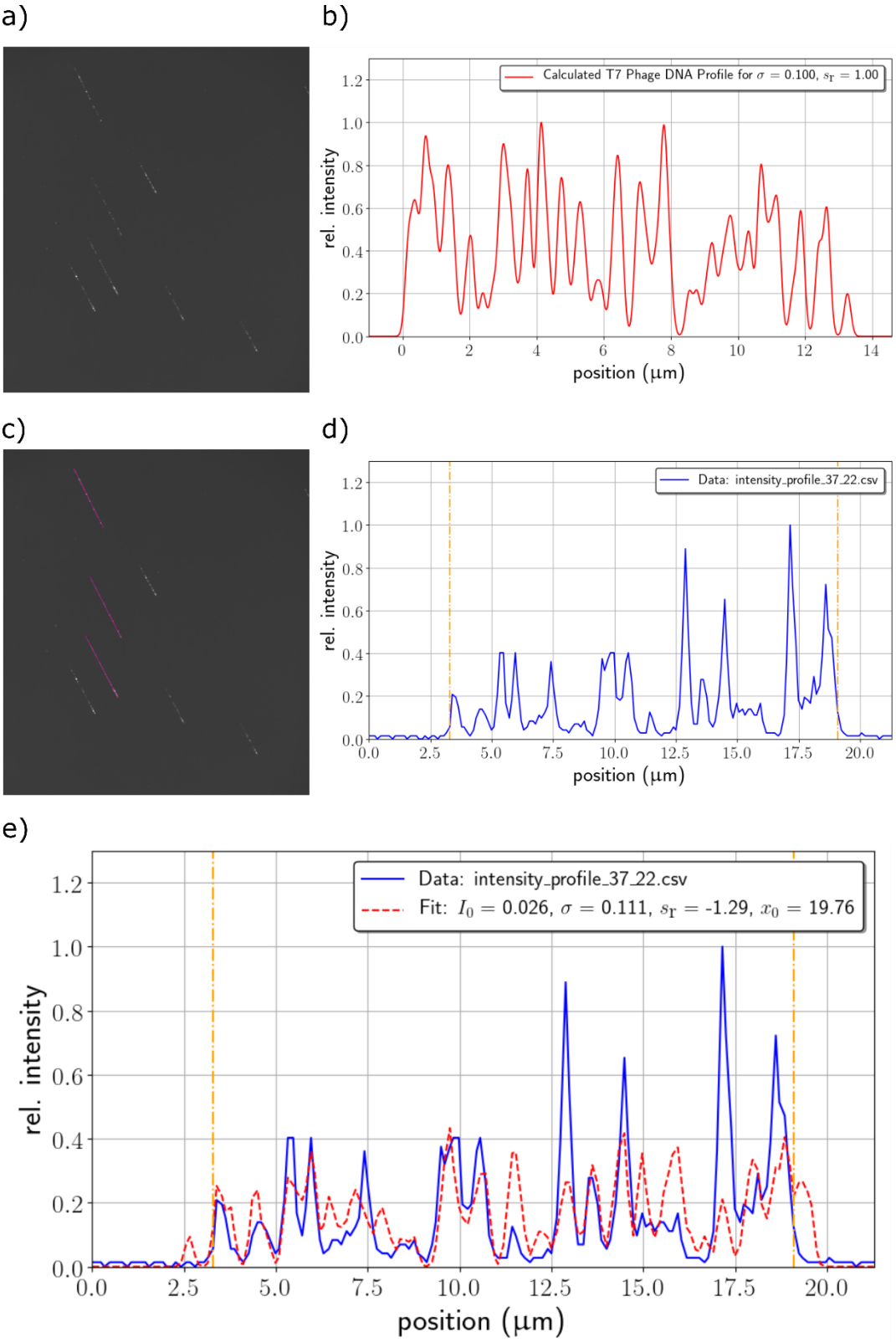

S.I. 8-40: Example image in the 561 nm channel with proportional contrast is depicted (a). The profile lines are marked in red (b). The calculated profile for T7 phage DNA is depicted in (c). A normalized experimental profile (blue) with marked fit region (yellow) is illustrated in (d). The resulting fitted profile is presented through the red-dotted line (e).

Figures

Schemes

Tables

Bibliography

Abbe, E. (1873). "Beiträge zur Theorie des Mikroskops und der mikroskopischen Wahrnehmung." Archiv für mikroskopische Anatomie **9**(1): 413-418.

Ali, M. M., et al. (2007). "Enzymatic manipulations of DNA oligonucleotides on microgel: towards development of DNA–microgel bioassays." Chemical Communications(43): 4459-4461.

Allemand, J., et al. (1997). "pH-dependent specific binding and combing of DNA." Biophysical journal **73**(4): 2064-2070.

Altshuler, D., et al. (2008). "Genetic mapping in human disease." Science **322**(5903): 881-888.

Backes, S., et al. (2017). "Poly (N-isopropylacrylamide) microgels under alcoholic intoxication: When a lcst polymer shows swelling with increasing temperature." ACS Macro Letters **6**(10): 1042-1046.

Baker, W. (1949). "Microgel, a new macromolecule." Industrial Engineering Chemistry **41**(3): 511-520.

Balamurugan, S., et al. (2005). "Reversible protein adsorption and bioadhesion on monolayers terminated with mixtures of oligo (ethylene glycol) and methyl groups." Journal of the American Chemical Society **127**(42): 14548-14549.

Barltrop, J., et al. (1966). "Photosensitive protective groups." Chemical Communications(22): 822-823.

Berndt, I. and W. Richtering (2003). "Doubly Temperature Sensitive Core− Shell Microgels." Macromolecules **36**(23): 8780-8785.

Betzig, E., et al. (2006). "Imaging intracellular fluorescent proteins at nanometer resolution." Science **313**(5793): 1642-1645.

Biggs, C. I., et al. (2015). "Thiol–ene immobilisation of carbohydrates onto glass slides as a simple alternative to gold–thiol monolayers, amines or lipid binding." Biomaterials science **3**(1): 175-181.

Bochet, C. G. (2004). "Chromatic orthogonality in organic synthesis." Synlett **2004**(13): 2268-2274.

Boott, C. E., et al. (2015). "In Situ Visualization of Block Copolymer Self-Assembly in Organic Media by Super-Resolution Fluorescence Microscopy." Chemistry–A European Journal **21**(51): 18539-18542.

Born, M. and E. Wolf (2013). Principles of optics: electromagnetic theory of propagation, interference and diffraction of light, Elsevier.

Botev, Z. I., et al. (2010). "Kernel density estimation via diffusion." The annals of Statistics **38**(5): 2916-2957.

Brautzsch, M., et al. (2016). "Sustainable, inexpensive and easy-to-use access to the super-reductant e˙− aq through 355 nm photoionization of the ascorbate dianion—an alternative to radiolysis or UV-C photochemistry." Green Chemistry **18**(17): 4761-4771.

Brown, P. O. and D. Botstein (1999). "Exploring the new world of the genome with DNA microarrays." Nature Genetics **21**(1): 33-37.

Brugnoni, M., et al. (2018). "Swelling of a responsive network within different constraints in multi-thermosensitive microgels." Macromolecules **51**(7): 2662-2671.

Buist, P. H., et al. (1995). "(S)-α-methoxyphenyl acetic acid: a new NMR chiral shift reagent for the stereochemical analysis of sulfoxides." Tetrahedron: Asymmetry **6**(1): 7-10.

Burmistrova, A., et al. (2011). "Effect of cross-linker density of P (NIPAM-co-AAc) microgels at solid surfaces on the swelling/shrinking behaviour and the Young's modulus." Colloid and Polymer Science **289**(5-6): 613-624.

Burmistrova, A., et al. (2010). "Temperature response of PNIPAM derivatives at planar surfaces: Comparison between polyelectrolyte multilayers and adsorbed microgels." Chemphyschem **11**(17): 3571-3579.

Camerin, F., et al. (2019). "Microgels Adsorbed at Liquid-Liquid Interfaces: A Joint Numerical/Experimental Study." ACS nano.

Cao, R., et al. (2004). "A recoverable enzymatic microgel based on biomolecular recognition." Journal of the American Chemical Society **126**(3): 726-727.

Carrillo, J.-M. Y., et al. (2010). "Adhesion of nanoparticles." Langmuir **26**(15): 12973-12979.

Cassie, A. (1948). "Contact angles." Discussions of the Faraday Society **3**: 11-16.

Chasles, F., et al. (2007). "Optimization and characterization of a structured illumination microscope." Optics Express **15**(24): 16130-16140.

Chen, G., et al. (2007). "Grid pattern of nanothick microgel network." Langmuir **23**(11): 5864-5867.

Ciamician, G. and P. Silber (1901). "Chemische Lichtwirkungen (Chemical effects of light)." Berichte der deutschen chemischen Gesellschaft **34**: 2040-2046.

Conley, G. M., et al. (2016). "Superresolution microscopy of the volume phase transition of pNIPAM microgels." Colloids Surfaces A: Physicochemical Engineering Aspects **499**: 18-23.

Consortium, G. P. (2010). "A map of human genome variation from population-scale sequencing." Nature **467**(7319): 1061-1073.

Cors, M., et al. (2017). "Core–Shell Microgel-Based Surface Coatings with Linear Thermoresponse." Langmuir **33**(27): 6804-6811.

Cram, D. (1965). "Fundamentals of Carbanion Chemistry, Acad." Press, New York-London: 19.

Cras, J., et al. (1999). "Comparison of chemical cleaning methods of glass in preparation for silanization." Biosensors bioelectronics **14**(8-9): 683-688.

Crick, F. (1970). "Central dogma of molecular biology." Nature **227**(5258): 561-563.

Cui, J., et al. (2013). "Light-triggered multifunctionality at surfaces mediated by photolabile protecting groups." Macromolecular Rapid Communications **34**(4): 310-329.

Das, M., et al. (2006). "Biofunctionalized pH-responsive microgels for cancer cell targeting: rational design." Advanced Materials **18**(1): 80-83.

Deen, J., et al. (2017). "Methyltransferase-Directed Labeling of Biomolecules and its Applications." Angewandte Chemie International Edition **56**(19): 5182-5200.

Dempsey, G. T., et al. (2009). "Photoswitching mechanism of cyanine dyes." Journal of the American Chemical Society **131**(51): 18192-18193.

Deng, X. and N. S. Mani (2006). "A facile, environmentally benign sulfonamide synthesis in water." Green Chemistry **8**(9): 835-838.

Dittert, L. W. and T. Higuchi (1963). "Rates of hydrolysis of carbamate and carbonate esters in alkaline solution." Journal of Pharmaceutical Sciences **52**(9): 852-857.

Donkin, I., et al. (2016). "Obesity and bariatric surgery drive epigenetic variation of spermatozoa in humans." Cell Metabolism **23**(2): 369-378.

Duda, R. O. and P. E. Hart (1972). "Use of the Hough transformation to detect lines and curves in pictures." Communications of the ACM **15**(1): 11-15.

Dunn, D. and J. Smith (1958). "The occurrence of 6-methylaminopurine in deoxyribonucleic acids." Biochemical Journal **68**(4): 627.

Dunn, J. J., et al. (1983). "Complete nucleotide sequence of bacteriophage T7 DNA and the locations of T7 genetic elements." Journal of Molecular Biology **166**(4): 477-535.

Edwards, J. R., et al. (2017). "DNA methylation and DNA methyltransferases." Epigenetics chromatin **10**(1): 23.

Eisold, S. (2018). "Dissertation: Goldnanopartikel-Hybridsysteme." publications.rwth-aachen.de.

Ekblad, T., et al. (2008). "Poly (ethylene glycol)-containing hydrogel surfaces for antifouling applications in marine and freshwater environments." Biomacromolecules **9**(10): 2775-2783.

El Beheiry, M. and M. Dahan (2013). "ViSP: representing single-particle localizations in three dimensions." Nature Methods **10**(8): 689-690.

Endesfelder, U. and M. Heilemann (2015). Direct stochastic optical reconstruction microscopy (dSTORM). Advanced fluorescence microscopy, Springer**:** 263-276.

Feinberg, A. P. and M. D. Fallin (2015). "Epigenetics at the crossroads of genes and the environment." JAMA **314**(11): 1129-1130.

Flors, C. (2010). "Photoswitching of monomeric and dimeric DNA-intercalating cyanine dyes for super-resolution microscopy applications." Photochemical Photobiological Sciences **9**(5): 643-648.

Fölling, J., et al. (2008). "Fluorescence nanoscopy by ground-state depletion and single-molecule return." Nature Methods **5**(11): 943-945.

Gao, J. and Z. Hu (2002). "Optical properties of N-isopropylacrylamide microgel spheres in water." Langmuir **18**(4): 1360-1367.

Gaulding, J. C., et al. (2012). "Reversible inter-and intra-microgel cross-linking using disulfides." Macromolecules **45**(1): 39-45.

Geisel, K., et al. (2015). "Hollow and core–shell microgels at oil–water interfaces: Spreading of soft particles reduces the compressibility of the monolayer." Langmuir **31**(48): 13145-13154.

Gelissen, A. P., et al. (2016). "3D structures of responsive nanocompartmentalized microgels." Nano Letters **16**(11): 7295-7301.

Giegrich, H., et al. (1998). "New photolabile protecting groups in nucleoside and nucleotide chemistry—synthesis, cleavage mechanisms and applications." Nucleosides Nucleotides **17**(9-11): 1987-1996.

Gilles, S., et al. (2012). "Control of cell adhesion and neurite outgrowth by patterned gold nanoparticles with tunable attractive or repulsive surface properties." Small **8**(21): 3357-3367.

Gnan, N., et al. (2017). "In silico synthesis of microgel particles." Macromolecules **50**(21): 8777-8786.

Grunwald, A., et al. (2015). "Bacteriophage strain typing by rapid single molecule analysis." Nucleic Acids Research **43**(18): e117-e117.

Gumerov, R. A., et al. (2019). "Amphiphilic microgels adsorbed at oil–water interfaces as mixers of two immiscible liquids." Soft Matter **15**(19): 3978-3986.

Gumerov, R. A., et al. (2017). "Amphiphilic arborescent copolymers and microgels: from unimolecular micelles in a selective solvent to the stable monolayers of variable density and nanostructure at a liquid Interface." ACS applied materials interfaces **9**(37): 31302-31316.

Gustafsson, M. G. (2005). "Nonlinear structured-illumination microscopy: wide-field fluorescence imaging with theoretically unlimited resolution." Proceedings of the National Academy of Sciences **102**(37): 13081-13086.

Hansen, C. M. (2002). Hansen solubility parameters: a user's handbook, CRC press.

Hansen, K. D., et al. (2011). "Increased methylation variation in epigenetic domains across cancer types." Nature Genetics **43**(8): 768.

Harnett, C., et al. (2000). "Low-energy electron-beam patterning of amine-functionalized self-assembled monolayers." Applied Physics Letters **76**(17): 2466-2468.

Hecht, E. (2001). 3. Auflage: Optik, München: Oldenbourg Wissenschaftsverlag GmbH.

Heilemann, M., et al. (2009). "Super-resolution imaging with small organic fluorophores." Angewandte Chemie International Edition **48**(37): 6903-6908.

Heilemann, M., et al. (2008). "Subdiffraction-resolution fluorescence imaging with conventional fluorescent probes." Angewandte Chemie International Edition **47**(33): 6172-6176.

Hell, S. W. (2007). "Far-field optical nanoscopy." Science **316**(5828): 1153-1158.

Hell, S. W., et al. (2003). "Imaging and writing at the nanoscale with focused visible light through saturable optical transitions." Applied Physics A **77**(7): 859-860.

Hendrickson, G. R. and L. A. Lyon (2009). "Bioresponsive hydrogels for sensing applications." Soft Matter **5**(1): 29-35.

Hendrickson, G. R. and L. A. Lyon (2010). "Microgel translocation through pores under confinement." Angewandte Chemie International Edition **49**(12): 2193-2197.

Hentschel, K. (2001). "Das Brechungsgesetz in der Fassung von Snellius." Archive for history of exact sciences **55**(4): 297-344.

Herruzo, E. T., et al. (2014). "Fast nanomechanical spectroscopy of soft matter." Nature communications **5**: 3126.

Heskins, M. and J. E. Guillet (1968). "Solution properties of poly (N-isopropylacrylamide)." Journal of Macromolecular Science—Chemistry **2**(8): 1441-1455.

Hirons, G., et al. (1994). "TOTO and YOYO: new very bright fluorochromes for DNA content analyses by flow cytometry." J Cytometry: The Journal of the International Society for Analytical Cytology **15**(2): 129-140.

Ho, D. K., et al. (1991). "Stereochemical studies of the C-methylation of deoxycytidine catalyzed by Hha I methylase and the N-methylation of deoxyadenosine catalyzed by EcoRI methylase." Archives of biochemistry biophysics **284**(2): 264-269.

Hoppe Alvarez, L. (2017). "Development of Lithographic Processes Towards targeted Surface-binding Microgels." RWTH-Aachen University.

Hoppe Alvarez, L., et al. (2019). "Deformation of Microgels at Solid–Liquid Interfaces Visualized in Three-Dimension." Nano letters **19**(12): 8862-8867.

Hough, P. V. (1962). Method and means for recognizing complex patterns, Google Patents.

Huang, B., et al. (2008). "Three-dimensional super-resolution imaging by stochastic optical reconstruction microscopy." Science **319**(5864): 810-813.

Iinuma, R., et al. (2014). "Polyhedra self-assembled from DNA tripods and characterized with 3D DNA-PAINT." Science **344**(6179): 65-69.

Islam, M. R. and M. J. Serpe (2013). "Poly (N-isopropylacrylamide) microgel-based etalons and etalon arrays for determining the molecular weight of polymers in solution." APL Materials **1**(5): 052108.

Jennings, W. B. (1975). "Chemical shift nonequivalence in prochiral groups." Chemical Reviews **75**(3): 307-322.

Jo, S. and K. Park (2000). "Surface modification using silanated poly (ethylene glycol) s." Biomaterials **21**(6): 605-616.

Johannsen, W. (1911). "The genotype conception of heredity." The American Naturalist **45**(531): 129-159.

Juette, M., et al. (2008). "3D sub-100 nm resolution by biplane fluorescence photoactivation localization microscopy." Nature Methods **5**(6): 527-529.

Karlsson, J. K., et al. (2019). "Photo-isomerization of the Cyanine Dye Alexa-Fluor 647 (AF-647) in the Context of dSTORM Super-Resolution Microscopy." Chemistry–A European Journal **25**(65): 14983-14998.

Keidel, R., et al. (2018). "Time-resolved structural evolution during the collapse of responsive hydrogels: The microgel-to-particle transition." Science advances **4**(4): eaao7086.

King, J., et al. (1992). "pH optimization of nucleophilic reactions in water." Journal of the American Chemical Society **114**(8): 3028-3033.

King, T. A., et al. (2000). Optics and photonics: an introduction, Wiley.

Klimašauskas, S. and E. Weinhold (2007). "A new tool for biotechnology: AdoMet-dependent methyltransferases." Trends in Biotechnology **25**(3): 99-104.

Kubitscheck, U. and R. Peters (2013). Fluorescence microscopy, Wiley Online Library.

Küller, A., et al. (2003). "Nanostructuring of silicon by electron-beam lithography of self-assembled hydroxybiphenyl monolayers." Applied Physics Letters **82**(21): 3776-3778.

Lam, E. T., et al. (2012). "Genome mapping on nanochannel arrays for structural variation analysis and sequence assembly." Applied physics letters **30**(8): 771.

Lander, E. S., et al. (2001). "Initial sequencing and analysis of the human genome."

Latt, S. A., et al. (1975). "Recent developments in the detection of deoxyribonucleic acid synthesis by 33258 Hoechst fluorescence." Journal of Histochemistry Cytochemistry **23**(7): 493-505.

Le Pecq, J.-B. and C. Paoletti (1966). "A new fluorometric method for RNA and DNA determination." Analytical Biochemistry **17**(1): 100-107.

Lebofsky, R. and A. Bensimon (2003). "Single DNA molecule analysis: applications of molecular combing." Briefings in Functional Genomics **1**(4): 385-396.

Léonforte, F. and M. Müller (2015). "Poly (N-isopropylacrylamide)-based mixed brushes: a computer simulation study." ACS applied materials interfaces **7**(23): 12450-12462.

Lercel, M., et al. (1996). "Sub-10 nm lithography with self-assembled monolayers." Applied Physics Letters **68**(11): 1504-1506.

Lester, G. (1961). "Contact angles of liquids at deformable solid surfaces." Journal of Colloid Science **16**(4): 315-326.

Levy-Sakin, M. and Y. Ebenstein (2013). "Beyond sequencing: optical mapping of DNA in the age of nanotechnology and nanoscopy." Current Opinion in Biotechnology **24**(4): 690-698.

Levy-Sakin, M., et al. (2014). "Toward single-molecule optical mapping of the epigenome." ACS nano **8**(1): 14-26.

Levy, J. A. and R. J. Huebner (1970). "Association of murine leukaemia virus from a Mouse lymphoma (2731/L) with reovirus Type 3 infection." Nature **225**(5236): 949-950.

Li, B., et al. (2019). "Goosebumps-Inspired Microgel Patterns with Switchable Adhesion and Friction." Small **15**(35): 1902376.

Liu, Y.-Y., et al. (2004). "Ionic effect on combing of single DNA molecules and observation of their force-induced melting by fluorescence microscopy." The Journal of Chemical Physics **121**(9): 4302-4309.

Lopez, V. C., et al. (2005). "The use of colloidal microgels as a (trans) dermal drug delivery system." International Journal of Pharmaceutics **292**(1-2): 137-147.

Lowe, A. B. (2014). "Thiol-yne 'click'/coupling chemistry and recent applications in polymer and materials synthesis and modification." Polymer **55**(22): 5517-5549.

Lu, Y. and M. Drechsler (2009). "Charge-induced self-assembly of 2-dimensional thermosensitive microgel particle patterns." Langmuir **25**(22): 13100-13105.

Lynn, D. M., et al. (2001). "pH-responsive polymer microspheres: Rapid release of encapsulated material within the range of intracellular pH." Angewandte Chemie International Edition **40**(9): 1707-1710.

Markovich, I. and D. Mandler (2001). "Preparation and characterization of octadecylsilane monolayers on indium–tin oxide (ITO) surfaces." Journal of Electroanalytical Chemistry **500**(1-2): 453-460.

Menz, W. and O. Paul (2012). Mikrosystemtechnik für Ingenieure, John Wiley & Sons.

Merrifield, R., et al. (1977). "Peptides, Proceedings of the Fifth American Peptide Symposium." John Wiley, New York: 488.

Metzker, M. L. (2010). "Sequencing technologies—the next generation." Nature Reviews Genetics **11**(1): 31-46.

Michaeli, Y. and Y. Ebenstein (2012). "Channeling DNA for optical mapping." Nature Biotechnology **30**(8): 762-763.

Michalet, X., et al. (1997). "Dynamic molecular combing: stretching the whole human genome for high-resolution studies." Science **277**(5331): 1518-1523.

Möckl, L., et al. (2014). "Super-resolved Fluorescence Microscopy: Nobel Prize in Chemistry 2014 for Eric Betzig, Stefan Hell, and William E. Moerner." Angewandte Chemie International Edition **53**(51): 13972-13977.

Mortensen, K. I., et al. (2010). "Optimized localization analysis for single-molecule tracking and super-resolution microscopy." Nature Methods **7**(5): 377.

Mourran, A., et al. (2016). "When colloidal particles become polymer coils." Langmuir **32**(3): 723-730.

Müller, B. (1989). Ein Beitrag zur Untersuchung der Elektronenstreuung und des Proximityeffektes an den Rändern inhomogener Strukturen bei der Elektronenstrahldirektbelichtung.

Müller, V. and F. Westerlund (2017). "Optical DNA mapping in nanofluidic devices: principles and applications." Lab on a Chip **17**(4): 579-590.

Murthy, N., et al. (2002). "A novel strategy for encapsulation and release of proteins: hydrogels and microgels with acid-labile acetal cross-linkers." Journal of the American Chemical Society **124**(42): 12398-12399.

Murthy, N., et al. (2003). "A macromolecular delivery vehicle for protein-based vaccines: acid-degradable protein-loaded microgels." Proceedings of the National Academy of Sciences, USA **100**(9): 4995-5000.

Nath, N. and A. Chilkoti (2004). "Label-free biosensing by surface plasmon resonance of nanoparticles on glass: optimization of nanoparticle size." Analytical Chemistry **76**(18): 5370-5378.

Nayak, S., et al. (2004). "Folate-mediated cell targeting and cytotoxicity using thermoresponsive microgels." Journal of the American Chemical Society **126**(33): 10258-10259.

Nayak, S. and L. A. Lyon (2005). "Soft nanotechnology with soft nanoparticles." Angewandte Chemie International Edition **44**(47): 7686-7708.

Neely, R. K., et al. (2011). "Optical mapping of DNA: Single-molecule-based methods for mapping genomes." Biopolymers **95**(5): 298-311.

Nevskyi, O., et al. (2016). "Nanoscopic visualization of soft matter using fluorescent diarylethene photoswitches." Angewandte Chemie International Edition **55**(41): 12698-12702.

Nevskyi, O., et al. (2018). Diarylethene photoswitches for super-resolution microscopy in polymer science, RWTH-Aachen University.

Nikolov, S., et al. (2018). "Mesoscale modeling of microgel mechanics and kinetics through the swelling transition." Applied Mathematics and Mechanics **39**(1): 47-62.

Nolan, C. M., et al. (2005). "Phase transition behavior, protein adsorption, and cell adhesion resistance of poly (ethylene glycol) cross-linked microgel particles." Biomacromolecules **6**(4): 2032-2039.

Nyström, L. and M. Malmsten (2016). "Surface-bound microgels—From physicochemical properties to biomedical applications." Advances in Colloid and Interface Science **238**: 88-104.

Ohtsuka, E., et al. (1974). "Studies on transfer ribonucleic acids and related compounds. IX (1) Ribo-oligonucleotide synthesis using a photosensitive o-nitrobenzyl protection at the 2′-hydroxyl group." Nucleic Acids Research **1**(10): 1351-1358.

Ostuni, E., et al. (2001). "A survey of structure− property relationships of surfaces that resist the adsorption of protein." Langmuir **17**(18): 5605-5620.

Ovesný, M., et al. (2014). "ThunderSTORM: a comprehensive ImageJ plug-in for PALM and STORM data analysis and super-resolution imaging." Bioinformatics **30**(16): 2389-2390.

Paige, C. C. and M. A. Saunders (1982). "LSQR: An algorithm for sparse linear equations and sparse least squares." ACM Transactions on Mathematical Software **8**(1): 43-71.

Parthasarathy, R. (2012). "Rapid, accurate particle tracking by calculation of radial symmetry centers." Nature Methods **9**(7): 724.

Pavani, S. R. P., et al. (2009). "Three-dimensional, single-molecule fluorescence imaging beyond the diffraction limit by using a double-helix point spread function." Proceedings of the National Academy of Sciences, USA **106**(9): 2995-2999.

Pelton, R. (2000). "Temperature-sensitive aqueous microgels." Advances in colloid interface science **85**(1): 1-33.

Peng, J., et al. (2013). "Cool Microcontact Printing To Fabricate Thermosensitive Microgel Patterns." **29**(38): 11809-11814.

Pepperkok, R. and J. J. N. r. M. c. b. Ellenberg (2006). "High-throughput fluorescence microscopy for systems biology." **7**(9): 690-696.

Pich, A. and W. Richtering (2010). Microgels by precipitation polymerization: synthesis, characterization, and functionalization. Chemical Design of Responsive Microgels, Springer**:** 1-37.

Plamper, F. A. and W. Richtering (2017). "Functional microgels and microgel systems." Accounts of Chemical Research **50**(2): 131-140.

Portnov, I. V., et al. (2018). "Microgel in a Pore: Intraparticle Segregation or Snail-like Behavior Caused by Collapse and Swelling." Macromolecules **51**(20): 8147-8155.

Poulter, N. S., et al. (2015). The physical basis of total internal reflection fluorescence (TIRF) microscopy and its cellular applications. Advanced Fluorescence Microscopy, Springer**:** 1-23.

Pray, L. (2008). "Discovery of DNA structure and function: Watson and Crick." Nature Education **1**(1): 100.

Quan, T., et al. (2010). "Localization capability and limitation of electron-multiplying charge-coupled, scientific complementary metal-oxide semiconductor, and charge-coupled devices for superresolution imaging." Journal of Biomedical Optics **15**(6): 066005.

Rey, M., et al. (2017). "Interfacial arrangement and phase transitions of PNiPAm microgels with different crosslinking densities." Soft Matter **13**(46): 8717-8727.

Rumyantsev, A. M., et al. (2016). "A polymer microgel at a liquid–liquid interface: theory vs. computer simulations." Soft Matter **12**(32): 6799-6811.

Rye, H. S., et al. (1992). "Stable fluorescent complexes of double-stranded DNA with bis-intercalating asymmetric cyanine dyes: properties and applications." Nucleic Acids Research **20**(11): 2803-2812.

Sachs, F. and S. Hilpert (1904). "Chemische Lichtwirkungen." Berichte der deutschen chemischen Gesellschaft **37**(3): 3425-3431.

Saunders, B. R., et al. (2009). "Microgels: From responsive polymer colloids to biomaterials." Advances in Colloid and Interface Science **147**: 251-262.

Schaal, P. A. and U. Simon (2013). Erzeugung metallischer Nanostrukturen auf silanisierten, oxidischen Oberflächen durch chemische Elektronenstrahllithographie, Nanopartikelimmobilisierung und stromlose Metallabscheidung, RWTH-Aachen University.

Schmidt, S., et al. (2008). "Packing density control in P (NIPAM-co-AAc) microgel monolayers: effect of surface charge, pH, and preparation technique." Langmuir **24**(21): 12595-12602.

Schmidt, S., et al. (2010). "Adhesion and mechanical properties of PNIPAM microgel films and their potential use as switchable cell culture substrates." Advanced Functional Materials **20**(19): 3235-3243.

Schmolze, D. B., et al. (2011). "Advances in microscopy techniques." Archives of Pathology and Laboratory Medicine **135**(2): 255-263.

Schneider, C. A., et al. (2012). "NIH Image to ImageJ: 25 years of image analysis." Nature Methods **9**(7): 671-675.

Schulte, M. F., et al. (2019). "Tuning the Structure and Properties of Ultra-Low Cross-Linked Temperature-Sensitive Microgels at Interfaces via the Adsorption Pathway." Langmuir **35**(46): 14769-14781.

Schulte, M. F., et al. (2018). "Probing the Internal Heterogeneity of Responsive Microgels Adsorbed to an Interface by a Sharp SFM Tip: Comparing Core–Shell and Hollow Microgels." Langmuir **34**(14): 4150-4158.

Scotti, A., et al. (2019). "Exploring the colloid-to-polymer transition for ultra-low crosslinked microgels from three to two dimensions." Nature communications **10**(1): 1418.

Serpe, M. J., et al. (2005). "Doxorubicin uptake and release from microgel thin films." Biomacromolecules **6**(1): 408-413.

Sharim, H., et al. (2019). "Long-read single-molecule maps of the functional methylome." Genome Research **29**(4): 646-656.

Sharma, S., et al. (2010). "Epigenetics in cancer." Carcinogenesis **31**(1): 27-36.

Shendure, J., et al. (2017). "DNA sequencing at 40: past, present and future." Nature **550**(7676): 345-353.

Shin, E., et al. (2016). "Differential expression of the epigenetic methylation-related protein DNMT1 by breast cancer molecular subtype and stromal histology." Journal of Translational Medicine **14**(1): 87.

Shtengel, G., et al. (2009). "Interferometric fluorescent super-resolution microscopy resolves 3D cellular ultrastructure." Proceedings of the National Academy of Sciences of the United States of America **106**(9): 3125-3130.

Siemes, E., et al. (2018). "Nanoscopic visualization of cross-linking density in polymer networks with diarylethene photoswitches." Angewandte Chemie International Edition **57**(38): 12280-12284.

Sisan, D. R., et al. (2006). "Spatially resolved fluorescence correlation spectroscopy using a spinning disk confocal microscope." Biophysical Journal **91**(11): 4241-4252.

Smiley-Wiens, J. B. and M. J. Serpe (2013). "Solvent exchange kinetics in poly (N-isopropylacrylamide) microgel-based etalons." Colloid and Polymer Science **291**(4): 971-979.

Snape, M. L. (2017). Increasing the Imaging Speed of Stochastic Optical Reconstruction Microscopy, University of Sheffield.

Song, X., et al. (2018). "Deswelling Dynamics of Thermoresponsive Microgel Capsules and Their Ultrasensitive Sensing Applications: A Mesoscopic Simulation Study." The Journal of Physical Chemistry B **123**(3): 1828-1838.

Sorrell, C. D. and M. J. Serpe (2012). "Glucose sensitive poly (N-isopropylacrylamide) microgel based etalons." Analytical and Bioanalytical Chemistry **402**(7): 2385-2393.

Staudinger, H. and E. Husemann (1935). "Über hochpolymere verbindungen, 118. Mitteil.: Viscositäts-untersuchungen an organischen sphäro-und linear-kolloiden." Berichte der deutschen chemischen Gesellschaft **68**(9): 1691-1697.

Thompson, R. E., et al. (2002). "Precise nanometer localization analysis for individual fluorescent probes." Biophysical Journal **82**(5): 2775-2783.

Treangen, T. J. and S. L. Salzberg (2012). "Repetitive DNA and next-generation sequencing: computational challenges and solutions." Nature Reviews Genetics **13**(1): 36-46.

Tsumagari, K., et al. (2010). "FSH dystrophy and a subtelomeric 4q haplotype: a new assay and associations with disease." Journal of Medical Genetics **47**(11): 745-751.

Uhlig, K., et al. (2016). "Patterned thermoresponsive microgel coatings for noninvasive processing of adherent cells." Biomacromolecules **17**(3): 1110-1116.

Valdés-Mora, F. and C. Stirzaker (2018). Epigenetic alterations in primary prostate cancer. Precision Molecular Pathology of Prostate Cancer, Springer**:** 193-211.

Varma, M. V., et al. (2005). "Influence of micro-environmental pH on the gel layer behavior and release of a basic drug from various hydrophilic matrices." Journal of Controlled Release **103**(2): 499-510.

Vasu, K. and V. Nagaraja (2013). "Diverse functions of restriction-modification systems in addition to cellular defense." Microbiol. Mol. Biol. Rev. **77**(1): 53-72.

Vega, M. C., et al. (1994). "Three-dimensional crystal structure of the A-tract DNA dodecamer d (CGCAAATTTGCG) complexed with the minor-groove-binding drug Hoechst 33258." European journal of biochemistry **222**(3): 721-726.

Vieu, C., et al. (2000). "Electron beam lithography: resolution limits and applications." Applied surface science **164**(1-4): 111-117.

Vinogradov, S. V. (2006). "Colloidal microgels in drug delivery applications." Current Pharmaceutical Design **12**(36): 4703-4712.

Virani, S., et al. (2012). "Cancer epigenetics: a brief review." ILAR journal **53**(3-4): 359-369.

von Fraunhofer, J. (1823). Kurzer Bericht von den Resultaten neuerer Versuche über die Gesetze des Lichtes, und die Theorie derselben, publisher not identified.

Walbert, S. (2003). Mechanistische Untersuchungen zur Abspaltung photolabiler Schutzgruppen, Der Andere Verlag.

Waring, M. (1965). "Complex formation between ethidium bromide and nucleic acids." Journal of molecular biology **13**(1): 269-282.

Waser, R., et al. (2004). "Nanoelectronics and information technology: Advanced electronic materials and novel devices." MRS BULLETIN

Watson, J. D. (1990). "The human genome project: past, present, and future." Science **248**(4951): 44-49.

Watson, J. D. and F. H. Crick (1953). "Molecular structure of nucleic acids." Nature **171**(4356): 737-738.

Wedel, B., et al. (2016). "Smart homopolymer microgels: Influence of the monomer structure on the particle properties." Polymers **8**(4): 162.

Wellert, S., et al. (2015). "Ethylene Glycol-Based Microgels at Solid Surfaces: Swelling Behavior and Control of Particle Number Density." Langmuir **31**(7): 2202-2210.

Wellert, S., et al. (2015). "Responsive microgels at surfaces and interfaces." Zeitschrift für Physikalische Chemie **229**(7-8): 1225-1250.

Wells, R., et al. (1970). "Physicochemical studies on polydeoxyribonucleotides containing defined repeating nucleotide sequences." Journal of Molecular Biology **54**(3): 465-497.

Whelan, D. R. and T. D. Bell (2015). "Super-resolution single-molecule localization microscopy: tricks of the trade." The journal of physical chemistry letters **6**(3): 374-382.

Whelan, D. R., et al. (2014). "Focus on super-resolution imaging with direct stochastic optical reconstruction microscopy (dSTORM)." Australian Journal of Chemistry **67**(2): 179-183.

Witte, J., et al. (2019). "A comparison of the network structure and inner dynamics of homogeneously and heterogeneously crosslinked PNIPAM microgels with high crosslinker content." Soft Matter **15**(5): 1053-1064.

Wöll, D. and C. Flors (2017). "Super-resolution Fluorescence Imaging for Materials Science." Small Methods **1**(10): 1700191.

Wöll, D. F. (2006). Neue photolabile Schutzgruppen mit intramolekularer Sensibilisierung: Synthese, photokinetische Charakterisierung und Anwendung für die DNA-Chip-Synthese, Universität Konstanz.

Wong, W. S., et al. (2020). "Microdroplet Contaminants: When and Why Superamphiphobic Surfaces Are Not Self-Cleaning." ACS nano

Woodward, N. C., et al. (2003). "Calorimetric investigation of the influence of cross-linker concentration on the volume phase transition of poly (N-isopropylacrylamide) colloidal microgels." Langmuir **19**(8): 3202-3211.

Wu, S., et al. (2018). "Microfluidic DNA combing for parallel single-molecule analysis." Nanotechnology **30**(4): 045101.

Wuts, P. G. and T. W. Greene (2006). Greene's protective groups in organic synthesis, John Wiley & Sons.

Yakovchuk, P., et al. (2006). "Robert J. Fisher, Matthew J. Fivash, Andrew G. Stephen, Nathan A. Hagan, Shilpa R. Shenoy, Maxine V. Medaglia, Lindsey R. Smith, Karen M. Worthy, John T. Simpson, Robert Shoemaker, Karen L. McNitt, Donald G. Johnson, Catherine V. Hixson, Robert J. Gorelick, Daniele Fabris, Louis E. Henderson and Alan Rein Nucleic Acids Res.(2006) 34, 472–484." Nucleic Acids Research **34**(3): 472-484.

Young, T. (1805). "III. An essay on the cohesion of fluids." Philosophical Transactions of the Royal Society of London(95): 65-87.

Yu, Q., et al. (2011). "Anti-fouling bioactive surfaces." Acta Biomaterialia **7**(4): 1550-1557.

Zeidler, J. (1994). Lithographie und Steindruck: in Gewerbe und Kunst, Technik und Geschichte, Ravensburger Buchverl.

Zhang, J., et al. (2004). "Polymer microgels: reactors for semiconductor, metal, and magnetic nanoparticles." Journal of the American Chemical Society **126**(25): 7908-7914.

Zharnikov, M., et al. (1999). "Modification of alkanethiolate monolayers on Au-substrate by low energy electron irradiation: Alkyl chains and the S/Au interface." Physical Chemistry Chemical Physics **1**(13): 3163-3171.

Zharnikov, M., et al. (2002). "Modification of thiol-derived self-assembling monolayers by electron and x-ray irradiation: Scientific and lithographic aspects." Journal of Vacuum Science **20**(5): 1793-1807.